

TBX3 and HAND2 Controlled Gene Regulatory Networks in Establishment of Axis Polarity in Mouse Limb Buds

Inauguraldissertation

zur

Erlangung der Würde eines Doktors der Philosophie

vorgelegt der

Philosophisch-Naturwissenschaftlichen Fakultät

der Universität Basel

von

Aušra Girdžiūšaitė

Basel, 2020

“Originaldokument gespeichert auf dem Dokumentenserver der Universität Basel

<https://edoc.unibas.ch>”

Genehmigt von der Philosophisch-Naturwissenschaftlichen Fakultät auf Antrag von

Prof. Dr. Rolf Zeller (Erstbetreuer), Prof. Dr. Markus Affolter (Zweitbetreuer), Prof. Dr. Sebastian Arnold (externer Experte)

Basel, 23. June 2020

Dekan Prof. Dr. Martin Spiess

1. Table of content

1. Table of content	3
2. Summary	7
3. List of abbreviations	9
4. Introduction	10
4.1 Limb development	10
4.1.1 Basic concepts of limb development	10
4.1.2 Signaling centers controlling limb bud development	11
4.1.3 Limb bud initiation	11
4.1.4 Proximo-distal limb axis patterning.....	12
4.1.4.1 The FGF feedback loop controls PD limb outgrowth.....	12
4.1.4.2 The functions of retinoic acid in PD limb bud outgrowth	13
4.1.4.3 <i>Hox</i> genes and their role in PD axis formation	14
4.1.5 AP axis patterning in mouse limb buds	15
4.1.5.1 <i>Shh</i> activation in the limb bud mesenchyme.....	15
4.1.5.2 SHH protein and SHH pathway in the limb.....	15
4.1.5.3 The SHH pathway in AP digit patterning	17
4.1.6 The self-regulatory feedback signaling system links AP and PD limb bud axis development.....	18
4.1.7 Limb mesenchymal polarization upstream of morphogenetic signaling	19
4.2 TBX3 is a key regulator of embryonic development	20
4.2.1 T-box transcriptional regulators.....	20
4.2.2 T-box domain.....	21
4.2.3 T-box family members in limb development.....	22
4.2.4 TBX4 and TBX5 mark the forelimb and hindlimb field	23
4.2.5 <i>Tbx2</i> and <i>Tbx3</i> function in limb bud development	24
4.2.5.1 TBX2 regulates limb bud outgrowth	25
4.2.5.2 TBX3 is essential for limb bud development	25
4.2.6 TBX3 functions in embryonic development and disease	28
4.2.6.1 TBX3 functions during mammary gland development	28
4.2.6.2 TBX3 in heart development.....	29
4.2.6.3 The human ulnar-mammary syndrome (UMS).....	30
4.2.7 <i>Cis</i> -regulatory modules in embryonic development	32
5 Aim of the thesis	35
6 Results	37
6.1 Identification of the direct targets of HAND2 during heart development.....	37
6.2 Identification of the genes regulated by TBX3 genes during mouse forelimb bud development.....	60
6.2.1 Validation of the <i>Tbx3</i> -deficient embryos as a tool for transcriptional profiling	60
6.2.2 Comparative transcriptome analysis of WT and <i>Tbx3</i> -deficient forelimb buds..	60

6.2.3	Identification of the TBX3 target CRMs during limb bud pre-patterning: the necessity to develop a new tool	62
6.2.3.1	Generation of <i>Tbx3</i> ^{3xFLAG} mice by CRISPR/ <i>Cas9</i> genome editing technology.....	64
6.2.3.2	<i>Tbx3</i> ^{3xF} allele is a new sensitive tool to detect endogenous TBX3 proteins via the 3xFLAG epitope tag.....	66
6.2.4	The TBX3 cistrome in mouse limb buds is identified using the <i>Tbx3</i> ^{3xF} allele...68	
6.2.5	Identification of the TBX3 transcriptional target genes and GRNs.....	71
6.2.6	Validation of TBX3 interacting CMRs in the landscapes of TBX3 target genes 73	
6.2.6.1	Bioinformatical analysis of TBX3 interacting CMRs	74
6.2.6.2	TBX3 interacts with CRM enhancers in the <i>Gli3 cis</i> -regulatory landscape 74	
6.2.6.3	TBX3 interacts with CRMs in the <i>Hand2 cis</i> -regulatory landscape.....	76
6.2.6.4	TBX3 interacts with CRM enhancers in the <i>Tbx3 cis</i> -regulatory landscape	79
6.2.6.5	TBX3 interacts with a CRM in the <i>Tbx2 cis</i> -regulatory landscape	79
6.2.6.6	TBX3 interacts with a CRM enhancer in the of <i>Lmo1 cis</i> -regulatory landscape.....	82
6.2.7	Comparative RNA-seq analysis of <i>Hand2</i> -deficient forelimb buds	82
6.2.8	Identification of unique TBX3 and shared targets with HAND2 during the onset of limb bud development	87
6.2.9	Spatiotemporal TBX3 and HAND2 controlled gene regulatory networks analysis in early forelimb buds	87
6.2.9.1	TBX3 and HAND2 functions AP limb bud axis patterning	89
6.2.9.2	TBX3 and HAND2 functions in patterning of the proximal-distal limb bud axis	93
6.2.10	In <i>Tbx3</i> - deficient mouse embryos early limb skeletal patterning is disrupted94	
6.2.11	TBX3-specific GRNs.....	95
7	Discussion.....	98
7.1	Identification of TBX3 target gene regulatory networks that function during early limb morphogenesis.....	98
7.2	Unbiased genome-wide analysis of the TBX3 cistrome.....	98
7.3	TBX3 transcriptional targets in early limb buds: direct and indirect interactions ...99	
7.4	TBX3 is an important epigenetic regulator of development.....	100
7.5	TBX3 auto-regulation in the early mouse forelimb buds	103
7.6	TBX3 regulates <i>Tbx2</i> in the early mouse forelimb buds	104
7.7	TBX3 functions in establishing limb bud mesenchymal axis polarity	105
7.8	TBX3 and HAND2 chromatin complexes regulate early limb bud axis polarization in a context dependent manner	106
7.9	TBX3 and HAND2 controlled GRNs during early mouse forelimb bud development.....	107

7.10	Evidence for altered retinoic acid pathway activity in <i>Tbx3</i> -deficient forelimb buds.	109
7.11	The role of the cellular environment for mammalian limb bud development	111
8	Conclusion and outlook	114
9	Material and methods	116
9.1	Mouse husbandry and experiments with mouse embryos	116
9.1.1	Ethics statement	116
9.1.2	Mouse strains and genotyping	116
9.1.3	Digoxigenin-labelled antisense riboprobe generation	116
9.1.4	Whole-mount <i>in situ</i> hybridization (WISH)	117
9.1.5	Lysotracker	119
9.1.6	Superovulation of females for oocyte collection	119
9.1.7	Pseudo-pregnant females priming for embryos implanting	119
9.2	Generation of the transgenic mouse line using CRISPR/<i>Cas9</i> genome editing	120
9.2.1	Genetic engineering of the single guide RNA (sgRNA) guides and repair templates constructs	120
9.3	Mammalian cell culture	121
9.3.1	Feeder cells culture	121
9.3.2	Embryonic Stem (ES) cell culture	123
9.3.3	ES cell transfection and positive clone selection	124
9.3.4	ES cells preparation for aggregation	124
9.4	Molecular Biology	125
9.4.1	General cloning procedures	125
9.4.2	RNA extraction from embryonic tissues for the cDNA synthesis	125
9.4.3	Quantitative PCR (qPCR) and ChIP-qPCR	126
9.4.4	Western Blot analysis	127
9.4.5	Silver staining	128
9.5	Next generation sequencing (NGS)	129
9.5.1	RNA Sequencing (RNA-seq)	129
9.5.2	ChIP-seq to identify TBX3 ^{3xF} cistrome in forelimb buds	130
9.5.3	ChIP-seq library synthesis and purification	132
9.6	Histology	132
9.6.1	Murine chromosome counting	132
9.6.2	Embryo embedding in O.C.T compound for cryosectioning	133
9.6.3	Immunohistochemistry using frozen sections	134
9.6.4	Immunocytochemistry for ESCs	134
9.7	Bioinformatical analysis: online tools and resources	135
9.8	Tables	135

9.8.1	Genotyping primers for mice and embryos	135
9.8.2	WISH screen probes cloning primers table	135
9.8.3	CRISPR/Cas9 sgRNA for cloning into p459.V2.0 plasmid	136
9.8.4	List of primary antibodies	136
9.8.5	List of secondary antibodies	136
9.8.6	qPCR primers table	137
9.8.7	ChIP-qPCR primers table	137
10	Acknowledgments	138
11	Bibliography	140
12	Appendix.....	164
12.1	List of 130 common DEGs identified by overlapping <i>Tbx3</i> - and <i>Hand2</i> - deficient forelimb bud transcriptomes.	168
12.2	List of 140 direct transcriptional targets of TBX3.....	172
12.3	List of 53 direct transcriptional targets of TBX3 that also common DEGs in <i>Hand2</i> -deficient mouse forelimb buds.....	176
12.4	List of 87 direct transcriptional targets of TBX3 that are unique to TBX3.....	177
12.5	List of 410 direct transcriptional targets of HAND2	180
12.6	List of 39 common direct transcriptional targets of TBX3 and HAND2	183
12.9	Collaboration: HAND2 and PBX coordinately control early hindlimb bud development.....	195
13	CV.....	202

2. Summary

The limb bud is an outstanding model to study the precise control of the spatial and temporal developmental genes expression and its alterations resulting in phenotypic manifestations. The limb bud outgrowth and patterning is governed by a mesenchymal organizing center called the zone of polarizing activity (ZPA). The ZPA secretes the Sonic Hedgehog (SHH) morphogen that patterns the limb bud mesenchyme along its anterior-posterior (AP) axis. However, the limb bud mesenchymal AP polarity is already set before *Shh* expression is activated. The AP polarity in the nascent mesenchyme is established by a mutually antagonistic interaction which restricts the GLI3 repressor isoform to the anterior and the HAND2 transcription factor to the posterior mesenchyme (Galli et al., 2010; Osterwalder et al., 2014; te Welscher et al., 2002). However, HAND2 itself is not sufficient to establish a sharp boundary between the *Hand2* and *Gli3* expression domains but also requires *Tbx3*, which is itself a direct transcriptional target of HAND2. Genetic analysis has shown that TBX3 participates in positioning the posterior *Gli3* expression boundary by inhibiting its expression in the posterior mesenchyme (Osterwalder et al., 2014). Prior to my study, the transcriptional target and networks governed by TBX3 during the establishment of AP limb bud polarity were mostly unknown. Thus, to identify the *trans*-acting interactions of TBX3 with the *cis*-regulatory modules (CRMs) located in the genomic landscapes of candidate target genes, I performed an unbiased genome-wide ChIP-seq analysis. As there is no ChIP-seq grade antibody, I first had to insert a 3xFLAG epitope tag into endogenous TBX3 protein using CRISPR/*Cas9* genome editing in the mouse. The resulting *Tbx3*^{3xF} allele provided me with a highly sensitive tool to detect TBX3 in embryonic stem cells and embryonic tissues. Therefore, I was able to use this allele for TBX3^{3xF} ChIP-seq analysis during the critical stages of early mouse forelimb bud development. By intersecting different genome-wide TBX3^{3xF} and HAND2^{3xF} ChIP-seq with ATAC-seq and RNA-seq datasets, I was able to identify both TBX3-specific gene regulatory networks (GRNs), and GRNs shared with HAND2. Follow-up analysis identified the TBX3-specific and shared target genes that function in mesenchymal AP polarity establishment during the onset of limb bud development. By combining gene regulatory network analysis with a whole-mount *in situ* hybridization (WISH) screen, I gained insights into *Tbx3*-deficiency-related limb skeletal phenotypes that affect AP and proximal-distal (PD) axis patterning. Furthermore, my analysis showed that TBX3 transcriptional complexes interact with CRMs in the *Gli3* *cis*-regulatory landscape, possibly contributing to repression to its expression from the posterior limb bud

mesenchyme. In addition, my analysis reveals the existence of the TBX3 autoregulatory loop. Finally, the in-depth analysis showed that both TBX3 and HAND2 interact with CRMs in the *Tbx2*, *Lmo1*, and *Gli3* cis-regulatory landscapes. I was also involved in a second project, which revealed an unexpected essential function of HAND2 in heart valve development. In particular, HAND2 is a key regulator of the endothelial-mesenchymal transition (EMT) of atrioventricular canal (AVC) cells that initiate cardiac cushion formation, which subsequently will give rise to the mitral and tricuspid valves.

Taken together, my PhD project sheds light onto the TBX3-specific and HAND2 shared GRNs that have essential morpho-regulatory functions during mouse embryonic development.

3. List of abbreviations

a.a.	amino acid	H3K27me3	histone 3 lysine 27 trimethylation
AB	antibody	H3K4me3	histone 3 lysine 4 trimethylation
AER	Apical Ectodermal Ridge	HL	hindlimb
AP	antero-posterior	HLB	hindlimb bud
ATAC	Assay for Transposase-Accessible Chromatin	IF	immunofluorescence
AVC	atrioventricular canal	IM	intermediate mesoderm
AVN	atrioventricular node	l	liter
BB/BA	Benzyl Benzoate/Benzyl Alcohol	lacZ	Beta-galactosidase gene
BCA	bicinchoninic acid	LB	limb buds
bHLH	basic Helix-Loop-Helix	LIF	Leukemia Inhibitory Factor
BMP	Bone Morphogenetic Protein	LPM	Lateral Plate Mesoderm
bp	base pair	ml	milliliter
°C	Celsius	NGS	Next Generation Sequencing
cDNA	complementary DNA	O.C.T.	Optimum Cutting Temperature
ChIP	chromatin immunoprecipitation	OFT	outflow tract
Cq	relative quantification cycle	ON	overnight
CRISPR	Clustered Regulatory Interspaced Short Palindromic Repeats	ORF	Open Reading Frame
CRM	<i>cis</i> -regulatory module	PAM	Protospacer Adjacent Motif
CTCF	CCCTG-binding factor	PBS	Phosphate Buffered Saline
DEG	Differentially Expressed Gene	PBT	PBS, 0.1% Tween
dig-UTP	digoxigenin-labelled uracil	PD	proximo-distal
DMEM	<i>Dulbecco's Modified Eagle Medium</i>	PFA	paraformaldehyde
DMSO	Dimethyl sulfoxide	PGR	Polymerase Chain Reaction
DPBS	desalinated PBS	PK	Proteinase K
DV	dorso-ventral	pIDNA	plasmid DNA
E	embryonic day	polyA	polyadenylation
ECM	extracellular matrix	qPCR	quantitative PCR
EDTA	Ethylenediaminetetraacetic acid	RA	Retinoic Acid
EMFI	embryonic mouse fibroblast	RNA-seq	RNA Sequencing
EMT	Epithelial-Mesenchymal Transition	rpm	revolutions per minute
ES cells	Embryonic Stem Cells	RT	room temperature
FCS	Fetal Calf Serum	RT-qPCR	Real-time quantitative PCR
FGF	Fibroblast Growth Factor	s	somites
FL	forelimb	SAN	sinoatrial node
FLB	forelimb bud	SDS	Sodium Dodecyl Sulfate
g	g-force	sgRNA	single guided RNA
gDNA	genomic DNA	SHH	Sonic Hedgehog
GLI3	Kruppel family member GLI3	SNAI1	Snail family zinc finger 1
GO	Gene Ontology	ssODN	single stranded ultramer DNA oligo
GREAT	Genomic Regions Enrichment Annotation Tool	TAD	Topologically Associated Domain
GRN	Gene Regulatory Network	TF	Transcription Factor
h	hours	TSS	Transcriptional Start Site
HAND2	Heart, Autonomic nervous system and Neural crest Derivatives 2	UMS	Ulnar-mammary syndrome
HBSS	Hank's buffer	VEGF	Vascular Endothelial Growth Factor
hCG	human chorionic gonadotropin	WISH	Whole-mount <i>in situ</i> hybridization
HDR	Homology Directed Repair	WT	Wild-type
H3K27ac	histone 3 lysine 27 acetylation	ZPA	Zone of Polarizing Activity

4. Introduction

4.1 Limb development

4.1.1 Basic concepts of limb development

The fundamental question in developmental biology is how differential gene expression is controlled and implemented into sculpting of complex tissues and organs during morphogenesis. As differentiated cells are organized into defined structures and tissues, the limb bud serves an excellent model to study how alterations in gene expression impact morphological outcomes. Mouse fore- and hindlimbs originate from lateral plate mesoderm (LPM) at defined positions around embryonic day (E) 9.5. The limb bud (LB) consists of a pocket of proliferative mesenchyme enveloped by an ectodermal layer that grows out perpendicular to the primary body axis (Zeller et al., 2009) (Fig. 1). The developing limb bud is patterned along the proximo-distal (PD), antero-posterior (AP) and dorso-ventral (DV) axes. Fore- and hindlimbs are homologous structures that contain morphologically and functionally distinct skeletal elements arranged along the PD axis: stylopod (humerus/femur), zeugopod (ulna/radius and tibia/fibula) and autopod (carpals/tarsals, metacarpals/metatarsals, phalanges). The AP axis patterning defines the identity of the autopod from the most anterior digit 1 (thumb) to the most posterior digit 5 (pinky) and zeugopodal elements (radius/ulna). DV axis patterning creates nail to finger-pad polarity and is relevant for extensor and flexor muscle attachment and innervation.

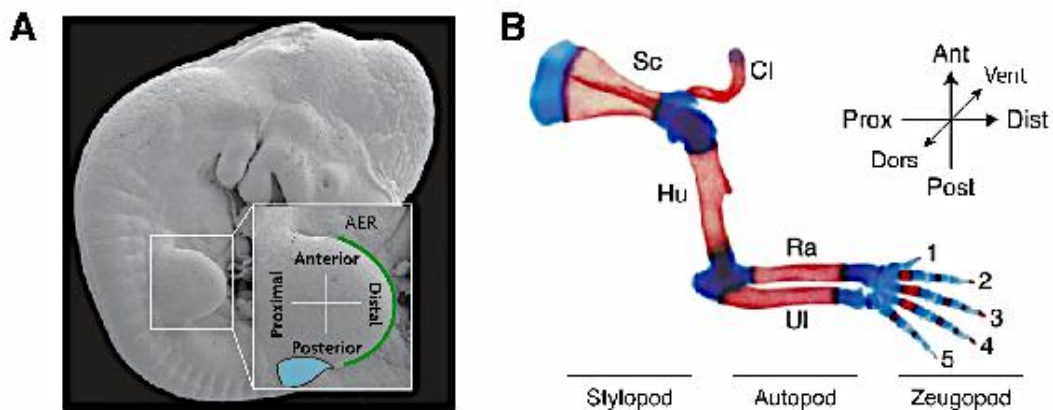


Figure 1. Vertebrate limb patterning along its three anatomical axes in the embryo. (A) A mouse embryo at E10.5 with an enlargement of the forelimb bud (FLB). Two crucial signaling centers controlling LB outgrowth and patterning are indicated. The apical ectodermal ridge (AER), which is the main center producing FGFs, is labeled in green. The zone of polarizing activity (ZPA) corresponds to the cells producing the SHH signal is marked in blue. Adapted from Zeller et al. 2009. **(B)** Newborn mouse forelimb showing the proximo-distal (PD), antero-posterior (AP) and dorso-ventral (DV) axes. Limb skeletal preparation shows cartilage in blue and bone in red. Skeletal elements indicated: Sc, Scapula;

Cl, clavicle; Hu, humerus; Ra, radius; Ul, ulna; digits are numbered 1-5. Adapted from Bénazet & Zeller, 2009.

4.1.2 Signaling centers controlling limb bud development

Vertebrate limb growth and patterning relies on coordinated development that is precisely orchestrated by the activity of two main signaling centers. The early chicken LB transplantation experiments by Saunders & Gasseling in 1968 revealed that transplantation of groups of cells from the posterior into the recipient's anterior limb mesenchyme causes cell re-specification and produces mirror digit duplications. This group of cells organizer activity was called the zone of polarizing activity (ZPA). Only a few decades later, Riddle et al., 1993 identified Sonic Hedgehog (SHH) as diffusible and the concentration-dependent morphogen secreted by ZPA that patterns the AP limb bud axis. The ectodermal thickening at the distal margin of the LB defines the second signaling center which is called the apical ectodermal ridge (AER). Saunders et al., 1957 performed surgical ablations of AER, which resulted in severe limb truncations indicating that AER functions in distal limb bud patterning and outgrowth. AER is an essential signaling center that produces fibroblast growth factors (FGFs) that control PD limb axis outgrowth and patterning. Individually AER FGF family ligands (*Fgf4*, *Fgf8*, *Fgf9*, and *Fgf17*) are dispensable for the limb bud development as they function in a combinatorial manner with *Fgf8* to control PD outgrowth and patterning in a dose-dependent manner (Mariani et al., 2008; Niswander et al., 1993). Nearly 50 years ago, Saunders and his colleagues showed that the ectoderm governs limb DV patterning by instructing the underlying mesoderm (MacCabe et al., 1974, MacCabe et al., 1973). DV interactions were linked to the formation of the AER as it defines the border between dorsal and ventral ectoderm (Altabef et al., 1997; Kimmel et al., 2000; Michaud et al., 1997; Tanaka et al., 1997) and produces the WNT signals required for DV patterning (Fernandez-Teran & Ros, 2008). DV patterning is orchestrated by BMP signaling from the ventral ectoderm, which activates *Engrailed-1* (*En1*) expression. *En1* restricts *Wnt7a* to the dorsal ectoderm expression and dorsal WNT7A induces the expression of *Lmx1b* transcription factor (TF) in dorsal mesenchyme, which is necessary and sufficient to establish DV polarity of the limb bud (Chen & Johnson, 2002).

4.1.3 Limb bud initiation

The first step during the vertebrate limb development is the specification of cells within the lateral plate mesoderm (LPM) that give rise to the limb primordium. Forelimbs always develop at the cervical-thoracic junction while hindlimbs develop at the lumbar-sacral

intersection. Therefore this implies that limb location along the rostro-caudal axis is fixed in tetrapod embryos (Burke et al., 1995). The mechanism responsible for forelimb initiation is still elusive. Previous experiments with chicken embryos suggested that FGF8 can be considered as a candidate signal for limb induction as it is transiently expressed by the intermediate mesoderm (IM) at the prospective forelimb and hindlimb levels during initiation (Cohn et al., 1995; Crossley et al., 1996; Vogel et al., 1996; Yonei-Tamura et al., 1999). However, *Fgf8* deletions in the mouse IM and before limb initiation, had no effect on initiation of the limb bud outgrowth (Boulet & Capecchi, 2004). In addition, *Wnt* family members have been implicated in the limb bud initiation (Kawakami et al., 2001). In particular, *Wnt2b* was implicated in FLBs initiation as it is expressed in the IM and later in the LPM at the level of the forelimb, while *Wnt8c* is detectable in the IM and later in the LPM at the level of the hindlimbs in chicken embryos.

However, these WNT ligands are not expressed during mouse LBs induction (Agarwal et al., 2003). During the early stages of mouse development *Fgf10* is expressed by the LBs mesenchyme. Experiments in both chicken and mouse revealed that FGF10 is required for the induction of *Fgf8* expression in the forming AER (Min et al., 1998; Ohuchi et al., 1997; Sekine et al., 1999; Yonei-Tamura et al., 1999). This results in the establishment of a growth-promoting feedback loop between AER and mesenchyme (Ohuchi et al., 1997). The essential role of FGF10 in limb initiation is highlighted by *Fgf10*-deficiency in mice, which results in severe limb truncations (Min et al., 1998; Sekine et al., 1999). In addition, formation of the nascent limb mesenchyme requires TBX5 and FGFs as they control a localized epithelial-to-mesenchymal transition (EMT) in the coelomic epithelium that gives rise to the limb bud primordia (Gros & Tabin, 2014). Furthermore, TBX5, TBX4 and retinoic acid (RA) are also required for initiation of fore- and hindlimb buds.

4.1.4 Proximo-distal limb axis patterning

4.1.4.1 The FGF feedback loop controls PD limb outgrowth

PD axis formation starts as the fore- and hindlimb fields are defined. During the onset of mouse FLBs formation, the T-box transcription factor TBX5 initiates *Fgf10* expression in the limb bud mesenchyme (Naiche & Papaioannou, 2007; Rallis et al., 2005). In hindlimb buds (HLBs) *Pitx1* is necessary for normal expression of TBX4 and to initiate the limb outgrowth (Duboc & Logan, 2011). Mesenchymal *Fgf10* signals to the overlying ectoderm and induces *Fgf8* expression, which signals back to the mesenchyme to maintain *Fgf10* expression

(Ohuchi et al., 1997; Sun et al., 2002). This positive-feedback loop between AER and limb mesoderm is essential for limb bud outgrowth and cell survival. Genetic inactivation of *Fgf8* in mouse results in smaller LBs and delayed *Shh* activation, which causes skeletal abnormalities (Lewandoski et al., 2000), while early inactivation of *Fgf10* causes complete limb agenesis (Min et al., 1998; Sekine et al., 1999). This reciprocal regulatory interaction is mediated by the FGF receptors expressed in ectoderm and mesenchyme. Inactivation of the ectoderm expressed *Fgfr2* or FGFR2-IIIb isoform results in absence of the forelimbs, (Arman et al., 1999; De Moerlooze et al., 2000; Revest et al., 2001; Xu et al., 1998) while mice lacking mesodermal FGFR2-IIIc isoform have limbs with growth and ossification defects (Eswarakumar et al., 2002).

4.1.4.2 The functions of retinoic acid in PD limb bud outgrowth

Retinoic acid (RA) is a morphogen crucial for embryonic development (Conlon, 1995; Ross et al., 2000; Stratford et al., 1999). In the mouse, RA is synthesized by the *Raldh2* enzyme expressed in the lateral mesoderm at E7.0–7.5 and then in the condensing somites and adjacent LPM (Niederreither et al., 1999; Rosello-Diez et al., 2011). During FLBs development, RA induces the expression of *Meis* genes (Niederreither et al., 1999). *Meis1/2* are RA-responsive genes that are initially expressed through the limb bud mesenchyme. Subsequently, FGF activity emanating from the AER restricts *Meis* genes expression to the proximal limb bud mesenchyme and creates a proximal high, distal low *Meis2* expression gradient (Mercader et al., 2000; Oulad-Abdelghani et al., 1997). Recent studies indicate that these polarized levels of *Meis2* in the mouse FLBs are generated by the antagonism between Polycomb group factors and RA signaling (Yakushiji-Kaminatsui et al., 2018). This polarized expression creates a temporal and spatial dynamic RA/FGF ratio (Fig. 2) (Cooper et al., 2011; Rosello-Diez et al., 2011), where the distal domain of the LB is RA-free. The observation of these two, PD gradient-like, mutually opposing diffusible signals, gave rise to the "two-signal model" for patterning the PD limb bud axis (Mercader et al., 2000).

The graded RA distribution along the PD axis is created by the AER-FGF induced *Cyp26b1* enzyme that metabolizes RA expression in the distal ectoderm and sub-ectodermal zone (MacLean et al., 2001; Yashiro et al., 2004). Genetic inactivation of *Cyp26b1* results in reduced *Hoxd12/d13* and *Hoxa13* expression as the *Meis1/2* genes expand into distal regions of the limb mesenchyme, where it causes distal to proximal transformations (Mercader et al., 2009). Subsequently, this manifests as digit loss and long bones fusion due to increased

mesenchymal cell death (Yashiro et al., 2004). While RA is required during limb bud formation, distal outgrowth only proceeds if RA levels are kept low by AER-FGF mediated up-regulation of *Cyp26b1*. In case of excess, RA forelimbs exhibit a range of AP and PD axis defects correlated with RA dose and timing, whereas the hindlimbs are normal (Mic et al., 2004).

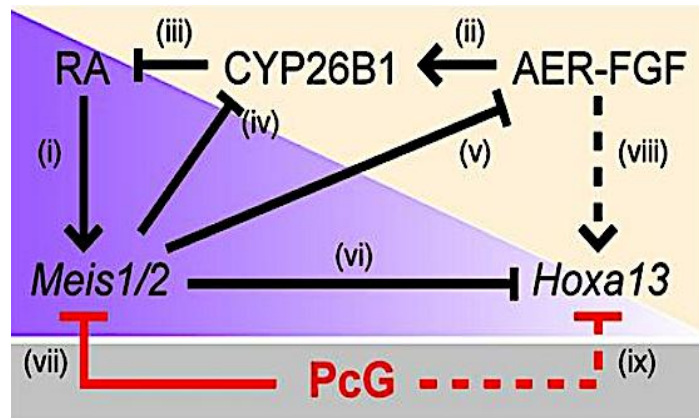


Figure 2. GRN controlling early PD axis specification. *Meis2* is activated by RA-related signals (i), while FGFs are signal from AER to activate *CYP26B1* expression (ii). *CYP26B1* degrades RA, while *Meis2* suppresses the proximal expression of *Cyp26b1* (iv) and *Fgf8* (v). *Meis2* also represses *Hoxa13* in the presumptive autopod region (vi). Polycomb factors inhibit *Meis1/2* (vii). Taken from Yakushiji-

Kaminatsui et al., 2018.

4.1.4.3 *Hox* genes and their role in PD axis formation

Hox genes are homeodomain-containing transcription factors required for proper embryonic development. In the mammalian genome, *HoxA*, *HoxB*, *HoxC*, and *HoxD* gene clusters are found. These clusters share redundant functions with the paralogous group members, and their temporal and spatial collinearity describes the correlation between the expression pattern along the main body axis with their order within the gene cluster (Mallo & Alonso, 2013). Practically, this means the more 5' the *Hox* gene is located, the more distal and later it is expressed during LB development (Dolli et al., 1989). During limb bud development *Hox* genes are expressed in two waves. During the first wave, 5' *Hoxd* expression is restricted to the posterior limb bud mesenchyme by the zinc finger TF GLI3 where it is required to initiate *Shh* expression (Deschamps, 2004; A. Zúñiga & Zeller, 1999). During the second phase of *Hoxd* genes are expressed in the distal part of the limb bud mesenchyme, where they participate in formation of the autopod (Zakany & Duboule, 2007).

Genetic studies in mice revealed that *Hox* genes are required for PD limb patterning. Inactivation of either of the *Hox9* or *Hox10* paralogues, proximal skeletal development (stylopod) is perturbed (Fromental-Ramain et al., 1996; Wellik & Capecchi, 2003). The combined inactivation of the distally expressed *Hoxa11* and *Hoxd11* genes perturbs zeugopod

morphogenesis, while the inactivation of the *Hoxa13* and *Hoxd13* paralogues disrupts autopod and digit development (Davis et al., 1995; Fromental-Ramain et al., 1996).

4.1.5 AP axis patterning in mouse limb buds

4.1.5.1 *Shh* activation in the limb bud mesenchyme

Several transcriptional regulators were implicated in *Shh* activation in the posterior LB. In particular, RA was shown to position ZPA in the posterior limb bud mesenchyme, while *Fgf8* signaling was associated with *Shh* maintenance (Lewandoski et al., 2000; Niederreither et al., 2002). Also, members of 5' *Hoxa* and *Hoxd* gene cluster are required for activation of the far upstream located ZRS enhancer that regulates *Shh* expression (Tarchini & Duboule, 2006). Previous studies implicated the key basic helix-loop-helix (bHLH) transcription factor HAND2 in activation of *Shh* expression in the posterior limb bud mesenchyme (Charité et al., 2000; Galli et al., 2010; Yelon et al., 2000). *Hand2* expression in the posterior mesenchyme is induced by the activity of the four *Hox9* paralogs (Xu & Wellik, 2011) and *HoxA* and *HoxD* genes in forelimb buds (Sheth et al., 2013). In the hindlimb field, *Hand2* expression is activated by the ISL1 transcription factor (Itou et al., 2012; Xu & Wellik, 2011) and PBX proteins participate in the early transcriptional upregulation of *Hand2* (Capellini et al., 2006). HAND2 directly interacts with E-box consensus binding regions in the ZRS enhancer to activate *Shh* expression (Dai & Cserjesi, 2002; Galli et al., 2010). In addition, HAND2 regulates other target genes in the posterior limb mesenchyme by functioning either as a transcriptional activator or repressor by forming heterodimers with other transcriptional regulators (Zhang et al., 2010). Overexpression of *Hand2* in the anterior mesenchyme result in ectopic *Shh* expression and associated preaxial polydactyly and/or mirror image digit duplications (Fernandez-Teran et al., 2000; McFadden et al., 2002).

4.1.5.2 SHH protein and SHH pathway in the limb

Digit numbers and identities are determined as a result of the AP limb bud patterning by SHH signaling, which is expressed from E9.5 to E12 in mouse forelimb buds (Platt et al., 1997). Before secretion, the SHH C-terminal domain is cholesterated and cleaved (Lee et al., 1994), while the N-terminal domain gets post-translationally palmitoylated (Y. Li et al., 2006). The precise SHH post-translation modifications (PTMs) of SHH are essential for digit patterning

as disruptions lead to digit malformations (Chen et al., 2004; Li et al., 2006). The secreted mature SHH polypeptide diffuses to form a posterior to anterior gradient in the limb bud mesenchyme that reaches cells up to ~300 μm away from its source (Li et al., 2006; Zeng et al., 2001; Zhu & Scott, 2004). The transmembrane receptor PTCH1 restricts the spread of the SHH morphogen and promotes its internalization and lysosome-mediated degradation by responding cells (Varjosalo & Taipale, 2008). The "French Flag model" proposed by Lewis Wolpert few decades ago predicted that the posterior mesenchyme secreted morphogen would form the posterior-to-anterior gradient and would lead to the different digit identities specification. Indeed, the descendants of the SHH-producing ZPA cells form a broad posterior limb domain that includes the mesenchymal cells giving rise to digits IV, V, the posterior part of digit III and the posterior part of the zeugopod. The duration of the exposure to SHH signaling may be critical to specification of posterior and anterior digit identities. This suggests that morphogenetic SHH signaling patterns limb bud mesenchymal cells by both temporal and spatial gradients (Harfe et al., 2004), (Fig. 3).

The SHH pathway is activated by the interaction of the SHH ligand with its receptor PTCH1. This interaction weakens the inhibition of smoothed (SMO) at the primary cilia and leads to the activation of signal transduction via GLI transcription factors (Goetz & Anderson, 2010). In vertebrates *Gli1* and *Gli2*, are dispensable for limb development, while *Gli3* is essential for AP limb patterning before and during SHH expression (Ahn & Joyner, 2004; te Welscher et al., 2002; Wang et al., 2000). At primary cilia of limb bud cells, GLI3 is processed into either activator (GLI3-A) or repressor isoforms (GLI3-R). In the absence of SHH signaling, GLI3 is proteolytically cleaved, and the truncated GLI3R protein isoform acts as a transcriptional repressor. SHH signaling inhibits the proteolytic processing of GLI3, which results in an AP gradient in the limb mesenchyme (Litingtung et al., 2002; Wang et al., 2000; Wen et al., 2016).

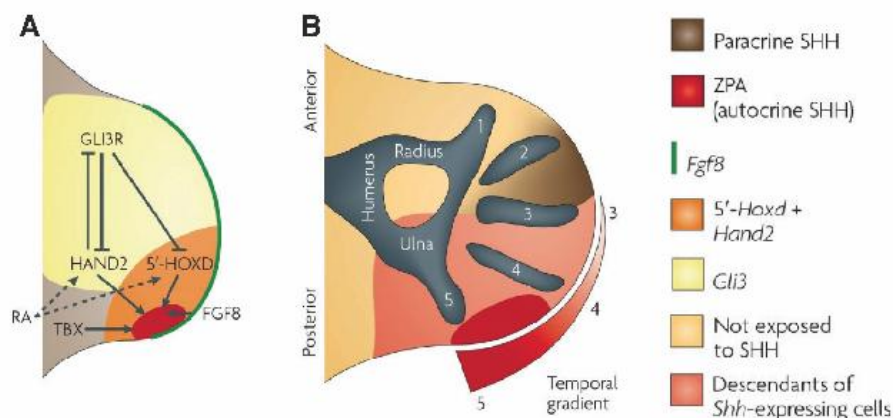
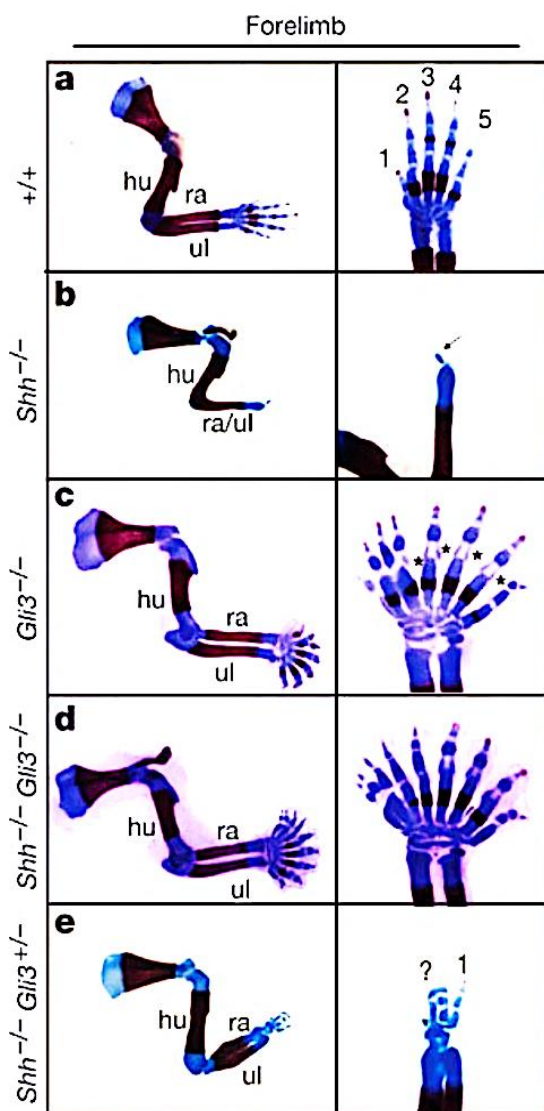


Figure 3. SHH activation and AP limb bud axis development. (A) The scheme represents the gene regulatory network (GRN) involved in the *Shh* activation, posterior restriction and maintenance during the early stages of LB outgrowth. (B) Mouse limb bud AP axes identity is specified by a spatio-temporal gradient of SHH signaling. Digit 1, humerus and radius are specified in a SHH-independent way, while digit 2 and part of digit 3 are specified by long-range SHH signaling. The mesenchymal cells that give rise to digit 5, 4, and part of digit 3 are derived from *Shh* descendants. Adapted from Zeller et al., 2009.

4.1.5.3 The SHH pathway in AP digit patterning

The *Shh*-deficiency (Chen & Struhl, 1996; Gallet & Therond, 2005; Incardona et al., 2000) leads to the formation of hypoplastic limbs with only one rudimentary anterior digit and a single zeugopodal bone (Litingtung et al., 2002; Riddle et al., 1993; Tabin, 1991). This is a result of extensive apoptosis of the progenitors giving a rise to these limb skeletal structures (Sanz-Ezquerro & Tickle, 2000; Zhu et al., 2008) and due to the loss of the mitogenic function of *Shh* (Lopez-Rios et al., 2012).



Skeletal analysis of E16.5 WT (a), *Shh*^{-/-} (b), *Gli3*^{-/-} (c), *Shh*^{-/-} *Gli3*^{-/-} (d) and *Shh*^{-/-} *Gli3*^{+/-} (e) limbs. Skeletal elements: hu, humerus; fe, femur; ra, radius; ul, ulna; ti, tibia; fi, fibula and autopod (digits 1-5) (Litingtung et al., 2002).

In contrast, *Gli3*-deficient mice exhibit severe polydactyly and loss of digit identities, while the proximal skeletal elements are normal (Büscher et al., 1997; Büscher & Rüther, 1998; Litingtung et al., 2002). *Shh*^{ΔΔ}, *Gli3*^{ΔΔ} mice develop polydactylous limbs which are indistinguishable from *Gli3*^{ΔΔ} limbs (Litingtung et al., 2002; te Welscher, 2002). This highlights an important role of *Shh* to restrict GLI3R activity to the anterior limb bud mesenchyme during limb development. In *Shh*^{ΔΔ}, *Gli3*^{Δ/+} limb two identifiable zeugopod elements with clear AP asymmetry are formed, while only 3-4 digits are formed (Fig. 4). Furthermore, the balance between GLI3A and GLI3R is critical as mice that express only the truncated GLI3R isoform exhibit central polydactyly as a result of excessive repressor activity (Bose, 2002). This direct correlation between *Gli3* levels and digit numbers suggested that *Gli3*, rather than *Shh* is

critical for digit number (Litlington et al., 2002). Indeed, *GLI3* controls digit morphogenesis and restrains the number of digits by regulating cell cycle transition and by terminating *Grem1* expression in a spatiotemporally controlled manner in the anterior autopod mesenchyme. This promotes the BMP-dependent exit of progenitors from proliferation to chondrogenic differentiation (Lopez-Rios et al., 2012). Keeping in mind the tremendously complex limb patterning, a new model for the digit formation was proposed. Sheth et al. (2012) proposed that digit formation is controlled by a Turing-type mechanism based on FGF and HOX modulated WNT, BMP, and SOX9 interactions. This model relies on the interplay of diffusible activators and inhibitors that determine pattern of the digit condensations, which then undergo chondrogenic differentiation. Thus, SHH appears to control the AP specification and proliferation of handplate progenitors by modulating the cell cycle and patterning by *5'Hoxd* genes. In contrast, the number and periodicity of digits depend on the Turing-type mechanism that is modulated by the *5'Hoxd* and AER-FGFs (Delgado & Torres, 2016; Lopez-Rios, 2016; Raspopovic et al., 2014; Sheth et al., 2012).

4.1.6 The self-regulatory feedback signaling system links AP and PD limb bud axis development

Coordinated limb bud growth and patterning is controlled by the cooperative interactions of AER and ZPA in a largely self-regulatory manner (Fig. 5) SHH signaling from the polarizing region is required for maintenance of AER-FGF expression (Laufer et al., 1994; Niswander et al., 1994). In turn, FGFs maintain *Shh* expression, which results in both organizers maintaining each other's activity by an epithelial-mesenchymal feedback loop. Another key player in this feedback signaling system the bone morphogenetic protein (BMP) antagonist Gremlin1 (GREM1; Capdevila et al., 1999; Zúñiga et al., 1999). *Grem1* is activated in the posterior limb bud mesenchyme and expands anteriorly during LB outgrowth. During limb bud formation high levels of BMP signaling establish the AER and activate *Grem1* expression (Ahn et al., 2001; Benazet et al., 2009; Nissim et al., 2006). During limb bud outgrowth, GREM1 antagonizes BMP signaling, which restricts the length of the AER (Benazet et al., 2009) and these interactions result in establishment of the SHH/GREM1/FGF epithelial-mesenchymal feedback signaling system that controls distal progression of LB outgrowth (Niswander et al., 1994; Scherz et al., 2004; Zúñiga et al., 1999). GREM1 plays a crucial role in this loop, as its genetic inactivation in mouse embryos leads to metacarpal fusion and loss of digits (Michos et al., 2004). During distal limb bud outgrowth, autopod

progenitors are prevented from acquiring proximal fates. Ultimately, the gap between *Grem1* and *Shh* expressing cells in the posterior limb bud and increasing AER-FGF levels start to repress *Grem1* in the underlying mesenchyme (Benazet et al., 2009; Nissim et al., 2006; Scherz et al., 2004; Verheyden & Sun, 2008). This leads to termination of *Grem1* expression and the epithelial-mesenchymal signaling system, which results in a rise of BMP activity that induces chondrogenesis (Lopez-Rios et al., 2012).

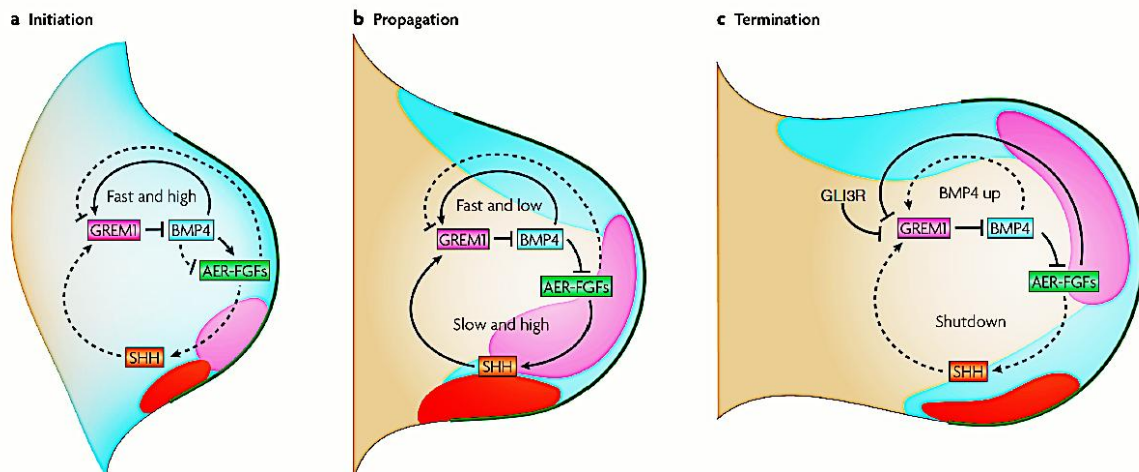


Figure 5. The SHH/GREM1/AER-FGF signaling system controls limb bud development. (A) High levels of BMP (in blue) activates *Grem1* and AER-FGF expression during the initiation of limb bud outgrowth. (B) During the propagation phase, SHH ensures *Grem1* expression, which is required to antagonize BMPs to sustain proliferation. (C) As LB outgrowth progresses, SHH is no longer able to upregulate *Grem1* and the rising levels of AER-FGFs terminate *Grem1* expression and feedback signaling. Taken from Zeller et al., 2009.

4.1.7 Limb mesenchymal polarization upstream of morphogenetic signaling

The first pre-patterning regulators, HAND2 and GLI3, were identified in mouse genetic studies and provided the first insights into the AP compartmentalization of the limb bud mesenchyme before activation of SHH signaling. Initially, GLI3 and HAND2 are co-expressed in the nascent limb mesenchyme, but subsequently their mutually antagonistic interactions establish the anterior GLI3R and posterior HAND2-positive mesenchyme domains (Galli et al., 2010; Osterwalder et al., 2014; te Welscher et al., 2002). During the early stages, GLI3R restricts *5'Hoxd* expression to the posterior limb mesenchyme (Galli et al., 2010) and polarizes nascent limb mesenchyme by restricting the ZPA to the posterior of the limb bud mesenchyme (Zakany et al., 2007; te Welscher et al., 2002). The precise AP polarity is crucial for the limb patterning. The anterior expansion of *Hand2* expression into *Gli3*-deficient mice anterior limb mesenchyme causes preaxial polydactyly. Conversely, *Gli3*

expansion into the *Hand2*-deficient mice posterior causes disruption of *Shh* activation (Galli et al., 2010; te Welscher, Fernandez-Teran, et al., 2002) and this manifests as only one rudimentary digit. Ultimately, mouse FLBs lacking both *Gli3* and *Hand2* lack AP polarity and limbs are severely polydactylous (Galli et al., 2010), (Fig. 6).

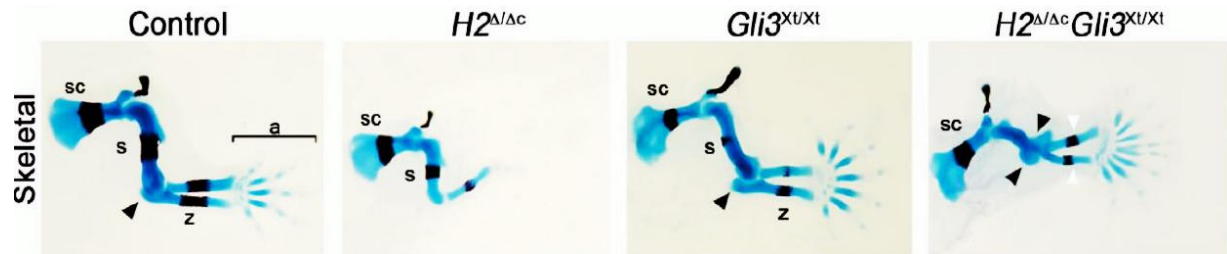


Figure 6 *Hand2* and *Gli3* functions in the establishment of AP polarity in mouse forelimb buds. Skeletal preparations of WT and $H2^{\Delta/\Delta}$, $Gli3^{Xt/Xt}$ and $H2^{\Delta/\Delta} Gli3^{Xt/Xt}$ forelimbs at E14.5. ($Gli3^{Xt}$ represents *Gli3* null allele). The black arrowheads point to the duplicated elbow-like structure while the white arrowheads point to the symmetrical zeugopodal skeletal elements. Taken from Galli et al., 2010.

However, genetic evidence revealed that HAND2 itself is not sufficient to establish a sharp *Gli3* expression boundary. HAND2 activates its transcriptional target TBX3, which also functions in defining the anterior *Gli3*-positive and posterior *Gli3*-negative limb mesenchymal boundary (Osterwalder et al., 2014). In fact, that TBX3 functions downstream of HAND2 is verified as in *Hand2* deficient mouse limb buds the expression of *Tbx3* and *Tbx2* is lost in fore, but not in the hindlimb buds (Galli et al., 2010; Osterwalder et al., 2014). However, *Hand2* expression is also downregulated in *Tbx3*-deficient limb buds, which points to cross-regulation between TBX3 and HAND2 (Davenport et al., 2003; Osterwalder et al., 2014). The major transcriptional interactions and GRNs controlled by TBX3 and its functionally relevant interactions with HAND2 during AP axis patterning in mouse limb buds are still unknown.

4.2 TBX3 is a key regulator of embryonic development

4.2.1 T-box transcriptional regulators

The *T-box* genes comprise a unique and versatile ancient TF family conserved across species. The *T-box* family members have crucial roles in early cell-fate decisions necessary for basic vertebrate body patterning, specification and proliferation during development (Papaioannou & Silver, 1998; Wilson & Conlon, 2002). The pioneering member of the family, *Brachyury* (Greek for short tail, also known as *T*) was described nearly a century ago in a study that reported short-tailed mice carrying a mutation that affected embryonic viability and tail

development in heterozygotes (Dobrovolskaia-Zavadskaiia, 1927). However, the *T* gene was cloned only about 60 years later (Herrmann et al., 1990). Subsequently, it was shown that *T* is able to recognize and bind a consensus DNA binding site, called the T-box (Kispert & Herrmann, 1993) and functions as a TF (Kispert et al., 1995). As more diverse animal genomes were sequenced, other *T-box* orthologs and homologs across metazoans were discovered based on the similarity of the DNA binding domain (Bollag et al., 1994; Papaioannou & Silver, 1998). The T-box gene family consists of more than 100 members (Bruce, 2014) that are grouped into five subfamilies: *T*, *Tbx1*, *Tbx2*, *Tbx6*, and *Tbr1* (Papaioannou, 2014; Papaioannou & Silver, 1998). Interestingly, the majority of the *T-box* genes are randomly dispersed through the chordate genomes. However, several gene clusters were discovered. The linkage between *Tbx8* and *Tbx9* was observed in *C. elegans* (Agulnik et al., 1994), while the linkage between the gene pairs *Tbx2* - *Tbx4* and *Tbx3* - *Tbx5* was first observed in the mouse genome. It is thought that the robust chromosomal linkage of these gene pairs has arisen due to an ancestral tandem duplication that was followed by cluster duplication and dispersion (Agulnik et al., 1996), (Fig. 7). The tight genome linkage between the *Tbx2* - *Tbx4* and *Tbx3* - *Tbx5* contiguous gene pairs is preserved in most animal lineages before the divergence of protostomes and deuterostomes ~600 million years ago. These T-box gene pair

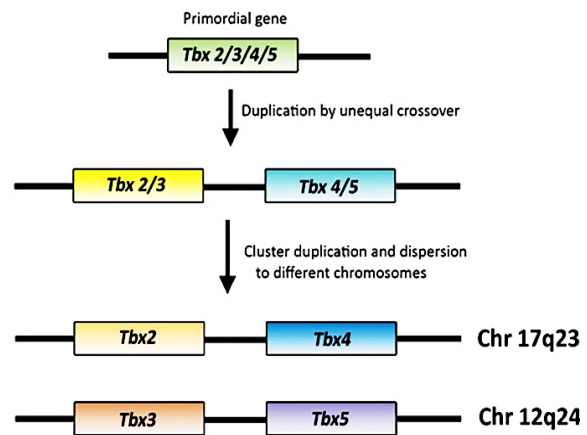


Figure 7. Evolutionary model of *Tbx 2/3/4/5* gene family. Scheme based on Agulnick et al., 1996. Taken from Ballim and Prince 2013.

are functioning in evolutionary conserved developmental programs that regulate paired fin/limb outgrowth and patterning, eye and heart development. In addition, these linkages are maintained in the primitive basal chordate amphioxus (*Branchiostoma floridae*) that lacks paired appendages. Conservation of this ancient linkage points the presence of essential *cis*-regulatory modules in the intragenic or flanking regions, likely located in the close proximity of these loci (Horton et al., 2008).

4.2.2 T-box domain

The T-box domain is defined as a minimal region that is necessary and sufficient to bind DNA in a sequence-specific way. All T-box family members bind to the 20–24 nucleotide near-palindromic, DNA consensus half-site (AGGTGTGAAA) called the T-box binding element (TBE) (Kispert & Herrmann, 1993). Crystallographic analysis showed that the T-box domain contacts DNA in the major and minor grooves at the half-sites (Herrmann & Müller, 1997).

The T-box DNA-binding domain makes up one-third of the protein and is highly conserved (Herrmann & Müller, 1997). The T-box domain position in the protein is not conserved and can vary among different family members. Sequence conservation outside the T-box domain can help to identify closely related family members, e.g., human TBX3 and TBX2 exon 6 and 7 encoded sequences share 70% similarity (Bamshad et al., 1999; Papaioannou & Silver, 1998). Binding specificity to different TBE sites is achieved by variations in the palindromic sequences and the different T-box domains have slightly different affinities for the same T-sites (Naiche et al., 2005). Thus, varying binding site orientations, numbers and spacing controls target specificity *in vivo* (Conlon et al., 2001).

4.2.3 T-box family members in limb development

During limb development, several *T-box* family genes are expressed with distinct expression patterns and dynamics. *T* (*Brachyury*) is an activator that plays a role in the WNT and FGF signaling between the limb bud ectoderm and the sub-ridge mesenchyme, which results in formation and maintenance of a functional AER (Liu et al., 2003). In the limb bud mesenchyme, *Eomes* expression is detected from E11.5 onward at the base of digit 4 and functions in delineating progenitors as genetic inactivation of *Eomes* leads to digit 4 loss (Farin et al., 2013). Furthermore, *Tbx18* and *Sox9* expression in the pre-cartilaginous condensations at E12.5 controls the mesenchymal cell differentiation into hypertrophic chondrocytes (Haraguchi et al., 2015). However limb development is not altered in *Tbx18*-deficient mouse embryos (Bussen et al., 2004). *Tbx15* functions in controlling the number of mesenchymal precursor cells and chondrocytes (Candille et al., 2004). A homozygous *Tbx15*-deficiency in humans causes Cousin syndrome, which is characterized by complex craniofacial dysmorphism, scapula and pelvis hypoplasia and short stature (Lausch et al., 2008). Deletion of *Tbx15* in the mouse results in limb skeletal bone reductions and the hole in the center of the scapula blade.

4.2.4 TBX4 and TBX5 mark the forelimb and hindlimb field

The *Tbx2* subfamily paralogous gene pair *Tbx4* and *Tbx5* mark the presumptive limb fields, with *Tbx5* being expressed FLBs and *Tbx4* in HLBs (Gibson-Brown et al., 1996). The link between *Tbx5* and *Tbx4* expression of and the corresponding limb-type morphologies was demonstrated by FGF-soaked beads implantation induced ectopic limbs in chick embryos the interlimb flank mesenchyme. The limb-type specific expression patterns, evidence from manipulating chicken limb development and gene misexpression studies led to the proposal that *Tbx4* and *Tbx5* determine fore and hindlimb identity, respectively (Isaac et al., 1998; Logan et al., 1998; Rodriguez-Esteban et al., 1999; Takeuchi et al., 1999). However, subsequent loss-of gain of function experiments showed that *Tbx5* and *Tbx4* have a common function in controlling LB outgrowth, but do not determine the limb-type specific morphologies (Duboc & Logan, 2011; Minguillon et al., 2005). The proposed role in outgrowth is supported by the ancestral amphioxus *T-box* gene *Amphi4/5*, which can rescue forelimb bud formation in *Tbx5* conditional mutant mice. This showed that the ancestral *T-box* gene from amphioxus (lacking paired appendages) can induce limb bud outgrowth in mouse embryos, but does not alter limb-type morphology (Minguillon et al., 2009).

Inactivation of *Tbx5* and *Tbx4* in mouse embryos leads to perinatal lethality. In particular, the *Tbx4* homozygous mutation leads to embryonic lethality at E10.5 due to allantois defects. At this stage, mutant embryos have normally initiated hindlimb buds, but as outgrowth is not maintained limb bud development arrests (Naiche & Papaioannou, 2003). The human haploinsufficiency for *Tbx4* leads to an autosomal dominant skeletal dysplasia called Small Patella syndrome. This syndrome is characterized by patella aplasia, abnormal or absent pelvis ossification and foot abnormalities including short 4th and 5th metatarsals (Bongers et al., 2004).

The *Tbx5* deficiency in mice results in embryonic lethality at E10.5 due to cardiac morphogenesis defects. Conditional deletion of *Tbx5* in the mouse forelimb bud mesenchyme leads to the loss of the forelimb and pectoral girdle skeleton (scapula and clavicle) (Rallis et al., 2003). A *Tbx5* haploinsufficiency in humans causes the Holt-Oram syndrome (HOS): a rare disorder, also called heart-hand syndrome due it to its typical manifestation. Affected individuals present sloping shoulders, radial ray defects in combination with defects in the cardiac conduction system. In addition, the atrial and ventricular septation can also be affected. The HOS limb phenotypes are pleiotropic and can range from subtle digit abnormalities to phocomelia (Packham, 2003).

Also, *Tbx5* and *Tbx4* are expressed in muscle connective tissue cells surrounding the muscle progenitors, where they regulate limb muscle patterning by controlling cell adhesion molecules such as β -catenin and N-cadherin that required for the integrity of the connective muscle tissues (Hasson et al., 2010). Deletion of *Tbx5* in forelimbs and *Tbx4* in hindlimbs between E9.5 and E10.5 disrupts the organization of the muscle connective tissues and results in abnormal muscle and tendon patterning without disrupting skeletal development (Hasson et al., 2010).

4.2.5 *Tbx2* and *Tbx3* function in limb bud development

The expression patterns of transcriptional repressors *Tbx2* and *Tbx3* in developing mouse limb buds are highly similar. As the forelimb bud emerges at E9.5, *Tbx2* and *Tbx3* are expressed in the posterior domain. At E10.5, *Tbx2* and *Tbx3* expression domains become restricted to two proximal-to-distal stripes of expression in the anterior and posterior limb bud mesenchyme. By E12.5-13.5, expression becomes restricted to the interdigital domains and fades away (Farin et al., 2008; Gibson-brown et al., 1998; Gibson-Brown et al., 1996), (Fig. 8). *Tbx2* and *Tbx3* are expressed in overlapping domains in the limb bud mesenchyme, whereas unique *Tbx3* expression is detected in the AER. *Tbx3* is the only T-box gene expressed by the AER signaling center (Farin et al., 2013), but *Tbx3* AER-specific inactivation does not alter limb bud development (Emechebe et al., 2016).

The largely overlapping expression suggest that *Tbx2* and *Tbx3* might have redundant functions during limb development. However, human disease association studies and the analysis of mouse embryos lacking *Tbx2* or *Tbx3* established that *Tbx3* is the dominant factor as its inactivation causes striking limb bud phenotypes (Bamshadl et al., 1997).

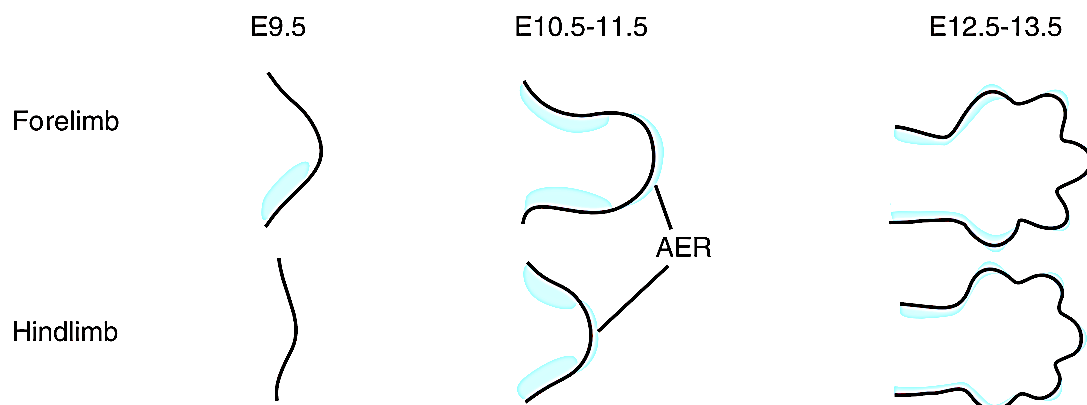


Figure 8. TBX3 expression during limb bud development. At the beginning of the limb outgrowth, *Tbx3* (in blue) is expressed in the posterior limb bud mesenchyme. Subsequently, the expression expands to the anterior mesenchyme and the AER. Finally, *Tbx3* expression

gets restricted to the tips of the developing digits by E12.5. Adapted from Washkowitz et al., 2012.

4.2.5.1 TBX2 regulates limb bud outgrowth

Mutations in *Tbx2*, unlike *Tbx3*, are not implicated in any systematic human developmental disorders. However, TBX2 overexpression in humans is linked to mild mental retardation, prenatal growth retardation and complex heart septation defects. In addition, minor skeletal anomalies with hypoplasia of the distal phalanges are also observed (Radio et al., 2010). Mice lacking *Tbx2* display bilateral distal duplication of the hindlimb digit 4, while forelimbs are normal (Farin et al., 2013). This digit 4 phenotype could be a consequence of the posterior *Tbx2* expression in the limb bud mesenchyme giving rise to the interdigital region between digits 4 and 5. This duplication of digit four arises due to reduced apoptosis of the interdigital mesenchyme and prolonged-expression of AER-*Fgf4/9/17* and *Shh*. These studies showed that TBX2 participates in termination of the SHH/GREM1/AER FGF feedback signaling system by repressing *Grem1* expression in the posterior limb bud mesenchyme at late stages (Farin et al., 2013). At earlier stages, TBX2 positively regulates *Shh* and represses posterior *Gli3* expression in the posterior limb bud mesenchyme, which suggests that it participates in establishment of the AP axis (Nissim et al., 2007; Suzuki et al., 2004).

4.2.5.2 TBX3 is essential for limb bud development

The human *TBX3* gene is composed of 7 exons, which encode a 743 amino acid (a.a.) protein, while the mouse *Tbx3* locus (on chromosome 4) encodes a 741 a.a. protein (Bamshadl et al. 1997; www.uniprot.org, last entry modified on 11/12/2019). Several human *TBX3* transcripts were identified in various adult and fetal tissues (Bamshad et al., 1999), while only two *Tbx3* transcripts were identified in mouse (Uniprot, last modified December 11, 2019). In both species, alternative splicing of the 60bp from 2a exon produces two TBX3 coding transcripts: TBX3 and TBX3 + 2a protein isoforms, there the TBX3 + 2a isoform has 20 a.a. in-frame insertion in the T-box DNA binding domain (Bamshad et al., 1999). Both TBX3 protein isoforms are broadly expressed, binds to DNA and are functionally equivalent (Hoogaars et al., 2008). The TBX3 protein is the dominant isoform, but the isoforms ratio is tissue and species specific (Fan et al., 2004). The TBX3 + 2a isoform is conserved in mammals but absent in avian genomes (DeBenedittis & Jiao, 2011). Both TBX3 protein isoforms interact with RNA binding proteins and bind to mRNAs to promote or inhibit

splicing in a context-dependent manner (Kumar et al., 2014). Two additional human isoforms encode an interrupted T-box domain or are produced by joining exon 1 to exon 7 in frame which eliminates the T-box domain (Uniprot, last modified December 11, 2019). In addition to the DNA binding T-box domain, the TBX3 protein encodes a nuclear localization signal, two repressive domains (R1/R2) and an activation domain. The R1 domain is located in the C-terminal part of TBX3 is essential and functions as a weak repressor. The nuclear localization domain is located in the N-terminal domain and mutation alter the predominant perinuclear localization. A putative activation domain resides in the C-terminal domain and several PTM sites were predicted for ubiquitination, acetylation, and methylation, but only few phosphorylation sites were validated (Carlson et al., 2001). The serine-proline phosphorylation motif at a.a. 190 within the DNA binding domain is highly conserved. This pseudo-phosphorylation site regulates the ability of TBX3 to promote proliferation (Willmer et al., 2016), controls protein stability and nuclear localization (Peres et al., 2014), (Fig. 9).

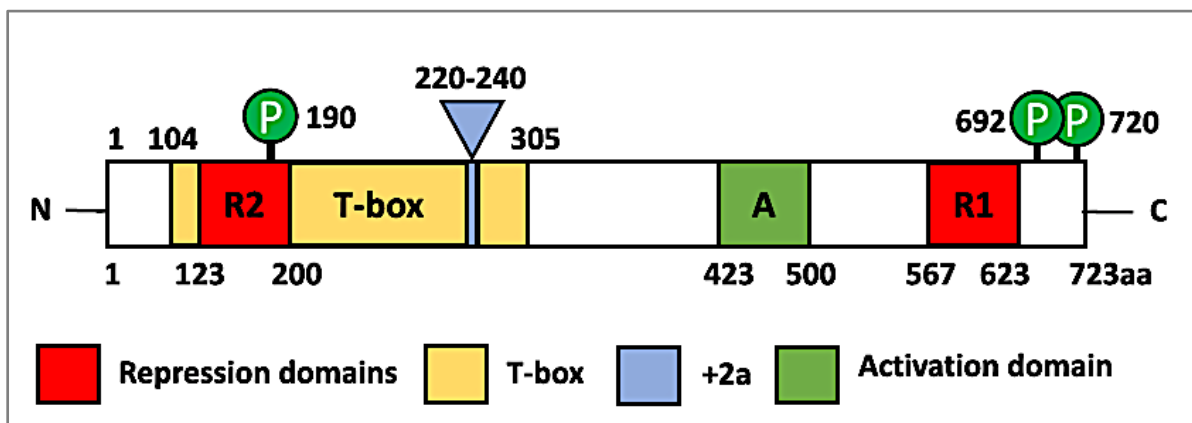


Figure 9. Schematic representation of the human TBX3 protein. The highly conserved human TBX3 protein shares 98% a.a. identity with mouse TBX3 (Bamshad et al., 1999). TBX3 protein binds to DNA via its N-terminally located T-box domain (yellow). Two repression domains, R1 and R2, are represented by red boxes and the activation domain is labeled in green. The +2a splice variant in exon 2 is depicted as a blue box. The green circles above the protein indicate phosphorylation sites and their a.a. positions (adapted from Willmer et al., 2017).

TBX3 is an essential transcription factor that plays an important role in limb bud pre-patterning and mesenchymal polarization (chapter 4.1.7). *Tbx3*-deficient embryos die due to yolk sack defects between E11.5 and E16.5 (Davenport et al., 2003). In contrast to *Tbx2*, heterozygosity for *Tbx3* does not cause abnormalities in mice, while in humans it underlies Ulnar-mammary syndrome (chapter 4.2.6.3). Analysis of mouse embryos showed that *Tbx3* is expressed in the presumptive limb field of the LPM and in nascent limb buds prior to initiation of outgrowth (Emechebe et al., 2016; Rallis et al., 2005). *Tbx3* expression in LPM is activated by the RA signaling and the RA-receptor complex binds to a retinoic acid

response element (RARE) in the *Tbx3* promoter (Ballim et al., 2012). Misexpression in chicken limb buds revealed that TBX3 participates in positioning the limb bud along the rostro-caudal embryonic axis. Ectopic expression of the TBX3 repressor form throughout the forelimb bud mesenchyme leads to an expansion of the *Hand2* expression domain and causes a rostral shift in the limb bud position. The transcriptional activator form of TBX3 induces *Gli3* expansion and the *Hand2* expression domain and limb position are shifted to more caudal positions (Rallis et al., 2005). TBX3 is indirectly required to upregulate *Hand2* upstream of *Shh* via maintaining *Tbx5* expression (Emechebe et al., 2016). Furthermore, *Tbx2* and *Tbx3* appear to function in a feedback loop with SHH, whereby they contribute to maintaining the ZPA (Nissim et al., 2007; Davenport et al., 2003), while the posterior *Tbx3* and *Tbx2* expression domains are maintained by SHH signaling (Galli et al., 2010).

While the complete absence of the TBX3 protein in mouse embryos leads to variable lethality in combination with severe posterior hindlimb skeletal defects (absent ulna, and digits 4 and 5) and heart phenotypes. Mutations truncating the TBX3 protein resulting in cytoplasmic accumulation results in lethality already by E12.5, which suggests that the truncated protein is pathogenic (Farin et al., 2013).

It is important to realize that the posterior *Tbx3* expression depends on SHH and BMP signaling that is linked to AP digit specification (Tümpel et al. 2002) and experiments in chicken limb buds showed that *Tbx3* (and *Tbx2*) specifies hindlimb digit 3 and 4 in cooperation with interdigital BMP signaling and 5' *HoxD* genes (Suzuki et al., 2004).

Anterior *Tbx3* expression depends on the balance between anterior BMP signaling and inhibition by SHH signaling from the posterior limb bud (Tümpel et al. 2002). In the anterior mesenchyme, TBX3 functions in the SHH-independent, cilium-based patterning of anterior digits. In particular, TBX3 is an essential component of a protein complex with KIF7 and SUFU, which control GLI3A and GLI3R processing and stability, respectively. In *Tbx3*-deficient limb buds, the KIF7-SUFU interactions are reduced which results in excess GLI3 processing and reduced levels of both the GLI3A and GLI3R isoforms that manifests itself as preaxial polydactyly (Emechebe et al., 2016).

Also, TBX3 promotes chondrocyte cell proliferation and suppresses/delays osteoblast differentiation, which results in elongation of the posterior skeletal elements (Govoni et al., 2009). In particular, TBX3 upregulates the expression of BMP expression (Suzuki et al., 2004), including BMP2, which is known to stimulate cartilage proliferation and increases digit length in embryonic bat forelimbs (Sears et al., 2006).

4.2.6 TBX3 functions in embryonic development and disease

TBX3 is expressed in various embryonic and adult tissues. The particular importance of the TBX3 functional role is highlighted in the human haploinsufficiency called Ulnar-mammary syndrome that severely affects limbs and mammary glands. Interestingly, other *TBX3* expressing organs display no phenotypes in TBX3 haploinsufficiency, which indicated that different tissues require different TBX3 levels or that other T-box genes with overlapping expression domains compensate the reduction in TBX3 (Bamshad et al., 1999).

4.2.6.1 TBX3 functions during mammary gland development

The development of mammary glands starts at E10.5 in mouse embryos. First, an ectodermal ridge expressing *Wnt10b*, the so-called a mammary line, forms between the forelimb and hindlimb buds (Veltmaat et al., 2004). At E11.5 the mammary placodes form and by E14.0 the mammary buds arise. Perinatally (E18.5), the branching ductal system develops and five individual mammary glands are formed. *Tbx3* expression is detected during all stages of mammary glands development (Davenport et al., 2003; Douglas & Papaioannou, 2013; Richert et al., 2000), (Fig. 10). In *Tbx3*-deficient mutant mice, the induction of placode formation is disrupted (Davenport et al., 2003) while a reduced ductal tree development and nipple formation are disrupted in heterozygous mice (Jerome-Majewska et al., 2005). Previous experimental data placed TBX3 upstream of the earliest known markers of placode induction which are FGF and WNT signaling (Davenport et al., 2003). Inhibition of WNT or FGF signaling during early mammary bud formation disrupted *Tbx3* expression, which points to the existence of a WNT, FGF, and TBX3 regulatory feedback loop during mammary gland development (Eblaghie et al., 2004).

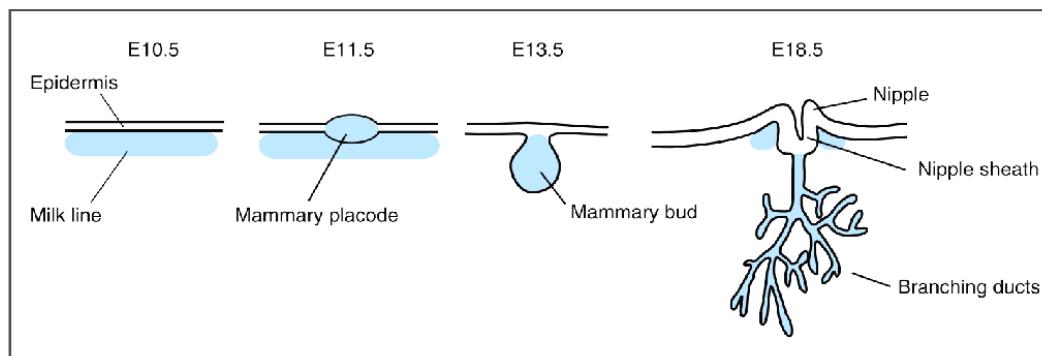


Figure 10. TBX3 expression during mammary gland development. During mouse mammary gland development, *Tbx3* expression (blue) is first detected at E10.5 in the mesenchymal milk lines. Later on, *Tbx3* expression marks the mammary placodes, and subsequently, its expression continues in the epithelium as the placode expands into the mammary bud. Finally, the branching ductal system forms and *Tbx3* expression is still

detectable in the mesenchyme surrounding the nipple at E18.5. Taken from Washkowitz et al. 2012.

4.2.6.2 TBX3 in heart development

Cardiogenesis in mouse embryos starts at E7.5 when the mesodermal myocardial progenitors form first and second heart fields. At E8.0, the first heart field undergoes morphogenesis to form an early tubular heart. *Tbx3* expression is first detected by E8.5 when cells from the second heart field move into inflow and outflow poles of the heart and the heart tube begins to loop (Brade et al., 2013). Starting at E9.5, the linear heart tube transforms into the four-chambered heart, which consists of ventricular and atrial chambers and a non-chamber myocardium forming the inflow and outflow tract (OFT), atrioventricular canal (AVC) and the inner curvatures. By E10.5, *Tbx3* is expressed in the developing conduction system where its expression delineates the sinoatrial (SAN) and atrioventricular nodes (AVN), endocardial cushions in the AVC and OFT (Christoffels et al., 2004), (Fig. 11). During heart development, myocardial cells divide rapidly and sustained proliferation results in formation of ventricular and atrial chambers of the heart. During this period, the primary cells of the cardiac conduction system remain mitotically relatively inactive and form the constrictions between the chambers (Bakker et al., 2008; Boogerd et al., 2008; Hoogaars et al., 2007; Washkowitz et al., 2012). TBX3 controls cell proliferation and represses the chamber-specific genetic program in the non-chamber myocardium (Boogerd et al., 2008; Hoogaars et al., 2007; Ribeiro et al., 2007). Previous studies implicated *Tbx3*, alongside with *Tbx18* and *Shox2*, in the development of the SAN-a pacemaker of the heart that initiates the heartbeat and controls the rate and the rhythm of contraction (Protze et al. 2017; Espinoza-Lewis et al. 2009; Hoogaars et al. 2007). Therefore, it is not surprising that the human TBX3 haploinsufficiency results in cardiac rhythm abnormalities (Bogarapu et al., 2014). In *Tbx3*-deficient mouse embryos, heart looping is delayed, the ventricular septation is incomplete, the morphology of double outlet right ventricle is altered, OFT is malformed and aortic arch formation is delayed (Bakker et al., 2008; Mesbah et al., 2008; Ribeiro et al., 2007). Also, the ectopic expression of chamber myocardial genes was detected in *Tbx3*-deficient embryonic hearts AVC (Bakker et al., 2008; Hoogaars et al., 2007). Conversely, ectopic TBX3 expression induces ectopic conduction tissue development (Hoogaars et al., 2007). To date, not much is known about the upstream regulators of *Tbx3* during heart development. I participated in a study that established that HAND2 acts upstream of *Tbx3*, as in *Hand2*-deficient mouse embryonic hearts *Tbx3* expression is lost and AVC cardiac cushion

formation is disrupted (Laurent et al. 2017). In addition, the BMP signaling pathway has been implicated in modulation of *Tbx3* expression during heart formation (Yamada et al., 2000; Yang et al., 2006).

4.2.6.3 The human ulnar-mammary syndrome (UMS)

The ulnar-mammary syndrome (UMS or Pallister UMS, Pallister, 1976, OMIM #181450) is a rare (~1 out of 25 000 births, Koskimies et al. 2011) autosomal dominant disorder caused by mutation resulting in *TBX3* haploinsufficiency in humans (Bamshad et al., 1997). For nearly 20 years, the underlying cause of the syndrome was unknown until the gene for UMS was mapped by linkage analysis to the human 12q23-q24.1 locus (Bamshad et al., 1995). This genomic region encodes two T-box family members: *Tbx3* and *Tbx5* and further analysis showed that mutations in *TBX3* are the underlying genetic cause of UMS (Bamshad et al., 1997).

UMS is a pleiotropic disorder that has different intrafamilial and interfamilial phenotypic manifestations. To date at least 22 pathogenic *TBX3* variants or big deletions/insertions have been reported (Alby et al., 2013; Bamshad et al., 1999; Bogarapu et al., 2014; Joss et al.,

2011; Klopocki et al., 2006; Linden et al., 2009; Meneghini et al., 2006; Tanteles et al., 2017; Wollnik et al., 2002). Different phenotypic manifestation among individuals carrying the same mutation implies that so far unidentified modifiers cause variable expressivity.

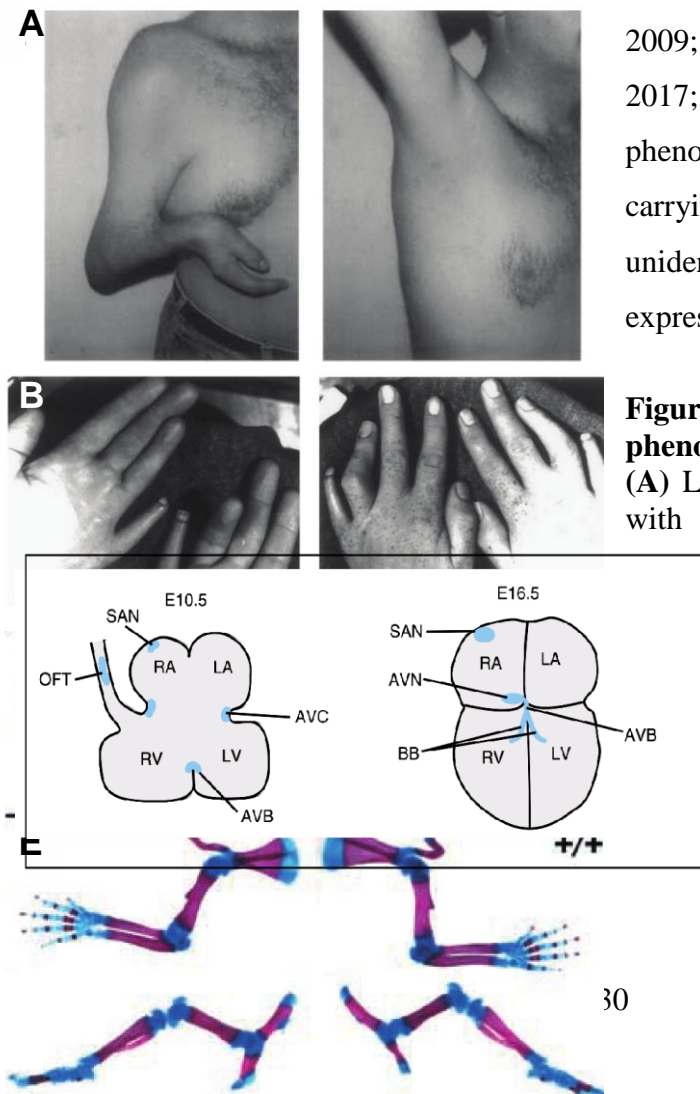


Figure 12. *Tbx3*-deficiency-related phenotypes in humans and mice.

(A) Limb defects observed in an adult male with UMS. The limb picture on the left shows a shortened forearm and

Figure 11. *Tbx3* expression during mouse heart development.

Tbx3 is expressed (in blue) in the mouse AVC, SAN and OFT. *Tbx3* expression delineates the cardiac conduction system at E14.5. Taken from Washkowitz et al. 2012.

absence of digits 3-5. The right picture reveals the lack of the

axillary hair and the hypoplastic right areola. **(B)** The ventral surface of the right and left hands shows the dorsalized ventral surface of digit 5, including a duplication of their nailbed on the ventral side. Pictures from (Bamshad et al., 1999). **(C)** Skeletal preparations of limbs from *Tbx3*-deficient mouse embryos at E17.5. Forelimbs exhibit variable abnormalities of the posterior elements, including ulna and digits. Hindlimbs show severe posterior truncations affecting the zeugopod and the absence of the autopod. **(D)** Higher magnification of the right hindlimb shows the single-digit attached to the single zeugopod element. **(E)** Skeletal preparation of age-matched WT animals. Pictures from Bamshad et al., 1999; Davenport et al., 2003.

One of the mechanisms underlying the phenotypic variability of UMS could be an aberrant TBX3 pre-mRNA splicing activity. Unbiased proteomic screening identified that TBX3 interacts with multiple RNA splicing factors, RNA binding proteins, which indicates that TBX3 function in regulation of splicing. Indeed, mutated TBX3 proteins exhibit different splicing functions and interfere with the splicing regulatory activity of the endogenous TBX3 protein (Kumar et al., 2014).

UMS is typically characterized by asymmetrical defects ranging from shortening of the fifth digit to complete absence of ulna/radius and autopod (Tanteles et al., 2017). In a small fraction of UMS patients upper arm (humeri, scapulae, clavicles) and shoulder girdle abnormalities are observed together with hypoplasia of pectoralis major muscles (Bamshad et al., 1997). The associated postaxial limb defects in UMS patients vary from hypoplasia of the distal phalanges of digit V to complete loss of digits III–V. Hypoplasia of the little finger may be combined with incomplete duplication and is often different between the left and right limb. Also, UMS patients exhibit dorsalization of the ventral surface of the digits (the most commonly the V digit is affected), stiff distal interphalangeal joints, and forearms may have bowed radius and stiff elbow. Feet of UMS patients show hypoplasia of the little and fourth toes, including nails. The overall penetrance of limb defects in UMS patients is > 85% (Meneghini et al., 2006), (Fig.12). Furthermore, Emechebe et al. 2016 provided additional insight into the posterior limb digit number of defects observed in human UMS patients by ablating *Tbx3* at different stages of mouse limb development. In the case of an early *Tbx3*-deficiency, SHH signaling is perturbed, and it results in a failure to initiate limbs and leads to extensive limb abnormalities. However, later ablation of *Tbx3* expression in the posterior limb mesenchyme caused digit 5 loss.

Another key feature of UMS is hypoplasia or aplasia of the mammary glands and nipples, hypoplasia of axillary apocrine glands that manifests as an absence of axillary hair, reduced or absent perspiration, sparse body hair (Schinzel, 1987) and dental abnormalities (Bamshad et al., 1997). Male UMS patients typically have a delayed onset of puberty, exhibit hypoplasia of the external genitalia, and reduced fertility (Packham, 2003; Schinzel, 1987). In

contrast to females, males are obese and experience delayed growth and skeletal maturation. Short stature is predominantly caused by anatomical pituitary gland anomalies (Linden et al., 2009; Tanteles et al., 2017). Rare cases of UMS exhibit cardiac defects (Meneghini et al., 2006) manifesting themselves as septal defects or conduction abnormalities and are usually linked to large deletions that also affect *Tbx5* genes (Bogarapu et al., 2014; Forzano et al., 2017), which in rare cases can lead to death (Alby et al., 2013; Shamseldin et al., 2016).

Although *Tbx3* mutations are the only ones causally linked to UMS, the variable phenotypic manifestation points to the involvement of other genes, regulatory elements or environmental factors. In case of large deletions covering the *TBX3* locus nearby genes could also be deleted or affected as is the case for *TBX5* (Alby et al., 2013; Bogarapu et al., 2014; Forzano et al., 2017; Shamseldin et al., 2016). Klopocki et al. (2006) proposed that large deletions harboring *TBX3* also alter or remove *cis*-regulatory elements required for transcriptional regulation of *THRAP2* (thyroid hormone receptor-associated protein 2). *THRAP2* is known to be expressed in a sub-region of the brain, and therefore the case in which UMS is linked to mental retardation could be caused by the *Tbx3* haploinsufficiency removing or altering the *cis*-regulatory elements of *THRAP2*.

Interestingly, the forelimbs of *Tbx3*-deficient mice bear resemblance to the human UMS forelimb phenotype but a few striking differences are apparent. In humans, the *TBX3* haploinsufficiency most often leads to severe forelimbs abnormalities, while mice heterozygous for *Tbx3* are normal and in *Tbx3*-deficient mice, the hindlimb phenotypes are more severe than forelimb phenotypes (Davenport et al., 2003).

4.2.7 *Cis*-regulatory modules in embryonic development

Cis-regulatory modules (CRMs) are non-coding DNA sequences that regulate the spatio-temporal kinetics of gene expression. CRMs provide a structural scaffold for TFs and cofactors and bridging them to promoters results in precise control of gene expression (Davidson, 2006). CRMs, such as enhancers, promoters, and anchors, are predicted to encompass 20%–40% of all non-coding sequences in the human genome (Kellis et al., 2014). CRMs are unevenly distributed and in particular their density is increased in super-enhancers or in enhancer regions associated with cell identity (Boeva et al., 2017). In *cis*-regulatory landscapes, CRMs are both found in close proximity to the transcription-starting site (TSS) or far up- or downstream to regulate gene expression. CRMs can be located within introns, intergenic regions, gene deserts or even be part of coding exons. The 3D chromatin

architecture plays an important role in gene regulation and enhancer specificity in mammals, where the genome is organized into different-sized topologically associating domains (TADs), (Fig. 13A). TADs are delineated by boundaries enriched in CTCF insulator proteins, which ensures specific interactions between enhancers and the promoter of the target genes (Dixon et al., 2012). Genetic alterations or deletions of TAD boundaries underlies different congenital limb malformations (Barrington et al., 2017; Lupiáñez et al., 2015).

CRMs are bound by TFs, histones, and chromatin-remodeling complexes. Currently, the best methods to identify specific and likely functionally relevant CRMs are ChIP-seq for histone modifications (e.g., histone 3 lysine 27 acetylation, H3K27ac) (Heintzman et al., 2007) and chromatin-bound proteins (e.g., EP300, CTCF) (Bailey et al., 2015; Heintzman et al., 2007) or chromatin accessibility assays (DNase-seq and ATAC-seq) (Buenrostro et al., 2013; Thurman et al., 2012), (Fig. 13B). The activity of CRMs can be modulated by different PTMs of histones, which in turn will influence chromatin structure and transcriptional activities. H3K4me1 marks active and primed (poised) enhancers (Rada-Iglesias, 2018), while H3K27ac helps to distinguish active enhancers from primed ones (Voigt et al., 2013). Actively transcribed CRMs marked by H3K4me3 are enriched near the active promoters (Liang et al., 2004) and H3K36me3 modifications are detected in actively transcribed gene bodies (Schwartz et al., 2009). marks facultatively repressed chromatin (Barski et al., 2007). Bivalent chromatin domains are large segments of DNA enriched in H3K27me3, while a smaller region within is

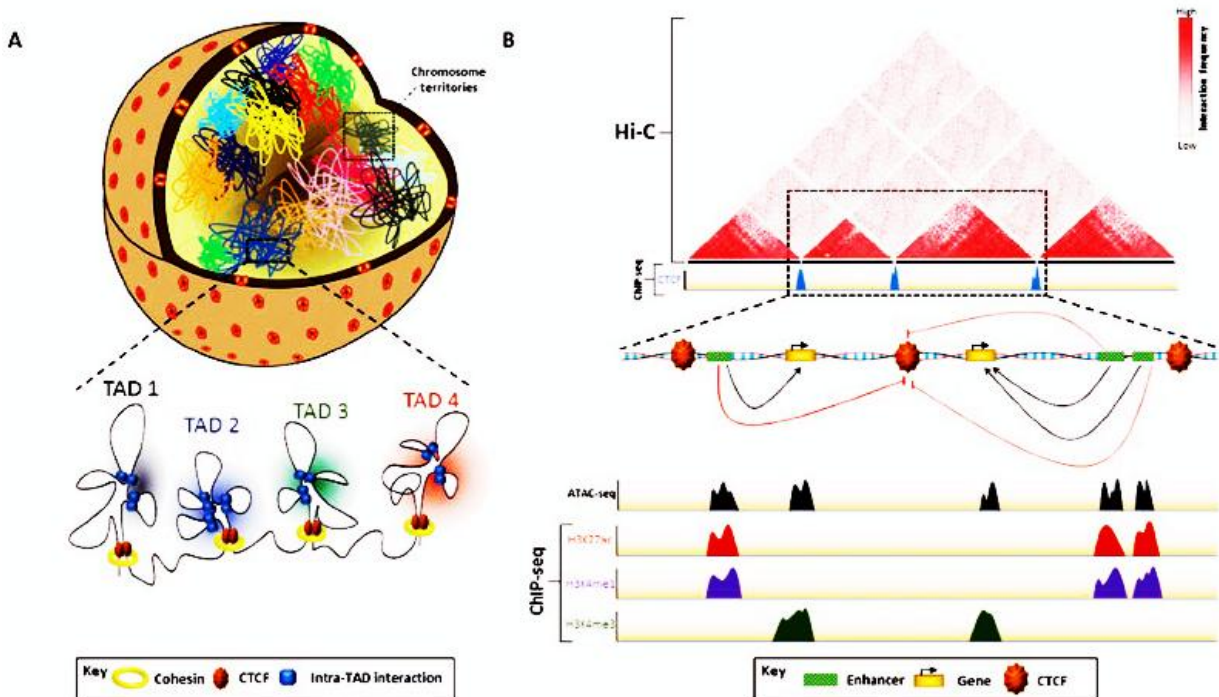


Figure 13. TADs chromatin organization and its relevance for gene regulation. (A) Schematic representation of the chromatin architecture in the nucleus. At the chromosomal level, chromatin is organized in TADs by cohesin and CTCF complexes that promote formation of TADs and intra-TADs. The TAD organization is stable and conserved among tissues and species, while intra-TAD interactions can be highly dynamic. (B) TADs act as the regulatory units and the CRMs within a TAD can directly interact with gene promoters. Hi-C technique helps to reveal these interactions between CRMs within and neighboring TADs. ChIP-Seq, ATAC-seq and functional assays are used to characterize the CRM status within a particular TAD. Epigenetic histone marks are used to identify active or repressed enhancers and promoter regions (Nowosad et al., 2020).

enriched in H3K4me3 marks. These elements tend to map to promoters and distal enhancers of key developmental regulator genes (Bernstein et al., 2006). Bivalent domains are particularly important as the target genes are repressed state, but poised for lineage-specific activation as long as the inducing signals are absent (Voigt et al., 2013).

A genome-wide limb bud development studies identified and classified more than 400 limb associated *cis*-regulatory landscapes (Andrey et al., 2017). Almost nothing is known about TBX3 *cis*-target modules during limb development. Therefore, this project serves a stepping stone to provide insights into TBX3 role in limb development and diseases.

5 Aim of the thesis

The highly complex limb morphology is the result of precise and tissue-specific spatio-temporally controlled gene expression in the undifferentiated limb bud mesenchymal progenitors during embryonic development. The coordination of gene expression is achieved by integration of various inputs from signaling pathways and *trans*-acting transcription factors via the *cis*-regulatory modules (CRMs) located in the *cis*-regulatory landscapes of their target genes. The developing limb bud serves as an excellent model that provides often straight-forward phenotypical readouts for alterations affecting the molecular mechanisms that control growth and patterning. The analysis of these mechanisms provides novel insights into developmental processes and the alterations underlying human congenital diseases.

TBX3 and HAND2 are essential transcriptional regulators during embryogenesis (see chapters before). In particular, HAND2 controls expression of genes in the proximal limb bud mesenchyme and establishes AP polarity by antagonizing *Gli3* expression in the posterior mesenchyme (Galli et al., 2010; Welscher, Fernandez-Teran, Ros, & Zeller, 2002). However, HAND2 is itself not sufficient to precisely establish the posterior *Gli3* expression boundary that defines the initial anterior and posterior limb bud mesenchymal territories. Genetic analysis indicated that this boundary formation is mediated by the developmental repressor *Tbx3*, which is itself a direct transcriptional target of HAND2 (Osterwalder et al., 2014). It is important to note that these early pre-patterning events occur prior to activation of SHH signaling in the posterior limb bud mesenchyme. Furthermore, TBX3 was identified as the main underlying cause of the human Ulnar-mammary syndrome (Basmshad et al., 1997). Despite its importance, little is known about the functions of TBX3 during limb bud development.

Therefore, the research toward my PhD aimed:

1. to generate a TBX3^{3xF} mice line as a new and highly sensitive tool to detect the endogenous TBX3 protein and its cisome during early forelimb bud development;
2. to identify the TBX3 target GRNs that orchestrate early limb bud development;
3. to study how HAND2 and its direct transcriptional target TBX3 control transcriptional interactions and networks that govern early limb bud development to establish AP polarity in the nascent limb bud mesenchyme upstream of SHH signaling;
4. to provide insight into the transcriptional functions of TBX3 at its *cis*-regulatory loci.

Besides its essential roles during early limb bud development, HAND2 is also required for normal heart development as *Hand2*-deficient mouse embryos display severe heart defects (Srivastava et al., 1997), which result in growth retardation and embryonic lethality around E10.5. Frederic Laurent, another PhD student in the group showed that in *Hand2*-deficient mouse embryos cardiac cushion development is also disrupted in addition to the already known heart defects that include the outflow tract malformations and the right ventricle hypoplasia. The cardiac cushions are normally formed by delaminating endocardial cells. These endocardial cells then migrate into the cardiac jelly in response to signals from the myocardium to give a raise to the cardiac cushions, which subsequently form the atrioventricular node and tricuspid valves. In addition to the HAND2^{3xF} ChIP-seq done by F. Laurent, I performed comparative RNA-seq from hand-dissected AVCs of wild-type *Hand2*-deficient embryos. This analysis revealed *Snail* as one of the direct transcriptional targets of HAND2 in the AVC. *Snail* is known as a master regulator of endothelial to mesenchymal transition (EMT) and thus, we could establish that the loss of HAND2 perturbs a target GRN that controls the cardiac valve formation in the AVC (Laurent et al., 2017).

6 Results

6.1 Identification of the direct targets of HAND2 during heart development

“Identification of the direct transcriptional targets of the HAND2 transcription factor during heart development”

“HAND2 Target Gene Regulatory Networks Control Atrioventricular Canal and Cardiac Valve Development”

Laurent, F., **Girdziusaite, A.**, Gamart, J., Barozzi, I., Osterwalder, M., Akiyama, J.A., Lincoln, J., Lopez-Rios, J., Visel, A., Zuniga, A., et al. (2017). *Cell Rep.* 19, 1602–1613.

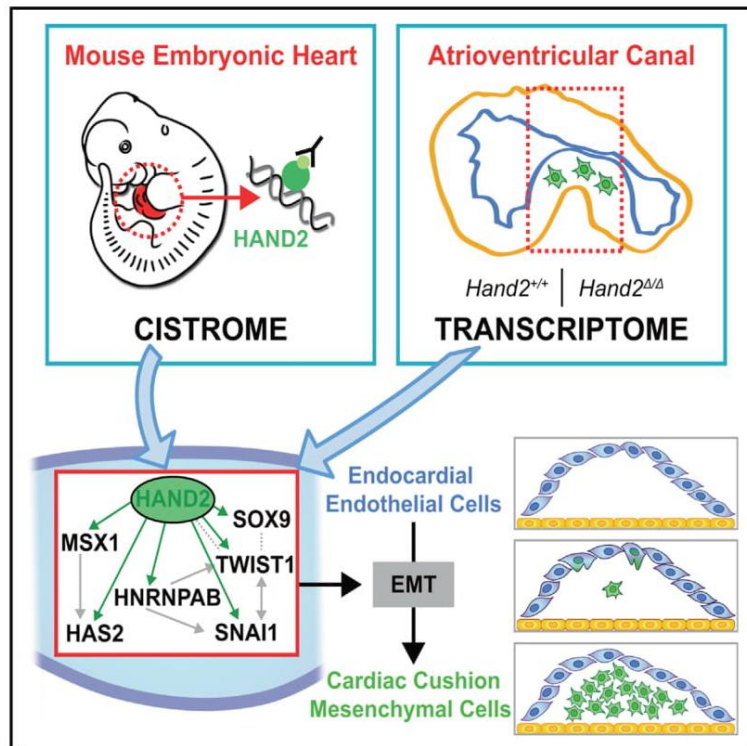
Congenital malformations affecting the heart are among the leading conditions that cause birth defect-related deaths in humans. HAND2 is an essential transcription factor that is indispensable for normal heart development as *Hand2*-deficient embryos display severe heart defects that leads to embryonic lethality around E10.5. I participated in a study by Laurent et al. (2017) which establishes that in addition to the known outflow tract malformations and right ventricle hypoplasia, *Hand2*-deficient mouse hearts fail to form the cardiac cushions in the atrioventricular canal (AVC) that give rise to the atrioventricular node and tricuspid valves. In wild-type hearts, endocardial cells delaminate and migrate into the cardiac jelly and give rise to cardiac cushions in response to signals from the myocardium. We showed that in *Hand2*-deficient developing hearts, the AVC cardiac cushions agenesis is a likely result of losing the expression of the HAND2 direct transcriptional target *Snai1*, which is a master regulator of the endothelial to mesenchymal transition (EMT) in the embryonic heart. Thus, the absence of AVC cardiac cushions in *Hand2*-deficient hearts is due to a complete disruption of EMT of the endocardial cells.

I contributed to the article of Laurent et al., 2017 by conducting diverse experiments such as lysotracker staining to evaluate cell death in *Hand2*^{ΔΔ} mouse embryonic hearts at E9.5 (Figure S1c). As part of the team, I performed an RNA-seq analysis of WT and *Hand2*^{ΔΔ} AVCs to identify the differentially expressed genes (DEGs) in WT and *Hand2*-deficient AVCs (Figure 4 and S4). Also, I performed a comparative spatio-temporal expression analysis of DEGs in WT and *Hand2*-deficient AVCs. For this purpose, I cloned and prepared riboprobes for an in-depth whole-mount *in situ* analysis of the *Hhex*, *Kdr*, *Pitx2*, *Hey1*, *Gja5*, *Cyr61*, *Hnrnpab*, *Twist1*, *Lbh*, *Dkk3*, *Cyp26a1*, *Tmem100*, *Acvrl1* and *Tbx3* DEGs. These results are shown in Figure 5 and Supplementary Figures S5 and Thesis Supplementary Fig. 42-47).

Cell Reports

HAND2 Target Gene Regulatory Networks Control Atrioventricular Canal and Cardiac Valve Development

Graphical Abstract



Authors

Frédéric Laurent, Austra Girdziusaite, Julie Gamart, ..., Axel Visel, Aimée Zuniga, Rolf Zeller

Correspondence

rolf.zeller@unibas.ch

In Brief

Laurent et al. combine ChIP-seq with transcriptome analysis to identify the HAND2 target gene network that controls the EMT and mesenchymal cell migration during cardiac cushion formation in the atrioventricular canal (AVC). The HAND2 transcriptional targets include *Snai1*, whose re-expression in *Hand2*-deficient AVC partially restores mesenchymal cell migration.

Highlights

- HAND2 controls development of the AVC cardiac cushions forming mitral/tricuspid valves
- HAND2 is a key regulator of the EMT underlying cardiac cushion mesenchyme formation
- Identification of the HAND2 target gene networks that control EMT and AVC development
- HAND2 acts upstream of the EMT key regulator *Snai1* in AVC and other embryonic tissues

Accession Numbers

GSE73368
GSE94246



Laurent et al., 2017, Cell Reports 19, 1602–1613
May 23, 2017 © 2017 The Author(s).
<http://dx.doi.org/10.1016/j.celrep.2017.05.004>

CellPress

HAND2 Target Gene Regulatory Networks Control Atrioventricular Canal and Cardiac Valve Development

Frédéric Laurent,^{1,7} Ausra Girdziusaite,^{1,7} Julie Gamart,¹ Iros Barozzi,² Marco Osterwalder,^{1,2} Jennifer A. Akiyama,² Joy Lincoln,³ Javier Lopez-Rios,⁴ Axel Visel,^{2,5,6} Aimée Zuniga,^{1,8} and Rolf Zeller^{1,8,9,*}

¹Developmental Genetics, Department of Biomedicine, University of Basel, 4058 Basel, Switzerland

²Functional Genomics Department, Lawrence Berkeley National Laboratory, Berkeley, CA 94720, USA

³Center for Cardiovascular and Pulmonary Research, The Research Institute at Nationwide Children's Hospital, Columbus, OH 43205, USA

⁴Development and Evolution, Department of Biomedicine, University of Basel, 4058 Basel, Switzerland

⁵U.S. Department of Energy Joint Genome Institute, Walnut Creek, CA 94598, USA

⁶School of Natural Sciences, University of California, Merced, CA 95343, USA

⁷These authors contributed equally

⁸Senior author

⁹Lead Contact

*Correspondence: rolf.zeller@unibas.ch

<http://dx.doi.org/10.1016/j.celrep.2017.05.004>

SUMMARY

The HAND2 transcriptional regulator controls cardiac development, and we uncover additional essential functions in the endothelial to mesenchymal transition (EMT) underlying cardiac cushion development in the atrioventricular canal (AVC). In *Hand2*-deficient mouse embryos, the EMT underlying AVC cardiac cushion formation is disrupted, and we combined ChIP-seq of embryonic hearts with transcriptome analysis of wild-type and mutant AVCs to identify the functionally relevant HAND2 target genes. The HAND2 target gene regulatory network (GRN) includes most genes with known functions in EMT processes and AVC cardiac cushion formation. One of these is *Snai1*, an EMT master regulator whose expression is lost from *Hand2*-deficient AVCs. Re-expression of *Snai1* in mutant AVC explants partially restores this EMT and mesenchymal cell migration. Furthermore, the HAND2-interacting enhancers in the *Snai1* genomic landscape are active in embryonic hearts and other *Snai1*-expressing tissues. These results show that HAND2 directly regulates the molecular cascades initiating AVC cardiac valve development.

INTRODUCTION

Perturbations affecting cardiac progenitors result in embryonic lethality and severe congenital heart defects, which are a major cause of infant and even adult mortality (Bruneau, 2008). In particular, different types of congenital heart defects are caused by alterations in the progenitors of the second heart field (SHF;

reviewed by Kelly, 2012). SHF progenitors migrate into the developing heart tube, where they contribute to most developing structures including the inflow pole, both atria and ventricles, and the outflow tract (OFT). The four heart chambers are formed by rapid proliferative expansion, while the cardiomyocytes in the OFT and atrioventricular canal (AVC) proliferate less and remain undifferentiated (Christoffels et al., 2010; Greulich et al., 2011). The AVC connects the left ventricle to the forming atria, is required for chamber septation, and gives rise to the atrioventricular node and mitral and tricuspid valves (Christoffels et al., 2010; Lin et al., 2012). In mouse embryos, development of the AVC valves begins at embryonic day E9.5, when endocardial cells undergo an endothelial to mesenchymal transition (EndMT or EMT) in response to signals from the myocardium. The delaminating endocardial cells migrate into the cardiac jelly and give rise to the cardiac cushion mesenchyme, which are then remodeled into the mature valve structures (MacGrogan et al., 2014). The EMT in the AVC is controlled by BMP2 signaling from the myocardium, which synergizes with myocardial TGF β 2 and endocardial NOTCH signaling to activate downstream effectors that include the *Snai1* transcriptional regulator (Luna-Zurita et al., 2010; Ma et al., 2005; Niessen et al., 2008; Timmerman et al., 2004). SNAI1 is a key EMT regulator in embryos and various diseases such as tumor metastasis (reviewed by Nieto, 2011). Its inactivation in the endothelial compartment disrupts the EMT underlying AVC cardiac cushion formation (Wu et al., 2014).

Another transcription factor essential for heart development is HAND2, which also functions in developing branchial arches and limb buds (Srivastava et al., 1997). In the developing heart, HAND2 is expressed in the myocardial compartment of the right ventricle and OFT, the epicardium, and valve progenitors in both OFT and AVC (VanDusen and Firulli, 2012; VanDusen et al., 2014b). Consistent with its complex expression pattern, genetic inactivation of *Hand2* in mice disrupts development of limb buds, branchial arches, aortic arch arteries, and the right ventricle, which causes embryonic lethality (Srivastava et al., 1997).

Specific inactivation in developing heart tissues has revealed essential *Hand2* functions in the cardiac neural crest cells that contribute to cardiac cushions in the OFT, survival of SHF progenitors, heart chamber trabeculation, and epicardial cell differentiation (Barnes et al., 2011; Holler et al., 2010; Tsuchihashi et al., 2011; VanDusen et al., 2014a). Previous studies had also pointed to HAND2 functions in cardiac cushion formation, but the potential essential functions have not been identified (Holler et al., 2010; Liu et al., 2009; VanDusen et al., 2014a). In humans, mutations in *HAND2* have been linked to congenital heart malformations that include ventricular septal defects (Shen et al., 2010; Sun et al., 2016).

We have used chromatin immunoprecipitation sequencing (ChIP-seq) to define the genome-wide interaction profile of endogenous HAND2 chromatin complexes in mouse embryonic hearts. This analysis shows that HAND2 interacts with non-coding regions associated with a large number of genes functioning during heart development. Most importantly, our analysis revealed essential HAND2 functions in the EMT underlying AVC cardiac cushion formation, which is disrupted in *Hand2*-deficient embryos. Combining transcriptome analysis of wild-type and *Hand2*-deficient AVCs with the HAND2 ChIP-seq dataset identified the HAND2 target genes that function in AVC cardiac cushion development. In particular, this analysis revealed that the EMT regulator *Snai1* is a transcriptional target of HAND2. The failure of endocardial cells to invade the cardiac jelly in *Hand2*-deficient AVCs is partially restored by re-expressing *SNAI1* in mutant explants. Last but not least, we show that the two *Snai1*-associated enhancers interacting with HAND2 chromatin complexes recapitulate major aspects of *Snai1* expression in mouse embryos.

RESULTS

Genomic Regions Enriched in Endogenous HAND2 Chromatin Complexes Identify the Range of HAND2 Target Genes in Mouse Embryonic Hearts

The *Hand2*^{3xFL} allele, which encodes a HAND2 protein with a 3xFLAG epitope tag inserted in its N-terminal part (Osterwalder et al., 2014), was used to profile the genomic regions enriched in HAND2-chromatin complexes. Anti-FLAG antibodies were used for chromatin immunoprecipitation, which was followed by massive parallel sequencing (ChIP-seq). To obtain sufficient chromatin for ChIP-seq, ~300 hearts per biological replicate were dissected from *Hand2*^{3xFL/3xFL} mouse embryos at embryonic days E10.25–10.5. Two biological replicates were analyzed, and the genome-wide binding profiles using model-based analysis of ChIP-seq (MACS) (Zhang et al., 2008) identified 12,117 significantly enriched genomic regions. Genomic Regions Enrichment of Annotations Tool (GREAT) analysis (McLean et al., 2010) was used to assign these 12,117 regions to 7,792 neighboring genes, which defines the initial set of putative HAND2 targets (Table S1; Supplemental Experimental Procedures). Most of the genomic regions enriched in HAND2 chromatin complexes are located ≥ 10 kb away from transcriptional start sites (TSS) and encode evolutionary conserved sequences that overlap the peak summit (Figures 1A and 1B). Functional enrichment was assessed by GREAT using increasingly larger set of peaks

(pool of incremental deciles; for details, see Supplemental Experimental Procedures). This analysis revealed that terms related to abnormal cardiac morphology and heart development were already enriched when using only the most enriched regions, while terms referring to specific processes such as OFT, right ventricle, and AVC development reached significance using the larger dataset (Figure S1A). In particular, 15 of the 16 most enriched Gene Ontology (GO) terms are relevant to heart development, while the remaining term identifies genes functioning in EMT processes (Figure 1C, see below). De novo motif discovery using HOMER (Heinz et al., 2010) identified the consensus *Ebox* motif (CATCTG; Dai and Cserjesi, 2002) as the most prevalent among HAND2 peaks (Figure 1D). Other significantly enriched motifs include binding sites for GATA transcription factors (Figure S1B), which are key regulators of heart development (Stefanovic and Christoffels, 2015). Indeed, computational comparison of the HAND2 (Table S1) with a published GATA4 ChIP-seq dataset (using whole mouse embryonic hearts at E12.5; He et al., 2014) shows that 28.3% of the enriched genomic regions are shared between the two datasets, which is 15-fold higher than expected by chance (data not shown). As development of *Hand2*-deficient mouse embryos results in lethality by ~E10.5 (Srivastava et al., 1997), we limited our analysis to mutant embryos at E9.0–9.5. During this early organogenic stage, no aberrant apoptosis occurs in the developing heart in contrast to branchial arches and frontonasal mass (Figure S1C). Therefore, all interactions of HAND2 chromatin complexes with candidate *cis*-regulatory modules (CRMs) associated with genes of interest were also verified by ChIP-qPCR using embryonic hearts at E9.25–9.5 (Figures 1, 4, S3, and S6).

To validate the ChIP-seq dataset as a resource for identifying HAND2 target genes, we determined which of the genes with known alterations in their expression are associated with HAND2 ChIP-seq peaks (Table S2 and references therein). This analysis showed that about half of these genes are associated with at least one HAND2 ChIP-seq peak ($n = 56/114$; Table S2, see also Table S1). This suggests that their altered expression in *Hand2*-deficient hearts could be a consequence of direct transcription regulation by HAND2. Next, we overlapped the HAND2 binding profiles with enhancers active in mouse embryonic hearts that were identified by a large enhancer screen (VISTA Enhancer Browser: <https://enhancer.lbl.gov>, Visel et al., 2007). This analysis showed that 71 of the 193 VISTA enhancers active in mouse embryonic hearts overlap with HAND2 ChIP-seq peaks (Figures 1E, 1F, and S2; Table S3). These enhancers include CRMs in the genomic landscapes of the *Gata4*, *Gata6*, *Myocd*, and *Tbx20* transcriptional regulators, which are essential for OFT and/or right ventricle development. Whole-mount in situ hybridization (WISH) showed that the expression of *Gata4*, *Myocd*, and *Gata6* is reduced in *Hand2*-deficient hearts, while the expression of *Tbx20* appears unchanged (E9.25–9.5, Figure 1G). The requirement of *Hand2* for OFT and right ventricle development is also supported by GO analysis as more than half of the genes with annotated functions in OFT and right ventricle (RV) development are associated with HAND2 ChIP-seq peaks (Figure S3A; Table S4). In particular, several ligands of the signaling pathways required for development of these structures are identified as HAND2 target genes (Figures S3B

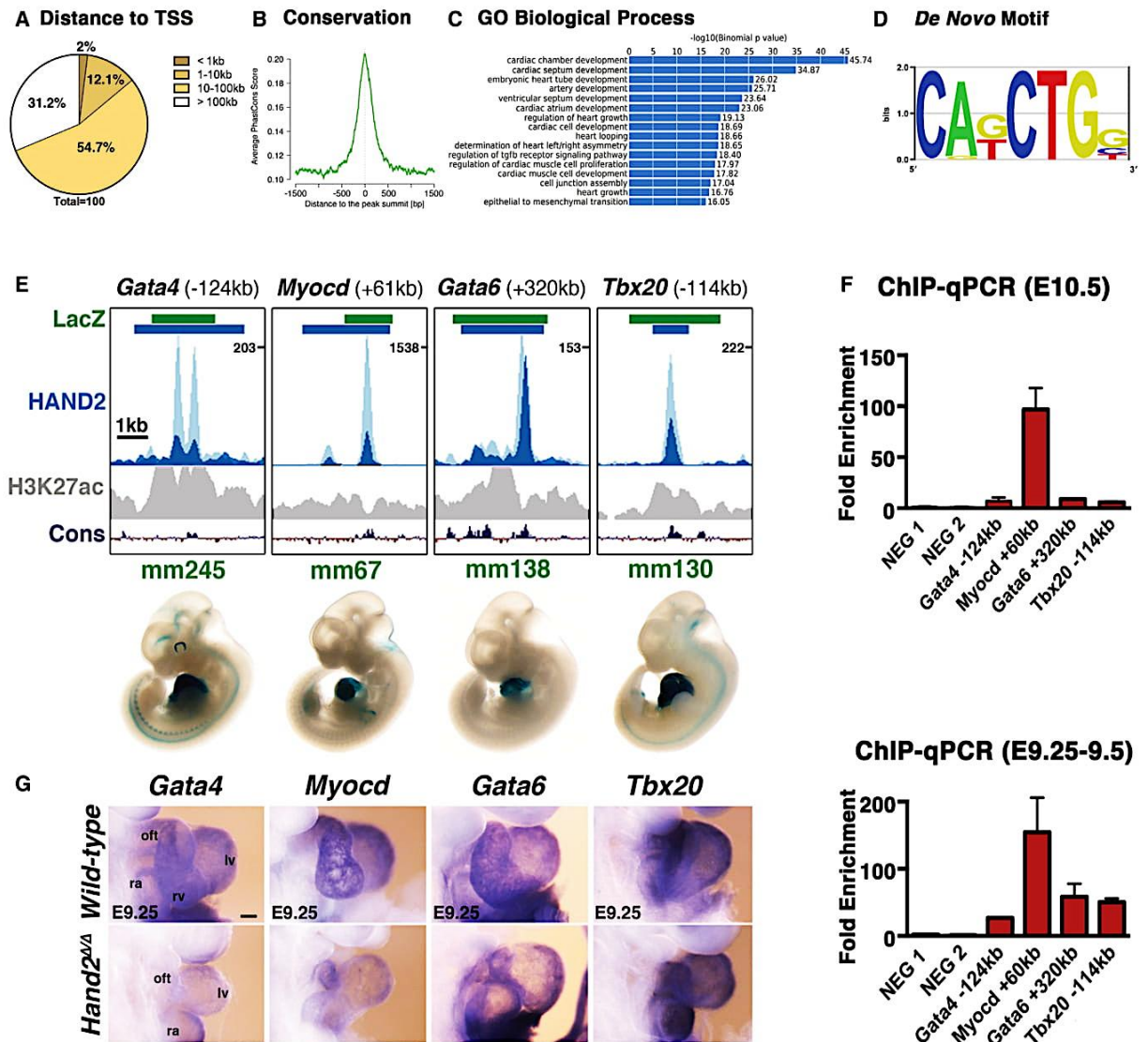


Figure 1. CHIP-Seq Analysis Using the *Hand2*^{3x_F} Allele Identifies the HAND2 Cistrome in Mouse Embryonic Hearts
 (A) The majority of the genomic regions enriched in HAND2 chromatin complexes from mouse embryonic hearts at E10.5 map ≥ 10 kb away from the closest transcription start site (TSS).
 (B) In addition, the majority of the HAND2-interacting genomic regions are evolutionarily conserved.
 (C) The top GO terms associated with HAND2 candidate targets reveal the preferential enrichment of genes functioning in cardiac development.
 (D) The consensus *Ebox* motif is most enriched by de novo motif discovery.
 (E) Selection of VISTA enhancers enriched in HAND2 chromatin complexes. Green intervals indicate the regions with enhancer activity (VISTA enhancer database); blue intervals highlight the regions enriched in HAND2 chromatin complexes (MACS peaks). Distances to the nearest TSS within the TAD are indicated on top. ChIP-seq profiles of the two biological replicates (E10.5) are shown in light and dark blue, respectively. The H3K27ac ChIP-seq profile for mouse hearts (E11.5) is shown in gray (Nord et al., 2013). The scheme at the bottom shows the placental mammal conservation (Cons) plot (PhyloP). Representative transgenic *LacZ* reporter embryos for VISTA enhancers associated with genes functioning in OFT and/or right ventricle development (*Gata4*, *Myocd*, *Gata6*, and *Tbx20*) are shown below.
 (F) ChIP-qPCR validation of the ChIP-seq peaks (E) for mouse embryonic hearts at E10.5 (n = 3 biological replicates) and E9.25 (n = 2; mean \pm SD).
 (G) Expression of the HAND2 targets *Gata4*, *Myocd*, *Gata6*, and *Tbx20* in wild-type and *Hand2* ^{Δ/Δ} embryonic hearts (E9.25). Scale bars, 100 μ m. oft, outflow tract; ra, right atrium; rv, right ventricle; lv, left ventricle; avc, atrioventricular canal; la, left atrium. See also Figures S1–S3 and Tables S1 and S2–S4.

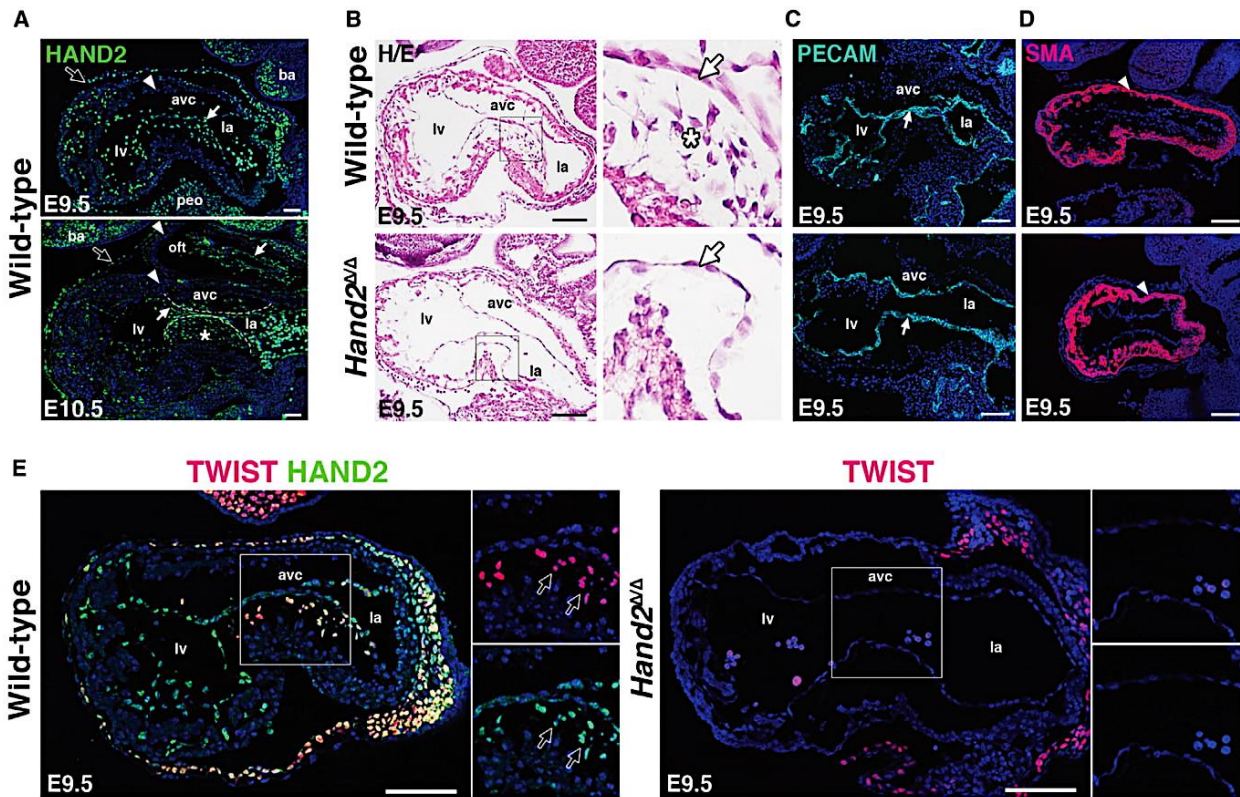


Figure 2. AVC Cardiac Cushion Agenesis in *Hand2*-Deficient Mouse Embryos

(A) Distribution of the endogenous *HAND2*^{3xFLAG} protein (using anti-FLAG antibodies, green fluorescence) during in mouse embryonic hearts at E9.5 and E10.5. Representative sagittal sections are shown. White arrows, endocardium; white arrowheads, myocardium; white asterisks, *HAND2* expressing AVC cardiac cushion mesenchymal cells; black arrows, epicardium. Scale bars, 50 μ m.
 (B) H&E staining reveals the absence of delaminating endocardial cells with mesenchymal characteristics (white asterisks) in the AVC of *Hand2*-deficient mouse embryos. White arrow, endocardium. Scale bars, 100 μ m.
 (C) Detection of the platelet endothelial cell adhesion molecule (PECAM) in the endocardium of wild-type and *Hand2*-deficient embryos (white arrow).
 (D) Detection of smooth muscle actin (SMA) in the AVC myocardium of wild-type and *Hand2*-deficient embryos (white arrowhead). Myocardium (A–D).
 (E) Colocalization of the *HAND2*^{3xFLAG} (green fluorescence) with TWIST1 transcriptional regulators (red fluorescence) in the AVC of wild-type (*Hand2*^{3xFLAG/3xFLAG}) and *Hand2*-deficient (*Hand2* <sup>Δ/Δ) embryos at E9.5. Colocalization is detected in delaminating mesenchymal cells (indicated by arrows, left panel), which are missing from the mutant AVC (right panel).
 Scale bars in panels (E) AND (F), 100 μ m. avc, atrioventricular canal; ba, branchial arches; la, left atrium; lv, left ventricle; oft, outflow tract; peo, proepicardial organ.</sup>

and S3C). This includes *Wnt11*, *Wnt5a*, *Bmp4*, *Tgf β 2*, and *Fgf10*, whose expression is either reduced or lost from the OFT and/or RV of *Hand2*-deficient mouse embryos (E8.75–9.25, Figure S3C). Collectively, this first analysis shows that a significant fraction of genes functioning in mouse OFT and RV morphogenesis are likely *HAND2* target genes (Figures 1G and S3). However, not all candidate target genes analyzed are altered in *Hand2*-deficient hearts, which points either to *cis*-regulatory redundancy or raises the possibility that the interaction of *HAND2* complexes with the candidate CRMs is not essential for the adjacent genes.

HAND2 Is a Key Regulator of the EMT during AVC Cardiac Cushion Formation

Strikingly, the GO analysis identified EMT as one of the key biological processes associated with the *HAND2* cistrome (Figure 1C).

An essential process during heart valve development is formation of the mesenchymal compartment of the AVC cardiac cushions as endocardial cells undergo an EMT (see Introduction). In wild-type hearts, *HAND2* proteins are expressed by endocardial cells in the AVC, the cells undergoing EMT and the delaminating cells forming the cushion mesenchyme continue to express *HAND2* (asterisk, Figure 2A and data not shown). Furthermore, histological analysis reveals the complete absence of mesenchymal cells in the AVC cardiac cushions of *Hand2*-deficient hearts at E9.0–9.5, which points to disruption of the EMT process (Figure 2B). As the distribution of platelet endothelial cell adhesion molecule (PECAM) and smooth muscle actin (SMA) positive cells is not altered in *Hand2*-deficient hearts, the endocardial and myocardial compartments of the AVC appear to have formed normally, which underscores the specific nature of the observed cellular defect

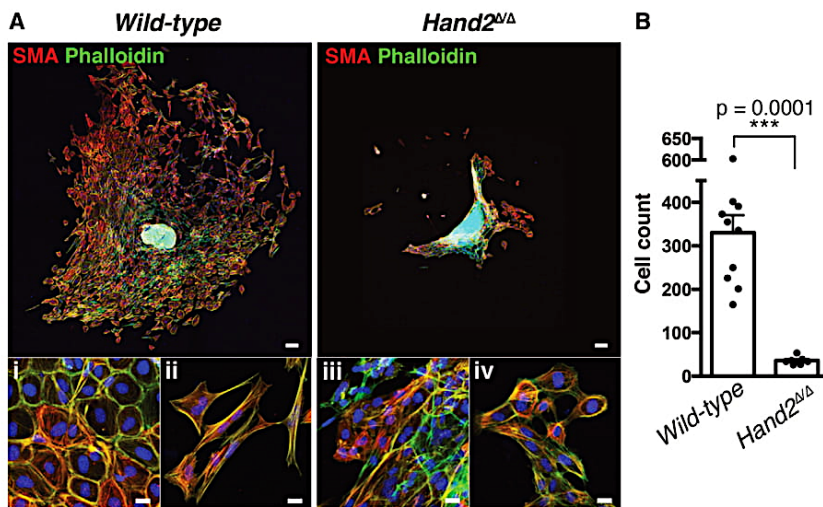


Figure 3. *Hand2*-Deficient AVC Endocardial Cells Fail to Initiate EMT and Mesenchymal Cell Migration

(A) Smooth muscle actin (red) and F-actin (green Phalloidin staining) distribution in cells that have migrated into the matrix from AVC explants of wild-type and *Hand2*-deficient embryos after 72 hr in culture. Scale bars, 100 μ m. Bottom panels show cells in proximity to the explant (i and iii) and at the far edge of migration (ii and iv). Scale bars, 20 μ m. (B) Quantification of the numbers of cells that migrated into the matrix from wild-type ($n = 10$) and *Hand2*-deficient AVC explants ($n = 7$). The mean \pm SD ($p = 0.0001$, Mann-Whitney test) and all individual data points are shown.

(Figures 2C and 2D). TWIST1 forms hetero-dimeric transcriptional complexes with HAND2 and regulates cardiac cushion development (Firulli et al., 2005; VanDusen and Firulli, 2012). Therefore, the distribution of both proteins was comparatively analyzed in developing AVC cardiac cushions (Figure 2E). In wild-type embryos, HAND2 and TWIST1 are co-expressed by the delaminating mesenchymal cells that form the AVC cardiac cushions in wild-type hearts (left panels, Figure 2E). In contrast, these TWIST1-positive cells are absent in *Hand2*-deficient hearts (right panel, Figure 2E). Together, these results point to complete disruption of AVC cardiac cushion formation in *Hand2*-deficient mouse embryos.

To study this processes further, AVCs were dissected from wild-type and mutant hearts at E9.5 and cultured on collagen matrices for 72 hr (Figure 3A, Camenisch et al., 2000). Then, the mesenchymal cells that had migrated from the explant into the matrix were quantitated (Figure 3B): on average 330 ± 40 cells colonize the matrix in wild-type AVC explants ($n = 10$), while ~ 10 -fold fewer mesenchymal cells (36 ± 3) are detected in AVC explants isolated from *Hand2*-deficient embryos ($n = 7$). In particular, wild-type endocardial cells in proximity of the AVC explant retain their cobblestone-like morphology and a cortical actin ring (Figure 3A, i), while cells that migrated further develop actin stress fibers and long filopodia characteristic of mesenchymal cells (Figure 3A, ii). In contrast, the few cells invading the matrix in cultures of *Hand2*-deficient AVCs mostly retain their cobblestone-like morphology (Figure 3A, iii and iv). This loss of mesenchymal characteristics shows that the endocardial cells of *Hand2*-deficient AVCs fail to undergo the EMT giving rise to the mesenchymal cell forming the cardiac cushions.

HAND2 Controls the Expression of Genes that Function in the EMT Underlying AVC Cardiac Cushion Formation

To identify the gene regulatory networks (GRNs) controlled by HAND2 during AVC cardiac cushion formation, the transcriptomes of dissected wild-type and *Hand2*-deficient AVCs were analyzed (E9.0–9.25: 18–23 somites; see Supplemental Experimental Procedures). Statistical analysis showed that

1,051 genes are differentially expressed (DEGs: 695 are upregulated and 365 downregulated, Figure 4A; Table S5; Figure S4A for GO analysis). Among these genes, the transcriptional targets of HAND2 were identified as those genes harboring one or more HAND2 ChIP-seq peaks in their topologically associating domains (TADs, Dixon et al., 2012; Figures 4B, 4C, and S4B; Table S5). This analysis shows that the TADs of DEGs contain on average a significantly larger number of HAND2-interacting regions (median ~ 5) than genes whose expression is not altered (median ~ 1 ; Figure 4B). GO analysis of these HAND2 transcriptional targets indicates that the 167 DEGs, whose expression is downregulated in *Hand2*-deficient AVCs function preferentially in heart and organ development (including cardiac EMT and mesenchyme development), while the 372 upregulated DEGs function preferentially in cardiovascular and blood vessel development (Figure 4C). In particular, this functional annotation identified a subset of 24 DEGs that function in EMT processes and/or AVC cushion formation (Figure S4C). Combining the transcriptome analysis with HAND2 ChIP-qPCR analysis establishes 19 of these DEGs as direct transcriptional targets of HAND2 in developing hearts at E9.25–9.5 (Figures 4D and 4E). Transcriptome analysis showed that the expression of seven of these HAND2 targets is downregulated, while 12 are upregulated in mutant AVCs (Figure 4D; Table S6). These differential effects are not unexpected as HAND2 transcriptional complexes are known to differentially activate or repress gene expression (see Discussion). Together, this analysis uncovers the HAND2 target GRN functioning in AVC cardiac cushion formation and reveals the differential effects of the *Hand2* deficiency on gene expression in the mutant AVC (Figures 4D and 4E).

Next, we used WISH to detect spatial alterations in the AVC of *Hand2*-deficient hearts at E9.25–9.5 (Figures 5 and S5). To uncover potential global molecular changes in the mutant AVC, we first analyzed the spatial distribution of key regulators whose transcript levels are not changed (*Bmp2*, *Hey2*, *Notch1*, *Rbpj*, *Snai2*, *Epha3*, *Tbx20*; Figures 5A and 5B; Table S5 and data not shown). The spatial distribution of all of these genes is comparable to wild-types in mutant AVCs, as exemplified by the EMT-inducer *Bmp2* and the NOTCH transcriptional target *Hey2* (Figures 5A and 5B). This indicates that the AVC domain

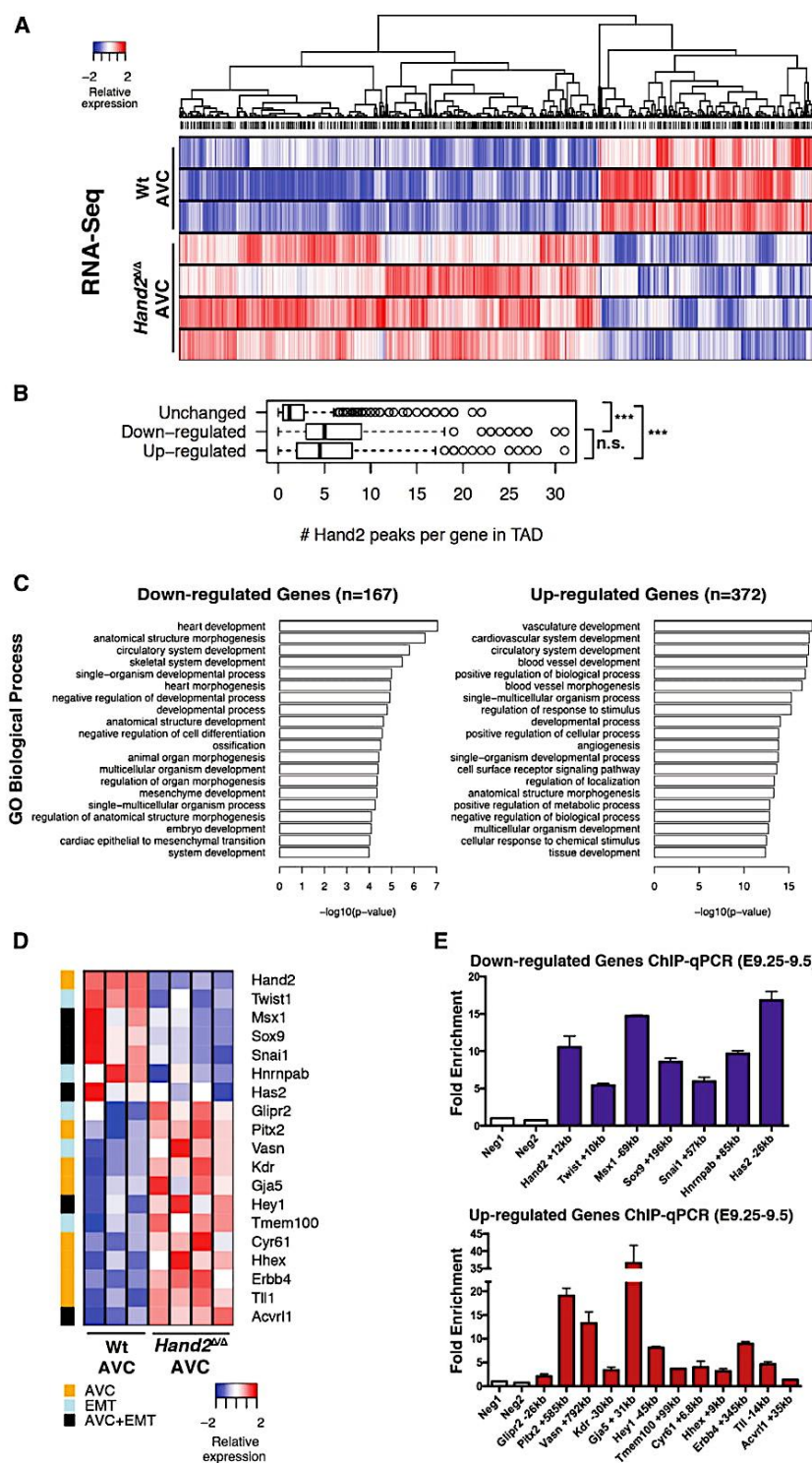


Figure 4. Transcriptome Analysis Identifies the Transcriptional Targets of HAND2 in the AVC

(A) Heatmap of the differentially expressed genes (DEGs) identified by comparing the transcriptomes of wild-type and *Hand2*-deficient AVCs from mouse embryonic hearts at E9.25–9.5 ($n = 4$ and $n = 3$ biological replicates were analyzed for mutant and wild-type AVCs, respectively). DEGs are genes whose expression is significantly changed (≥ 1.5 -fold) between wild-type and mutant samples ($p < 0.05$).

(B) The boxplot shows the number of HAND2 ChIP-seq peaks in the TADs harboring genes with unchanged, down- or upregulated expression in mutant AVCs, respectively. The TADs of genes with altered expression encode more HAND2-interacting genomic regions. To account for the different numbers of genes and HAND2 ChIP-seq peaks per TAD, peak counts were normalized as numbers of peaks per gene for each TAD.

(C) GO enrichment analysis for biological processes for the 167 downregulated and 372 upregulated genes (in mutant AVCs) that contain HAND2 ChIP-seq peaks in their TADs.

(D) GO analysis to identify the HAND2 target genes with annotated functions in EMT processes and AV cushion morphogenesis.

(E) Mouse embryonic hearts isolated at E9.25–9.5 were used for ChIP-qPCR validation of the most prominent HAND2 ChIP-seq peaks in the TADs of the genes shown in D ($n = 4$ using two biological replicates, mean \pm SD, $p \leq 0.05$). See also Figure S4 and Tables S5 and S6.

target genes with significantly changed transcript levels (Figure 4D; Table S6) failed to detect spatial alterations for several of them due to low and/or uniform expression (low: *Vsn*, *Tmem100*, *Erb4*, *Tll1*, and *Acvrl*, uniform: *Cyr61* and *Hnnpab*, data not shown). Furthermore, the small but significant differences in transcript levels for several additional DEGs could not be reliably detected by WISH (*Pitx2*, *Glipr2*, *Kdr*, *Gja5*, Figure S5A and data not shown), likely due to the qualitative nature of in situ hybridization that best detects spatial changes. This is exemplified by the fact that WISH revealed the ectopic expression of two transcriptionally upregulated HAND2 target genes in mutant AVCs, namely, the NOTCH1 transcriptional mediator *Hey1* and the homeobox transcription factor *Hhex* (Figures 5C and 5D).

is correctly specified in mutant hearts and corroborates the specificity of the molecular alterations underlying the cardiac cushion agenesis (Figures 2 and 3). WISH analysis of HAND2

In agreement with the reduced expression detected by RNA-seq (Figure 4D; Table S6), WISH corroborates the loss of the transcriptional regulators *Twist1* (Figure 5E, see also Figure 2E),

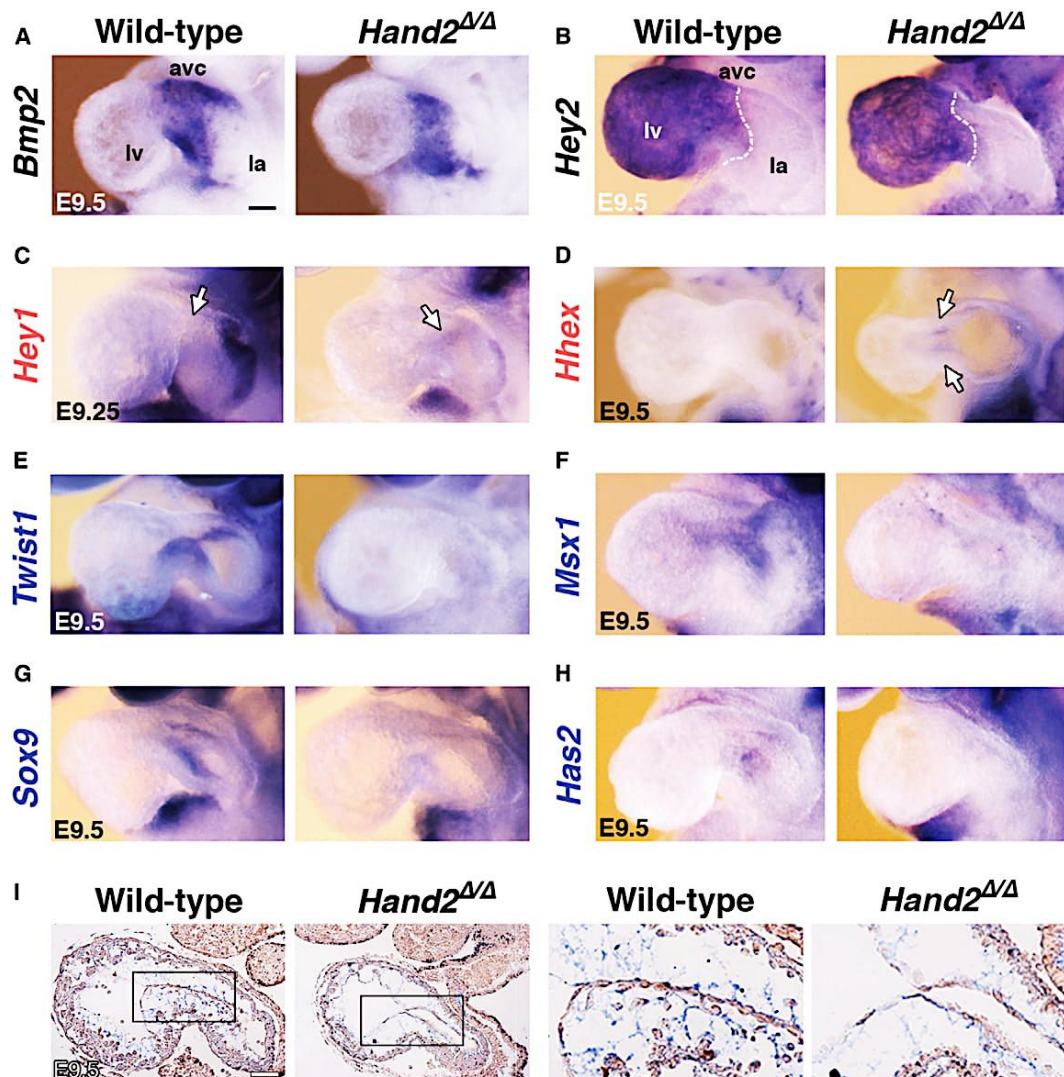


Figure 5. Whole-Mount in Situ Hybridization Reveals Spatial Changes in Some of the Differentially Expressed HAND2 Target Genes
 (A and B) Unaltered expression of *Bmp2* (A) and *Hey2* (B) indicates that the AVC domain is established correctly in *Hand2*-deficient hearts.
 (C and D) Ectopic expression of the *Hey1* (C) and *Hhex* transcriptional regulators (D) in the mutant AVC corroborated their upregulation detected by RNA-seq analysis.
 (E–H) Loss of *Twist1* (E), *Msx1* (F), *Sox9* (G), and *Has2* (H) from the mutant AVC is in agreement with their transcriptional downregulation detected by RNA-seq analysis.
 (I) Alcian blue staining of glycosaminoglycans shows the reduced deposition of extra-cellular matrix in the cardiac jelly of *Hand2*-deficient mouse embryos. Right panels show the enlargements indicated by frames in the left panels. Gene names in black, unaltered; red, increased; blue, reduced transcript levels as determined by RNA-seq analysis (Figure 4).
 Scale bars, 100 μ m. See also Figure S5.

Msx1 (Figure 5F), and *Sox9* (Figures 5G and S5B) from mutant AVCs by E9.5. The downregulation of *Msx1* indicates that BMP signal transduction is disrupted in the mutant AVC (Figure 5F; Table S6). SOX9 regulates the proliferation of the mesenchymal progenitor cells, and its loss agrees with the lack of delaminating mesenchymal cells in mutant AVCs (Figures 5G and S5B; Akiyama et al., 2004). Most relevant to the disrupted EMT (Figure 3), the expression of *Has2* and *Snai1* is significantly downre-

gulated in *Hand2*-deficient AVCs (Figure 4D). *Has2* encodes the enzyme that produces hyaluronic acid in the cardiac jelly (Camenisch et al., 2000). Genetic inactivation of the mouse *Has2* gene disrupts both cardiac jelly deposition and mesenchymal cell migration during cardiac cushion development. In *Hand2*-deficient hearts, the loss of *Has2* is paralleled by reduced extra-cellular matrix/cardiac jelly deposition (Figures 5H and 5I). Camenisch et al. (2000) showed that treatment of *Has2*-deficient

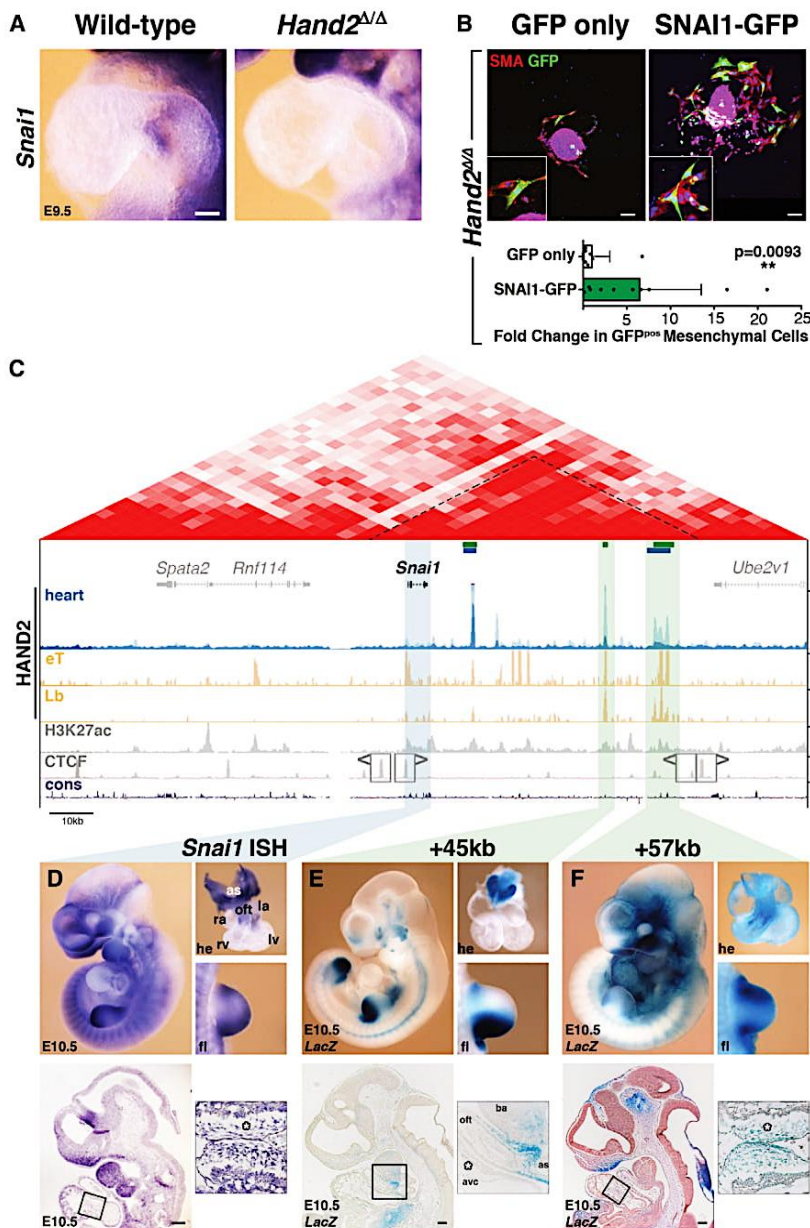


Figure 6. Re-expression of *Snai1* in *Hand2*-Deficient AVC Explants Partially Restores Mesenchymal Cell Migration and Regulation of *Snai1* Expression by Enhancers Enriched in *HAND2* Chromatin Complexes

(A) *Snai1* expression is lost from the endocardium of *Hand2*-deficient hearts.

(B) Upper panels: *Hand2*-deficient AVC explants were infected either with GFP (control) or SNAI1-GFP adenovirus to re-express SNAI1. Samples were analyzed 72 hr after infection. All infected cells that migrated into the matrix are marked by GFP expression (green). Smooth muscle actin (SMA, red) was detected to reveal cellular morphology. Lower panel: quantitation of cell migration in *Hand2*-deficient AVC explants. The mean \pm SD and all individual data points are shown. The observed increase in mesenchymal cells in SNAI1-GFP infected explants is significant ($p = 0.0093$, Mann-Whitney test). Scale bars, 100 μ m.

(C) Scheme of the mouse *Snai1* TAD (red, HiC-data). The *HAND2* ChIP-seq profiles in the heart (this study), *Hand2*-expressing tissues (eT) and limb buds (Lb) (Osterwalder et al., 2014) are shown below together with the H3K27ac profile in developing hearts (E11.5, Nord et al., 2013). The *Snai1* TAD boundaries are marked by CTCF-binding regions in opposite orientation (Gómez-Marín et al., 2015). Green bars indicate the *HAND2* target CRMs located +14kb, +45kb, and +57kb that were analyzed by *LacZ* reporter assays in transgenic founder embryos.

(D) *Snai1* transcript distribution in wild-type mouse embryos (E10.5).

(E) A representative transgenic founder embryo (E10.5) shows the activity of *LacZ* reporter construct encoding the +45kb CRM. (F) A representative transgenic founder embryo (E10.5) shows the activity of *LacZ* reporter construct encoding the +57kb CRM. The upper panels in (E) and (F) depict whole embryos, dissected hearts, and forelimb buds. The lower panels show sagittal sections at the level of the heart. The boxed areas indicate the enlargements shown in the right panels.

Asterisks, AVC cardiac cushion mesenchyme; as, aortic sac; avc, atrioventricular canal; ba, branchial arch; la, left atria; lv, left ventricle; oft, outflow tract; ra, right atria; rv, right ventricle. Scale bars, 200 μ m. See also Figures S5 and S6.

AVC explants with hyaluronic acid restores mesenchymal cell migration. In contrast, culturing *Hand2*-deficient AVC explants in hyaluronic acid does not suffice to restore migration (data not shown). This is in line with the fact that the genetic inactivation of *Hand2* affects the expression of multiple genes required for AVC cushion development (Figures 4 and S4).

HAND2 Regulates the Transcription of *Snai1*, a Key Regulator of the EMT and Mesenchymal Cell Migration in the AVC

The transcriptome combined with ChIP-seq/qPCR analysis (Figures 4D and 4E) and WISH (Figure 6A) establishes *Snai1* as

a direct transcriptional target of *HAND2*. As *Snai1* is a EMT key regulator (Nieto, 2011), its loss from the mutant AVC (Figure 6A) is likely causally linked to the observed cardiac cushion agenesis (Figure 2). To test this experimentally, *Hand2*-deficient AVC explants were infected either with adenovirus producing both SNAI1 and GFP proteins (SNAI1-GFP) or control GFP virus (GFP only; Figure 6B; Tao et al., 2011). Quantitative analysis shows that infection of *Hand2*-deficient AVC explants with SNAI1-producing virus induces migration of a significantly larger fraction of GFP-positive mesenchymal cells into the collagen matrix than GFP alone (Figure 6B, $p = 0.0093$ Mann-Whitney test; see Figure S5C for wild-type controls).

This partial restoration of mesenchymal cell migration reveals the functional importance of the HAND2-*Snai1* interactions for the EMT during cardiac cushion formation. Therefore, we analyzed the potential enhancer activities of the three HAND2-interacting CRMs located in the *Snai1* TAD (Figures 6C and S6A). Our previous analysis has shown that these three candidate CRMs are also enriched in HAND2 chromatin complexes isolated from mouse limb buds (Osterwalder et al., 2014) and overlap regions of active chromatin in embryonic hearts (H3K27ac profile in Figure 6C). Their transcription enhancing potential was assessed in transgenic mouse founder embryos using *LacZ* reporter constructs (Figures 6E and 6F). In particular, *LacZ* activity reminiscent of *Snai1* expression (Figure 6D) was detected for reporters encoding the CRMs located +45kb and +57kb downstream of the *Snai1* transcription start site (Figures 6E and 6F). In contrast, no *LacZ* activity was detected using the *Snai1* +14kb genomic region, whose sequence is not well conserved in mammals (data not shown). The *Snai1* +45kb CRM is active in cells located between the OFT and aortic sac ($n = 7/10$), the posterior ($n = 10/10$) and anterior ($n = 3/10$) limb bud mesenchyme, and branchial arches and cranial mesenchyme ($n = 5/10$, Figure 6E). Most relevant with respect to the AVC, the *Snai1* +57kb CRM is active in the cardiac cushion mesenchyme of the AVC and OFT ($n = 7/9$, Figure 6F) and in most other embryonic tissues expressing *Snai1* (Figure 6D). Together, the activities of these two HAND2-interacting CRMs recapitulate most of the *Snai1* expression pattern in mouse embryos (Figures 6D and S6B–S6D). Indeed, in *Hand2*-deficient embryos, *Snai1* expression is not only lost from the AVC (Figure 6A), but also significantly reduced in the second branchial arch and forelimb bud mesenchyme (Figure S6E).

DISCUSSION

We show that HAND2 chromatin complexes interact with genomic regions such as enhancers located in the *cis*-regulatory landscapes of genes functioning in heart morphogenesis. Previous molecular analysis showed that the altered expression of many of these genes correlates well with the defects in right ventricle and OFT morphogenesis observed in *Hand2*-deficient mouse embryos (Cohen et al., 2012; Tsuchihashi et al., 2011; Zhao et al., 2008). We provide evidence that about half of all previously known genes with altered expression are direct transcriptional targets of HAND2. In addition, our ChIP-seq analysis reveals that a significant fraction of the genomic regions enriched in HAND2 chromatin complexes are also bound by GATA4 complexes (He et al., 2014). This is interesting in light of previous studies, which showed that HAND2 and GATA4 form transcriptional complexes regulating gene expression in developing hearts (Dai et al., 2002). In addition, it has been shown that AVC enhancers are repressed in the atrial and ventricular myocardium by complexes containing GATA4, HEY1, and/or HEY2 transcriptional repressors (Firulli et al., 2000; Stefanovic et al., 2014). These three repressors plus RUNX2 and TWIST1 are all able to form heterodimers with HAND2 (Firulli et al., 2005; Funato et al., 2009). As the expression of many HAND2 target genes is upregulated in *Hand2*-deficient AVCs (this study),

HAND2-mediated transcriptional repression is likely functionally relevant to normal AVC development. For example, the HAND2 target *Hhex* is ectopically expressed in the AVC of *Hand2*-deficient embryos. Indeed, genetic inactivation of *Hhex* increases the number of mesenchymal cells in AVC cardiac cushions and causes valve dysplasia (Hallaq et al., 2004).

One key finding of our analysis is that constitutive inactivation of *Hand2* disrupts the EMT underlying cardiac cushion formation in the AVC. This disruption of AVC morphogenesis contrasts with the phenotypes resulting from specific inactivation of *Hand2* in either the endocardium or mesenchyme. Neither inactivation disrupts AVC cardiac cushion formation but specifically alters the AVC-derived tricuspid valves (tricuspid atresia; VanDusen et al., 2014a, 2014b). This discrepancy is a likely consequence of different *Hand2* inactivation kinetics. As genetic inactivation of *Hand2* in SHF progenitors also alters AVC development, we cannot formally exclude that recruitment of progenitors to the AVC is compromised in *Hand2*-deficient embryos (Tsuchihashi et al., 2011), even though the expression of early markers for AVC morphogenesis remains normal (this study).

However, our analysis shows that most genes with known functions in the EMT underlying AVC cardiac cushion formation are direct transcriptional targets of HAND2. Together with the cellular analysis, these results point to specific disruption of the EMT rather than a general arrest of AVC development and suggest that HAND2 is a very upstream regulator of AVC cardiac cushion morphogenesis. In agreement, re-expression of the HAND2 target *Snai1* in *Hand2*-deficient AVCs explants only partially restores mesenchymal cell migration, which indicates that other HAND2 target DEGs have essential functions in the EMT and/or mesenchymal cell migration during cardiac cushion development. Ingenuity pathway analysis of HAND2 target genes shows that HAND2 enhances the expression of genes such as *Msx1* and *Hnrnapab*, which, in turn, reinforce the expression of the HAND2 targets *Has2*, *Twist1*, and *Snai1* (Figure 7). This type of dual transcriptional reinforcement likely increases the robustness of the expression of HAND2 target genes with key functions in AVC morphogenesis. In fact, it is reminiscent of the dual transcriptional reinforcement seen for key genes during limb bud development. In early limb buds, HAND2 reinforces the expression of the *Shh* morphogen by directly regulating its transcription and indirectly via upregulating E26 transformation-specific (ETS) transcription factors, which also positively regulate *Shh* expression (Osterwalder et al., 2014).

Remarkably, this study identifies HAND2 as key regulator of most genes with known functions in EMT processes and cardiac cushion formation in the developing AVC including *Snai1* (Garside et al., 2013). We also provide evidence that HAND2 directly regulates *Snai1* transcription in other embryonic tissues. The notion that the direct transcriptional regulation of *Snai1* by HAND2 maybe of more general importance is supported by genetic analysis as *Hand2* and *Snai1* are both essential for the EMT of epicardial cells and morphogenesis of craniofacial structures such as the palate (Barnes et al., 2011; Murray et al., 2007; Tao et al., 2013; Xiong et al., 2009). In summary, our study identifies the HAND2 target GRN that controls the initiation of

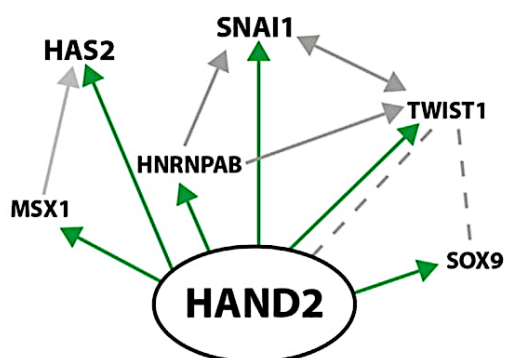


Figure 7. Scheme Depicting the Interactions among Positively Regulated HAND2 Target Genes

The HAND2 GRN was constructed using Ingenuity pathway analysis in combination with manual annotation (Chen et al., 2008). Arrows indicate transcriptional upregulation and direct upregulation by HAND2 transcriptional complexes is indicated in green. Broken gray lines direct protein-protein interactions. This graph represents the simplest possible scheme to illustrate the relevant direct interactions.

cardiac valve formation and provides evidence for its general role in regulating the expression of *Snai1* during mouse embryogenesis. Last but not least, the identification of HAND2 as key regulator of AVC cardiac cushion morphogenesis may have important implications for regenerative medicine (see, e.g., review by Levine et al., 2015).

EXPERIMENTAL PROCEDURES

Ethics Statement, Mouse Strains, and Embryos

All experiments conducted with mice and embryos of both sexes at the developmental ages indicated (see Results and below) were performed in strict accordance with Swiss law. All animal studies were evaluated and approved by the Regional Commission on Animal Experimentation (license 1951). The 3Rs were taken into account in designing the animal studies. The procedures for generating transgenic mice at the Lawrence Berkeley National Laboratory (LBNL) were reviewed and approved by the LBNL Animal Welfare and Research Committee. The *Hand2^d* and *Hand2^{3xF}* alleles (Galli et al., 2010; Osterwalder et al., 2014) were outbred into an NMRI background as this prolongs survival of *Hand2*-deficient embryos in comparison to the previously used 129SvJ/C57BL6 background.

ChIP-Seq Analysis

To obtain sufficient material for ChIP-seq analysis, about 600 hearts had to be dissected from *Hand2^{3xF/3xF}* mouse embryos at E10.5. After collection, these were split in two batches and processed as completely independent biological replicates for ChIP-seq analysis using the M2 anti-FLAG antibody (F1804; Sigma) (Osterwalder et al., 2014). Library construction and sequencing were performed by the Genome Technology Access Center using an Illumina HiSeq 2500 system. More details are included in the Supplemental Experimental Procedures.

Transcriptome Analysis

AVCs dissected from wild-type and *Hand2^{Δ/Δ}* mutant embryos at E9.0–9.25 were flash frozen in RLT buffer (QIAGEN). Four AVCs were pooled per replicate, keeping the same gender ratio for all replicates (AVCs of two male and female embryos). RNA was extracted using the QIAGEN RNeasy mini kit. The quality of total RNA (30–60 ng) was analyzed using the Agilent 2100 Bioanalyzer, and both wild-type and mutant samples had an RNA integrity number (RIN) of 8.8–9.6. Libraries were prepared using the Clontech SMARTer kit and

sequenced on a HiSeq3000 using a single-read 50 cycle protocol. More details on the computational analysis are provided in the Supplemental Experimental Procedures.

AVC Explant Cultures

AVC explant cultures were set on matrices of rat-tail collagen type I (Luna-Zurita et al., 2010, see Supplemental Information for more details). Only wild-type and mutant AVC explants that were still beating, i.e., alive after 72 hr in culture were analyzed. Supplementation with hyaluronic acid (HA): both the collagen matrix and serum-free culture medium were supplemented with 0.75 mg/mL HA (Camenisch et al., 2000). Adenoviral infections: the titers of the SNAI1-GFP or GFP adenoviruses (Tao et al., 2011 and Vector Biolabs) were determined in mitomycin-treated mouse embryonic fibroblasts and adjusted such that equal numbers of active virus particles were used. Following attachment to the matrix, mutant and wild-type AVC explants were incubated with 6×10^6 plaque-forming units (PFUs) of either SNAI1-GFP or GFP virus for 12 hr in serum-free medium. Then, the AVC explants were cultured for 60 hr in fresh serum-free medium. After fixation in 4% paraformaldehyde (PFA) (30-min room temperature), antigens were detected using anti-SMA-Cy3 antibodies (1:250, Sigma) and Phalloidin-Alexa 488 (1:250, Life Technologies) and nuclei counterstained with Hoechst-33258 and analyzed using a Leica SP5 confocal microscope. The analysis of wild-type controls shows that GFP-virus tends to infect AVC cells more efficiently than SNAI1-GFP virus (Figure S5C). Therefore, the restoration of cell migration following infection of mutant AVCs with SNAI1-GFP virus is rather underestimated (Figure 6B).

Statistical Analysis

ChIP-seq

Following initial alignment of sequences, the genome-wide pattern of binding of HAND2 was determined using MACS (version 1.4.2) with a p value threshold of $1e-5$.

ChIP-qPCR

Mean \pm SD were calculated using the Prism (GraphPad Software) Student-t test.

Transcriptome

Following initial sequence alignment, *edgeR* was used to normalize the datasets (trimmed mean of M-values [TMM] normalization) and to identify the differentially expressed genes (DEGs). Only genes expressed in all samples were considered (reads per million [RPM] ≥ 1). DEGs are defined as genes with a q value ≤ 0.05 and a linear fold change ≥ 1.5 .

AVC Explant Cultures

The Mann-Whitney test was used to determine significant differences in numbers of migrating mesenchymal cells. More details on statistical validation of the ChIP-seq and transcriptome analyses are included in the Supplemental Experimental Procedures.

Histology and Immunofluorescence Analysis

Embryos were collected and fixed overnight in 4% PFA at 4°C and embedded in paraffin wax. Standard protocols were used for histological staining (H&E; Alcian blue) of 7- μ m paraffin sections. Minimally three biological replicates were analyzed for each stage, genotype, and antigen shown. Antibodies are listed in the Supplemental Experimental Procedures.

Generation and Analysis of LacZ Transgenic Founder Embryos

Genomic regions were amplified by PCR from mouse genomic DNA (*Snai1* +45kb, *Snai1* +14kb) or recovered as restriction fragment (*Snai1* +57kb, BAC clone RP23-193B17) and cloned into the *Hsp68*-promoter-*LacZ* reporter vector (Osterwalder et al., 2014). Transgenic founder embryos were generated by pronuclear injection and analyzed by *LacZ* staining, and transgenic embryos were identified by genotyping.

ACCESSION NUMBERS

The accession numbers for the primary ChIP-seq and transcriptome datasets reported in this paper are GEO: GSE73368 and GSE94246, respectively.

SUPPLEMENTAL INFORMATION

Supplemental Information includes Supplemental Experimental Procedures, six figures, and six tables and can be found with this article online at <http://dx.doi.org/10.1016/j.celrep.2017.05.004>.

AUTHOR CONTRIBUTIONS

F.L. performed the ChIP-seq and follow-up functional analysis, A.G. performed the transcriptome and WISH analysis for revision, J.G. participated in different aspects of the experimental studies, and I.B. performed the bioinformatics analysis. M.O. was involved in initiating this study, J.L. generated the SNAI1-GFP virus, J.A.A. generated the *LacZ* reporters, and A.V. provided the resources for the transgenic and bioinformatics analysis. The experimental study design was done and the manuscript written by F.L., J.L.-R., A.Z., and R.Z. with input from all authors.

ACKNOWLEDGMENTS

The Genome Technology Access Center (Department of Genetics at Washington University School of Medicine) is acknowledged for deep sequencing, and R. Ivanek (DBM Bioinformatics Core) performed the bioinformatics analysis of the ChIP-seq datasets. All calculations were performed using the sciCORE (<https://scicore.unibas.ch/>) scientific computing core facility at University of Basel. We thank D. Speziale for technical assistance, A. Offinger's team for excellent animal care, and P. Lorentz (DBM Bio-Optics Core Facility) for imaging support. V. Afzal, B. Mannion, and I. Plajzer-Frick provided assistance with transgenics, and L. Bazzani provided the GFP adenovirus preparations. T. Papoutsis, C. Rolando, and O. Pertz are acknowledged for advice on AVC explants and infections. We are grateful to V. Christoffels for helpful input and anonymous reviewers for critical input that resulted in a significantly improved study. This research was mostly supported by SNF grants 31003A_146248 and 310030B_166685 to A.Z. and R.Z. and by funds from the University of Basel. The stay of M.O. in the group of A.V. was supported by an SNSF early mobility postdoctoral fellowship. I.B., J.A., and A.V. were supported by NIH grants R24HL123879, UM1HL098166, R01HG003988, and U54HG006997, and research at LBNL was performed under Department of Energy Contract DE-AC02-05CH11231 to University of California. J.L. was supported by NIH/NHLBI grant 1R01HL127033.

Received: May 20, 2016

Revised: March 20, 2017

Accepted: April 28, 2017

Published: May 23, 2017

REFERENCES

- Akiyama, H., Chaboissier, M.C., Behringer, R.R., Rowitch, D.H., Schedl, A., Epstein, J.A., and de Crombrughe, B. (2004). Essential role of Sox9 in the pathway that controls formation of cardiac valves and septa. *Proc. Natl. Acad. Sci. USA* *101*, 6502–6507.
- Barnes, R.M., Firulli, B.A., VanDusen, N.J., Morikawa, Y., Conway, S.J., Cserjesi, P., Vincenz, J.W., and Firulli, A.B. (2011). Hand2 loss-of-function in Hand1-expressing cells reveals distinct roles in epicardial and coronary vessel development. *Circ. Res.* *108*, 940–949.
- Bruneau, B.G. (2008). The developmental genetics of congenital heart disease. *Nature* *451*, 943–948.
- Camenisch, T.D., Spicer, A.P., Brehm-Gibson, T., Biesterfeldt, J., Augustine, M.L., Calabro, A., Jr., Kubalak, S., Klewer, S.E., and McDonald, J.A. (2000). Disruption of hyaluronan synthase-2 abrogates normal cardiac morphogenesis and hyaluronan-mediated transformation of epithelium to mesenchyme. *J. Clin. Invest.* *106*, 349–360.
- Chen, Y.H., Ishii, M., Sucov, H.M., and Maxson, R.E., Jr. (2008). Msx1 and Msx2 are required for endothelial-mesenchymal transformation of the atrioventricular cushions and patterning of the atrioventricular myocardium. *BMC Dev. Biol.* *8*, 75.
- Christoffels, V.M., Smits, G.J., Kispert, A., and Moorman, A.F. (2010). Development of the pacemaker tissues of the heart. *Circ. Res.* *106*, 240–254.
- Cohen, E.D., Miller, M.F., Wang, Z., Moon, R.T., and Morrisey, E.E. (2012). Wnt5a and Wnt11 are essential for second heart field progenitor development. *Development* *139*, 1931–1940.
- Dai, Y.S., and Cserjesi, P. (2002). The basic helix-loop-helix factor, HAND2, functions as a transcriptional activator by binding to E-boxes as a heterodimer. *J. Biol. Chem.* *277*, 12604–12612.
- Dai, Y.S., Cserjesi, P., Markham, B.E., and Molkentin, J.D. (2002). The transcription factors GATA4 and dHAND physically interact to synergistically activate cardiac gene expression through a p300-dependent mechanism. *J. Biol. Chem.* *277*, 24390–24398.
- Dixon, J.R., Selvaraj, S., Yue, F., Kim, A., Li, Y., Shen, Y., Hu, M., Liu, J.S., and Ren, B. (2012). Topological domains in mammalian genomes identified by analysis of chromatin interactions. *Nature* *485*, 376–380.
- Firulli, B.A., Hadzic, D.B., McDaid, J.R., and Firulli, A.B. (2000). The basic helix-loop-helix transcription factors dHAND and eHAND exhibit dimerization characteristics that suggest complex regulation of function. *J. Biol. Chem.* *275*, 33567–33573.
- Firulli, B.A., Krawchuk, D., Centonze, V.E., Vargesson, N., Virshup, D.M., Conway, S.J., Cserjesi, P., Laufer, E., and Firulli, A.B. (2005). Altered Twist1 and Hand2 dimerization is associated with Saethre-Chotzen syndrome and limb abnormalities. *Nat. Genet.* *37*, 373–381.
- Funato, N., Chapman, S.L., McKee, M.D., Funato, H., Morris, J.A., Shelton, J.M., Richardson, J.A., and Yanagisawa, H. (2009). Hand2 controls osteoblast differentiation in the branchial arch by inhibiting DNA binding of Runx2. *Development* *136*, 615–625.
- Galli, A., Robay, D., Osterwalder, M., Bao, X., Bénazet, J.D., Tariq, M., Paro, R., Mackem, S., and Zeller, R. (2010). Distinct roles of Hand2 in initiating polarity and posterior Shh expression during the onset of mouse limb bud development. *PLoS Genet.* *6*, e1000901.
- Garside, V.C., Chang, A.C., Karsan, A., and Hoodless, P.A. (2013). Co-ordinating Notch, BMP, and TGF- β signaling during heart valve development. *Cell. Mol. Life Sci.* *70*, 2899–2917.
- Gómez-Marín, C., Tena, J.J., Acemel, R.D., López-Mayorga, M., Naranjo, S., de la Calle-Mustienes, E., Maeso, I., Beccari, L., Aneas, I., Vielmas, E., et al. (2015). Evolutionary comparison reveals that diverging CTCF sites are signatures of ancestral topological associating domains borders. *Proc. Natl. Acad. Sci. USA* *112*, 7542–7547.
- Greulich, F., Rudat, C., and Kispert, A. (2011). Mechanisms of T-box gene function in the developing heart. *Cardiovasc. Res.* *91*, 212–222.
- Hallaq, H., Pinter, E., Enciso, J., McGrath, J., Zeiss, C., Brueckner, M., Madri, J., Jacobs, H.C., Wilson, C.M., Vasavada, H., et al. (2004). A null mutation of Hhex results in abnormal cardiac development, defective vasculogenesis and elevated Vegfa levels. *Development* *131*, 5197–5209.
- He, A., Gu, F., Hu, Y., Ma, Q., Ye, L.Y., Akiyama, J.A., Visel, A., Pennacchio, L.A., and Pu, W.T. (2014). Dynamic GATA4 enhancers shape the chromatin landscape central to heart development and disease. *Nat. Commun.* *5*, 4907.
- Heinz, S., Benner, C., Spann, N., Bertolino, E., Lin, Y.C., Laslo, P., Cheng, J.X., Murre, C., Singh, H., and Glass, C.K. (2010). Simple combinations of lineage-determining transcription factors prime cis-regulatory elements required for macrophage and B cell identities. *Mol. Cell* *38*, 576–589.
- Holler, K.L., Hendershot, T.J., Troy, S.E., Vincenz, J.W., Firulli, A.B., and Howard, M.J. (2010). Targeted deletion of Hand2 in cardiac neural crest-derived cells influences cardiac gene expression and outflow tract development. *Dev. Biol.* *341*, 291–304.
- Kelly, R.G. (2012). The second heart field. *Curr. Top. Dev. Biol.* *100*, 33–65.
- Levine, R.A., Hagège, A.A., Judge, D.P., Padala, M., Dal-Bianco, J.P., Aikawa, E., Beaudoin, J., Bischoff, J., Bouatia-Naji, N., Bruneval, P., et al.; Leducq Mitral Transatlantic Network (2015). Mitral valve disease—morphology and mechanisms. *Nat. Rev. Cardiol.* *12*, 689–710.

- Lin, C.J., Lin, C.Y., Chen, C.H., Zhou, B., and Chang, C.P. (2012). Partitioning the heart: mechanisms of cardiac septation and valve development. *Development* **139**, 3277–3299.
- Liu, N., Barbosa, A.C., Chapman, S.L., Bezprozvannaya, S., Qi, X., Richardson, J.A., Yanagisawa, H., and Olson, E.N. (2009). DNA binding-dependent and -independent functions of the Hand2 transcription factor during mouse embryogenesis. *Development* **136**, 933–942.
- Luna-Zurita, L., Prados, B., Grego-Bessa, J., Luxán, G., del Monte, G., Benguría, A., Adams, R.H., Pérez-Pomares, J.M., and de la Pompa, J.L. (2010). Integration of a Notch-dependent mesenchymal gene program and Bmp2-driven cell invasiveness regulates murine cardiac valve formation. *J. Clin. Invest.* **120**, 3493–3507.
- Ma, L., Lu, M.F., Schwartz, R.J., and Martin, J.F. (2005). Bmp2 is essential for cardiac cushion epithelial-mesenchymal transition and myocardial patterning. *Development* **132**, 5601–5611.
- MacGrogan, D., Luxán, G., Driessen-Mol, A., Bouten, C., Baaijens, F., and de la Pompa, J.L. (2014). How to make a heart valve: from embryonic development to bioengineering of living valve substitutes. *Cold Spring Harb. Perspect. Med.* **4**, a013912.
- McLean, C.Y., Bristol, D., Hiller, M., Clarke, S.L., Schaar, B.T., Lowe, C.B., Wenger, A.M., and Bejerano, G. (2010). GREAT improves functional interpretation of cis-regulatory regions. *Nat. Biotechnol.* **28**, 495–501.
- Murray, S.A., Oram, K.F., and Gridley, T. (2007). Multiple functions of Snail family genes during palate development in mice. *Development* **134**, 1789–1797.
- Niessen, K., Fu, Y., Chang, L., Hoodless, P.A., McFadden, D., and Karsan, A. (2008). Slug is a direct Notch target required for initiation of cardiac cushion cellularization. *J. Cell Biol.* **182**, 315–325.
- Nieto, M.A. (2011). The ins and outs of the epithelial to mesenchymal transition in health and disease. *Annu. Rev. Cell Dev. Biol.* **27**, 347–376.
- Nord, A.S., Blow, M.J., Attanasio, C., Akiyama, J.A., Holt, A., Hosseini, R., Phouanavong, S., Plajzer-Frick, I., Shoukry, M., Afzal, V., et al. (2013). Rapid and pervasive changes in genome-wide enhancer usage during mammalian development. *Cell* **155**, 1521–1531.
- Osterwalder, M., Speziale, D., Shoukry, M., Mohan, R., Ivanek, R., Kohler, M., Beisel, C., Wen, X., Scales, S.J., Christoffels, V.M., et al. (2014). HAND2 targets define a network of transcriptional regulators that compartmentalize the early limb bud mesenchyme. *Dev. Cell* **31**, 345–357.
- Shen, L., Li, X.F., Shen, A.D., Wang, Q., Liu, C.X., Guo, Y.J., Song, Z.J., and Li, Z.Z. (2010). Transcription factor HAND2 mutations in sporadic Chinese patients with congenital heart disease. *Chin. Med. J. (Engl.)* **123**, 1623–1627.
- Srivastava, D., Thomas, T., Lin, Q., Kirby, M.L., Brown, D., and Olson, E.N. (1997). Regulation of cardiac mesodermal and neural crest development by the bHLH transcription factor, dHAND. *Nat. Genet.* **16**, 154–160.
- Stefanovic, S., and Christoffels, V.M. (2015). GATA-dependent transcriptional and epigenetic control of cardiac lineage specification and differentiation. *Cell. Mol. Life Sci.* **72**, 3871–3881.
- Stefanovic, S., Barnett, P., van Duijvenboden, K., Weber, D., Gessler, M., and Christoffels, V.M. (2014). GATA-dependent regulatory switches establish atrioventricular canal specificity during heart development. *Nat. Commun.* **5**, 3680.
- Sun, Y.M., Wang, J., Qiu, X.B., Yuan, F., Li, R.G., Xu, Y.J., Qu, X.K., Shi, H.Y., Hou, X.M., Huang, R.T., et al. (2016). A HAND2 loss-of-function mutation causes familial ventricular septal defect and pulmonary stenosis. *G3 (Bethesda)* **6**, 987–992.
- Tao, G., Levay, A.K., Gridley, T., and Lincoln, J. (2011). Mmp15 is a direct target of Snai1 during endothelial to mesenchymal transformation and endocardial cushion development. *Dev. Biol.* **359**, 209–221.
- Tao, G., Miller, L.J., and Lincoln, J. (2013). Snai1 is important for avian epicardial cell transformation and motility. *Dev. Dyn.* **242**, 699–708.
- Timmerman, L.A., Grego-Bessa, J., Raya, A., Bertrán, E., Pérez-Pomares, J.M., Diez, J., Aranda, S., Palomo, S., McCormick, F., Izpisua-Belmonte, J.C., and de la Pompa, J.L. (2004). Notch promotes epithelial-mesenchymal transition during cardiac development and oncogenic transformation. *Genes Dev.* **18**, 99–115.
- Tsuhishashi, T., Maeda, J., Shin, C.H., Ivey, K.N., Black, B.L., Olson, E.N., Yamagishi, H., and Srivastava, D. (2011). Hand2 function in second heart field progenitors is essential for cardiogenesis. *Dev. Biol.* **351**, 62–69.
- VanDusen, N.J., and Firulli, A.B. (2012). Twist factor regulation of non-cardiomyocyte cell lineages in the developing heart. *Differentiation* **84**, 79–88.
- VanDusen, N.J., Casanovas, J., Vincentz, J.W., Firulli, B.A., Osterwalder, M., Lopez-Rios, J., Zeller, R., Zhou, B., Grego-Bessa, J., De La Pompa, J.L., et al. (2014a). Hand2 is an essential regulator for two Notch-dependent functions within the embryonic endocardium. *Cell Rep.* **9**, 2071–2083.
- VanDusen, N.J., Vincentz, J.W., Firulli, B.A., Howard, M.J., Rubart, M., and Firulli, A.B. (2014b). Loss of Hand2 in a population of Periostin lineage cells results in pronounced bradycardia and neonatal death. *Dev. Biol.* **388**, 149–158.
- Visel, A., Minovitsky, S., Dubchak, I., and Pennacchio, L.A. (2007). VISTA Enhancer Browser—a database of tissue-specific human enhancers. *Nucleic Acids Res.* **35**, D88–D92.
- Wu, Z.Q., Rowe, R.G., Lim, K.C., Lin, Y., Willis, A., Tang, Y., Li, X.Y., Nor, J.E., Maillard, I., and Weiss, S.J. (2014). A Snai1/Notch1 signalling axis controls embryonic vascular development. *Nat. Commun.* **5**, 3998.
- Xiong, W., He, F., Morikawa, Y., Yu, X., Zhang, Z., Lan, Y., Jiang, R., Cserjesi, P., and Chen, Y. (2009). Hand2 is required in the epithelium for palatogenesis in mice. *Dev. Biol.* **330**, 131–141.
- Zhang, Y., Liu, T., Meyer, C.A., Eeckhoutte, J., Johnson, D.S., Bernstein, B.E., Nusbaum, C., Myers, R.M., Brown, M., Li, W., and Liu, X.S. (2008). Model-based analysis of ChIP-Seq (MACS). *Genome Biol.* **9**, R137.
- Zhao, R., Watt, A.J., Battle, M.A., Li, J., Bondow, B.J., and Duncan, S.A. (2008). Loss of both GATA4 and GATA6 blocks cardiac myocyte differentiation and results in acardia in mice. *Dev. Biol.* **317**, 614–619.

Supplemental Information

HAND2 Target Gene Regulatory

Networks Control Atrioventricular

Canal and Cardiac Valve Development

Frédéric Laurent, Ausra Girdziusaite, Julie Gamart, Iros Barozzi, Marco Osterwalder, Jennifer A. Akiyama, Joy Lincoln, Javier Lopez-Rios, Axel Visel, Aimée Zuniga, and Rolf Zeller

incremental bin (top term: cardiovascular system phenotype), GO terms related to more specific aspects of cardiac development (such as: abnormal heart right ventricle morphology) are only detected when considering an increasing number of peaks or the entire dataset. (B) Hierarchical clustering of the high-affinity matches for each of the enriched known motifs across the HAND2-contacted regions is shown. The top five binding motifs that were identified *de novo* are highlighted on the left. (C) Analysis of the patterns of cell death in *Hand2*-deficient mouse embryos. Panel Lysotracker: whole mount Lysotracker staining reveals increased apoptosis in branchial arches (Ba) and frontonasal mass (Fnm) of mutant mouse embryos at E9.5 (red fluorescence), while no aberrant apoptosis is detected in the developing heart. He: heart; Flb: forelimb bud. Panel TUNEL: analysis of serial section by TUNEL staining confirmed that the fraction of apoptotic cells (green fluorescent) is not increased in the mutant heart at E9.5. Panel KI67: the majority of all cells are KI67 positive (red fluorescent), which indicates that there is no major effect on cell proliferation in mutant hearts at E9.5. Right-most panel TUNEL: Only by E10.5, the apoptosis is significantly increased in mutant hearts in comparison to wild-type controls. Representative images are shown for all samples analyzed (n=3). Scale bars: 100µm. avc: atrioventricular canal; lv: left ventricle; la: left atria; oft: outflow tract.

Figure S2

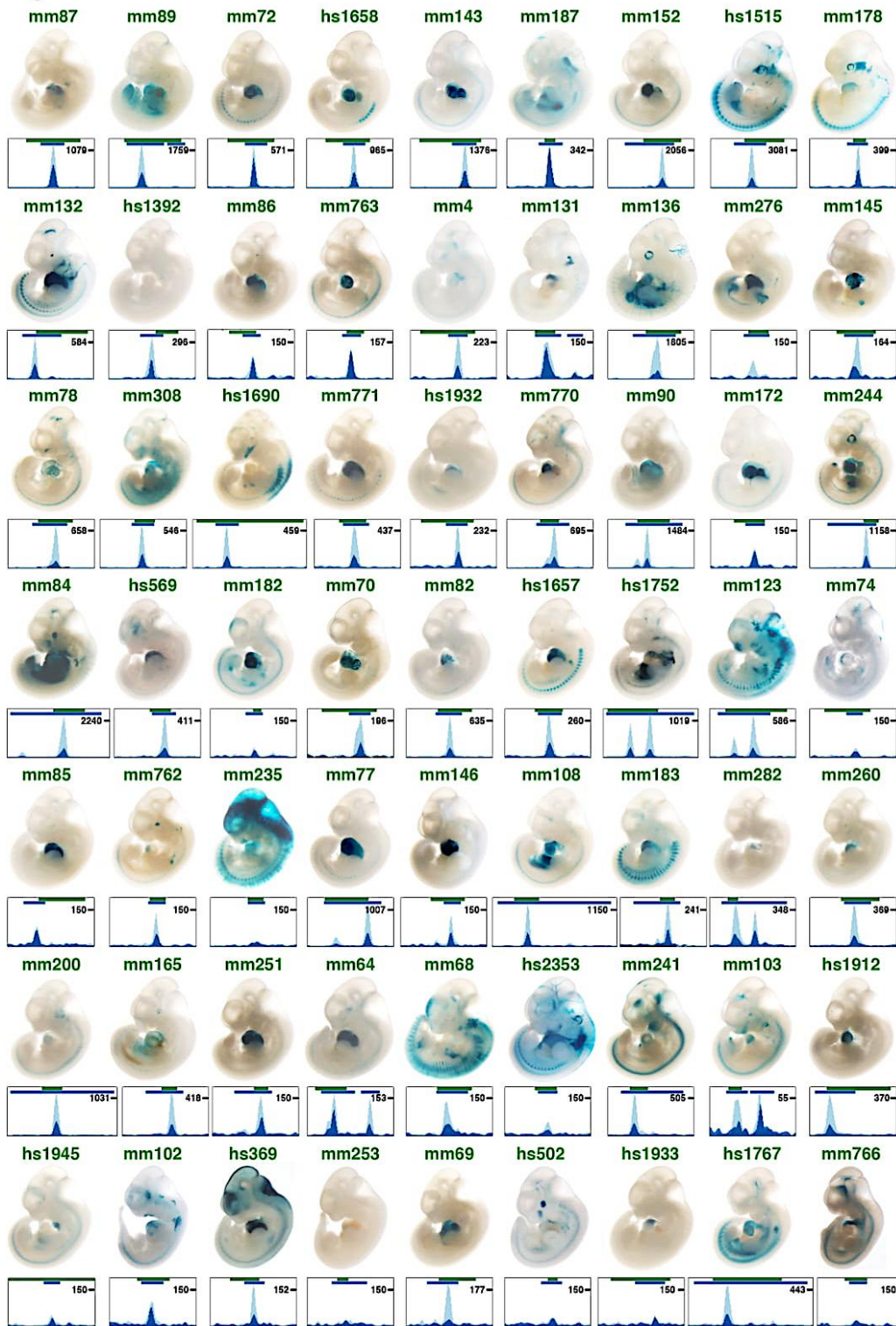


Figure S2 (related to Figure 1). Activities of the VISTA cardiac enhancers that overlap genomic regions enriched by HAND2 ChIP-seq (E10.5).

Representative transgenic founder embryos from the public VISTA enhancer database collection (<https://enhancer.lbl.gov>; Visel et al., 2007) are shown. The transgenic embryos were not generated as part of this study, but images from the database collection were used for the purpose of this analysis. For each VISTA enhancer, the HAND2 ChIP-seq peak identified by MACS analysis is indicated by a blue bar. The genomic regions used for *LacZ* reporter analysis are indicated by a green bar. mm: mouse element; hs: human element. Nomenclature used is according to the VISTA database.

Figure S3

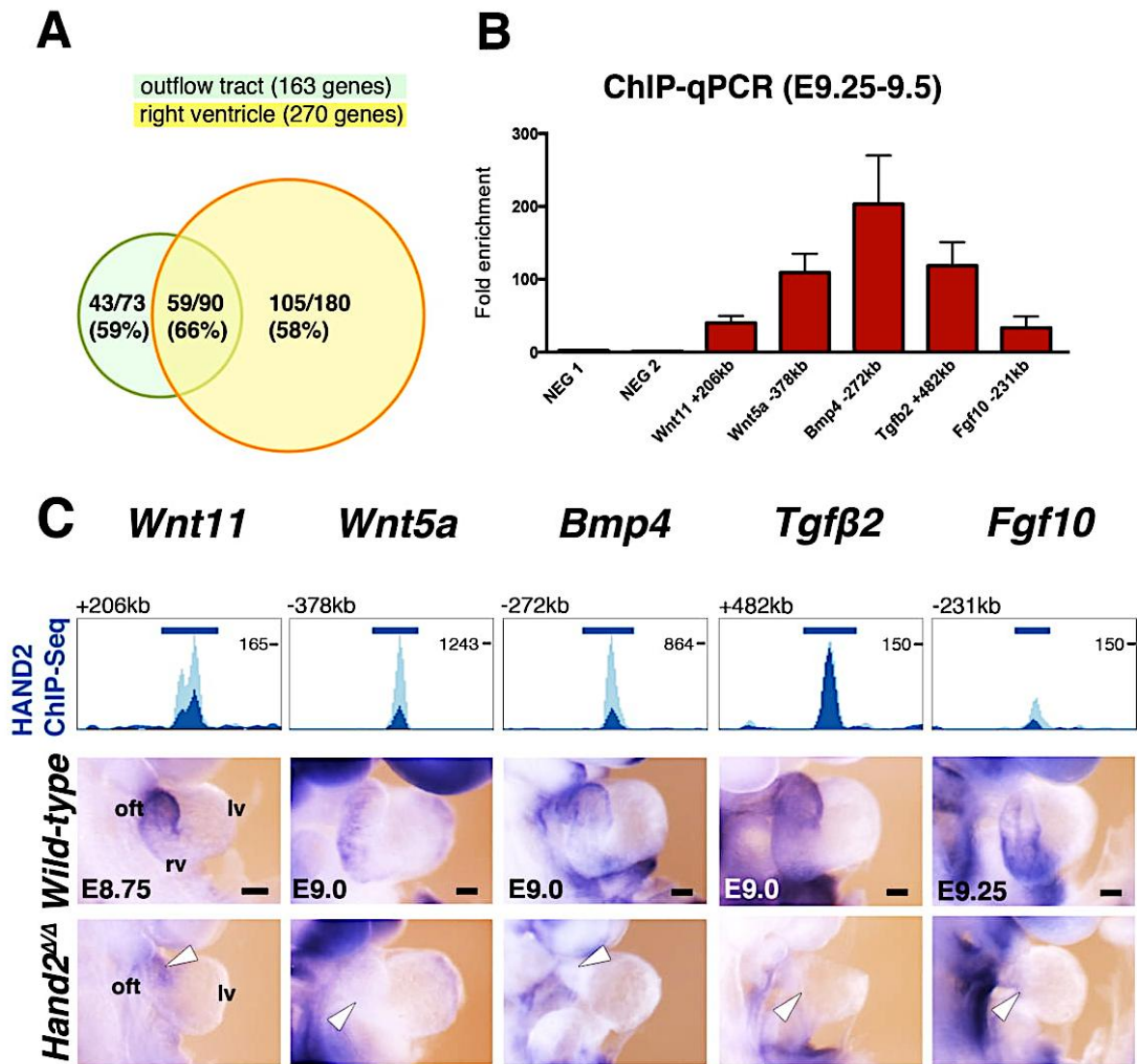


Figure S3 (related to Figure 1). HAND2 target genes encoding ligands for signaling pathways that function in OFT and/or right ventricle morphogenesis.

(A) Venn diagram shows the intersection of genes associated with the following mouse phenotype and GO terms, respectively: MP:0006126: abnormal outflow tract development; MP:0003920: abnormal heart right ventricle morphology; GO:0003151: outflow tract morphogenesis; GO:0003205: cardiac chamber development. Numbers and percentages indicate how many of the genomic landscapes associated to the terms encode regions enriched in HAND2 chromatin complexes. (B) ChIP-qPCR validation of HAND2 target regions associated to genes encoding ligands in embryonic hearts at E9.25 (n=2; mean \pm SD). (C) Comparative WISH analysis of HAND2 target genes encoding signaling ligands in wild-type and *Hand2*-deficient mouse embryos. Graphs show the highest enriched HAND2 ChIP-seq peaks associated with the genes analyzed. White arrowheads: reduction/loss of expression in *Hand2*-deficient embryos. oft: outflow tract, rv: right ventricle, lv: left ventricle. Scale bar: 100 μ m.

Figure S4

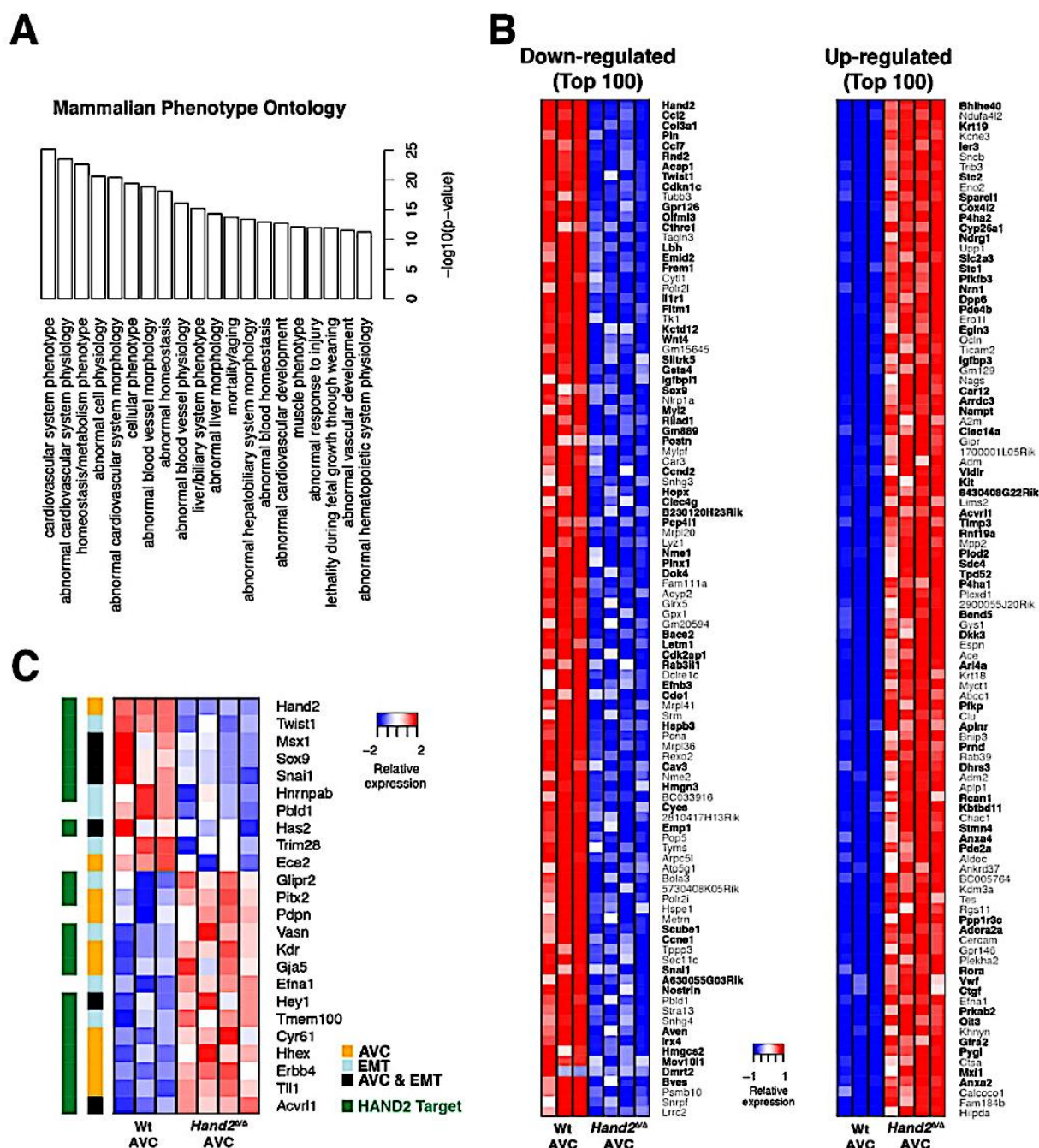


Figure S4 (related to Figure 4). Transcriptome analysis identifies the HAND2 target genes with significantly altered expression in *Hand2*-deficient AVCs.

(A) Enrichment analysis for mammalian phenotypes including all 1051 DEGs identified by comparative transcriptome analysis of *Hand2*^{ΔΔ} and wild-type AVCs. (B) Top 100 up- and down-regulated genes in *Hand2*-deficient AVCs in comparison to wild-type controls. Genes with regions enriched in HAND2 chromatin complexes within their TADs are indicated in bold black, others in grey. (C) Heat map of up- and down-regulated genes in *Hand2*-deficient AVCs annotated using the following gene ontology categories: MP:0000297 (abnormal AV cushion morphology + child terms) BP:0001837 (epithelial-mesenchymal transition) and BP:0010717 (regulation of EMT). Most of the DEGs in these categories are HAND2 target genes (indicated in green).

Figure S5

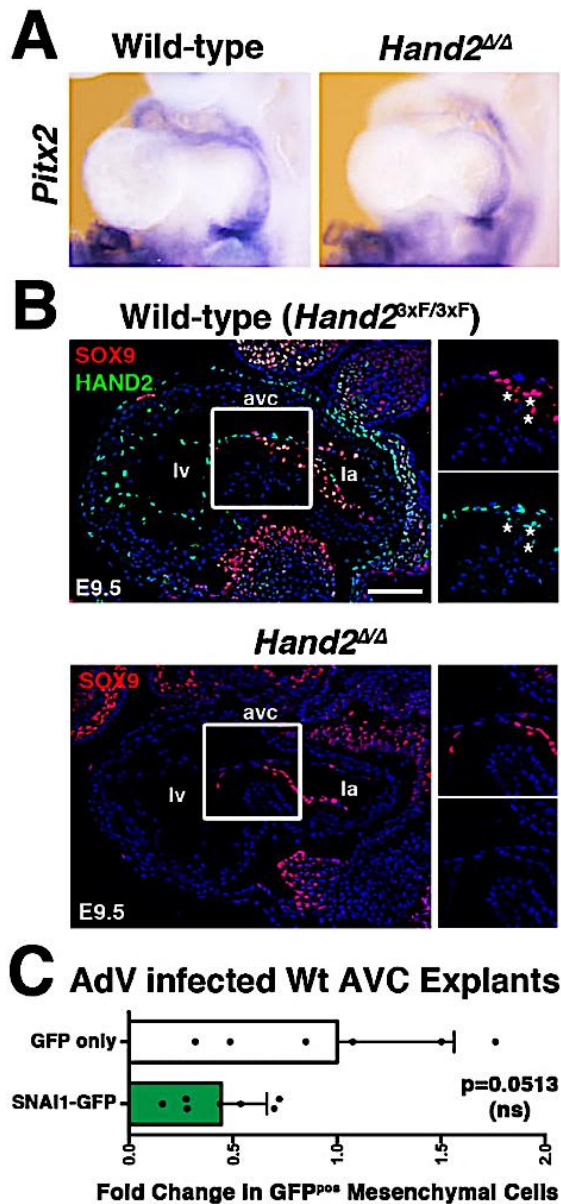


Figure S5 (related to Figures 5 and 6). Analysis of HAND2 target genes in the developing AVC.

(A) WISH analysis of the HAND2 target gene *Pitx2*, whose transcript levels are significantly altered in mutant AVCs by RNA-seq analysis. No changes in the spatial distribution of *Pitx2* transcripts are detected. (B) Colocalization of HAND2^{3xF} proteins (green fluorescence) with the SOX9 transcriptional regulators (red fluorescence) in the AVC of wild-type (*Hand2^{3xF/3xF}*) and *Hand2*-deficient (*Hand2^{Δ/Δ}*) mouse embryos at E9.5. Asterisks in the enlargement (upper panels) point to SOX9-positive delaminating mesenchymal cells in the AVC, which are lacking in the *Hand2*-deficient AVC. Scale bar: 100 μ m. (C) Infection of wild-type AVC explants with GFP and SNAI1-GFP adenovirus (using 6x10⁶ PFU for either virus per sample) indicates that GFP virus infects AVC cells slightly more efficiently than SNAI1-GFP virus. Therefore, the observed partial restoration of cell migration in *Hand2*-deficient AVCs infected with SNAI1-GFP virus is likely underestimated (Figure 6B).

Figure S6

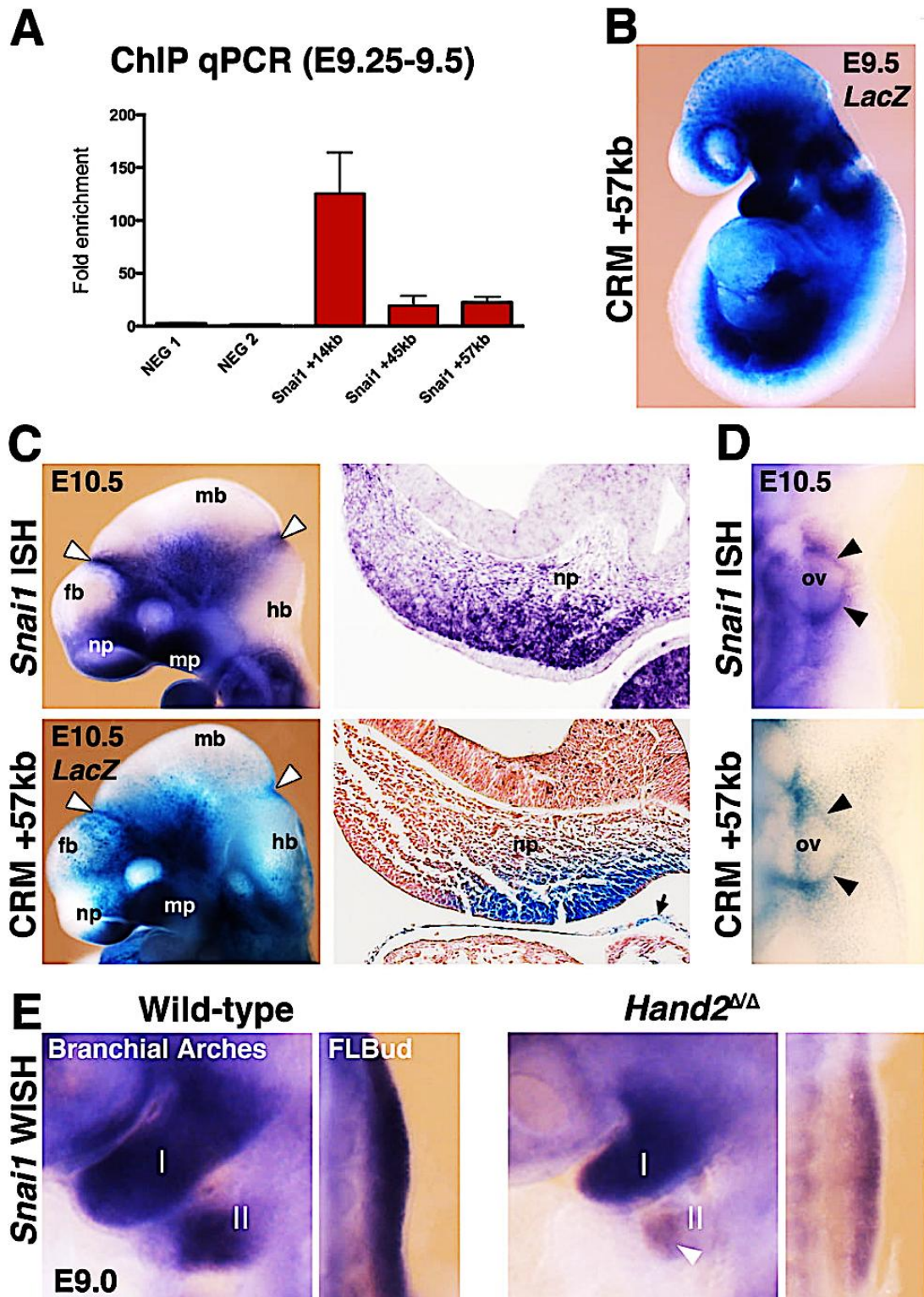


Figure S6 (related to Figure 6). The *Snai1* transcript distribution overlaps the CRM+57kb activity in craniofacial structures, branchial arches and early limb buds.

(A) ChIP-qPCR validation of the enrichment of the three CRMs in HAND2 chromatin complexes from embryonic hearts (E9.25-E9.5, n=2; mean \pm SD). (B) The expression pattern of the *Snai1* CRM +57kb *LacZ* reporter transgene at E9.5. (C) *Snai1* expression and activity of the CRM +57kb *LacZ* reporter

transgene in craniofacial structures. The enhancer activity overlaps well with the domain of *Snail* transcripts in the nasal prominence (np), maxillary process (mp), fore-midbrain and mid-hindbrain boundaries (white arrowheads). fb: forebrain, mb: midbrain, hb: hindbrain. Black arrow points to the epicardium. (D) Expression of *Snail* and the CRM +57kb LacZ reporter transgene in migrating cardiac neural crest cells (black arrowheads) enveloping the otic vesicle (ov). (E) *Snail* expression is reduced in the 2nd branchial arch (II) and early forelimb buds in *Hand2*-deficient mouse embryos (E9.0)

6.2 Identification of the genes regulated by TBX3 genes during mouse forelimb bud development

Previous mouse genetic studies implicated TBX3 as a transcriptional repressor functioning in precisely defining the posterior boundary of the *Gli3* gene expressed in the anterior limb bud mesenchyme downstream or in parallel to *Hand2* (Osterwalder et al., 2014). Beyond that little is known about how TBX3 regulates gene expression during limb bud outgrowth.

To identify the genes regulated by TBX3 during mouse forelimb bud development I used *Tbx3*^{dVenus} loss-of-function allele (*Tbx3*^Δ) for expression profiling.

6.2.1 Validation of the *Tbx3*-deficient embryos as a tool for transcriptional profiling

As it has been reported that the variable lethality of *Tbx3*-deficient mouse embryos starts at E10.5 (Davenport et al., 2003), I initially performed Lysotracker staining at E10.25 to evaluate the cell death pattern (Fig. 14). Comparative analysis of WT and *Tbx3*^{Δ/Δ} embryos (n=3) revealed no increase in the number of apoptotic cells in mouse forelimb buds at this embryonic stage. Therefore, forelimb buds could be used for transcriptional analysis. However, more apoptotic cells were detected in the first and second branchial arches at E10.25.

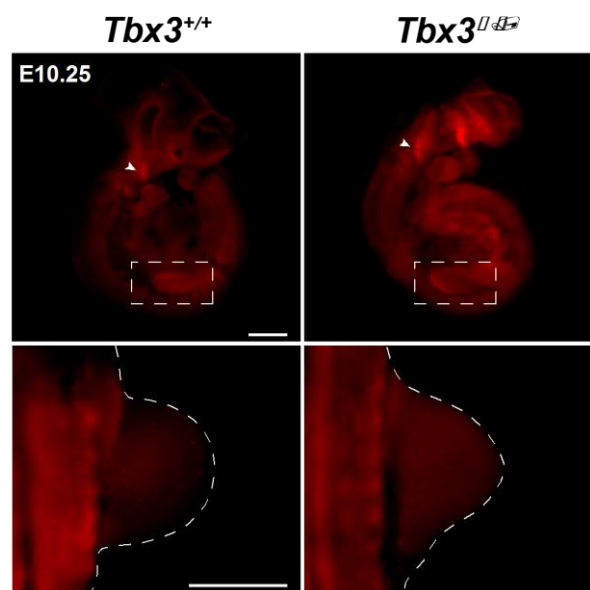


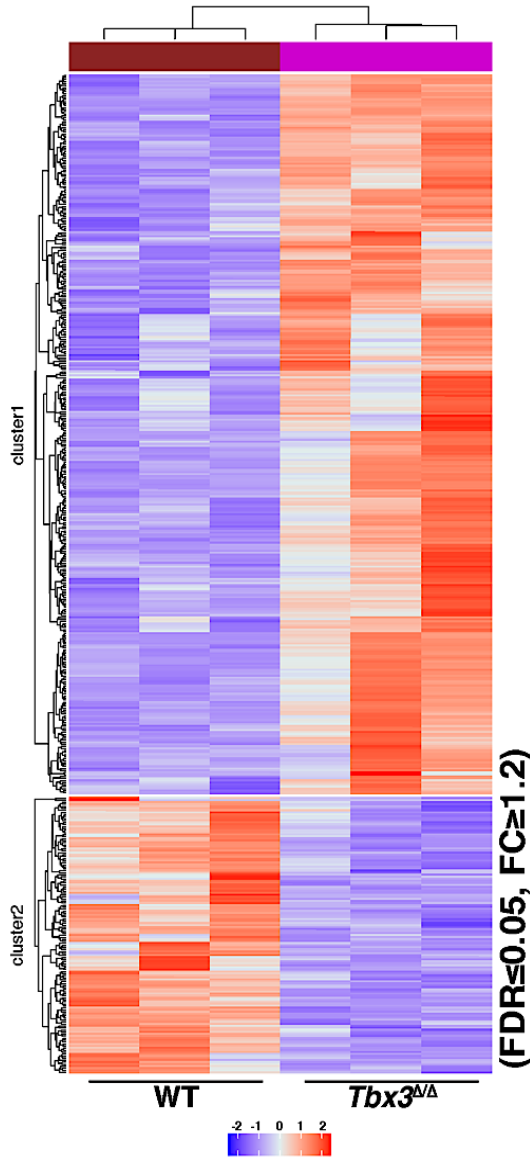
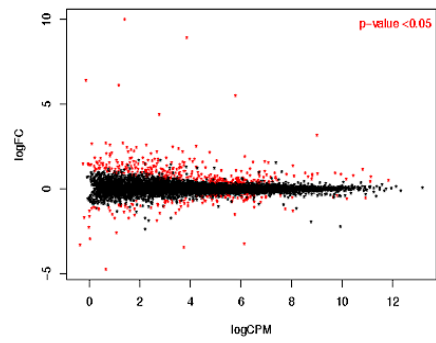
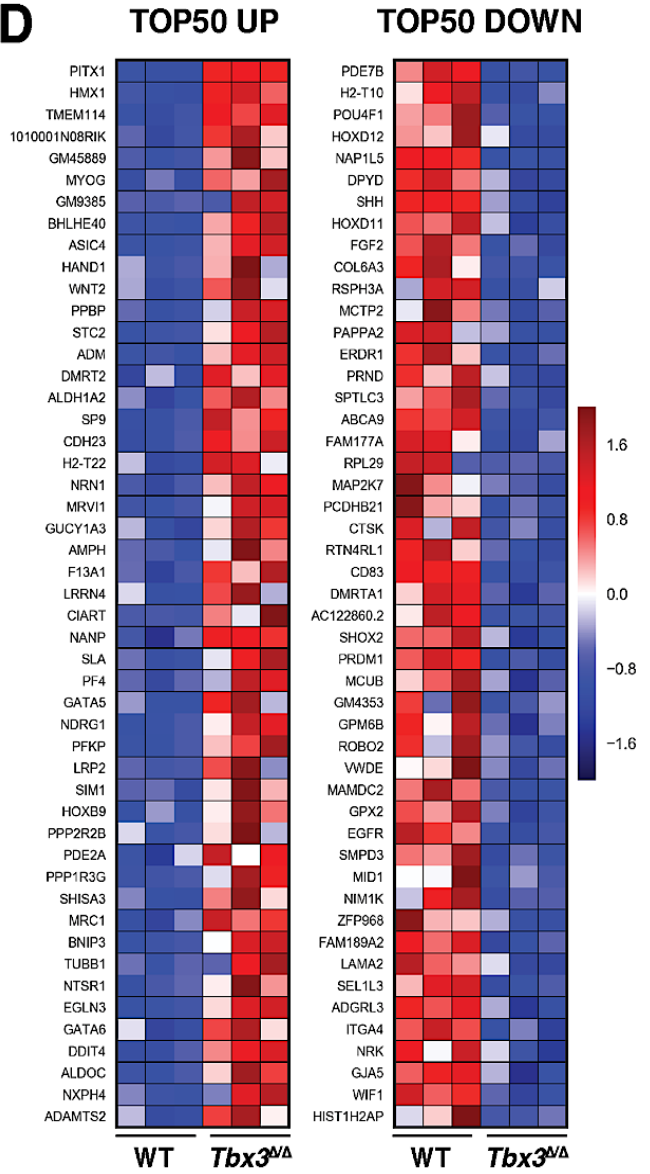
Figure 14. Lysotracker staining to evaluate cell death in *Tbx3*-deficient embryos. Scale bar: 0.5mm.

6.2.2 Comparative transcriptome analysis of WT and *Tbx3*-deficient forelimb buds

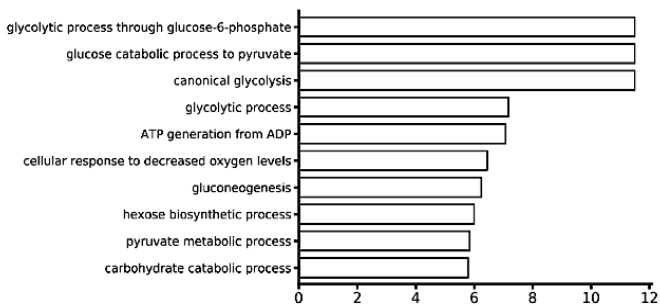
Comparative RNA-seq analysis was conducted using WT and *Tbx3*-deficient forelimb buds at E9.75-10.0 (28-31 somite stage) (Fig. 15A). One pair of forelimb buds was used per replicate (Fig. 15A). The comparative RNA-seq analysis revealed 494 differentially expressed genes (DEGs) between WT and *Tbx3*^{Δ/Δ} forelimb buds at E9.75-10.0 (fold change (FC) ≥ 1.2 , false discovery rate (FDR) < 0.05 ; Fig. 15B). The in-depth analysis showed that 137 of these genes were down-regulated, and 357 up-regulated (TOP50 up- and down-regulated genes, Fig. 15D). The spatiotemporal expression changes of a few DEGs were assessed by whole-mount *in situ*

A

RNA-seq E9.75-10.0
WT and *Tbx3*^{Δ/Δ} FLBs

B**C****D****E**

TOP 10 GO Biological processes
Up-regulated genes E9.75-10.25 (n=346)



TOP 10 GO Biological processes
Down-regulated genes E9.75-10.25 (n=130)

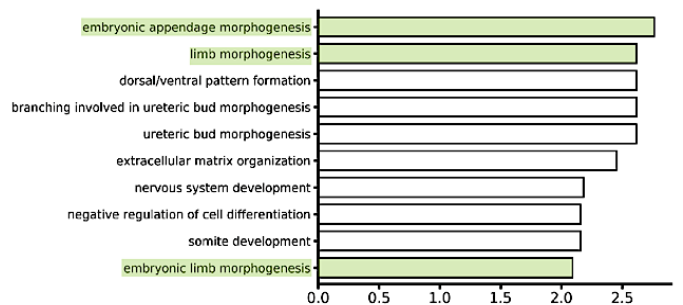
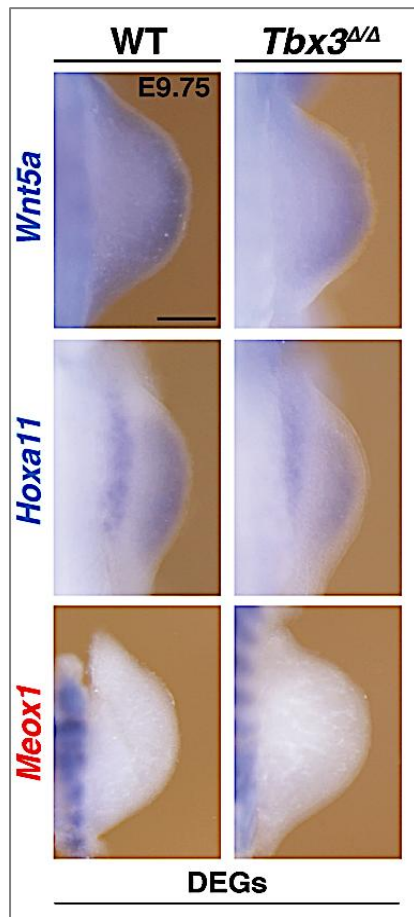


Figure 15. WT and *Tbx3*-deficient mouse forelimb bud's transcriptome analysis. (A) WT and *Tbx3*^{Δ/Δ} mouse FLBs at E9.75-10.0 (28-31 somite stage) were used for transcriptome analysis. (B) The heat map represents the clustering of the 494 DEGs that were identified by comparing transcriptomes of WT and *Tbx3*^{Δ/Δ} mouse embryos FLBs at E9.75-10.0 (n=3, FC ≤1.2, p-value <0.05). (C) The MA scatter plot visualize log fold gene expression changes and mean expression counts (p-value <0.05) for WT and *Tbx3*^{Δ/Δ} FLBs. (D) The heat map represents the top 50 up- and down-regulated genes that were identified by comparing transcriptomes of WT and *Tbx3*-deficient mouse embryos. (E) Representation of GO enrichment analysis top 10 terms for biological processes for the 137 down-regulated and 357 up-regulated genes in mutant FLBs (FDR <0.05).



hybridization (WISH, Fig. 16). It is worth to mention that majority of all DEGs being up-regulated supports the proposal that TBX3 primarily functions as a transcriptional repressor during limb bud development (Fig. 15C). DEGs were then subjected to GO biological functions analysis (Fig. 15E), which revealed that the TOP10 GO terms for up-regulated genes are linked to cell metabolism, while TOP10 GO terms for down-regulated genes are related to limb morphogenesis. MGI phenotype analysis (Sup. Figure 38) revealed that most of the limb development and skeleton morphogenesis terms were linked to genes down-regulated in *Tbx3*-deficient forelimb buds (Sup. Figure 37 lists all GO terms).

Figure 16. spatial expression patterns of *Tbx3* DEGs in WT and *Tbx3*-deficient FLBs at E9.75. As it was predicted by RNA-seq, *Wnt5a* and *Hoxa11* expression are reduced, while the *Meox1* upregulation is not detectable by WISH. Scale bar: 100μm.

6.2.3 Identification of the TBX3 target CRMs during limb bud pre-patterning: the necessity to develop a new tool

RNA-sequencing advances our understanding about gene regulation at the genome-wide level. However, RNA sequencing alone cannot provide reliable insights into the underlying gene regulatory networks (GRNs) and pinpoint the TFs binding sites in specific CRMs and promoters. Currently, little is known about the TBX3 interactions with CRMs and the associated GRNs during limb bud development. Most previously published TBX3 ChIP-Seq studies used cultured murine fibroblast and different tumor cell lines (Krstic et al., 2019; Rodriguez et al., 2008; Willmer et al., 2016; Yao et al., 2014). Mouse ES cells expressing endogenous TBX3 or TBX3-overexpressing ES cells were used in combination with different types of antibodies (Dan et al., 2013; Van Den Boogaard et al., 2012). Few TBX3 ChIP-seq studies were done using tissues expressing endogenous TBX3 levels such as mouse lung

tissue at E14.5 (Lüdtke et al., 2016) or adult mouse hearts with conditional TBX3 overexpression (Booger et al., 2011; Van Den Boogaard et al., 2012). One problem may be that there are no sensitive ChIP-grade TBX3 antibodies. Thus, we decided to identify the TBX3 cistrome in mouse limb buds by epitope tagging endogenous TBX3 protein.

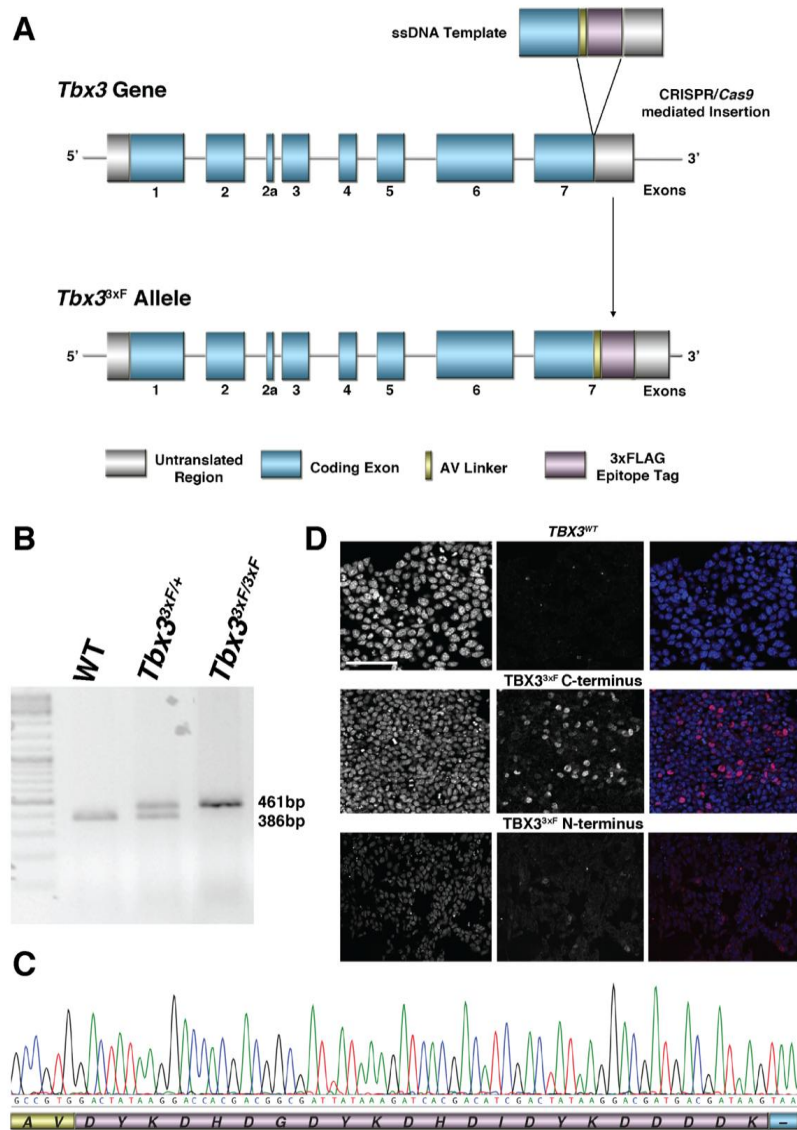


Figure 17. Insertion of a 3xFLAG epitope tag into the endogenous *Tbx3* locus using CRISPR/*Cas9* genome editing. (A) Insertion of a 3xFLAG sequence into 3' part of the *Tbx3* locus conducted using CRISPR/*Cas9*-facilitated homologous recombination. This approach allowed to epitope tag all TBX3 protein isoforms in their carboxy terminus. (B) An agarose gel shows the PCR-analysis for genotyping ES cells and mice harboring WT, *Tbx3*^{3xF/3xF}, and *Tbx3*^{3xF/+} alleles. (C) Precise C-terminal in-frame insertion of the 3xFLAG tag was verified by sequencing. Legend below shows the 3xFLAG and its A (alanine) V (valine) linker region and the STOP codon of the endogenous TBX3 Protein (-). Nucleotide sequence in color code (A: green, T: red, G: black, C: blue). The translated amino acid sequence is shown below. (D) Immunofluorescence detection of the TBX3^{3xF} protein in WT and C- or N-terminus tagged *Tbx3*^{3xF/+} mouse G4 ES cells. Only the C-terminal 3xFLAG tag insertion into the endogenous TBX3 protein C-terminus leads to successful detection of the TBX3^{3xF} protein (magenta; blue represents nuclei stained by Hoechst). Scale bar: 100µm

6.2.3.1 Generation of $Tbx3^{3xFLAG}$ mice by CRISPR/*Cas9* genome editing technology

The $Tbx3^{3xFLAG}$ allele line was generated using a CRISPR/*Cas9* strategy. In particular, a 200bp single-stranded DNA oligonucleotides (ssODNs) repair template was used to insert the 3xFLAG epitope tag in-frame into the endogenous *TBX3* protein (Fig. 17A, C) in mouse G4 ES cells. Mouse G4 ES cells were transfected with a mix containing the targeting vector encoding the *Cas9* nuclease and its sgRNAs together with ssODNs repair template (Fig. 18A). Subsequently, single G4 ES cell clones exhibiting the characteristic dome-like morphology after puromycin selection were picked for further screening (Fig. 17 B, C). In total 63 ES cells clones for the 3' 3xFLAG tagged *Tbx3* construct were picked, but only one clone had the desired in-frame insertion. However, 60% of the cells from this clone were aneuploid (20-40 metaphase spreads counted per clone, Fig. 18B). For N-terminally 3xFLAG tagged *Tbx3* construct, 99 ES cells clones were picked, but immunofluorescence of $TBX3^{3xF}$ revealed that 5' insertion of the epitope tag does not result in sensitive detection of the endogenously tagged protein (Fig. 17D). As the initial attempts were not successful, two different approaches were carried out in parallel to create the $Tbx3^{3xF}$ mouse strain.

First, mouse pronuclear zygote injections were used to introduce the 3xFLAG sequence into *Tbx3* locus. In total, 146 embryos were implanted, 36 animals were born, but only 7 transgenic animals were correctly targeted, but none of the insertions were precise due to in-frame deletions and point mutations.

In parallel, the CRISPR/*Cas9* efficiency for genome editing in ES cells was optimized. Different amount of sgRNA (2.5 μ g-10 μ g) and ssODN (0.5 μ g-6 μ g) were used to transfect mouse G4 ES cells. After puromycin selection, ES cell DNA was extracted analyzed by qPCR, which identified the most optimal sgRNA (5 μ g) and ssODN (4 μ g) conditions for targeting the *Tbx3* locus (Fig. 18C).

Using this optimized protocol 270 C-terminally tagged $TBX3^{3xF}$ ES cell clones were isolated, processed for quality analysis and frozen. Out of these, 54 ES cells clones (20%) had the expected band size in the PCR screen (Fig. 17B) and 10 clones (3,7%) carried the desired 3xFLAG in-frame insertion (Fig. 17C). Three of these ES cell clones were homozygous for $Tbx3^{3xF}$ allele. Only 6 clones had an acceptable karyotype with euploidy $\geq 70\%$.

To generate chimeric mice by aggregation a homozygous (43-5G) and heterozygous (53-3A) $Tbx3^{3xF}$ ES cells clone were used. ES cell clones were expanded for aggregation with E2.5 Swiss Albino blastocysts and the resulting blastocysts implanted into the uteri of pseudo-pregnant females. Chimeric pups were identified by the coat color as G4 ES cells originated

from 129S6xB6 mice that have an agouti coat color (A^w/a , $Tyr^{+/+}$). Successful incorporation of ES cells in chimeric albino embryos results in agouti or black fur. The percentage of agouti or black coat patches indicates the proportion of ES cells contributing to an animal. Only founder mice with $\geq 70\%$ chimerism were used for matings to establish the $Tbx3^{3xF}$ mouse strain by germline breeding. In addition to this, mice used to establish the $Tbx3^{3xF}$ were sequenced to verify the in-frame insertion of the 3xFLAG in the $Tbx3$ locus (Fig. 18A).

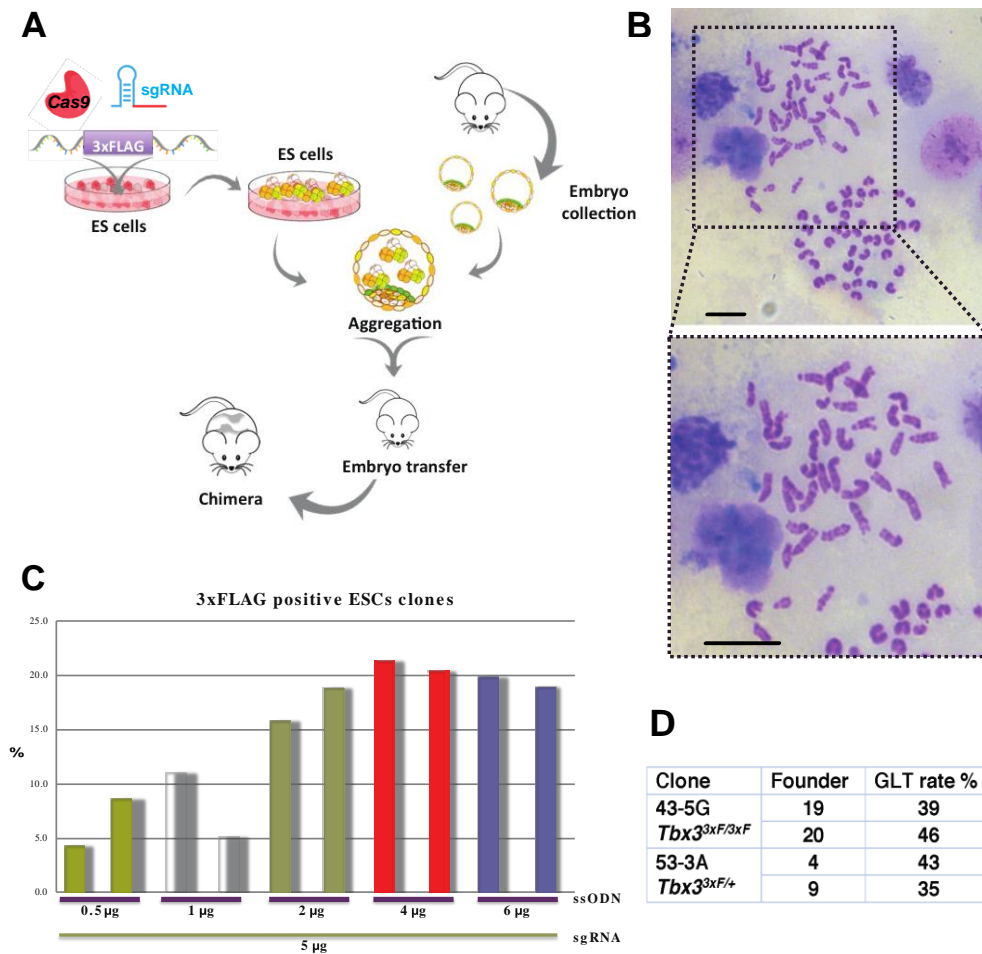


Figure 18. Pipeline of $Tbx3^{3xF}$ mouse strain establishment. (A) A scheme represents the workflow used to generate chimeric mice from $Tbx3^{3xF/3xF}$ ES cells. (B) The image represents low, and high magnification of chromosome spreads used to count mouse chromosomes to determine the percentage of euploid cells. Scale bar: 50 μ m. (C) The bar plot represents the strategy used to increase the efficiency of CRISPR/Cas9 by using different amounts of sgRNA and ssODN. (D) The table represents the percentage of successful germline transmissions by four different $Tbx3^{3xF}$ chimeric males derived from $Tbx3^{3xF/3xF}$ (43-5G) and $Tbx3^{3xF/+}$ (53-3A) ES cells clones. 43-5G ESCs clone derived offspring were kept for $Tbx3^{3xF}$ mouse colony establishment.

The table in Fig. 18D represents the germline transmission rates of 4 different $Tbx3^{3xF}$ chimeric males derived from $Tbx3^{3xF/3xF}$ (43-5G) and $Tbx3^{3xF/+}$ (53-3A) ES cells clones. 43-

5G ESCs clone derived offspring were used to establish the *Tbx3*^{3xF} mouse by breeding the *Tbx3*^{3xF} males with Swiss Albino females.

6.2.3.2 *Tbx3*^{3xF} allele is a new sensitive tool to detect endogenous TBX3 proteins via the 3xFLAG epitope tag

To validate the *Tbx3*^{3xF} mice strain as a sensitive tool to detect the endogenous TBX3 proteins, a set of experiments evaluating protein stability, cellular localization and also the wild-type nature of this modification were performed.

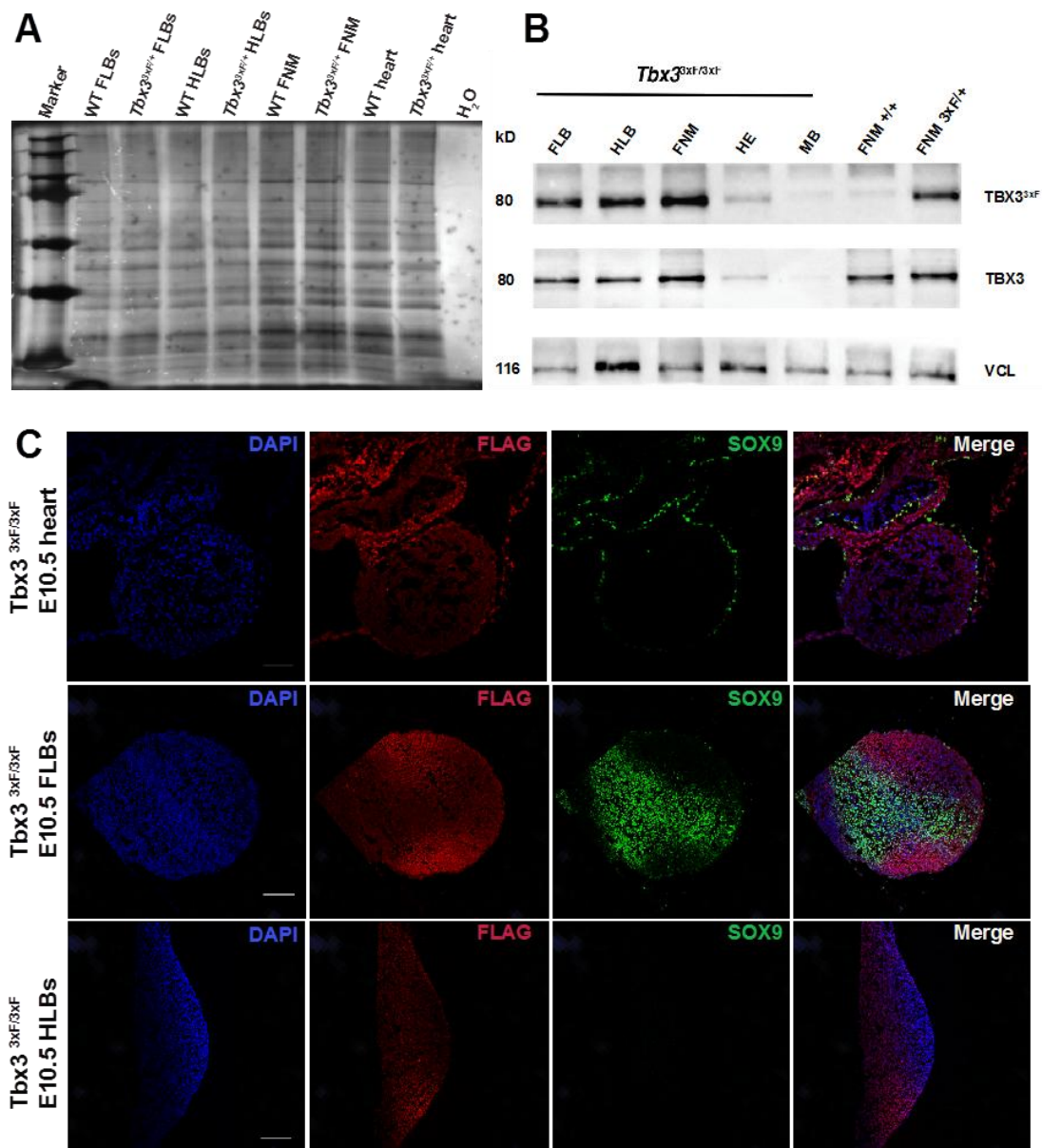


Figure 19. The 3xFLAG epitope tag provides a sensitive tool to detect the TBX3 protein. (A) Silver staining was used to detect proteins (5µg/lane) after electrophoretic separation on a polyacrylamide gel and assess possible protein degradation. (B) The 3xFLAG epitope tag provides a sensitive tool to detect TBX3 protein isoforms in embryonic tissues by Western blotting. TBX3^{3xF} protein is detected in forelimbs (FL), hindlimbs (HL), frontal nasal mass

(FNM) and hearts (HE) of mouse embryos (E10.75). Midbrain (MB) serves as non-expressing tissue control. Western blotting detects ~80 kDa full-length TBX3 protein. 10µg of total protein were loaded per lane. (C) Immunofluorescent staining of the TBX3^{3xFL} protein detects its specific expression in posterior and anterior parts of mouse forelimbs, posterior hind limb bud and heart (E10.5). Scale bar: 200 µm, cryosections thickness: 12µm.

First, the possible proteolytic degradation of extracted proteins from various E10.75 embryonic tissues was evaluated by silver staining (Fig. 19A). As no degradation was observed, expression levels and detection sensitivity of the endogenous TBX3^{3xFL} protein was assessed by Western Blot analysis using ChIP-grade M2 anti-FLAG antibody (ref., F3165). Western blotting detected the ~80 kDa full-length TBX3^{3xFL} protein in limb buds, frontal nasal mass, and hearts as expected from *Tbx3* expression in mouse embryos (Fig. 19B). Twice as much TBX3 protein was detected in homozygous than heterozygous embryos at E10.75. WT control and non-expressing tissue (midbrain) showed only a non-specific shadow band above the 80 kDa TBX3^{3xFL} protein. Thus, Western Blot analysis confirmed that the endogenously tagged TBX3^{3xFL} protein is expressed like the wild-type protein and that detection of endogenous TBX3^{3xFL} protein is sensitive.

Next, immunofluorescence (Fig. 19C) was used to verify spatiotemporal distribution of TBX3^{3xFL} protein. Staining of frontal *Tbx3*^{3xFL} embryonic sections at E10.5 verified previously reported TBX3 expression in embryonic hearts (Hoogaars et al., 2004), in posterior and anterior domains of fore- and hindlimb buds (Gibson-Brown et al. 1998, Fig. 19C).

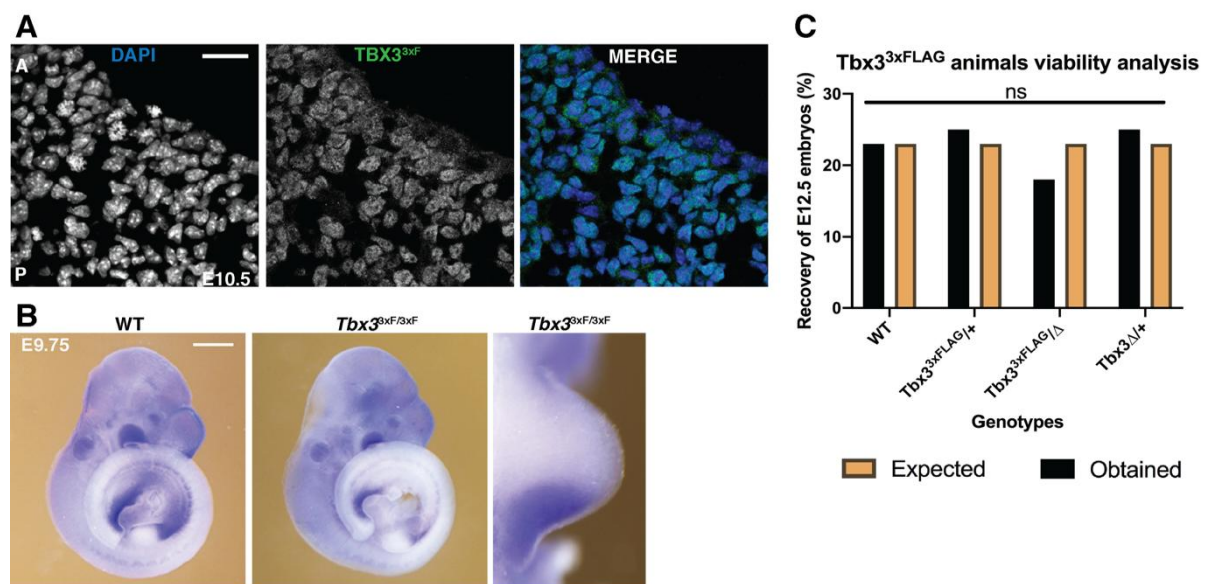


Figure 20. The 3xFLAG tag does not perturb TBX3 localization, expression, and biological functions. (A) High magnification of the immunofluorescence detection of the TBX3^{3xFL} protein in the anterior part of *Tbx3*^{3xFL/+} forelimb buds. TBX3^{3xFL} proteins preferentially localize to cell nuclei. Scale bar: 20 µm. (B) WISH detects *Tbx3*^{3xFL} mRNA in mouse embryonic tissues at embryonic day E9.75. Scale bar: 250 µm. (C) The 3xFLAG epitope does not alter endogenous TBX3 functions, as *Tbx3*^{3xFL/+} and *Tbx3*^{3xFL/Δ} embryos develop normally, no embryonic lethality and phenotypic abnormalities are detected. The Chi-square test (1.444 with 3 degrees of freedom) and the two-tailed t-test (p=0.6963) detected no statistically significant increase in embryonic lethality.

High magnification analysis of the anterior domain in forelimb buds (Fig. 20A) confirmed the predominant nuclear cellular location of the TBX3^{3xF} protein. Besides, WISH analysis of WT and *Tbx3*^{3xF} embryos failed to detect alterations in *Tbx3*^{3xF} transcript distribution (Fig. 20B). These data imply that the inserted 3xFLAG epitope tag does not perturb the spatio-temporal distribution of *Tbx3* transcripts and TBX3 protein nor its nuclear localization.

To assess potential effects of the 3xFLAG tag on TBX3 protein function genetically, *Tbx3*^{3xF/+}, and *Tbx3*^{Δ/+} mice were crossed and embryos analyzed at E12.5. In total, 95 embryos were collected and analyzed, which showed that both *Tbx3*^{3xF/+} and *Tbx3*^{3xF/Δ} mouse embryos do not display increased embryonic lethality and no phenotypes were detected (Fig. 20C).

Overall, these data indicate that the *Tbx3*^{3xF} allele is expressed, and endogenously tagged TBX3^{3xF} protein functions as a wild-type. Therefore, the *Tbx3*^{3xF} allele can be used to identify downstream interactions of TBX3 with CRMs.

6.2.4 The TBX3 cistrome in mouse limb buds is identified using the *Tbx3*^{3xF} allele

The TBX3 controlled GRNs that orchestrate early limb bud development, ChIP-seq using the *Tbx3*^{3xF} allele and ChIP-grade M2 anti-FLAG antibody identified the genomic regions enriched in TBX3 chromatin complexes and provided insights into TBX3-controlled GRNs that orchestrate early limb bud development.

After the initial phase of optimization, the TBX3 ChIP-seq from mouse forelimb buds was performed using the protocol by Sheth et al. (2016). In total, five ChIP-seq replicates were generated using 70 forelimb buds each, to identify TBX3^{3xF} cistrome by ChIP-seq. The first two replicates used *Tbx3*^{3xF/3xF} forelimb buds of embryos E9.75-E10.25 (27-32s), and three additional replicates used *Tbx3*^{3xF/3xF} forelimb buds at E9.75-E10.5 (28-34s, data not shown). At this developmental stage *Tbx3* expression in forelimb buds is predominantly posterior, only at later stages the anterior expression domain becomes more prominent. The analysis was focused at the earlier stages as AP polarity is set during the onset of limb bud outgrowth (E9.75). The ChIP-seq data analysis was performed by Dr. Shalu Jhanwar. The resulting ChIP-seq reads were mapped to the publicly available mouse reference genome (GRCm38/mm10). The enrichment analysis of ChIP in comparison to input samples was conducted using MACS-based peak calling. Each replicate's input control served as a control to verify the TBX3^{3xF} ChIP enrichment and to eliminate the false positive signals caused by non-specific antibody binding or computational biases. The TBX3^{3xF} ChIP-seq peaks were

visualized for further analysis using the UCSC genome browser. To ensure meaningful TBX3^{3xF} ChIP-seq analysis,

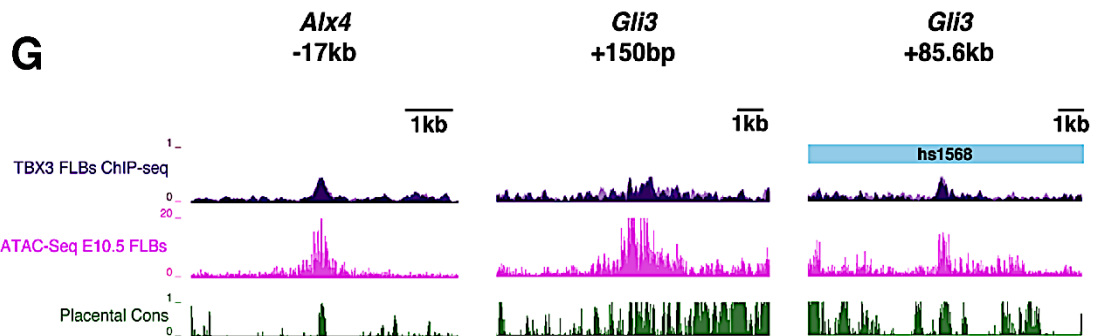
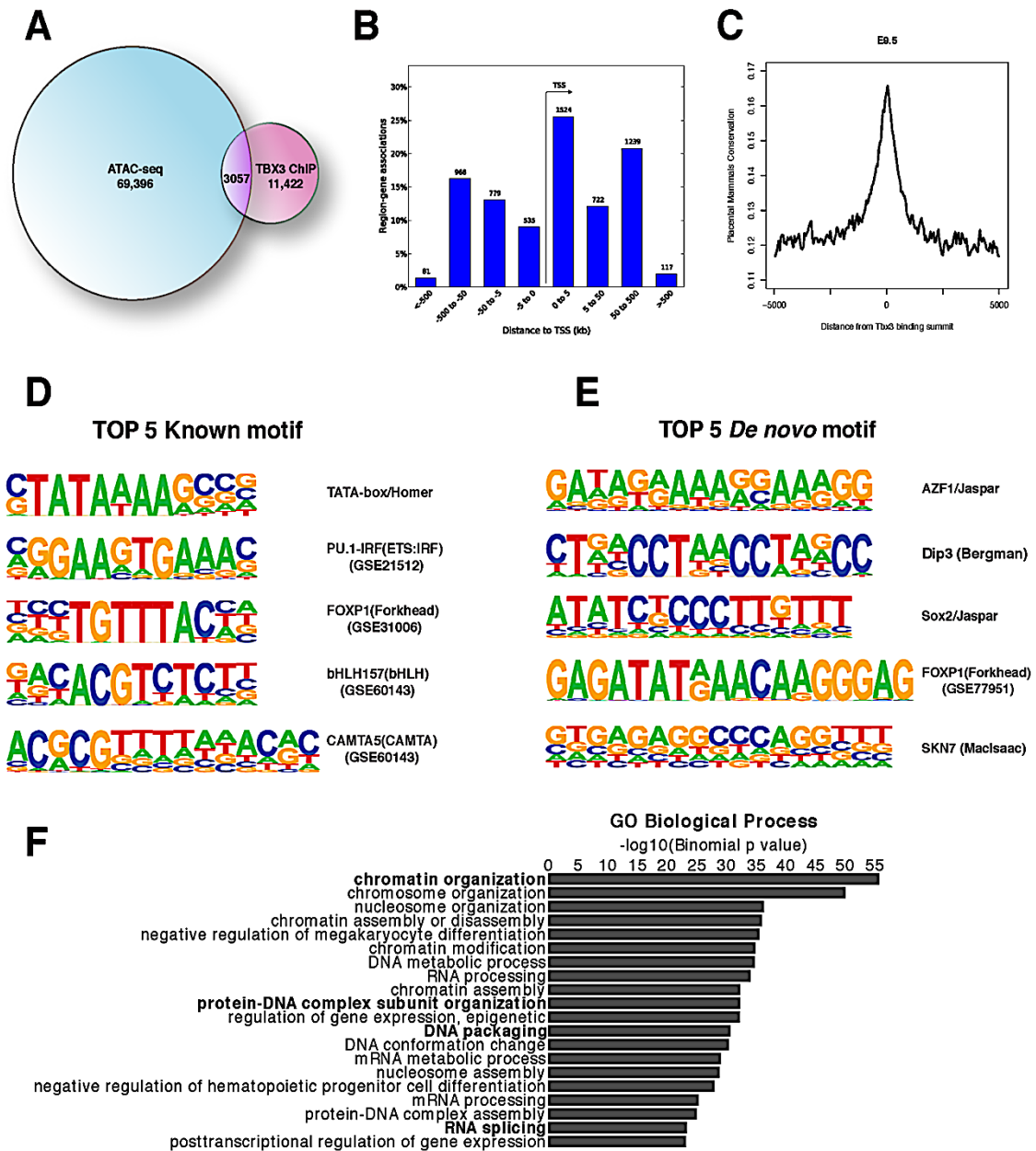
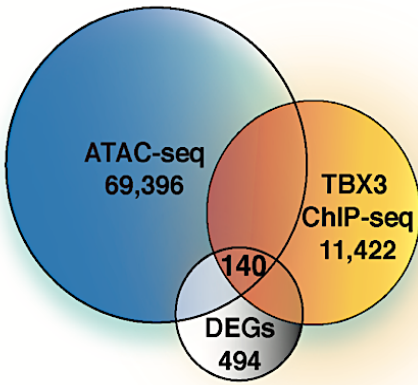
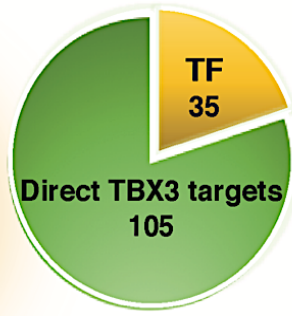
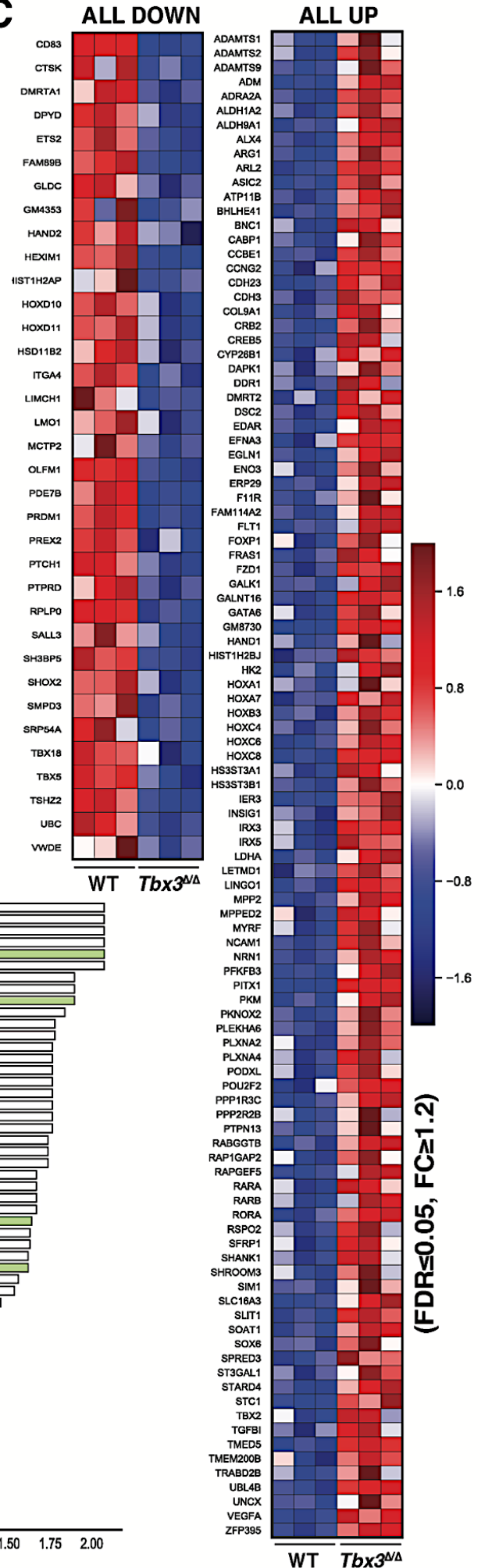


Figure 21. TBX3 ChIP-seq analysis using the *Tbx3*^{3xF} allele revealed TBX3 cistrome in early mouse forelimb buds. (A) A Venn diagram represents the 3057 statistically significant enriched (1e5) peaks of TBX3 in open chromatin that were found after the ATAC-seq dataset from WT FLBs at E10.5 (generated by Prof. Javier Lopez-Rios) was overlapped with E9.75-10.5 FLBs of TBX3 ChIP-seq consensus peaks (without X and Y chromosomes). (B) A bar plot represents the GREAT analysis revealed distribution of TBX3 consensus peaks found in open chromatin regions according to the distance to the transcription start site (TSS). (C) A histogram represents the PhastCon analysis of TBX3^{3xF} target regions enriched in mouse FLBs. Most of the enriched regions are highly evolutionary conserved in placental mammals. (D) HOMER motifs discovery analysis of TBX3 consensus peaks in mouse FLBs identified the top 5 known motifs that are bound by TBX3. (E) HOMER *de novo* motifs discovery analysis of TBX3 consensus peaks in mouse FLBs identified the top 5 *de novo* regions bound by TBX3. (F) GO terms for TBX3 consensus peaks found in open chromatin regions. (G) UCSC genome browser track shows genomic regions enriched in TBX3 chromatin complexes. Genomic tracts represent two overlapped biological replicates of TBX3 FLBs ChIP-seq peaks at E9.75-10.5, a track below shows open chromatin regions in FLBs identified by ATAC-seq at E10.5 (generated by Prof. Javier Lopez-Rios) and the lowest track represents placental mammals' evolutionary conservation. The blue bar over the *Gli3* element at +85.6 kb indicates that the TBX3 enrichment was found in a regulatory VISTA element (hs1568).

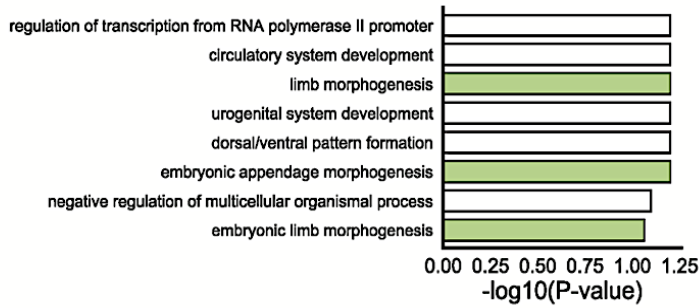
only statistically significant enriched (1e5) peaks were analyzed. In total, 11,422 significant TBX3^{3xF} ChIP-Seq peaks were identified. Furthermore, the TBX3^{3xF} ChIP-Seq dataset was overlapped with the ATAC-seq dataset from E10.5 wild-type FLBs (generated by Prof. Javier Lopez-Rios) to identify binding regions in open chromatin. This resulted in 3057 TBX3^{3xF} ChIP peaks in open chromatin that were used for further analysis using the Genomic Regions Enrichment Annotations Tool (GREAT, Fig. 21A). GREAT analysis revealed that TBX3 predominantly binds within 5kb of known transcriptional start sites (TSS). This means that TBX3 chromatin complexes are predominantly enriched in promoter regions (Fig. 21B). The PhastCon analysis indicates that TBX3 interacting regions are highly conserved in placental mammals (Fig. 21C). Surprisingly, *de novo* and known motifs analysis using HOMER have did not identify known TBOX motifs, but consistent with enrichment at promoters the TATA-box motif was identified as one of the TOP5 known motifs (Fig. 21E and D, respectively). Finally, TBX3 enriched genomic regions were associated with 3057 genes and the biological functions of these genes were revealed by Gene Ontology (GO) analysis (Fig. 21F). The majority of GO biological terms are supported by observations from previous studies, namely pointing to an involvement of TBX3 in processes like protein-DNA complex subunit organization assembly (Coll et al., 2002), chromatin organization (Dong et al., 2018) and RNA splicing (Kumar et al., 2014). However, surprisingly no limb tissue-specific mouse phenotype terms were detected (Supplement Figure 40). Overlapping the two TBX3^{3xF} ChIP-seq replicate datasets in the UCSC genome browser showed that genomic regions previously predicted to be enriched in TBX3 chromatin complexes displayed similar enrichment levels (Fig. 21G).

6.2.5 Identification of the TBX3 transcriptional target genes and GRNs

To identify the direct transcriptional targets of TBX3 complexes in mouse forelimb buds, the TBX3^{3xF} ChIP-seq at E9.75-10.5 (11,422 peaks), ATAC-seq peaks (69,396 peaks at E10.5, provided by Prof. Javier Lopez-Rios) and DEGs (494 DEGs at E9.75-E10.0) datasets were intersected. This analysis identified 3057 genomic regions that are located in the open

A**B****C****D**

GO: Direct TBX3 target down-regulated genes (n=35, FDR<0.1)

**E**

GO: Direct TBX3 target up-regulated genes (n=105, FDR<0.05)

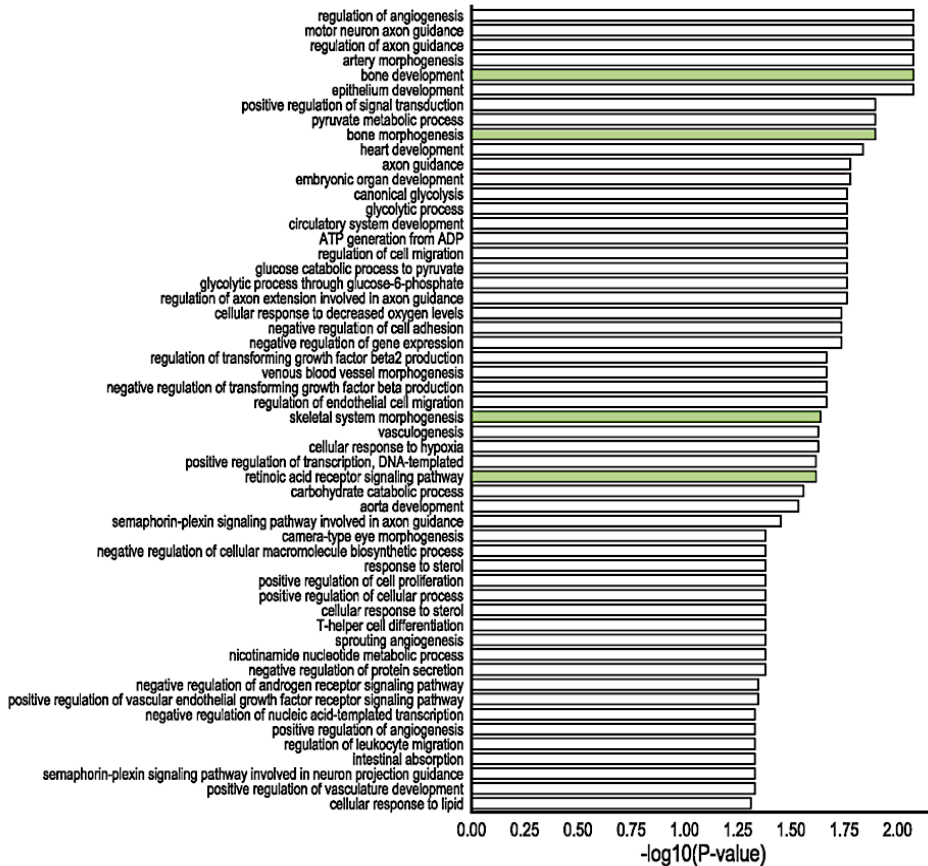


Figure 22. Identification of TBX3 direct transcriptional target genes (A) The Venn diagram represents the strategy used to identify direct transcriptional targets. 140 TBX3 target genes were identified by overlapping the open chromatin regions identified by ATAC-seq at E10.5 (data produced by Prof. Javier Lopez-Rios), genomic TBX3 binding sites revealed by ChIP-seq and the DEGs identified by comparing WT and *Tbx3*-deficient forelimb buds. (B) The pie chart represents the 20% fraction of the transcription factors (n=35) that are direct targets of TBX3 (n=140). (C) The heat map represents WT and *Tbx3*-deficient DEGs that are transcriptional targets of TBX3 in mouse FLBs at E9.75-10.0 (FC ≤ 1.2 , FDR < 0.05). In total, 35 genes were identified as down-regulated, and 105 genes as up-regulated. (D) GO analysis terms for biological processes of direct transcriptional TBX3 target genes that are down-regulated in *Tbx3*-deficient FLBs (n=35, FDR < 0.1). (E) GO analysis terms for biological processes of TBX3 target genes up-regulated in *Tbx3*-deficient FLBs (n=105, FDR < 0.05).

chromatin and are enriched in TBX3 chromatin complexes (Fig. 22A). Subsequently, the *Tbx3* DEGs were assigned to the corresponding TBX3 target CRMs using the GREAT two nearest genes approach with a recommended 1Mb span in both directions to the nearest TSS. This parameter was chosen to define the *cis*-regulatory landscapes as CRMs can be located far up-or downstream of the target gene and even be in other gene loci to interact with their *bona-vide* target genes (Lettice et al., 2003). Finally, by overlapping these three genome-wide datasets, 140 candidate TBX3 transcriptional target genes were identified in mouse forelimb buds at E9.75-10.25, Fig. 22A), The candidate genes, whose CRMs are not located in regions of open chromatin are listed in Supplementary Tables 13-15.

The majority of the TBX3 transcriptional target genes are up-regulated, whereas 105 genes were up-regulated and only 35 genes down-regulated (Fig. 22C, FC ≤ 1.2 , FDR < 0.05). As many genes appear to encode TF, the 140 TBX3 target genes were intersected with the RIKEN institute mouse TF list (2014, http://genome.gsc.riken.jp/TFdb/htdocs/tf_list.html). This analysis revealed that 20% (n=35), of TBX3 target genes are known transcription regulators (Fig. 22B, Supplementary Table 16). In fact, the majority of these transcription factors have a spatially restricted expression domain in early mouse limb buds.

To provide insights into the biological processes in which the TBX3 target genes function, GO analysis was performed. GO analysis for the 35 down-regulated TBX3 target genes (FDR < 0.1) pointed to an involvement in processes related to limb morphogenesis (Fig. 22D). In comparison, the 105 up-regulated TBX3 target genes (FDR < 0.05) are associated with bone and skeleton morphogenesis. They also seem to function in important development processes such as retinoic acid receptor signaling (Fig. 22E, Supplementary Figure 41).

6.2.6 Validation of TBX3 interacting CMRs in the landscapes of TBX3 target genes

The ultimate goal of this project is to identify the TBX3 cistrome and to provide insights into the role of TBX3 during AP patterning of the nascent forelimb bud mesenchyme. Thus, five

TBX3 target genes with key functions in early limb bud development were selected for further bioinformatics analysis. Furthermore, *Tbx3* was identified as a direct transcriptional target of

HAND2, that participates in posterior repression of *Gli3* expression in early limb buds (Osterwalder et al., 2014). Therefore, TBX3-specific, and interactions with HAND2 and GLI3 during limb AP patterning were assessed in the TADs of the select genes. Finally, to determine if select CRMs enriched in TBX3 complexes located in open chromatin function as transcriptional enhancers, their activity was assessed by *lacZ* reporter assays in transgenic mouse embryos (done by Dr. Marco Osterwalder in the laboratory of Prof. A. Visel, Berkeley, USA). The coordinates of all CRMs of interest and status with respect to *lacZ* reporter activity are included in Supplementary Tables 17-19.

6.2.6.1 Bioinformatical analysis of TBX3 interacting CMRs

To identify all the potential TBX3 bound CRMs and mutual binding partners in the locus of interest, the USCS genome browser was used to overlap the Hi-C profile (mm10, red triangle in figures below) of wild-type mouse embryonic fibroblasts (Barutcu et al., 2018) with the forelimb bud ATAC-seq datasets (E10.5) and the ChIP-seq datasets of TBX3^{3xF}, HAND2^{3xF} (provided by Dr. Marco Osterwalder) and GLI3 (E10.5, Kevin Peterson's dataset). TBX3 binding regions in open chromatin regions are highlighted by blue boxes (see Figures below). Furthermore, as histone modifications alter the CRM activities (reviewed in 4.2.7) the ChIP-seq datasets for the H3K27ac, H3K27me3, H3K36me3, H3K4me1, and H3K4me3 modifications at E10.5 (Gorkin et al. in press) were included in bioinformatics analysis. The analysis evaluated the combinatorial enhancer modifications: H3K4me1 and H3K27ac, low, if any, H3K4me3, and absence of H3K27me3 to define putative active enhancers (Rada-Iglesias et al., 2011). A combination of H3K4me1/H3K27ac modifications was used to distinguish active from poised enhancer elements (Dunham et al., 2012) as the H3K4me1 modification alone marks poised enhancer states (Voigt et al., 2013).

6.2.6.2 TBX3 interacts with CRM enhancers in the *Gli3* cis-regulatory landscape

Despite the spatial change in *Gli3* expression in *Tbx3*-deficient limb buds (Osterwalder et al., 2014), my transcriptome analysis failed to detect *Gli3* as a DEG. One possibility is that RNA-seq of total early mouse forelimb buds fails to detect the alteration in the *Gli3* transcripts as the overall averaged expression changes in limb bud cells are masked by the bulk RNA-seq

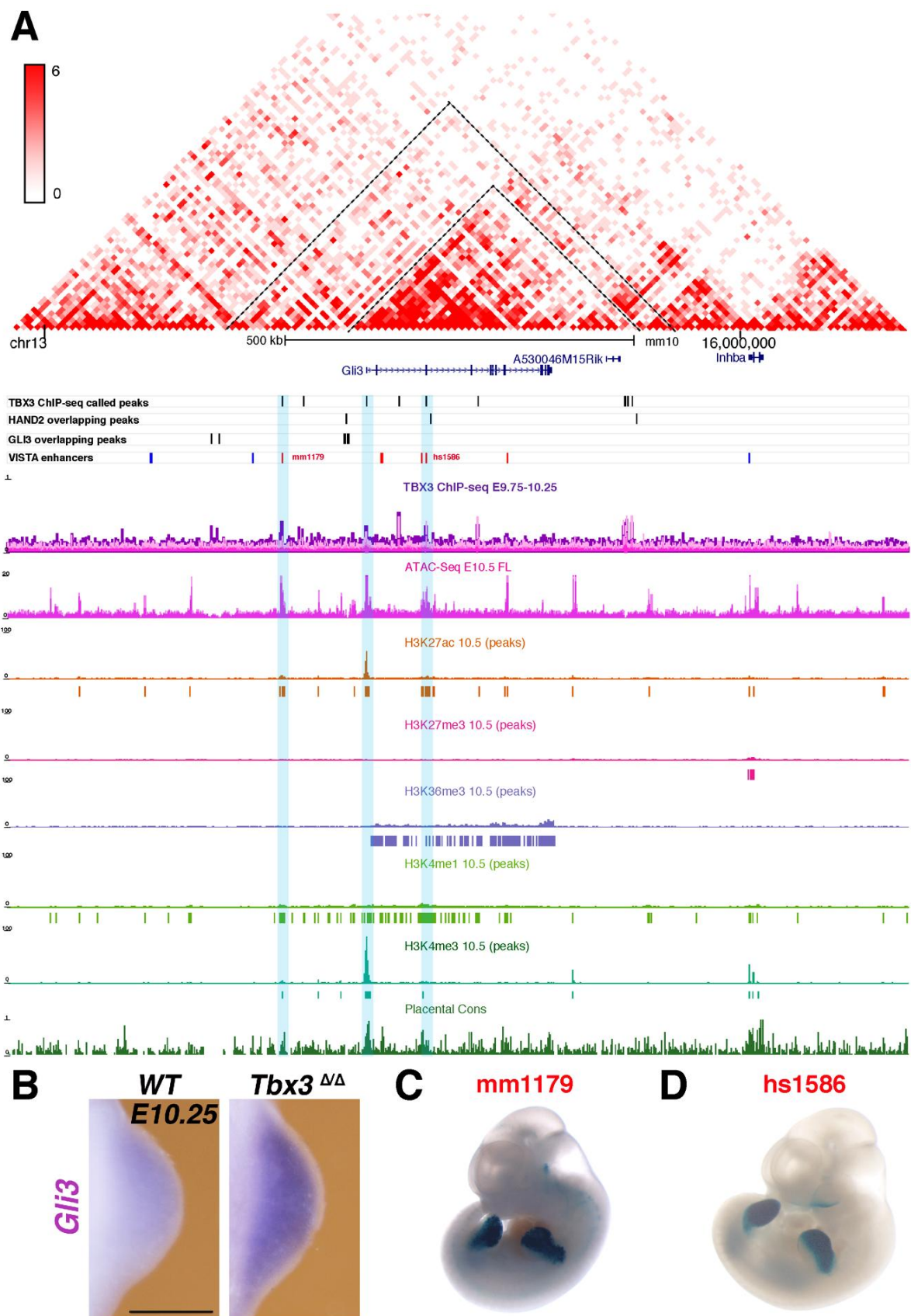


Figure 23. Analysis of the *Gli3* cis-regulatory landscape.

(A) USCS genome browser view showing the analyzed datasets for *Gli3* cis-regulatory landscape. The dashed line divides the Hi-C profile into sub-TADs for *Gli3*. Potential TBX3 controlled CRMs are highlighted by blue boxes. (B) WISH for *Gli3* in WT and *Tbx3*-deficient FLBs at E10.25 (n=3, scale bar 200 μ m). (C) The previously identified regulatory elements mm1179 and (D) hs1586 (Visel et al., 2007) overlap with TBX3 peaks and are active in specific anterior *lacZ* expression domains in fore- and hindlimb buds. These results indicate that these CRM participate in regulating *Gli3* expression in limb buds.

approach. Despite this, WISH at E10.25 (n=3) revealed that the *Gli3* expression domain is extended posteriorly in *Tbx3*-deficient forelimb buds (Fig. 23B). GREAT analysis revealed that TBX3 tends to be predominantly enriched in promoter regions. This analysis identified three candidate CRMs in the *Gli3* cis-regulatory landscape: -120.8kb up-stream, at the TSS and +85.5kb down-stream of *Gli3* TSS (Fig. 23A). All these CRMs display putative enhancer specific marks (H3K27ac, H3K4me1, and H3K4me3). In addition, the CRM located -120.8kb upstream of *Gli3* TSS was previously identified (Visel et al., 2007) as a mm1179 regulatory element (Fig. 23C) that drives *lacZ* expression in the anterior (n=3/8), entire mesenchyme except posterior domain (n=3) or the entire limb bud mesenchyme (n=2/8). These results imply that this CRM participates in regulating *Gli3* expression and binding of TBX3 could participate in its repression from the posterior mesenchyme. Another regulatory element is located at the TSS and is decorated by enhancer histone marks, but its functionality in regulating *Gli3* expression was not tested. A CRM located +85.5kb upstream of the *Gli3* TSS is bound by the TBX3 chromatin complexes in a genomic region close to the HAND2 binding region. This regulatory element is already known as the orthologous to human VISTA enhancer element hs1586 (Visel et al., 2007) drives *lacZ* reporter expression in the anterior part of mouse fore- and hindlimb buds (n=3/3) (Figure 23D).

6.2.6.3 TBX3 interacts with CRMs in the *Hand2* cis-regulatory landscape

The fact that TBX3 is necessary for *Hand2* expression was previously established (Osterwalder et al., 2014). Comparative analysis verified that *Hand2* expression is down-regulated in *Tbx3*-deficient forelimb buds at E10.0 (n=3) as predicted from RNA-seq analysis (Fig. 24B). Three candidate CRMs in the cis-regulatory landscape of *Hand2* were identified: -604.4kb, -357.4kb and at +1.1kb with respect to the TSS (Fig. 24A). A possible CRM located -604.4kb upstream the *Hand2* TSS was assigned to a sub-TAD1. This genomic region displays active enhancer marks (H3K27ac and, H3K4me1) and was identified as mm1832 (Fig. 24C). However, this CRM does not function as a limb bud enhancer as *lacZ* activity is restricted to the embryonic brain (diencephalon) and no signal was detected in forelimbs (n=4/5, data provided by Marco Osterwalder). Another candidate CRM located -357.4kb from the *Hand2* TSS in the sub-TAD2 displays active enhancer histone marks (H3K27ac and H3K4me1). This CRM mm1831 displays very low *lacZ* activity the proximal fore- (n=5/7)

and hindlimb buds (n=3/7, Fig. 24D, data provided by Marco Osterwalder). However, as the activity is low this CRM is termed as

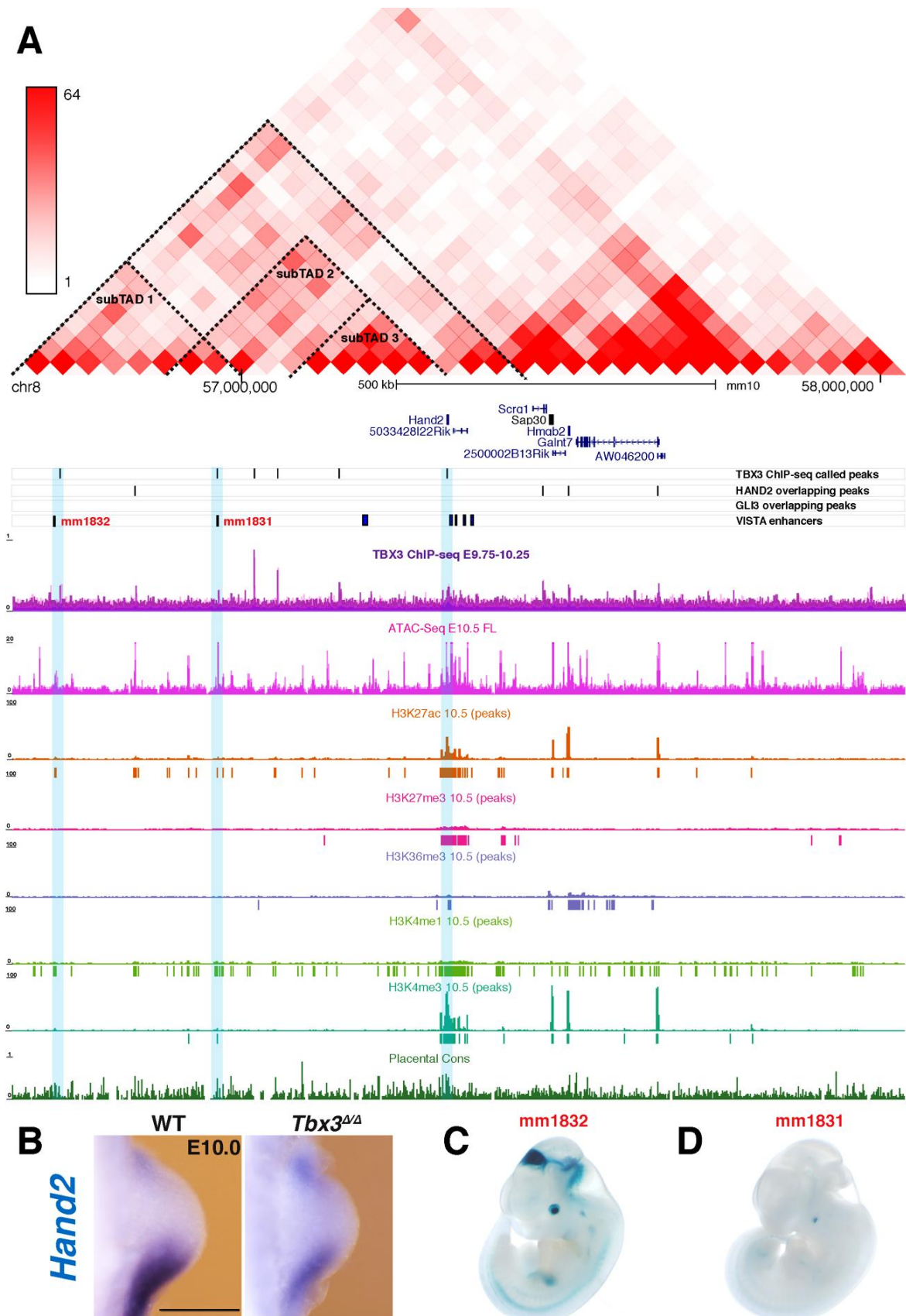


Figure 24. Analysis of the *Hand2* cis-regulatory landscape.

(A) USCS genome browser view showing the datasets for *Hand2* cis-regulatory locus. The dashed line divides the Hi-C profile into sub-TADs for *Hand2*. Potential TBX3 CRM are highlighted by blue boxes. (B) WISH for *Hand2* in WT and *Tbx3*-deficient FLBs at E10.0 (n=3, scale bar 200 μ m). (C) CRM mm1832 located in sub-TAD1 is only active in diencephalon and absent from forelimb buds (n=4/5, data provided by Marco Osterwalder). (D) CRM mm1831 is located in sub-TAD2 drives very low *lacZ* expression in the proximal forelimb (n=5/7) and hindlimb buds (n=3/7, data provided by Marco Osterwalder).

negative. A candidate CRM in the promoter region +1.1kb downstream of *Hand2* TSS is decorated by histone marks related to gene expression itself (H3K27ac, H3K36me3, H3K4me3) and might point to a presence a putative enhancer (H3K27ac, H3K4me1 and H3K4me3). So far, the enhancer potential of this CRM has not been tested.

6.2.6.4 TBX3 interacts with CRM enhancers in the *Tbx3* cis-regulatory landscape

Four candidate CRMs in the *cis*-regulatory landscape of *Tbx3* were identified: -32.4kb, -2.5kb (located in closed chromatin), +175bp and +78.2kb away from the TSS (Fig. 25A). The *Tbx3* -32.4kb CRM display poised enhancer characteristics (H3K27me3 and H3K4me1) and is located in a sub-TAD1. This CRM has been previously reported to function as enhancer mm1117 with *lacZ* expression in the posterior part of FLBs (n=5/5, Fig. 25B, Visel et al. 2007). The CRM located at -2.5kb from the *Tbx3* TSS exhibits putative enhancer marks (H3K27ac, H3K4me1, and H3K4me3) and is the mouse orthologous CRM of human hs483 drives distal-anterior *lacZ* expression in fore- and hindlimb buds (n=2/3, Fig. 25C). These results suggest that these two CRMs participate in auto-regulating of *Tbx3* expression.

The other two CRMs are located in the *Tbx3* promoter region and upstream to the TSS and are decorated by putative enhancers histone modifications (H3K27ac, H3K4me1 and H3K4me3, while H3K27me3 might be related to non-expressing cells). Their function as a transcriptional enhancers was not assessed.

6.2.6.5 TBX3 interacts with a CRM in the *Tbx2* cis-regulatory landscape

Comparative RNA-seq analysis revealed variable changes in *Tbx2* expression (down- or up-regulated depending on the embryo, Figure 15). The up-regulation was verified by WISH (Fig. 26B and Fig. 35) and bioinformatics analysis identified three candidate CRMs at -32.4kb, -14kb, and +170bp with respect to the *Tbx2* TSS (Fig. 26A). The candidate CRM located -32.4kb upstream shows poised enhancer specific histone modifications (H3K27me3 and H3K4me1) and is enriched in TBX3 and HAND2 chromatin complexes (my study and Osterwalder et al., 2014). This CRM mm1210 drives *lacZ* expression in forelimb buds and heart (Fig. 26C, D, data provided by Marco Osterwalder). Interestingly, the *lacZ* distribution resembles the endogenous *Tbx2* expression. The other two CRMs are located in another sub-TAD than the mm1210 element. Both these CRMs display putative enhancer histone modifications but their enhancer activities have not been assayed.

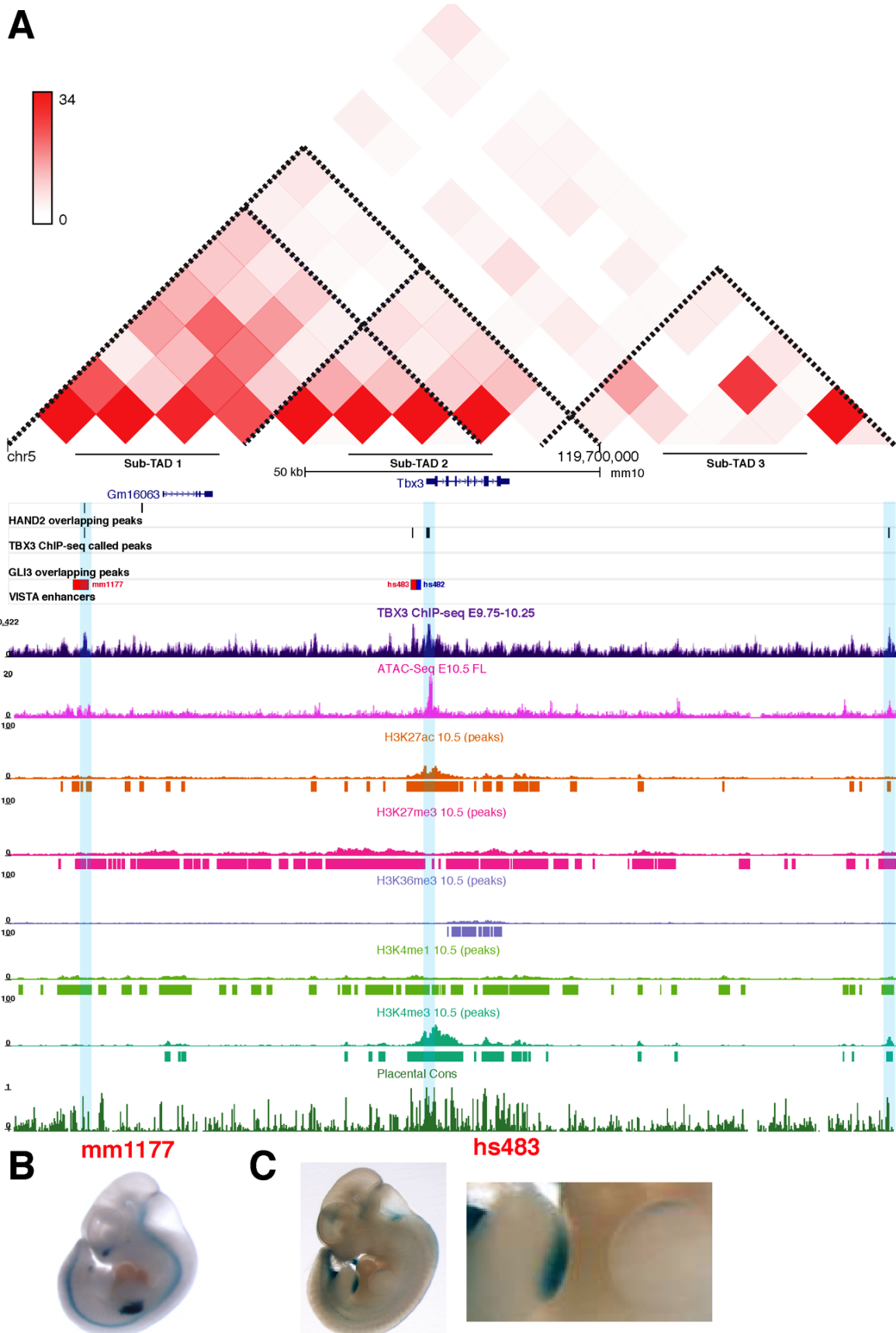


Figure 25. Analysis of the *Tbx3* cis-regulatory landscape.

(A) USCS genome browser view shows the datasets for *Tbx3* cis-regulatory landscape. The dashed line divides the Hi-C profile into sub-TADs of *Tbx3*. Potential TBX3 controlled CRM are highlighted by blue boxes (B) Already reported CRMs (Visel et al., 2007) mm1177 located in the sub-TAD1 and (C) hs483 located in sub-TAD2 of *Tbx3* regulatory landscape. Interestingly, CRM mm1177 is enriched TBX3 chromatin complexes and drives specific posterior *lacZ* expression in forelimb buds, while CRM hs483 drives anterior *lacZ* expression in limb buds.

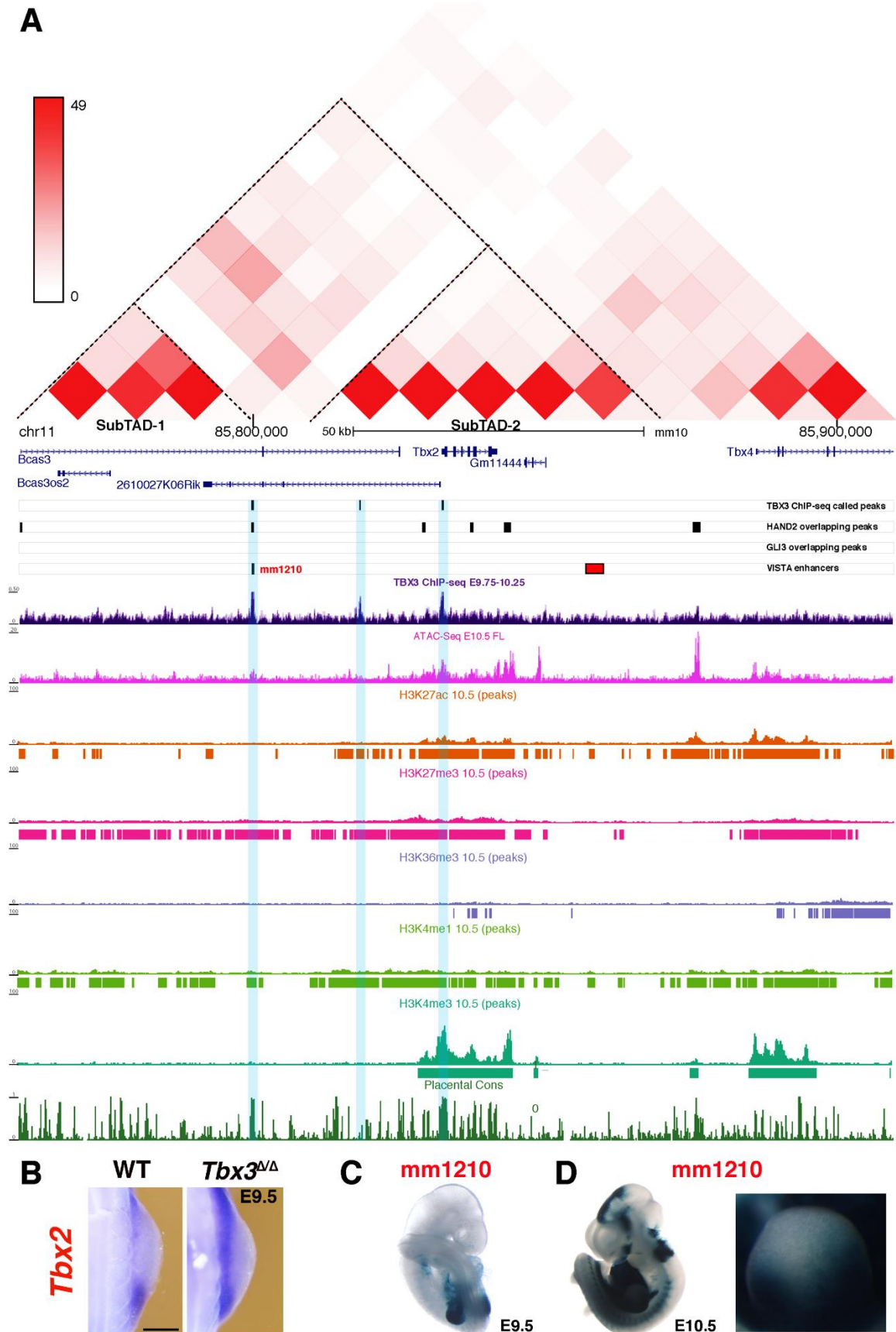


Figure 26. Analysis of the *Tbx2* cis-regulatory landscape.

(A) USCS genome browser view showing the datasets for the *Tbx2* cis-regulatory landscape. The dashed line divides the Hi-C profile into sub-TADs. Potential TBX3 controlled CRMs are highlighted by blue boxes. (B) WISH for *Tbx2* in WT and *Tbx3*-deficient FLBs at E9.75 (n=3, scale bar 200μm) (C) The TBX3 and HAND2 interacting CRM mm1210 (data provided by Marco Osterwalder) drives specific forelimb bud and heart *lacZ* expression at E9.5 and (D) E10.5.

6.2.6.6 TBX3 interacts with a CRM enhancer in the of *Lmo1* cis-regulatory landscape

As predicted by RNA-seq, *Lmo1* expression is down-regulated in the early FLBs of *Tbx3*-deficient embryos (Fig. 27B). A prominent TBX3 ChIP-seq peak was identified at -21.2kb upstream of the *Lmo1* TSS (Fig. 27A). Interestingly, TBX3 binding to this candidate CRM also overlaps with a HAND2 binding site. This CRM exhibits characteristic enhancer histone marks (H3K27ac, H3K4me1, and low H3K4me3). Indeed, the CRM mm1788 is active in the distal mesenchyme of forelimb (n=5/6) and hindlimb buds (n=3/6) to drive *lacZ* expression (Fig. 27C, data provided by Marco Osterwalder).

Taken together, this analysis establishes that TBX3 indeed binds to active enhancers and in some cases TBX3 enriched CRM enhancers are shared with HAND2. However, no overlaps in enrichment with GLI3 chromatin complexes was found in the CRMs analyzed. Furthermore, none of the CRMs tested by transgenic *lacZ* expression assay recapitulated the endogenous *Hand2* expression, but active CRM enhancers identified in *Tbx3*, *Tbx2* and *Gli3* genes resulted in *lacZ* patterns resembling the endogenous expression. Overall, my analysis indicates TBX3 can fine-tune its own expression and participates in regulating *Tbx2* and *Gli3* expression.

6.2.7 Comparative RNA-seq analysis of *Hand2*-deficient forelimb buds

Osterwalder et al. (2014) showed that *Tbx3* is a direct transcriptional target of HAND2. Therefore, it is possible, that the expression of a significant number of TBX3 target genes is co-regulated by HAND2 and that TBX3 and HAND2-TBX3 controlled GRNs are active during early forelimb bud development. Therefore, a comparative RNA-seq analysis was conducted to identify the HAND2 regulated genes in *Hand2*-deficient mouse forelimbs at exactly the same stage as in *Tbx3*-deficient forelimb buds (E10-10.25, 31-33somites, Fig. 28A). *Hand2* was conditionally inactivated in the forelimb bud mesenchyme using the *Prx1-Cre* transgene driver (Logan et al., 2002). Therefore, *Hand2*^{Δ/Δc} and *Prx1-Cre/+* (as WT control) mouse forelimb bud pairs were used for transcriptome analysis.

Comparative RNA-seq analysis identified 1021 DEGs (FC ≤1.2, FDR <0.05, Fig. 28B), of which 318 are down- and 703 up-regulated in *Hand2*-deficient forelimb buds (Fig. 28C). GO analysis revealed that the TOP10 GO terms for the DEGs (Fig. 28E) points to inhibitory functions in regulating chondrocyte differentiation, while TOP10 GO terms for down-

regulated genes (Fig. 28D) corroborate the HAND2 functions in mouse limb morphogenesis. The MGI mouse phenotype analysis is shown in Supplementary Figure 41.

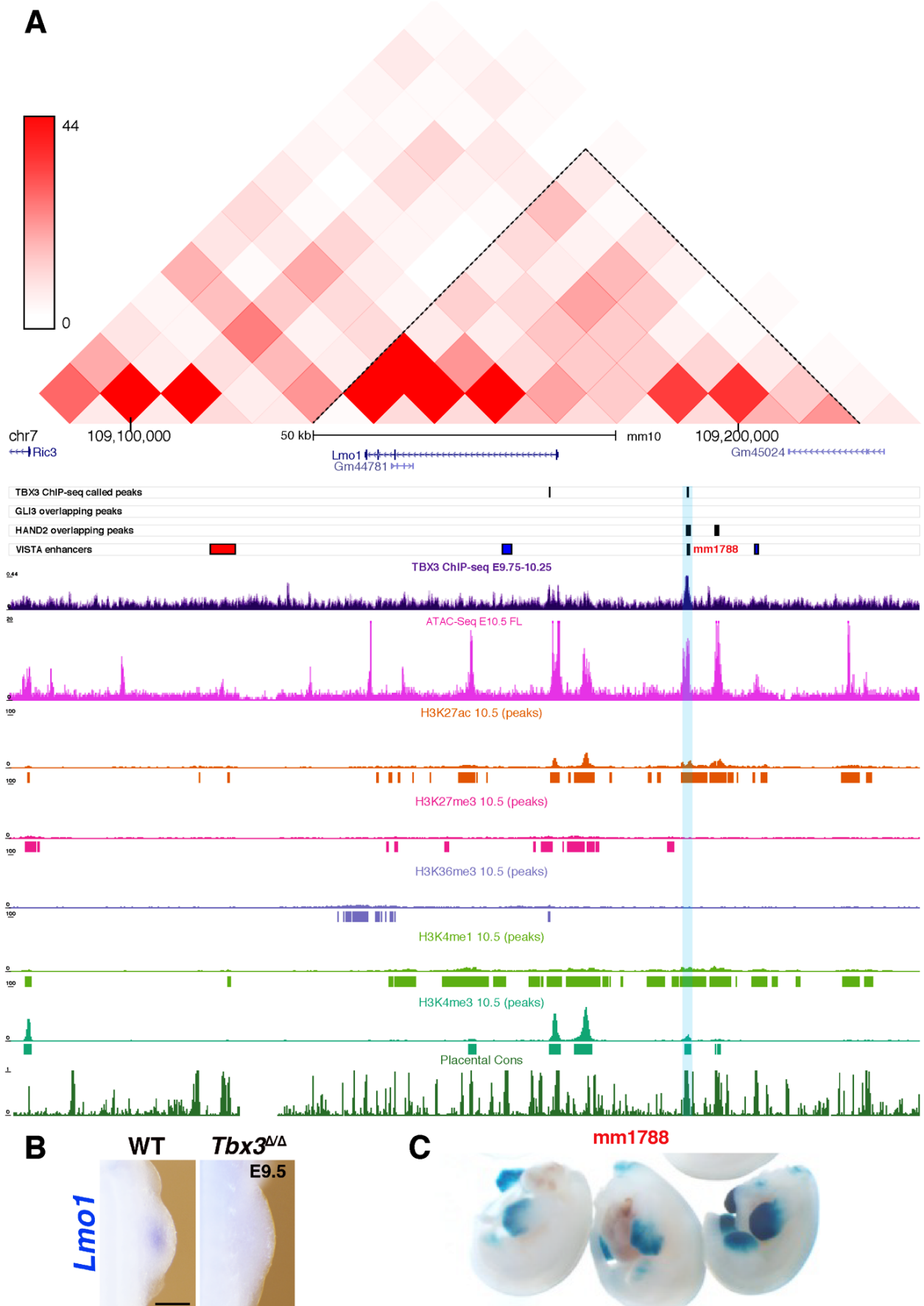


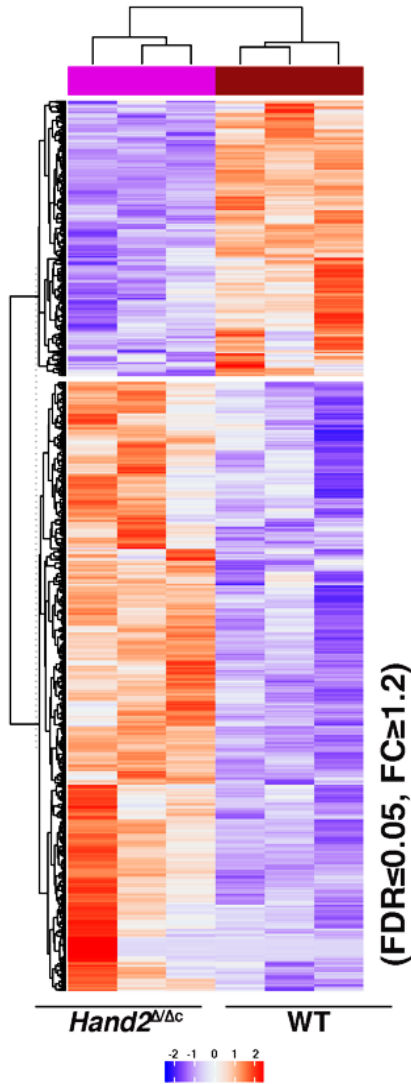
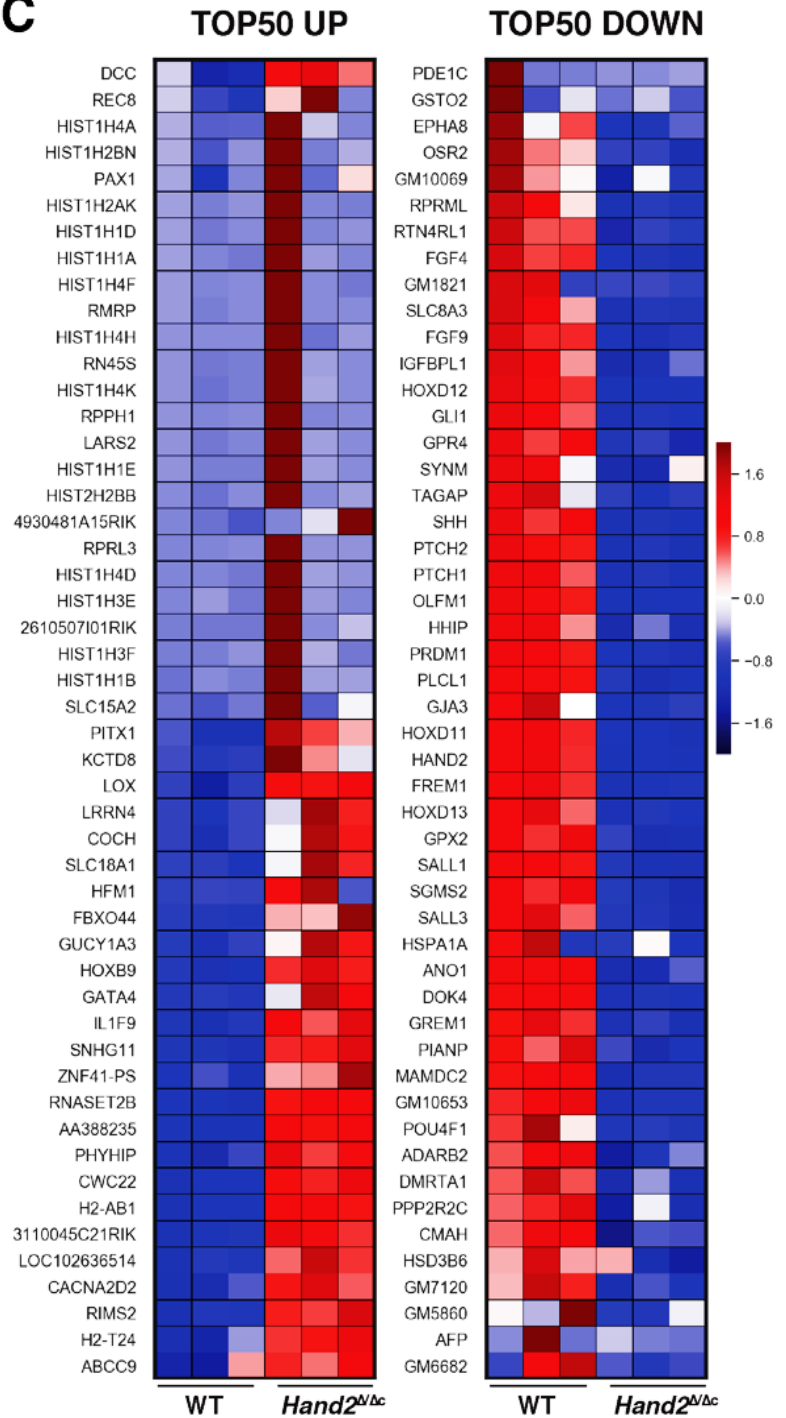
Figure 27. Analysis of the *Lmo1* cis-regulatory landscape.

(A) USCS genome browser view showing the datasets for *Lmo1* cis-regulatory landscape. The dashed line divides the Hi-C profile into the sub-TADs for *Lmo1*. Potential TBX3 controlled CRM is highlighted by blue boxes. (B) WISH for *Lmo1* in WT and *Tbx3*-deficient FLBs at E9.5 (n=3, scale bar 200 μ m). (C) The CRM mm1788 that is enriched TBX3 and HAND2

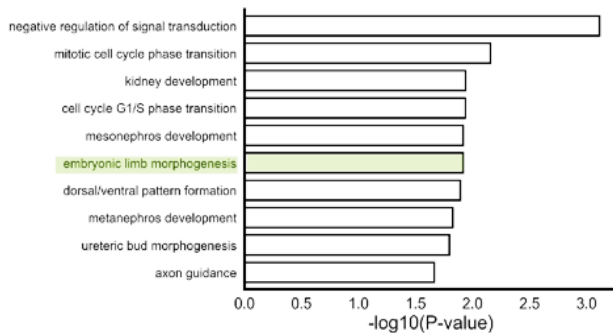
chromatin complexes is active in the distal limb bud mesenchyme (data provided by Marco Osterwalder).

A

RNA-seq E10.0-10.25
WT and *Hand2^{Δ/Δ}* FLBs

B**C****D**

TOP 10 GO Biological processes
Down-regulated genes E10.0-10.25 (n=318)

**E**

TOP 10 GO Biological processes
Up-regulated genes E10.0-10.25 (n=703)

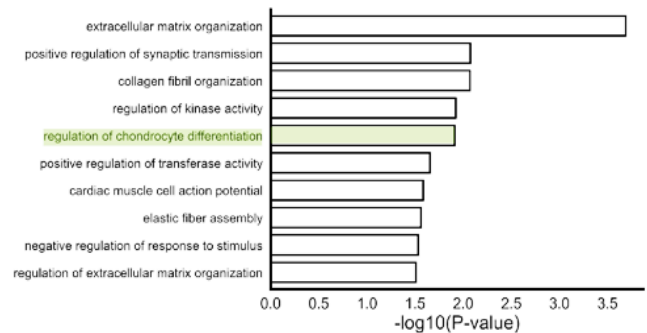


Figure 28. Transcriptome analysis of WT and *Hand2*-deficient mouse FLBs.

(A) *Hand2*^{Δ/Δc} and *Prx1Cre*/+ (as WT) mouse embryos FLBs at E10-10.25 were used for transcriptome analysis. (B) The heat map represents a clustering of the differently expressed genes (DEGs) that were identified by comparing transcriptomes of *Prx1Cre*/+ and *Hand2*^{Δ/Δc} mouse embryos FLBs at E10-10.25. For *Prx1Cre*/+ (n=4) and *Hand2*^{Δ/Δc} (n=3 biological replicates) 1021 DEGs were identified. DEGs were defined as genes whose expression is significantly changed (fold change ≤1.2) between WT and *Hand2*-deficient forelimb buds (p-value <0.05). (C) The heat map shows the top 50 DEGs identified. (D) GO enrichment analysis showing the top 10 terms for biological processes for the 318 down-regulated and (E) 703 up-regulated DEGs in mutant FLBs (FDR <0.05).

6.2.8 Identification of unique TBX3 and shared targets with HAND2 during the onset of limb bud development

One major aim is to identify and characterize the underlying TBX3-specific and shared with HAND2 GRNs that orchestrate early limb bud development upstream of activating SHH signaling. To identify the GRNs shared by HAND2 and its direct transcriptional target, TBX3 the HAND2 and TBX3 ChIP-seq datasets (Osterwalder et al., 2014) were intersected and 1711 genomic regions enriched in both types of chromatin complexes were identified (Fig. 29A). Furthermore, intersection of the RNA-seq datasets from *Tbx3*- and *Hand2*-deficient forelimb buds revealed 130 common DEGs (Fig. 29B). 36 DEGs were down- and 81 DEGs up-regulated, in both mutant limb buds, while 13 DEGs were changed in a discordant manner (Supplementary Table 1 and 2). Some DEGs with known spatio-temporal patterns in wild-type limb buds and/or associated with congenital limb malformations, whose transcription levels were altered in a similar or identical manner in both mutants were selected for WISH analysis (see the list in Fig. 29C).

To identify TBX3 specific target genes in early forelimb buds, the TBX3 direct targets dataset (140 genes) was overlapped with the shared 130 TBX3/HAND2 DEGs (Fig. 29D). This analysis revealed that 87 DEGs are unique TBX3 target genes (18 target genes are down- and 69 up-regulated, Supplementary Table 8 and 9). Target genes expressed in distinct patterns in wild-type limb buds were selected for further WISH analysis in mutant forelimb buds.

6.2.9 Spatiotemporal TBX3 and HAND2 controlled gene regulatory networks analysis in early forelimb buds

The bioinformatic analysis shown before identified TBX3 target genes that are also altered in *Hand2*-deficient forelimb buds. Next, a comparative WISH screen using WT and *Tbx3*-deficient, and *Prx1Cre*/+ (as WT) and *Hand2*^{Δ/Δc} mouse embryos at E9.75-10.25 was carried out. WISH screen included the shared genes selected on the basis of GO enrichment analysis

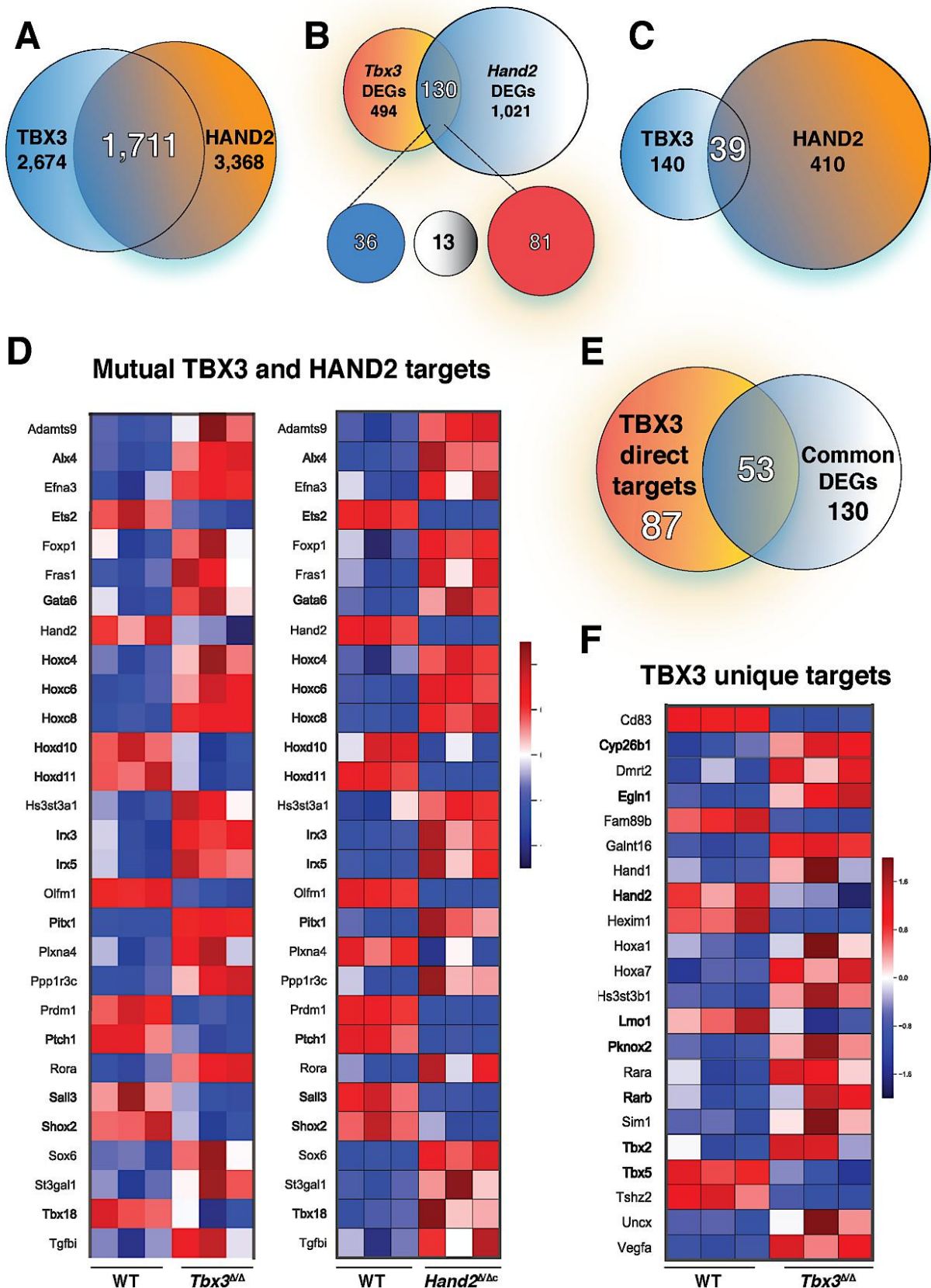


Figure 29. Identification of TBX3 specific and shared targets with HAND2 during the onset of limb bud development

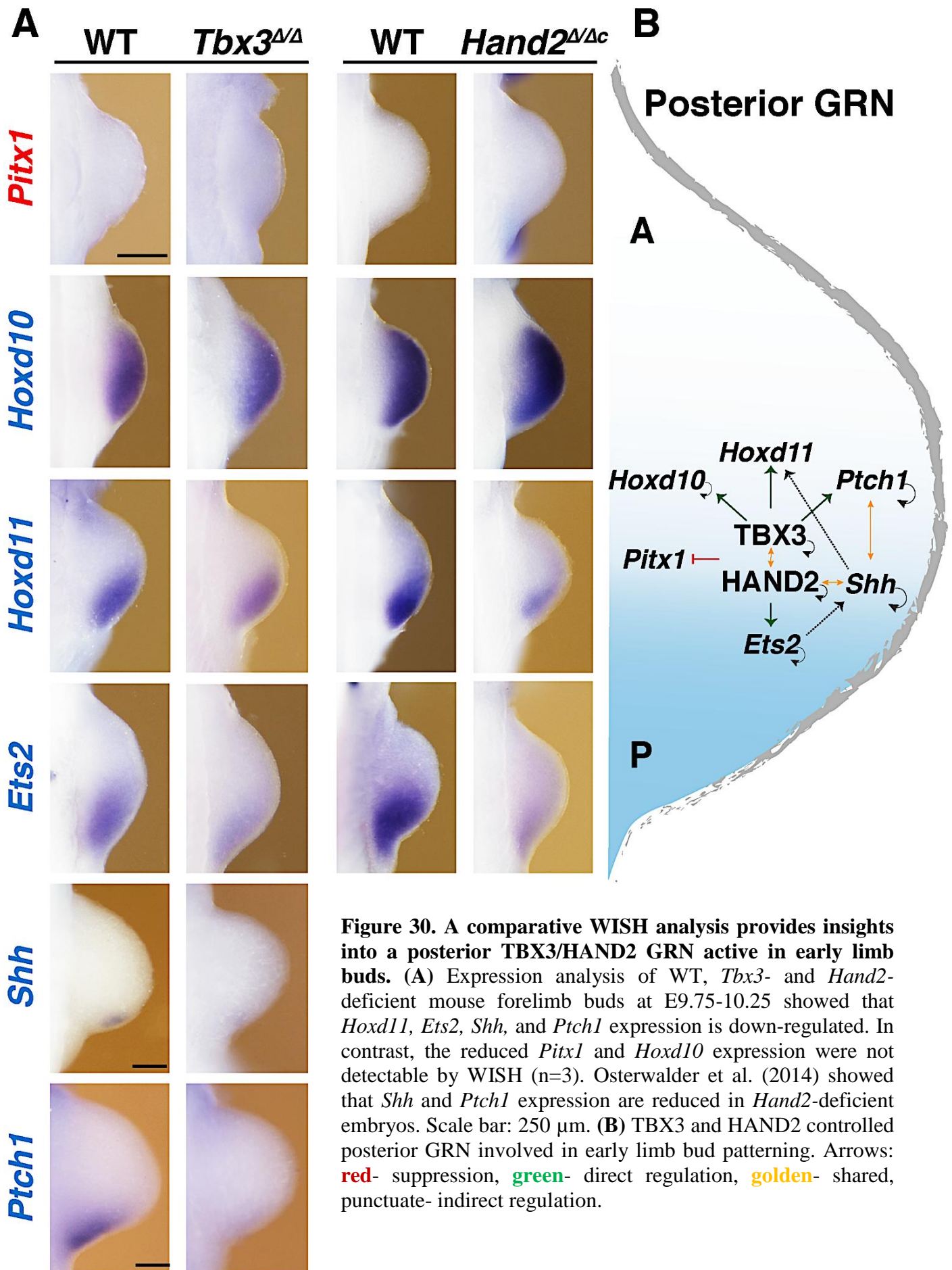
(A) The Venn diagram represents the strategy used to identify shared TBX3 and HAND2 targets. Genomic TBX3 and HAND2 binding sites revealed by ChIP-seq at E9.75-10.5 (2674 peaks) and E10.5 (3368 peaks) respectively were intersected, and 1711 shared targets were identified. (B) The Venn diagram represents strategy used to narrow down the candidate target list to only transcriptionally relevant ones by intersecting *Hand2^{Δ/Δc}* and *Prx1Cre/+* (as WT) forelimb bud transcriptome datasets (1021 DEGs) with the datasets of WT and *Tbx3-*

deficient FLBs (494 DEGs, FC \leq 1.2, FDR $<$ 0.05). 130 shared DEGs were identified, 36 DEGs were down-regulated and 81 up-regulated in both types of mutant forelimb buds; whereas 13 DEGs were discordant. **(C)** The Venn diagram represents the 39 shared direct transcriptional targets for TBX3 which are coregulated by HAND2. **(D)** The heat map represents previously identified shared target DEGs (Fig. 29C). Gene names in bold mark the genes selected for expression analysis by WISH. **(E)** The Venn diagram represents the strategy used to identify the 87 TBX3-specific target genes, 18 of which were down- and 69 up-regulated. **(F)** The heat map represents previously identified TBX3-specific target genes. Gene names in bold mark the genes selected for expression analysis by WISH.

for the up- or down-regulated TBX3 target genes. These genes were subdivided with respect to their spatiotemporal expression and /or functions in AP and PD axes patterning in early limb buds.

6.2.9.1 TBX3 and HAND2 functions AP limb bud axis patterning

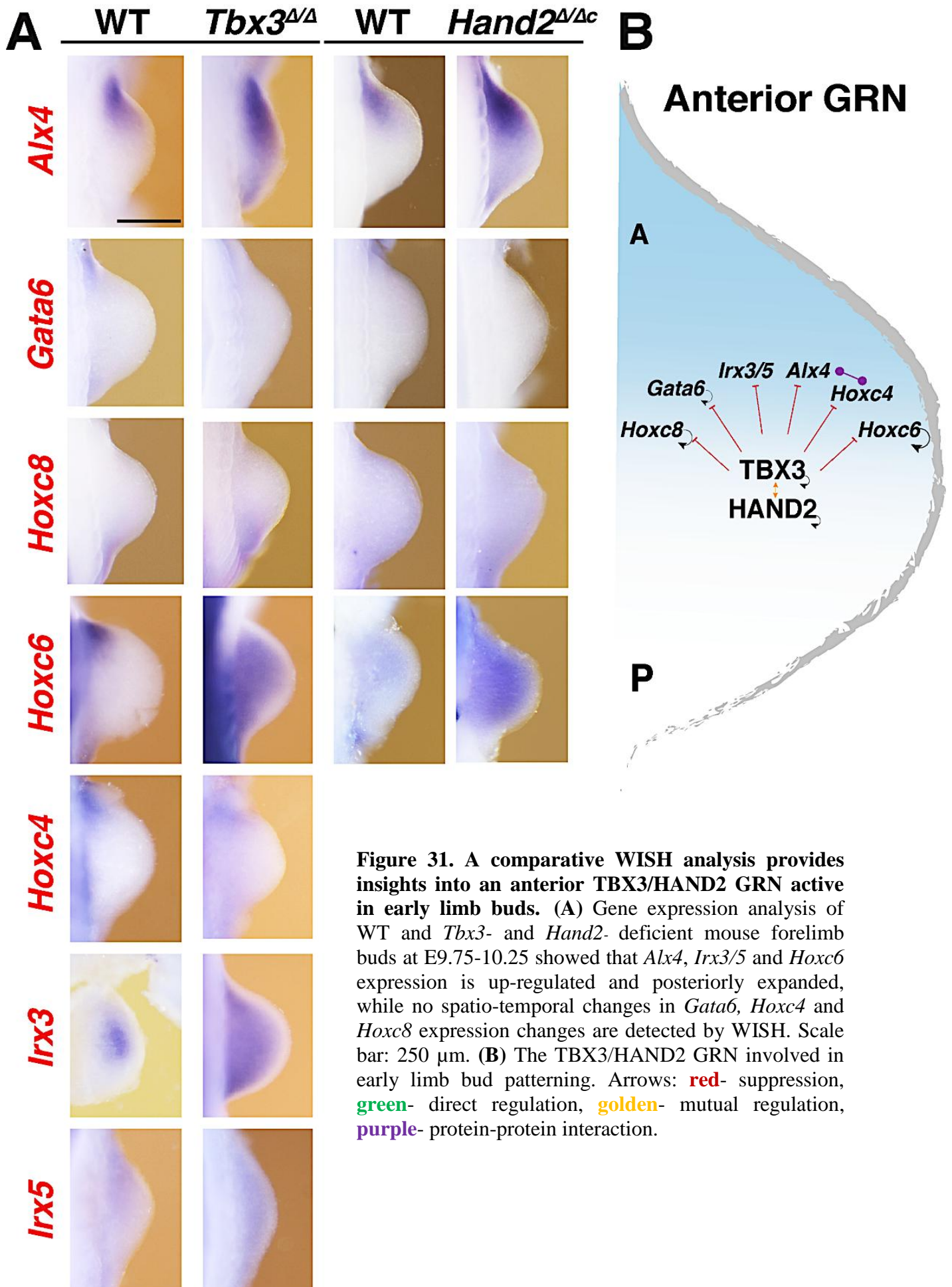
Not unexpectedly, the majority of down-regulated shared targets of TBX3 and HAND2 are found in the posterior limb bud mesenchyme (Fig. 15, Fig. 28, Fig. 30A). Indeed, it is well known that perturbing the expression of these posterior genes results in skeletal abnormalities. For example, in *Shh*-deficient forelimbs a zeugopod with unidentifiable AP polarity and only a single distal cartilage element forms (Chiang et al., 2001), while *Ptch1*-deficient forelimbs are predominantly oligodactylous (Butterfield et al., 2009). *Pitx1* is preferentially expressed in hindlimbs and mutant hind limbs length and width of all the long bones is reduced (Duboc & Logan, 2011a). In contrast, *Pitx1* overexpression during mouse limb bud development leads to limb defects affecting the proximal limb skeleton and muscular dystrophy (Pandey et al., 2012). However, *Pitx1* transcription level alterations were too low to be detected by WISH. Of particular relevance to my study, both *Hoxd11* (TBX3 target gene and HAND2 DEG) and *Hoxa11* (TBX3 and HAND2 DEG) are down-regulated in both *Tbx3*- and *Hand2*- deficient forelimb buds. In limb buds lacking both *Hoxa11* and *Hoxd11* an amorphous zeugopodal element rather than radius and ulna is formed (Boulet & Capecchi, 2004). *Hoxd10* expression changes were too low to be detected by WISH, but it is known that in addition to its primary function in stylopod development, *Hoxa9,10,11*^{-/-}/*Hoxd9,10,11*^{-/-} mutant mice exhibit a more severe ulna and radius reduction than *Hoxa11*^{-/-}/*Hoxd11*^{-/-} mice (Raines et al., 2015). *Ets2* is another interesting gene as its expression correlates with the forming radius and ulna in the developing chick zeugopod (Townsend et al., 2014). Collectively these *Hox* genes and *Ets2* function in AP patterning of the zeugopod. Downregulation of these posterior target genes, especially the *Hoxd10*, *Hoxd11* and *Ets2* transcription factors implies that TBX3 and HAND2 co-regulate posterior limb bud



morphogenesis in a positive manner and suppress the ectopic expression of the hindlimb specific TF *Pitx1* in forelimb buds (Fig. 30B).

In contrast, the majority of up-regulated shared TBX3 and HAND2 targets are expressed in the anterior mesenchyme of early limb buds. Several of them function in anterior skeleton development, such as *Irx3* and *Irx5*, which are TF participating in the early specification and determination of anterior limb identities (humerus/femur, radius/tibia, and digit 1, (Li et al., 2014). Furthermore, inactivation *Alx4* leads to perturbed AP patterning and polydactyly (Kuijper et al., 2005). ALX4 role in anterior skeleton patterning is even better highlighted in mouse limb buds lacking both *Gli3* and *Alx4*, which results in loss of the radius (the anterior element of the zeugopod) and severe stylopod malformations (Panman et al., 2005). In agreement with their transcriptional up-regulation, the expression of these three genes expands posteriorly in *Hand2*- and *Tbx3*- deficient forelimb buds (Figure 31A). Also, three *HoxC* cluster genes were identified as shared up-regulated targets of TBX3 and HAND2 target in early mouse forelimb buds. *Hoxc4* is expressed mostly in the mesenchyme of the presumptive forelimb area, whereas the *Hoxc6* and *Hoxc8* expression correlate with the interlimb flank mesenchyme. Interestingly, most mammalian forelimb buds are located in the most anterior part of the *Hoxc6* expression domain (Suemori & Noguchi, 2000). Despite this, mice lacking the entire *HoxC* cluster do not exhibit apparent defects in limb positioning (Suemori & Noguchi, 2000).

WISH of the spatio-temporal expression of *HoxC* cluster genes expression, revealed no significant changes in *Hoxc8* or *Hoxc4* expression, but *Hoxc6* expression was up-regulated and expanded posteriorly. Another TF whose transcript levels are up-regulated is GATA6, which is known to control cell identity. GATA6 expression in the anterior limb bud blocks hind limb polydactyly by repressing the ectopic expression of *Shh* and GATA6 overexpression in limb buds represses *Shh* expression, which results in hypomorphic limbs (Kozhemyakina et al., 2014). However, I did not detect significant ectopic expression of *Gata6* in early limb buds by WISH. This analysis shows that both in *Tbx3*- and *Hand2*-deficient forelimb buds, the expression of several up-regulated anterior genes such as *Alx4*, *Irx5*, *Irx3* and *Hoxc6* expands posteriorly. These implies that TBX3 and HAND2 both participate in suppressing ectopic anterior gene expression in the posterior limb bud mesenchyme and thereby negatively regulate anterior limb bud development (Fig. 31B).



6.2.9.2 TBX3 and HAND2 functions in patterning of the proximal-distal limb bud axis

Differences in TBX3 and HAND2 direct target genes spatio-temporal expression are apparent in the analysis of PD limb bud genes (Fig. 32A). In *Tbx3*-deficient FLBs, *Tbx18* expression is down-regulated, and *Jag1* expression is up-regulated, while the effects on their expression in *Hand2*-deficient forelimb buds is reverse, but no spatial changes in the low *Jag1* expression could be detected in early limb buds. GO analysis indicates that the majority of PD genes identified seems to function in bone morphogenesis, remodeling and chondrocyte

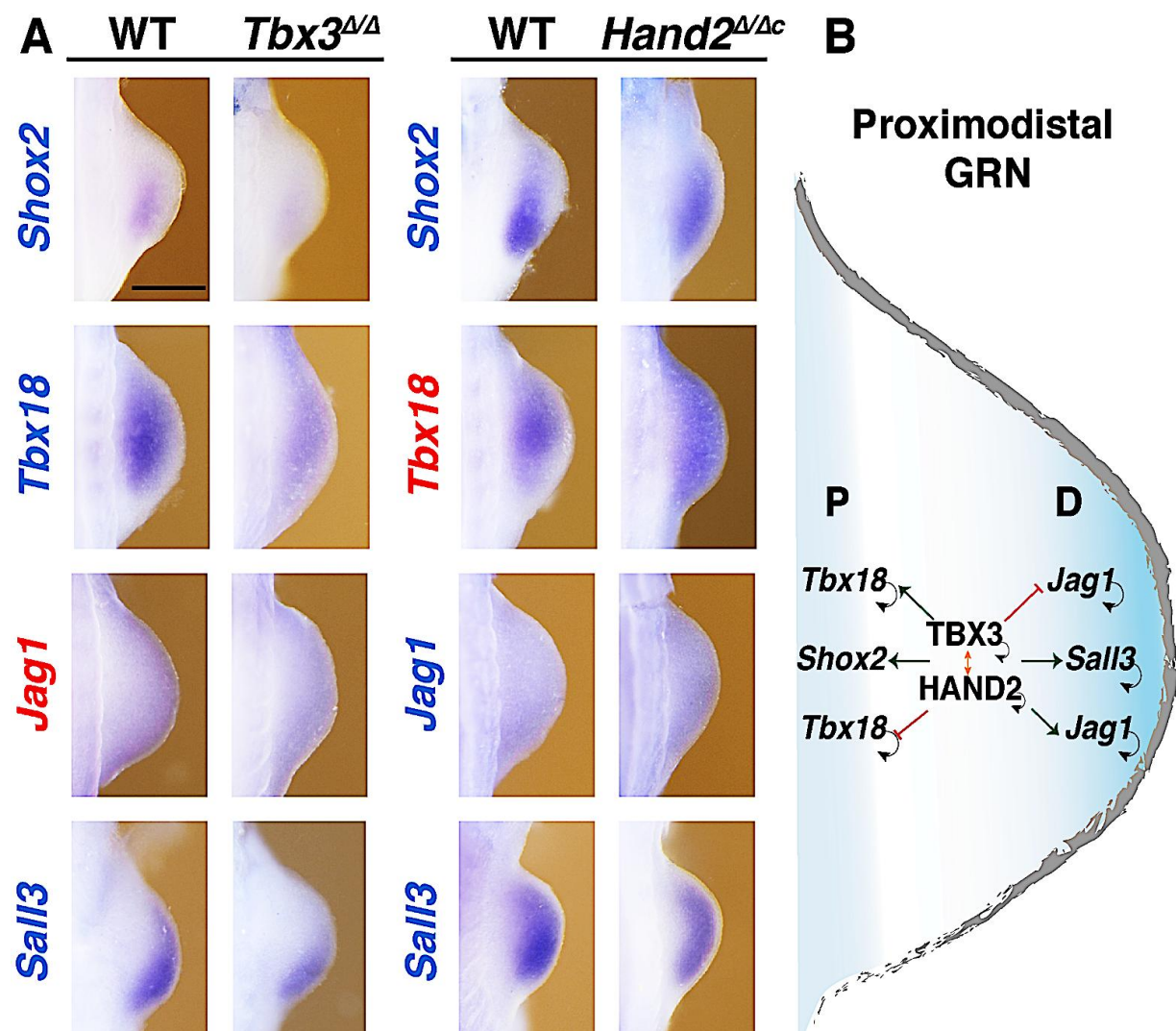


Figure 32. WISH analysis of proximal and distal genes participating in patterning early limb buds. (A) Spatiotemporal candidate gene expression analysis of WT and *Tbx3*- and *Hand2*- deficient mouse embryos at E9.75-10.25 revealed that *Shox2* and *Sall3* expression is indeed down-regulated, while *Tbx18* expression is down-regulated in *Tbx3*-deficient and is up-regulated in *Hand2*^{Δ/Δc} FLBs. *Jag1* expression changes were not detectable by WISH (n=3). Scale bar: 250 μm. (B) TBX3 and HAND2 controlled proximodistal GRN involved in early limb bud patterning. Arrows: red- suppression, green- direct regulation, golden- mutual regulation.

differentiation. A good example is the transcriptional repressor TBX18, which is co-expressed with *Sox9*, an early chondrogenic marker in mouse limb buds (Haraguchi et al., 2015). By E12.5, *Tbx18* protein is excluded from the *Sox9*-positive cartilage primordia, which is proposed to trigger mesenchymal cell differentiation into hypertrophic chondrocytes during the onset of endochondral ossification (Haraguchi et al., 2015). Therefore, it is particularly interesting that *Tbx18* is down-regulated in *Tbx3*-deficient FLBs. Another shared transcriptional repressor is *Shox2*, which participates in growth regulation of the stylopod by controlling chondrocyte maturation. *Shox2* expression is down-regulated in both *Hand2*- and *Tbx3*-deficient forelimb buds. *Jag1* is a gene expressed in the distal limb bud mesenchyme (Panman et al., 2006) and required for trabecular bone formation, inhibition of the periosteal expansion and regulation of bone metabolism (Youngstroma 2017). However, no spatial changes were detected by WISH, likely due to the low expression levels in early limb buds. Moreover *Sall3*, which functions in autopod development (Kawakami et al., 2009) is down-regulated in both *Tbx3*- and *Hand2*- deficient forelimb buds. Therefore, it is obvious TBX3 and HAND2 coregulate genes responsible for limb PD axis morphogenesis (Fig. 32B).

6.2.10 In *Tbx3*- deficient mouse embryos early limb skeletal patterning is disrupted

Sox9, and *Col2a1* expression patterns were studied to gain insights into potential functions of TBX3 in the patterning of the limb skeletal elements (Figure 33). These two genes serve as specific markers to study specification of the osteochondrogenic lineage and differentiation, respectively (Zhao et al., 1997). Analysis of forelimb buds at E12.5 revealed that the *Tbx3*-deficiency perturbs zeugopod and autopod patterning as both the *Sox9* and *Col2a1* distributions are severely altered.

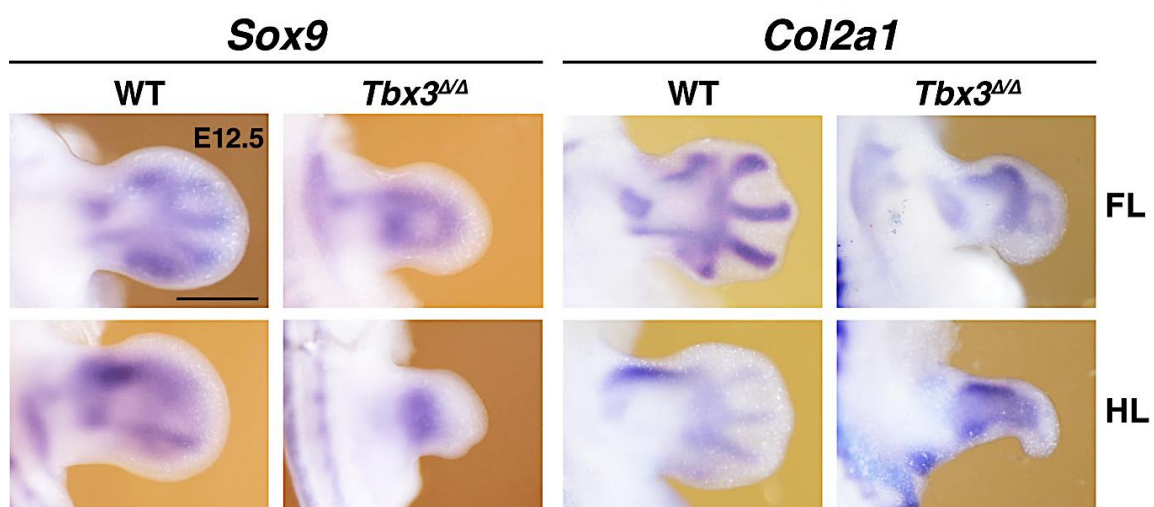


Figure 33. Analysis of chondrocytes specification and differentiation in *Tbx3*-deficient limb buds. Chondrocytes specification *Sox9* (n=1) and differentiation *Col2a1* (n=2) analysis in WT and *Tbx3*- deficient mouse embryos at E12.5 revealed the alterations in the expression of both genes, which layout the future limb skeletal elements. Mouse hindlimbs are more severely affected than forelimbs. Scale bar: 250 μ m.

6.2.11 TBX3-specific GRNs

Bioinformatics analysis identified 87 TBX3 specific transcriptional targets during the onset of limb bud development. Only genes expressed at levels sufficient for detection by WISH and distinct spatio-temporal expression were analyzed further (MGI database, Fig. 29F, Fig 34 and Fig. 35). One of these genes is *Tbx5*, which encodes an essential TF for forelimb bud development that is down-regulated in *Tbx3*-deficient forelimb buds (Fig. 34A, Rallis, Del Buono and Logan, 2005). Another TBX3 specific target gene is *Egln1*, which encodes the prolyl-hydroxylase-domain-containing protein-2 (PHD2) that functions as a positive regulator of osteoblast differentiation. In contrast, *PHD2* negatively regulates differentiation of chondrocytes and suppresses endochondral bone formation (Cheng et al., 2016). Interestingly, *Egln1* expression is down-regulated in mouse *Tbx3*-deficient forelimb buds (Fig. 34A). In addition, another TBX3-specific transcriptional target functioning in chondrocytes is *Itga4*, which is expressed in limb bud mesenchymal condensations (Ferguson et al., 2018). Transcriptome analysis indicated that *Itga4* transcript levels are down-regulated in *Tbx3*-deficient fore limb buds, but due to the diffuse expression at early stages no differences were detected by WISH. In contrast, the *Pknox2* transcriptional regulator of chondrocyte differentiation is up-regulated in *Tbx3*-deficient forelimb buds (Fig. 34A). This is interesting as overexpression of *Pknox2* in osteochondrogenic progenitors in the limb bud mesenchyme of transgenic mouse embryos leads to specific malformations of the stylopod deltoid crest and the zeugopod. This suggests that elevated *Pknox2* levels alter the mesenchymal condensations and the onset of chondrogenic differentiation in the zeugopod (Zhou et al., 2013).

The specific TBX3 targets that are up-regulated include genes of the retinoic acid (RA) signaling pathway. It has been postulated that RA acts as a morphogen to specify the proximal-distal identities of limb bud mesenchymal cells. Two TBX3-specific targets that are up-regulated in *Tbx3*-deficient limb buds are *Rarb* and *Cyp26a1*, expressed in the proximal and distal limb bud mesenchyme, respectively. *Rarb* expression is restricted to the proximal part of the limb bud mesenchyme with levels being highest in the most anterior and posterior mesenchyme. Its transcription senses RA activity as its expression is positively regulated by RA (Zhao et al., 2009). In contrast, *Cyp26b1* is expressed predominantly by the distal mesenchyme and non-AER ectoderm and functions to degrade RA in the distal limb bud mesenchyme (Yashiro et al., 2004). In *Tbx3*-deficient forelimb buds, the *Rarb* and *Cyp26a1* expression domains are expanded distally and proximally, respectively (Fig. 34A). This

shows that in *Tbx3*-deficient forelimb buds both of these mutually antagonistic RA pathway genes are up-regulated, which could play a role in the skeletal alterations the *Tbx3*-deficient limb buds (Fig. 34B).

Finally, the paralogous transcription factor *Tbx2*, which functions in autopod development (Farin et al., 2013) was identified as a TBX3-specific target gene. This target is particularly interesting as RNA-seq and WISH (Fig. 35) showed that its expression becomes variable in *Tbx3*-deficient forelimb buds at the early stages, such that it is either up- or down-regulated at E9.75-10.0.

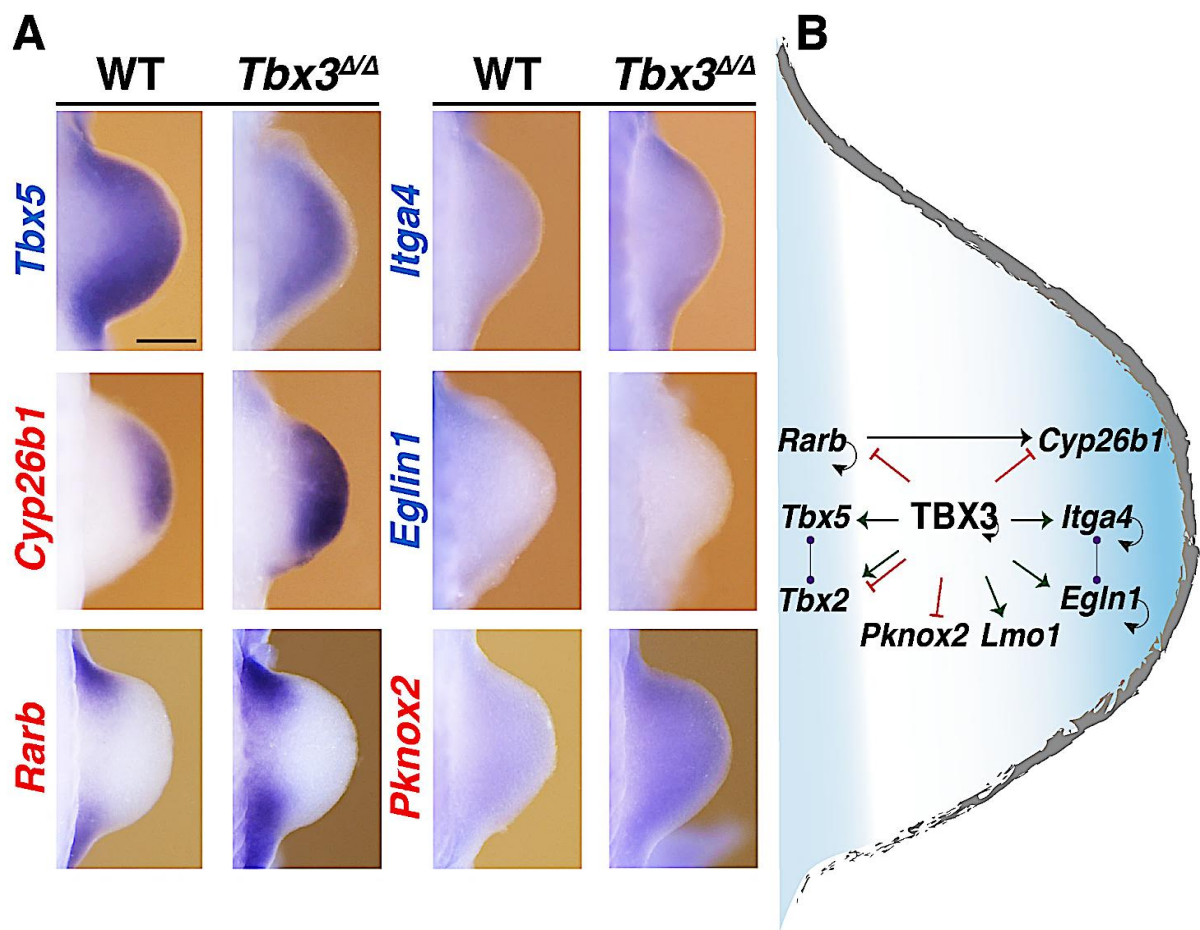


Figure 34. Analysis of the spatial expression of TBX3-specific transcriptional targets that function in early limb bud patterning. (A) Comparative spatial expression analysis of WT and *Tbx3*-deficient mouse forelimb buds at E9.75-10.25 shows that *Tbx5* and *Egln1* expression are reduced, whereas *Cyp26a1*, *Rarb*, and *Pknox2* expression are up-regulated in mutant forelimb buds. Scale bar: 250 μ m. (B) TBX3-specific GRN in early limb buds. Arrows: **red**- suppression, **green**- direct regulation, **golden**- mutual regulation, **purple**- protein-protein interaction.

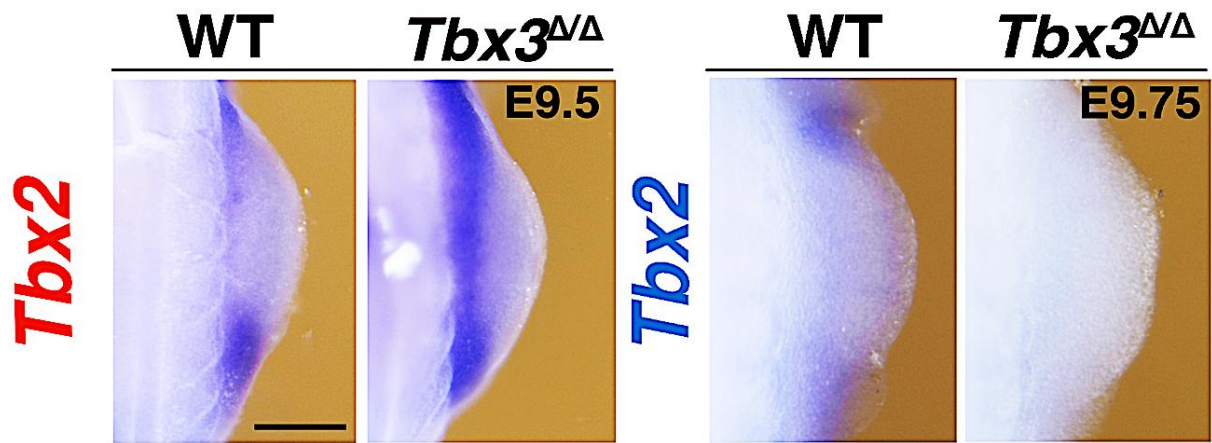


Figure 35. Variable alteration of *Tbx2* expression in *Tbx3*-deficient forelimb buds. WISH analysis confirms the observation by RNA-seq that *Tbx2* expression varies among early forelimb buds for different mutant embryos (n=3). Scale bar: 250 μ m.

7 Discussion

7.1 Identification of TBX3 target gene regulatory networks that function during early limb morphogenesis

The development of vertebrate limbs depends on complex spatial and temporal coordination of signaling pathways and TF interactions that direct proliferation and commitment of the limb bud mesenchymal progenitors that will give rise to the osteochondrogenic lineage of limb skeleton, tendons and connective tissue (Zuniga, 2015). Congenital limb abnormalities represent the broad spectrum of structural defects that arise due to perturbations of forelimb morphogenesis and affect approximately 1 per 500 live births (Ekblom et al., 2014; Giele et al., 2001). The wide range and abundance of abnormalities reflect the complexity and significance of the tightly regulated molecular mechanisms that govern vertebrate limb development (Barham & Clarke, 2008). Mutations altering TBX3 in humans are linked to the pleiotropic congenital Ulnar-mammary syndrome, which mainly perturbs forelimb zeugopod development (Bamshadl et al., 1997). Despite this, the molecular knowledge concerning the GRNs regulated by TBX3 and its direct transcriptional targets in the early limb buds was rather limited prior to my study. To identify the TBX3 target GRNs functioning during early limb bud morphogenesis, I generated the *Tbx3*^{3xF} mouse allele as a suitable tool to identify the cistrome of the endogenous TBX3 chromatin complexes as was previously done in the group for *Hand2*^{3xF} (Osterwalder et al. 2014) and *Smad4*^{3xF} (Gamart et al. unpublished). Intersection of the TBX3 ChIP-seq, RNA-seq and ATAC-seq datasets in combination with WISH revealed that TBX3 participates in the establishment AP polarity in forelimb buds. In particular, TBX3 positively regulates the expression of posterior genes in the forelimb mesenchyme, while it represses the expression of anterior genes in the posterior mesenchyme. Also, my study implicates TBX3 in the regulation of genes controlling PD limb bud outgrowth. Finally, my analysis revealed a role of TBX3 in the in controlling genes functioning retinoic acid pathway during mouse early limb bud development.

7.2 Unbiased genome-wide analysis of the TBX3 cistrome

The TBX3^{3xF} ChIP-seq analysis uncovered TBX3 cistrome during mouse forelimb bud development, which cistrome is 11,422 peaks. Out of these peaks, 3057 were associated to the regions of open chromatin and this analysis also showed that TBX3 chromatin complexes are predominantly enriched in proximity to TSS. Even if the majority of the previous studies

showed that promoter and distal enhancer interactions regulate the spatio-temporal expression of developmental genes, promoter-promoter interactions were also identified as relevant to transcriptional regulation (Joshi et al., 2015).

7.3 TBX3 transcriptional targets in early limb buds: direct and indirect interactions

Little is still known about the DNA binding interactions of T-box transcription factors. For example, it has been shown that the TBX2 subfamily members only bind to a T-box half-site instead of the entire palindromic sequence (Coll et al., 2002; Luna-Zurita et al., 2016). Thus so far, only such half-sites were identified in promoters of T-box target genes (Bruneau et al., 2001) and it was suggested that TBX3 might bind to DNA in promoter regions as a weak monomer/monomer complex (Coll et al., 2002). Indeed, the TATA box was among the motifs enriched by TBX3^{3xF} ChIP-seq analysis of early forelimb buds. Consensus TATA motifs are bound by TATA-binding protein (TBP) that are required for transcription from promoters mediated by all three nuclear RNA polymerases (rRNA (Pol I), mRNA and other RNAs (Pol II), and tRNA and other RNAs (Pol III)) (Cormack & Struhl, 1992). Together with specific activators and chromatin remodelers, TBP participate in regulating the temporal kinetics of transcription (Hasegawa & Struhl, 2019). Thus, TBX3 might directly influence transcription complex formation at promoters (Emechebe et al., 2016).

In addition, my TBX3^{3xF} ChIP-seq analysis revealed the complexity of the interactions of the endogenous TBX3 chromatin complexes with its target sequences. Rather unexpectedly, HOMER (Heinz et al., 2010) *de novo* and known motif analysis failed to identify T-box motifs, which could imply, that although TBX3 containing chromatin complexes are enriched at candidate CRMs, the TBX3 proteins binds DNA indirectly as part of a complex. However, previous studies had shown that TBX3 can directly bind to DNA as previous part of a structural complex with DNA (Coll et al., 2002). Subsequent analysis also showed that some TF associate with DNA through protein partners, while others exhibit both direct and indirect binding (Gordân et al., 2009). Thus, my analysis renders it likely that TBX3 belongs to the second group of TFs as *de novo* motif analysis identified a binding motif similar to the one of dorsal-interacting protein 3 (DIP3), which is a TF that binds to DNA in a sequence-specific manner to directly activate transcription (Bhaskar & Courey, 2002). Along these lines it was recently shown that T-box TFs that do not bind to the palindromic T-box site might be preferentially associated with other TFs, such as HOX factors (Jain et al., 2018). Interestingly, T-box TF interactions with different HOX TFs result in different transcriptional

outcomes and that in principle could take as many forms as there are protein family members, which might result in differential modulation of target gene expression (Jain et al. 2018). Therefore, it is highly likely that the TBX3 functions as either a transcriptional repressor or activator is defined by its interactions with different other transcriptional regulators in the TF complexes. Interestingly, the analysis of the TBX3^{3xF} enriched CRMs identified binding motifs for three pioneering TFs: PU.1 (Barozzi et al., 2014; Heinz et al., 2010), forkhead (Cirillo et al. 2002; Hsu et al. 2015) and SOX2 (Soufi et al., 2012). Pioneer TFs are key factors in gene regulation with critical roles in transitional developmental processes that include tissue development, organogenesis and differentiation. In particular, pioneering TFs control gene expression by binding to the nucleosomal DNA, and opening closed chromatin regions by, e.g., displacing nucleosomes such that non-pioneering transcription factors are able to bind. SOX2 is an essential TF that regulates development by controlling the pluripotency of embryonic stem cells (Rizzino & Wuebben, 2016) by facilitating active histone marks deposition (Soufi et al., 2012) and repressing lineage-specific gene expression (Avilion et al., 2003). Recently, SOX2 was implicated in functional interactions with long non-coding RNAs to facilitate proper regulation of gene expression (Holmes et al., 2020). Interestingly, it has been shown that TBX3 direct binding to RNA during splicing (Kumar et al., 2014). Thus, it seems that these TFs could participate in different aspects of RNA-dependent modulation of gene expression. Forkhead-type TFs control differentiation, maintenance of skeletal and heart muscle, skeletal and vascular tissues (Zhu, 2016). In addition, forkhead-type TFs bind to promoters to recruit RNA polymerase II (Pol II), often in a poised configuration for subsequent chromatin opening (Hsu et al. 2015).

7.4 TBX3 is an important epigenetic regulator of development

The TBX3^{3xF} ChIP-seq GO analysis points to chromatin and nucleosome organization, chromatin modification and chromatin assembly and disassembly. Recently, the evidence in support of T-box proteins controlling gene expression via epigenetic modifications is increasing. TBX3 participates in regulation of *de novo* methyltransferases (Dan et al., 2013; Russell et al., 2015) and SWI/SNF (SWItch/Sucrose Non-Fermentable) chromatin remodelers (Zhang et al., 2019). In addition, TBX3 forms complexes with histone deacetylases (HDACs) (Dong et al., 2018; Yarosh et al., 2008), and histone demethylases (Singh et al., 2009) which are upregulated in *Tbx3*-deficient forelimb buds. Such a diverse involvement implies the necessity of TBX3 for proper regulation during development. Also, even as TBX3 is

predominantly considered to function as a repressor, it is highly likely that the formed complexes composition could dictate TBX3 functionality to act either as a transcriptional repressor or transcriptional activator depending on the present co-factors.

Polycomb group proteins (PcG) are the histone demethylases that control gene expression by modulating histones methylation status (Grimaud et al., 2006; Swigut & Wysocka, 2007). There are two classes of PcG repressive complexes (PRC). PRC2 has histone methyltransferase activity and primarily methylates H3K27me3 to initiate silencing, while PRC1 is required for stabilizing this silencing and underlies cellular memory and marks histones by mono-ubiquitinates histone H2A on lysine 119 (H2AK119Ub1) (Chase & Cross, 2011; Yoo & Hennighausen, 2012). Both these complexes play a role in stem cell plasticity, induce differentiation during development, and help to maintain cellular identity (Creighton et al., 2010; Lee et al., 2006). Direct relevant to my study, TBX3 was shown to repress *Tbx2* under the control of the PRC2 complex in skeletal muscles (Oh et al., 2019).

Usually, the promoters of lineage regulatory genes in ES cells are enriched in bivalent chromatin histone marks (H3K4me3 and H3K27me3) (Bernstein et al., 2006; Pan et al., 2007; Zhou et al., 2007) that keeps lineage regulators poised for rapid activation. In response to differentiation, H3K27me3 is removed and the lineage-specific developmental genes are activated. The Jumonji domain-containing proteins, UTX (*Kdm6a*), and JMJD3 (*Kdm6b*) function as H3K27me3 demethylases (Agger et al., 2007; Sen et al., 2008). Another T-box family member, *Eomes* was shown to be maintained in a poised state (marked by H3K4me3 and H3K27me3) in ES cells. Under the influence of differentiation signals, TBX3 associates with the histone demethylase JMJD3 and activates the *Eomes* enhancer by promoting spatial reorganization to enable the necessary enhancer-promoter interactions. This spatial reorganization of the chromatin primes the cells to respond to signaling which induces differentiation towards endoderm (Russ et al., 2000).

JMJD3 and KDM6A H3K27m3 demethylases also interact with HOX genes and modulate H3K27me3 levels at their promoters (Agger et al., 2007; Swigut & Wysocka, 2007). My analysis of the promoter regions of the TBX3 target genes *Tbx2*, *Hand2* and *Tbx3* are marked by H3K27me3. It is possible that the H3K27me3 modifications at promoter regions of TBX3 target genes in forelimb buds could be modulated by TBX3 and JMJD3 family members as has been reported for *Hox* loci (Agger et al., 2007; Swigut & Wysocka, 2007). In fact, the TBX3^{3xF} ChIP-seq analysis identified TBX3-interacting regions in the JMJD3 (*Kdm6b*) (Swigut & Wysocka, 2007) locus, while *Kdm3a* that plays a role in transcriptional activation and *Kdm7a* (Wellmann et al., 2008), which specifically demethylates H3K9me2 and

H3K27me2 (Huang et al., 2010), are two genes upregulated in *Tbx3*-deficient forelimb buds. This implies that TBX3 might be responsible for regulating cellular plasticity and that observed limb development abnormalities caused by *Tbx3*-deficiency are caused by faster cell differentiation, e.g., as RNA-seq GO upregulated terms point to positive chondrocyte differentiation in *Tbx3*-deficient forelimb buds.

SWI/SNF is a subfamily of ATP-dependent chromatin remodeling complexes in eukaryotes required for regulation of gene expression (Stern et al., 1984). To date, little is known about a potential function of TBX3 in regulating and/or interacting with SWI/SNF chromatin remodelers. A recent study revealed that SWI/SNF family subunit DPF2 is critical for ESC differentiation and the meso-endoderm differentiation defects and maintenance of pluripotency in *Dpf2*-deficient ESC cells can be rescued by restoring *Tbx3* expression to normal levels (Zhang et al., 2019). TBX3^{3xF} ChIP-seq revealed TBX3 binding regions in the loci of SWI/SNF several family members including *Arid1a*, *Smarca4*, *Actl6a*, *Actl7b*, but no differential expression in *Tbx3*-deficient forelimb buds was detected by RNA-seq analysis.

TBX3 is the earliest T-box TF member expressed during embryogenesis and functions in maintenance and induction of pluripotency. It was shown that in *Tbx3*-deficient mouse ESCs pluripotency genes that are usually repressed by TBX3 are up-regulated, which includes *Dnmt3a* (Russell et al., 2015). There is two murine DNMT3 genes, *Dnmt3a* and *Dnmt3b*, which encode *de novo* methyltransferases essential for mammalian development (Okano et al., 1999). Furthermore, ES cells overexpressing TBX3 resemble the totipotent zygotes due to negative regulation of *de novo* methyltransferases at repeated sequences, which linked to telomere maintenance and ES cell self-renewal (Dan et al., 2013). My TBX3^{3xF} ChIP-seq identified *Dnmt3a* as a potential direct target gene, but no differences in expression between wild-type and *Tbx3*-deficient forelimb buds were identified. One possibility might be that TBX3 modulates *Dnmt3a* activity specifically during progenitor cell differentiation at later stages of limb bud outgrowth.

Previous studies revealed that TBX3 interacts with HDACs to repress downstream gene expression. It is thought that TBX3-mediate repression by recruiting HDACs to the T-box binding site in the promoter regions of genes (Yarosh et al., 2008b). In particular, HDACs and TBX3 complexes were implicated in downregulation of E-cadherin in hepato-cellular carcinomas to promote cell migration (Dong et al., 2018) or in repression of the tumor suppressor p14ARF in breast cancers (Dong et al., 2018; Yarosh et al., 2008). Interestingly, TBX3^{3xF} ChIP-seq identified TBX3 binding sites in HDAC2/4/7/9 genes regulatory loci, but again no aberrant gene expression was detected by RNA-seq. HDAC4 is expressed in

hypertrophic chondrocytes, regulates hypertrophic state and endochondral bone formation by interacting with and inhibiting the activity of *Runx2*. Interestingly, TBX3 is also functioning in negative regulation of the osteoblastogenesis by directly interfering within the *Runx2*-mediated activation of osteopontin promoter (Deepak et al., 2011). Thus, it is tempting to speculate that TBX3 and HDAC4 might form complexes to negatively regulate chondrocyte hypertrophy during more advanced limb bud stages.

7.5 TBX3 auto-regulation in the early mouse forelimb buds

The TBX3^{3xFLAG} ChIP-seq analysis identified several potential *cis*-regulatory elements in the ~100 kb regulatory landscape of *Tbx3* pointing to an auto-regulation of *Tbx3* expression. Previous studies already implied TBX3 autoregulatory positive-feedback loop in pathologies (Peres et al., 2014), and during embryonic development of mammary glands (Cho et al., 2006; Chu et al., 2004; Davenport et al., 2003) and limbs (Osterwalder et al., 2014). Two of the identified CRMs have been identified previously as limb bud enhancers (mm1117 and hs483, (Visel et al., 2007)). The first one, CRM mm1117 drives *lacZ* expression in the posterior forelimb buds in a pattern overlapping with the *Shh* expressing ZPA. Indeed, *Tbx3* functions in the posterior limb bud to establish and maintain the SHH signaling center (Davenport et al., 2003; Emechebe et al., 2016; Galli et al., 2010; Osterwalder et al., 2014). Thus, TBX3 chromatin complexes appear to positively regulate the mm1177 enhancer in the posterior limb bud mesenchyme. However, genetic inactivation of mm1177 enhancer does not cause limb abnormalities, which revealed the underlying *cis*-regulatory redundancy (Osterwalder et al., 2018). Another candidate CRM (hs483) enriched in TBX3 chromatin complexes is located close to the *Tbx3* promoter. It was previously shown that the orthologous human enhancer is active in distal anterior mesenchyme of both mouse embryonic fore- and hindlimbs buds. This enhancer is also conserved in fishes, but probing this enhancer in zebrafish failed to drive pectoral fin expression (Booker, Murphy, and Ahituv 2013). The anterior *Tbx3* expression depends on the balance between positive inputs by anterior BMP signal and repression by SHH signaling from the posterior limb bud mesenchyme (Tümpel et al. 2002). As *Tbx3* is predominantly expressed in the posterior mesenchyme and positively controlled by SHH during early limb development, it could be during the initial phase the CRM driving the anterior *Tbx3* expression located in sub-TAD2 is repressed by TBX3 chromatin complexes while the posterior TBX3 expression is enhanced by SHH signaling in tandem with TBX3. This self-regulatory mechanism could rely on the

interplay of repression by TBX3 and activating co-factors like HAND2 that interact with distinct CRMs in the *Tbx3* locus in a combinatorial fashion. In particular, TBX3 and co-activating chromatin complexes binding to CRMs in sub-TAD1 could positively regulate the posterior *Tbx3* expression, while TBX3 interactions with CRMs in sub-TAD2 could repress its expression at early stages.

7.6 TBX3 regulates *Tbx2* in the early mouse forelimb buds

The TBX3^{3xFLAG} ChIP-seq analysis identified three candidate CRMs in the *Tbx2* cis-regulatory landscape. Previous studies have already revealed that TBX3 regulates the *Tbx2* locus (Li et al., 2014; Oh et al., 2019). *In vitro* and *in vivo* assays revealed that TBX3 binds and regulates the *Tbx2* promoter in response to TGF- β 1 in cancer cells, which causes downregulation of the pro-proliferative factor TBX2 (Li et al., 2014; Peres & Prince, 2013). The downregulation of *Tbx2* expression decreases cell proliferation by inducing G1 cell cycle arrest and the cell cycle stalling is likely a consequence of increased *p21* levels (Li et al., 2014).

My ChIP-seq analysis identified an additional candidate CRM located at -32.4kb in the *Tbx2* locus (mm1210, Osterwalder, unpublished), which is active in forelimb buds and heart at E9.5, while at E10.5, activity is also detectable in optic cups, pharyngeal arches, and hypothalamus. Therefore, the activity of this novel CRM resembles the endogenous *Tbx2* expression. In particular, TBX2 is required for normal retinal development, ventral optic vesicle invagination and optic cup formation as it modulates tissue proliferation (Behesti et al., 2009). During heart development, *Tbx2* is expressed in the heart outflow tract, inner curvature, atrioventricular canal, and inflow tract at E9.5 and TBX2 is required in the corresponding myocardial zone to repress differentiation genes. *Tbx2* is expressed by the pharyngeal arch mesenchyme that contains neural crest cells migrating and giving rise to the outflow tract septum (Harrelson et al., 2004). It is known that zebrafish *tbx2a* is required for heart remodeling and differential cell proliferation (Ribeiro et al., 2007). Similarly, TBX2 controls limb bud mesenchymal proliferation by regulating SHH/GREM1/AER-FGF and BMP/TBX2/GREM1 signaling loops (Farin et al., 2013). In fact, overexpression of either *Tbx2* or *Tbx3* induces posterior homeotic transformation of digit III to digit IV and digit II to digit III, respectively (Suzuki et al., 2004b). Furthermore, a recent study shows that TBX3 indeed represses *Tbx2* under the control of the Polycomb repressive complex 2 (PRC2) in skeletal muscles (Oh et al., 2019). Finally, TBX2 is known to play a role in patterning and

development of the hypothalamus in chicken embryos by downregulating *Shh* expression via impacting the BMP-TBX2 pathway (Manning et al., 2006). In humans, aberrant TBX2 causes mild mental and prenatal growth retardation in conjunction with complex heart septation defects. In addition, mild skeletal anomalies with hypoplasia of the distal digit phalanges were also observed (Radio et al., 2010). My WISH analysis of *Tbx2* expression in *Tbx3*-deficient limbs shows its upregulation, which correlates with the evidence that the candidate CRM located -32.4kb in the *Tbx2* genomic landscape is rather repressed than activated by the interactions with TBX3 chromatin complexes.

7.7 TBX3 functions in establishing limb bud mesenchymal axis polarity

Previous studies showed that several TF like HOXA11, HOXA13 (Yamamoto et al. 2019), and HAND2 (Osterwalder et al., 2014) directly interact with CRMs in the *Gli3* locus to regulate its expression, while little was known about TBX3-mediated *Gli3* regulation (Mosca et al., 2009). My TBX3^{3xFLAG} ChIP-seq analysis of mouse forelimb buds identified three candidate CRMs in the ~ 500kb *Gli3* cis-regulatory landscape. TBX3 chromatin complexes interact with two already validated CRMs activity in the anterior limb bud mesenchyme (mm1179, hs1586 (Visel et al., 2007; Osterwalder et al., 2018)). Both of these CRMs drive *lacZ* expression in a spatial pattern reminiscent of the endogenous *Gli3* distribution, with *lacZ* being excluded from the posterior-most forelimb bud mesenchyme (Galli et al., 2010; Osterwalder et al., 2014). As *Tbx3* is not expressed in the anterior limb bud mesenchyme during the early stage analyzed, it is likely that these two CRM are repressed by TBX3 chromatin complexes. Furthermore, the analysis of *Tbx3*-deficient forelimb buds points to a repressive effect of TBX3, as *Gli3* expression is posteriorly expanded (Galli et al., 2010; Osterwalder et al., 2014). The functional importance of the CRMs controlling *Gli3* expression was assessed by the loss-of-function analysis by Osterwalder et al. (2018). While the inactivation of individual CRM enhancers did not alter limb morphogenesis, the combined inactivation results in duplication of the most anterior digit in forelimbs. This revealed that multiple enhancers ensures *Gli3* expression and limb development with phenotypic robustness (Osterwalder et al., 2018).

Previous mouse genetic analysis pointed to possible cross-regulation between TBX3 and HAND2 as in *Tbx3*-deficiency, the posterior expression of *Hand2* is downregulated while the reverse is true in *Hand2*-deficient forelimb buds (Davenport et al., 2003; Emechebe et al., 2016a; Osterwalder et al., 2014). Indeed, my TBX3^{3xFLAG} ChIP-seq analysis identified three

candidate CRMs in the *Hand2* cis-regulatory landscape. One of these, CRM (mm1832) is located at -604.4kb upstream and corresponds to a brain-specific enhancer not active in limb buds (Osterwalder, unpublished). It is known that *Hand2* controls genes regulating noradrenergic differentiation during development and participates in regulation of genes controlling neurotransmission in adult sympathetic neurons (Stanzel et al., 2016). Indeed, *Tbx3* is expressed during embryonic brain development, where it is required to repress *Shh* in the ventral diencephalon, thereby establishing an *Shh*-negative domain to permit formation of the infundibulum (Trowe et al., 2012). In the diencephalon, nuclear TBX3 proteins colocalize with heterochromatin foci (Pontecorvi et al., 2008). Thus, as TBX3 primary functions as a transcriptional repressor and represses *Shh* in the diencephalon, one can hypothesize that the interactions of TBX3 chromatin complexes with CRM mm18329 are of repressive nature. The second CRM located -357.4 kb upstream and has low or no limb bud activity as only very faint *lacZ* expression was detected in the proximal limb bud mesenchyme.

7.8 TBX3 and HAND2 chromatin complexes regulate early limb bud axis polarization in a context dependent manner

Previously, Osterwalder et al. 2014 revealed that *Tbx3* is a direct transcriptional target of HAND2 that interacts with HAND2 to define the posterior GLI3R expression boundary in the limb bud mesenchyme. In particular, *Tbx3* appears to act as a repressor required to establish a sharp boundary between the anterior *Gli3* and posterior *Hand2* and *Tbx3* expression domains.

Interestingly, the analysis identified the bHLH motif (common for E-box proteins such as HAND2) among the enriched TBX3 binding motifs. Furthermore, extensive comparative analysis of the TBX3^{3xF} and HAND2^{3xF} cisromes and in particular shared targets among limb bud AP patterning genes provided evidence for their interactions with the same CRMs. Together this analysis suggests that HAND2 and TBX3 might form heterodimers and interact to regulate specification of the posterior limb bud mesenchyme. With respect to the regulation of *Gli3* expression in early limb buds, my analysis revealed that TBX3 and HAND2 chromatin complexes interact with two CRMs located -120 kb up-stream and +85.5 kb downstream of the *Gli3* promoter, which could participate in *Gli3* repression in the posterior limb bud mesenchyme. In addition, a shared TBX3 and HAND2 CRM was identified in the *Tbx3* cis-regulatory landscape. This CRM (mm1117) enhancer is active in active in *Shh*-expressing ZPA in the posterior mesenchyme of forelimb buds at early stages.

This indicates that TBX3/HAND2 chromatin complexes positively regulate this CRM (mm1177) enhancer in the posterior limb bud mesenchyme as both TF are required to establish and maintain *Shh* expression by the ZPA (Davenport et al. 2003; Emechebe et al. 2016; Galli et al. 2010; Osterwalder et al. 2014; Charité et al., 2000; Yelon et al., 2000). My analysis also identified a CRM in the *Tbx2* cis-regulatory landscape, which is active in the developing brain, heart and limb buds. Furthermore, a CRM enriched in both TBX3 and HAND2 chromatin complexes was identified in the *Lmo1* cis-regulatory landscape and this CRM (mm1788) is active in the distal limb bud mesenchyme (Osterwalder, unpublished). In fact, its spatial activity resembles the endogenous *Tbx3* expression pattern in the interdigit mesenchyme at E12.5 (R. D. Ballim et al., 2012). It was proposed that at late stages TBX3, together with other apoptosis inducing factors such as BMPs and MMP11, participates in RA-induced apoptosis and remodeling of the interdigital mesenchyme during digit separation (R. D. Ballim et al., 2012). In addition it has been shown that both *Tbx3* and *Tbx2* regulate of interdigital BMP signaling during digit formation in chicken leg buds to specify the posterior identities (Suzuki et al., 2004b). Together, this analysis indicates that TBX3 predominantly functions as a repressor, but by forming heterodimers with HAND2 it might be able to either enhance or repress transcription depending possibly on other co-factors present in the transcription enhancing or repressing complexes. However, only a limited number of the genes were analyzed in-depth and a more thorough genome-wide manner analysis could provide additional insights.

7.9 TBX3 and HAND2 controlled GRNs during early mouse forelimb bud development

Therefore, I took an advantage of *Tbx3* and *Hand2*-deficient mouse forelimb buds to get insights into shared and unique differences in gene expression. RNA-sequencing allowed me to identify DEGs in an unbiased, genome-wide manner (Han et al. 2015, Wang et al. 2014, Wang, Gerstein, and Snyder 2009). Indeed, a quarter of *Tbx3* and *Hand2* DEGs overlapped and showed correlating expression profiles. This is not surprising, as genes co-regulated by shared TFs and functioning in the same biological pathways usually display similar or identical expression profiles (Ideker et al., 2001). In addition, about 10% of shared DEGs showed discordant expression profiles. In particular, coordinated AP and PD limb axes establishment, patterning and outgrowth depend on *Tbx3* and *Hand2*. For example, *Irx3/5* and *Alx4* are direct transcriptional targets of TBX3 and HAND2 that are part of the GRNs that

function in establishment of the anterior polarity. In particular, *Irx3/5* upregulate *Gli3* expression in the anterior mesenchyme (Li et al., 2014), while both *Gli3* and *Alx4* function in suppressing *Shh* expression from the anterior mesenchyme (Kuijper et al., 2005; te Welscher et al., 2002). These interactions control establishment of anterior mesenchymal identities during the onset of limb bud outgrowth. In *Tbx3*- and *Hand2*-deficient forelimb buds, the expression of these anterior genes expands posteriorly (Galli et al. 2010; Osterwalder et al. 2014), which disrupts the nascent AP polarity that subsequently leads to skeletal abnormalities (Kuijper et al., 2005; te Welscher et al., 2002). In addition, TBX3 and HAND2 target genes expressed in the posterior limb bud mesenchyme are also essential for proper establishment and patterning of AP limb bud axis and subsequent limb development. Several genes that control development of posterior limb elements are downregulated, but not completely lost in *Tbx3*- and *Hand2*-deficient forelimb buds (some findings were previously published by Galli et al. 2010; Osterwalder et al. 2014). In particular, *Shh* and its receptor *Ptch1* are required for specification of posterior limb skeleton elements like ulna and digits (Chiang et al. 2001; Harfe et al. 2004; Butterfield et al., 2009). The HAND2 target TF *Ets2* up-regulates *Shh* expression and is expressed by the primordia of radius and ulna in the developing chick zeugopod (Lettice et al. 2012, Townsend et al., 2014). The *Hoxd11* and *Hoxa11* TFs are also identified as direct targets and are required for zeugopod development (Boulet & Capecchi, 2004). Overall, my transcriptome analysis results revealed that in *Tbx3*- and *Hand2*-deficient forelimb buds the expression of posterior gene is decreased while the expression of anterior genes is upregulated and expanded into the posterior mesenchyme. Together, these alterations perturb the normal establishment of AP limb bud axes polarity. The observed shortening of the zeugopod in the *Tbx3*-deficient forelimbs can be explained by the underlying changes in the expression of genes controlling PD limb axis development. In addition, the TBX3 cistrome and transcriptome analysis revealed target genes that function in chondrocyte differentiation and/or skeletal development. One direct TBX3 target gene is *Egln1*, which negatively regulates chondrocytes differentiation and suppresses endochondral bone formation (Cheng et al., 2016). *Egln1* is downregulated in *Tbx3*-deficient mouse forelimb buds, while the TBX3 direct transcriptional target *Pknox2* is found upregulated. Previous studies showed that overexpression of *Pknox2* in osteochondrogenic progenitors in the limb bud mesenchyme of transgenic mice results in malformations of the zeugopodal skeletal elements, while the autopod and stylopod skeleton were not affected (Zhou et al., 2013). This implies that TBX3 might have an essential role in patterning of mesenchymal condensations that gives rise to zeugopod elements. In addition, the expression of *Cyp26a1*

and *Rarb*, which function in the retinoic signaling pathway, are upregulated and expanded in the mesenchyme of *Tbx3*-deficient forelimb buds (see below).

7.10 Evidence for altered retinoic acid pathway activity in *Tbx3*-deficient forelimb buds

Balanced levels of retinoic acid signaling are critical to normal embryonic development (Morriss-Kay & Wardt, 1999). If mouse embryos are exposed to excess of RA during blastocyst and pre-gastrulation stages (E4.5–5.5), the caudal region of the developing embryos is severely altered, which results in symmetrical hindlimb buds and duplication of lower body axis elements while forelimbs are rarely affected (Liao & Collins, 2008; Niederreither et al., 1996). Thus, even long before limb bud formation, RA excess induces long-lasting gene expression changes that have dramatic effects during later development. Exposure of embryos to excess RA just prior to or during limb bud development results in severe teratogenic effect on limb skeletal development. The teratogenic effects caused by excess RA are also observed in human embryos (Sekiya et al., 2001; Weston et al., 2002, 2000). The teratogenic effects of RA in mammalian embryos result in fusion, shortening or loss of long bones and loss of digits (Hunt, 1996; Kochhar, 1973). The precise level and severity of the phenotypic alterations can be correlated with developmental stage specific effects (Lee et al., 2005). Experimental but still controversial evidence suggests high levels of RA are required during induction of limb bud development and *Shh* expression; while distal limb bud outgrowth requires clearance of RA from the mesenchyme. Finally, RA signaling is required again for interdigital cell death during final shaping of digits (Maden, 2020). Previous studies of chicken and mouse limb bud development highlighted the role of RA in coordinated AP and PD limb bud axes outgrowth. It was proposed that AP and PD limb bud axes development are coordinately controlled SHH-mediated clearance of RA via an AER-FGF-CYP26B1 loop that enables PD limb bud axis outgrowth (Probst et al., 2011).

The levels of RA in the anterior and posterior halves of the limb buds are the same (Leonard et al., 1995), but the existence of an RA gradient was also implicated in PD axis patterning. Transplantation experiments of tissue adjacent to a RA source to different PD segments and transplantation RA-treated limb bud tissue into a quail limb bud, substantiated the potential involvement of RA in PD outgrowth (Tamura et al., 1997). *Meis1/2* are RA responsive genes involved in proximalization of the limb bud mesenchyme by a proximal high, distal low

Meis2 levels (N. Mercader et al., 2000; Oulad-Abdelghani et al., 1997). My analysis shows that TBX3 interacts with CRMs in the *Meis2* locus, but its expression is not altered in *Tbx3*-deficient limb buds at early stages (Supplementary Fig.48). RA is eliminated from the distal proliferating limb bud mesenchyme by the RA catabolizing enzyme CYP26b1 (Mic et al., 2004). In addition to promoting limb bud outgrowth by preventing apoptosis of the mesenchymal progenitors, CYP26b1 promotes chondrocyte maturation during progression of limb bud development. Genetic inactivation of *Cyp26b1* leads to excess RA in the distal limb bud mesenchyme, which results in loss of digits and fusion of long bones (Yashiro et al., 2004). My analysis shows that in *Tbx3*-deficient forelimb buds *Cyp26b1* expression is upregulated and expanded proximally, which will likely increase RA clearance and disrupt the postulated graded distribution of RA (N. Mercader et al., 2000; Oulad-Abdelghani et al., 1997), which could explain the shortening of the zeugopod. Together, these results indicate the alterations of limb bud axes development observed in *Tbx3*-deficient forelimb buds are caused by both altering SHH pathway activity and RA clearance.

Interestingly, the forelimb phenotypes of *Tbx3*-deficient mice resemble aspects of the human UMS forelimb phenotype; but a few striking differences are observed. In humans, the *Tbx3* haploinsufficiency most often leads to severe forelimb abnormalities, while no phenotypes are observed in *Tbx3* heterozygous mice and *Tbx3*-deficient mice exhibit more severe hindlimb than forelimb phenotypes (Davenport et al., 2003; Frank et al., 2013). Furthermore, *Tbx3* heterozygous mice exhibit only minor genital abnormalities, while humans display imperforate hymen and micropenis (Bamshad et al., 1999; Bamshad et al., 1997). The interspecies disparity could arise from different TBX3 dose sensitivity as the same tissues may require different quantities of the functional protein for proper morphogenesis in humans and mice. It is known that different tissue-specific co-factors participate in the regulation of TBX3 functions (Klopocki et al., 2006). Moreover, human and mouse *Tbx3* might have different species-specific functions in limb growth and patterning (Davenport et al., 2003).

The discrepancy in severity between the mouse fore- and hindlimb phenotypes is harder to explain. In particular, *Tbx3*^{Δ/Δ} hindlimbs closely resemble the limb phenotype seen in *Shh*^{Δ/Δ} and *Hand2*^{Δ/Δ} mice (Chiang et al. 2001; Kraus, Haenig, and Kispert 2001; Lewis et al. 2001, Galli et al., 2010), which implies that *Tbx3* functions either upstream or within the SHH pathway in hindlimb buds, which phenocopies the *Shh* loss-of-function phenotype (Davenport et al., 2003). The difference between fore- and hindlimb buds might arise due to *cis*-regulatory differences between fore- and hindlimb buds. Osterwalder et al. 2014 showed that HAND2 chromatin complexes interact with *Tbx3* CRM (-58 kb) that is only active fore-,

but not hindlimb buds. In addition, species-specific differences in *Tbx3* expression were observed between chicken and mouse limb buds (Gibson-Brown et al., 1998). Finally, even as *Tbx2* and *Tbx3* are virtually expressed in identical patterns in early limb buds, it is possible that these paralogous genes have evolved a different balance of function in humans and mice (Davenport et al., 2003).

7.11 The role of the cellular environment for mammalian limb bud development

Even at the earliest stages of development, the extracellular matrix (ECM) is synthesized and secreted by embryonic cells. It is the major component of the cellular microenvironment, thus it is not surprising that the ECM influences cell behaviors like proliferation, adhesion and migration, differentiation, and apoptosis (Hynes, 2009). During limb bud development, the direct TBX3 transcription target *Cd44*, the hyaluronic acid receptor, is expressed by AER (Sherman et al., 1998). In the AER, CD44 binds FGF ligands and represent them to the underlying mesenchyme. The ECM in the limb bud mesenchyme can selectively bind growth factors to influence the signaling direction of the epithelial-mesenchymal crosstalk. It is known that during limb bud development, heparan sulfate selectively binds FGF10 derived from the mesenchyme but not FGF8 derived from the AER, which helps to direct FGF10 signaling to the ectoderm (Norton et al., 2005). Moreover, the ECM proteoglycan versican is targeted by a disintegrin and metalloproteinase with thrombospondin motifs (ADAMTS) enzymes, to generate functional fragments that induce cell death and promote regression of interdigital webbing during mouse limb bud development (McCulloch et al., 2009). Thus, the normal progression of limb bud development depends on specific ECM organization and regulation.

Interestingly, GO analysis of the TBX3 direct transcriptional targets points to a positive role in extracellular matrix organization during early forelimb bud development. In particular, RNA-seq revealed expression changes in collagen group genes. *Col9a1*, a collagen important for cartilage formation is upregulated in *Tbx3*-deficient forelimb buds, which hints to a potential change in the onset of chondrogenesis. Previous studies have revealed indirect links between TBX3 and activation of *Col1a2* expression in fibrosarcoma and chondrosarcoma. In these two types of sarcomas, COL1A2 mediates the pro- and anti-migratory effects of TBX3 (Omar et al., 2019). It is well established that the early limb bud mesenchyme is rich in hyaluronic acid and collagen I (Lonai, 2003). Hyaluronic acid is synthesized by *Has2* (hyaluronic acid synthase 2), and mice deficient for *Has2* show defective chondrocyte

condensation and maturation and abnormal joint formation (Matsumoto et al., 2009). Another subfamily member, *Tbx2* was shown to upregulate the *Has2* during AVC cardiac jelly and subsequent cardiac cushion formation (Shirai et al., 2009). Dynamic erosion and replacement of the ECM is essential for proper bone development, which assures that specific ECM components are deposited and removed in a spatio-temporally controlled manner (Lu et al., 2011). Two families of metalloproteinases, including matrix metalloproteinase (MMP) and ADAMTS plays a role in ECM remodeling. *Adamts9* is a direct transcriptional target of TBX3 in mouse forelimb buds (my study) and is known to function in controlling organ shape during development and inhibiting angiogenesis (Clark et al., 2000), while the MMPs control the columnar organization of hypertrophic chondrocytes. Mice lacking MMP-9, -13, or -14 show disorganized columnar chondrocytes, which increases the hypertrophic chondrocyte pool (Page-McCaw et al., 2007). TBX3 interacts with a candidate CRM in the *Mmp-14* cis-regulatory landscape and *Mmp-17* is upregulated in *Tbx3*-deficient forelimb buds. Therefore, it is possible that TBX3 plays a role in regulating tissue architecture by regulating the expression of genes involved in ECM production and remodeling.

TBX3 might be required for cartilage formation as it is highly expressed in the pre-condensed mesenchyme giving rise to the primordia of tibia and fibula in mouse (Cameron et al., 2009). The primordia of the mouse limb skeletal elements form relatively early during limb development. The pre-cartilaginous SOX9-positive mesenchymal condensation of the proximal limb skeletal elements already detectable by E10.5 in forelimb buds (Zhao et al., 1997). During condensation, centrally located cells commit to a chondrogenic fate to form cartilage, whereas the peripheral cells will form the perichondrium (Shimizu et al., 2007). Furthermore, normal progression of chondrogenesis is controlled by *Hif-1 α* and *Vegfa* are regulated by TBX3 in early mouse forelimb buds (my study). Under normal physiological conditions, there is a gradient of oxygenation in the cartilaginous growth plate that correlates with Hypoxia-inducible factor 1-alpha (*Hif-1 α*) expression in chondrocytes. HIF-1 α activity is an essential modulator of hypoxic cell survival in this avascular tissue, and it has important implications for the survival of tissues even transiently lacking a functional vasculature. Furthermore, HIF-1 α was implicated in chondrocyte proliferation modulation, differentiation, and growth arrest (Schipani et al., 2001). Under hypoxia, the HIF-1 α protein is stabilized, translocated to the nucleus, and heterodimerizes with HIF-1 β . Then HIF-1 α and HIF-1 β complex bind to hypoxia response elements (HREs) located in gene promoters to subsequently regulate transcription of vascular endothelial growth factor (VEGF), erythropoietin, iNOS, and glycolytic enzymes that enhance cellular adaptation to hypoxia

(Hwang et al., 2008; Sharp & Bernaudin, 2004). Overall, the physiological role of HIF-1 α in cellular adaptation to hypoxia points to the essential role of the micro-physiological environment in mammalian development (Schipani et al., 2001). Indeed, further studies within *vitro* cultivated mesenchymal stromal or bone marrow cells subjected to hypoxia induced VEGF expression, but limited cell proliferation (Nguyen et al., 2020) and caused down-regulation of several osteoblastic markers (*Runx2*, osteocalcin, and osteopontin). This analysis suggested that exposure to hypoxia may affect the bone-forming potential of progenitor cells (Potier et al., 2007). Taken together, it is tempting to speculate that TBX3 impacts zeugopod skeletal development by regulating genes modulating the ECM, the hypoxic microenvironment and promoting progenitor cell proliferation, while perturbations in *Tbx3* expression results in premature differentiation during the early chondrogenic stages in mouse forelimb buds.

8 Conclusion and outlook

The major question of this project was to analyze TBX3 unique and mutually with HAND2 controlled GRNs that helps to establish early mouse limb bud mesenchyme axis polarity.

Different genome-wide approaches (ChIP-seq, ATAC-seq and RNA-seq) in combination with spatial insights from the WISH analysis helped to elucidate GRNs controlled by the TBX3 and HAND2 during early limb bud development in the unbiased way. The analysis uncovered that the vast majority of genes that participate in the early limb bud AP polarization are actually controlled in collaboration by TBX3 and HAND2. Furthermore, these two developmental TF even were found to bind to the same CRMs e.g., *Gli3* anterior expression controlling CRM (mm1179) is bound by TBX3 and HAND2 containing chromatin complexes. Besides this, both TBX3 and HAND2 potentially could also influence other embryonic tissues transcriptional regulation in addition to limbs. In fact, a novel *Tbx2* genomic locus encompassed enhancer (mm1210) was found to be bound by TBX3 and HAND2 chromatin complexes. It seems that these TF could participate in the control of *Tbx2* expression in heart, optic lobe and diencephalon development.

Also, a few new TBX3 unique direct transcriptional target genes were identified in the forelimb bud mesenchyme. The osteochondrogenesis controlling genes *Egln1* and *Pknox2* were identified as direct targets of TBX3. Furthermore, the retinoic signaling pathway players *Cyp26a1* and *Rarb* were found to be upregulated and their expressions domains were expanded in *Tbx3*-deficient FLBs. Thus, RA clearance could influence *Tbx3*-deficient FLBs zeugopod PD truncation.

Thus, data presented in this project constitute the first identification of the TBX3 direct transcriptional targets during limb bud development. Also, it highlights the value of the endogenously epitope-tagged transcription factors as tools in embryonic development controlling gene regulatory networks elucidation.

The mouse line expressing the TBX3^{3xFLAG} allele was successfully used in the early forelimb buds cistrome analysis by the ChIP-seq. Thus, this allele could serve as a new tool in the future studies to identify the direct targets of TBX3 chromatin complexes in other embryonic tissues expressing TBX3, like mammary glands and embryonic heart.

Furthermore, as TBX3 and HAND2 cistrome analysis revealed these TF binding to the same CRMs, this strongly implied that these TFs might make heterodimers and/or be involved in complexes with other proteins controlling chromatin accessibility. Thus, proteomic analysis and ChIP-re-ChIP approach could provide highly value insight not only in TBX3 and

HAND2 chromatin complexes formation, but also elucidate its direct and indirect binding to the target genes loci.

Furthermore, just recently the hosting group received the conditional TBX3 mouse line. Conditional TBX3 inactivation in the posterior and/or anterior limb bud mesenchyme domains at certain developmental timepoints might provide insights into anteriorly expressed TBX3 functional role and elucidate its controlled GRNs.

Furthermore, this project provided a glimpse into TBX3 role in RA signaling during limb development. Thus, it would be interesting, to further evaluate TBX3 and RA regulatory relationship and elucidate RA dosing influence on the limb phenotypes.

Finally, it would be interesting to ablate TBX3 bound CRMs in the AP polarity controlling gene regulatory landscapes and subsequently evaluate these CRMs role in AP boundary maintenance and phenotypic manifestation.

Thus, it is crucial to understand how GRNs interact to orchestrate the morphogenesis of limbs as it could provide new insights into developmental processes, genetic diseases and regenerative medicine of skeletal tissues (Hojo, Chung, and Ohba, 2017), improve methods for bone repair and facilitate tissue engineering of skeletal tissues (Ekblom et al., 2014).

9 Material and methods

9.1 Mouse husbandry and experiments with mouse embryos

9.1.1 Ethics statement

All the experiments with mice and mouse embryos were performed with strict adherence to the Swiss law, 3R principles, and Basel Declaration. Animal experimentation was performed only by licensed researchers holding LTK module 1 certificate and following the continued education requirements. All the animal research conducted for this dissertation was classified as grade 0, implying no suffering.

9.1.2 Mouse strains and genotyping

Mouse strains used in experiments described in this thesis/dissertation were: *Tbx3*^{dVenus} (Kunasegaran et al., 2014), *Hand2*^{3xF} (Osterwalder et al., 2014) and *Hand2*^Δ (Galli et al., 2010). Aforementioned alleles were maintained in NMRI/Swiss Albino background. The *Hand2*^{floxed} allele (Galli et al., 2010) was maintained in a 129SvJ/C57BL/6J/Swiss Albino mixed background. *Hand2* in the forelimb mesenchyme was inactivated with *Prx1-Cre* transgene (Logan et al., 2002). *Prx1-Cre* line was maintained in a C57BL/6 background. *Hoxb6-Cre* transgene (Lowe, Yamada, & Kuehn, 2000) was used to inactivate *Hand2* in the hindlimb mesenchyme. *Hoxb6-Cre* line was maintained in a mixed C57BL/6/NMRI/Swiss Albino background. *Tbx3*^{3xF} chimeric mice were developed by fusing *Tbx3*^{3xF} positive G4 ES cell clones with blastocysts obtained from Swiss Albino donors (done by Aline Baur). Male chimeras with ~60-100% agouti coat color were crossed with Swiss Albino females to obtain germline transmission. Mice carrying *Tbx3*^{3xF} allele were viable and maintained expected Mendelian ratios, and the line was maintained in Swiss Albino background.

Mice and embryo genotyping was based on the DNA extracted using isopropanol/ethanol precipitation from newborn mice toes, extra-embryonic membranes or a piece of the embryo's head was used as a biopsy to extract DNA. Genotypes were determined by agarose gel electrophoresis following PCR amplification for relevant alleles using primers listed in the table 9.8.1.

9.1.3 Digoxigenin-labelled antisense riboprobe generation

Mouse antisense riboprobes containing digoxigenin-labelled uracil (dig-UTP) were generated by *in vitro* transcription from the plasmids carrying the complementary DNA (cDNA) of interest. 20 µg of plasmid DNA (pDNA) was linearized to create 5' overhangs using appropriate restriction enzyme in 50 µl reaction volume. List of WISH cloning probes is

given in 9.8.2. Digestion was carried out overnight (ON) and linearization of the plasmid was verified on 1.5% agarose gel. Linearized pDNA was diluted up to 200 μ l with H₂O. Subsequently specimen was transferred to a phase lock gel tube (Quantabio, 2302830). Once 200 μ l phenol-chloroform (77617-500ML, Sigma) was added to the specimen, tubes were vigorously mixed and centrifuged for 5 min at 13000 rpm (16.2 g). The upper phase was then transferred to a new tube and DNA precipitated using 400 μ l of 100% EtOH and 20 μ l of 3M sodium acetate. Samples were incubated for 5 min at RT and centrifuged for 30 min at 13000 rpm. The supernatant was then discarded and the pellet was washed with 500 μ l of 70% EtOH. Subsequent to the sample centrifugation, the supernatant was discarded and the pellet dissolved in 100 μ l TE buffer (10 mM Tris-HCl, 1 mM EDTA in H₂O). Riboprobe antisense transcription from PCR-derived template was conducted using appropriate T3, T7 or SP6 RNA polymerase with nucleotide mixture with dig-UTP (Roche, 11277073910). 20 μ l synthesis reaction mixture containing 10x dig-UTP RNA labelling mixture and its 10x Transcription buffer, 10 M DTT (AppliChem, A1101.0025), 1 μ g linearized pDNA, 20 U protector RNase inhibitor (15103100, Roche), 20 U RNA polymerase and H₂O. Reaction mixture was incubated at 37°C for 2 h. To have pure RNA without DNA contamination, Turbo DNase (AM2238, Invitrogen) and its buffer were added, the samples were incubated at 37°C for 15 min. The dig-UTP labeled riboprobes were then purified using manufacturer's protocol for mini Quick Spin RNA columns (11814427001, Roche), or by precipitation with EtOH and linear polyacrylamide. In case of the latter, 100 μ l TE, 3 μ l of 0.5% linear polyacrylamide, 10 μ l 5 M LiCl and 300 μ l 100% EtOH were added to the samples, and the mixture was incubated at -20°C for 30 min. The tubes were then centrifuged for 15 min at 12000 rpm at 4°C. Once the supernatant was removed, 100 μ l TE, 10 μ l 5 M LiCl and 300 μ l 100% EtOH were added to the samples, which then were incubated at -20°C for 30 min, and later centrifuged for 15 min at 12000 rpm at 4°C. Subsequent to the removal of the supernatant, the pellet was washed with 500 μ l 70% EtOH. The samples were then centrifuged for 15 min at 12000 rpm at 4°C, riboprobe pellet was air dried, and probe was diluted in 100 μ l TE. Before using antisense riboprobes for whole-mount *in situ* hybridization (WISH) (Chapter 9.1.4) they were heated at 85°C for 5 min and diluted in prehybridization buffer at 70°C. The probes in prehybridization buffer were stored at -20°C and re-used up to 3 times.

9.1.4 Whole-mount *in situ* hybridization (WISH)

Mouse embryos were isolated in the ice-cold PBS and transferred into a 2 ml tube to be fixed overnight in 4% paraformaldehyde (PFA) in PBS at 4°C. The following day the embryos were rinsed twice in PBT (PBS, 0.1% Tween (937373, Sigma)), and subsequently dehydrated by immersing them for 5 min in a graded series of 25%, 50%, 75% MetOH/PBT and twice in 100% MetOH. The dehydrated embryos were then stored at -20°C in 100% MetOH. The embryos were rehydrated by immersing them in a reverse gradient series of 75%, 50%, 25% MetOH/PBT for 5 min and washed twice in PBT for WISH. They were then bleached in 6% H₂O₂ (141077.1211, AppliChem) in PBT for 15 min, washed 3x5 min in PBT, and treated with 10 µg/ml proteinase K in PBT for 15 min (samples for AER probes were treated with 5 µg/ml proteinase K for 5min). To stop proteinase K activity, the embryos were washed with freshly prepared 2 mg/ml glycine in PBT for 5 min. After two 5 min washes in PBT, they were re-fixed in a freshly made 0.2% glutaraldehyde, 0.1% Tween-20 and 4% PFA in PBS for 20 min, and washed as previously twice in PBT. The embryos were then equilibrated in 2 ml of pre-warmed prehybridization buffer (50% deionized formamide (A2156, AppliChem), 5xSSC pH 4.5, 2% BCL blocking powder (1096176, Boehringer Ingelheim), 0.1% Tween-20, 0.5% CHAPS (C5070, Sigma), 50 µg/ml yeast RNA (R-8759, Sigma), 5 mM EDTA and 50 µg/ml heparin (H5515, Sigma), and H₂O) at 70°C for at least 1 h on a rotating wheel. After prehybridization buffer was then replaced by 1 ml of pre-warmed prehybridization buffer containing 10 µl/ml of digoxigenin-labelled RNA riboprobe (see chapter 9.1.3), and the embryos were incubated overnight at 70°C on a rotating wheel. The following day, the RNA riboprobe containing prehybridization buffer was recovered, and replaced by pre-warmed prehybridization buffer to wash once for 5 min. The embryos were then washed once for 5 min at 70°C in a series of 75%, 50% and 25% prehybridization buffer in 2xSSC (0.3M NaCl, 0.03M sodium citrate pH 4.5), and twice for 30 min in 2xSSC, 0.1% CHAPS at 70°C on a rotating wheel. The unbound riboprobe was removed by treating embryos with 20 µg/ml RNase A (10109169001, Roche) in 2xSSC, 0.1% CHAPS for 45 min at 37°C. This was followed by two 10 min washes with maleic acid buffer (100 mM maleic acid disodium salt hydrate, 150 mM NaCl, pH 7.5) at RT. Two additional 30 min washes were then conducted at 70°C on a rotating wheel. Subsequently embryos were washed twice in PBS for 10 min and once in PBT for 5min at RT. The embryos were then blocked in 10% lamb serum (16070096, Life Technologies), 1% BSA (A2153-100G, Sigma) in PBT for 2-3 h or more, at RT. After the blocking solution was replaced with the fresh blocking solution containing anti-digoxigenin-AP (11093274910, Roche) AB diluted to 1:2000 and embryos were incubated overnight at 4°C on a rocking platform shaker. The next day the embryos were washed 5x45

min in PBT containing 0.1% BSA, followed by two 30 min washes in PBT. The embryos were then equilibrated 3x10 min in NTMT (100 mM NaCl, 100 mM Tris-HCl pH 9.5, 50 mM MgCl₂, 1% Tween-20) and transferred into BM purple Alkaline Phosphatase substrate (11 442 074 001, Roche) (1 ml/sample) at RT. The samples were developed at RT in a dark chamber on a rocking platform and checked roughly every 30 min until the appropriate probe-specific signal intensity was reached. The development of the signal was stopped by washing stained embryos 3x5 min in PBT. The pictures were taken using a Leica MZ FLII stereomicroscope with accompanying the Leica Application Suite V3 software, and NIKON DS-Ri2 microscope and NIS-Elements BR5.11.00 software. The embryos were stored in 0.05% sodium azide (8.22335.0100, Sigma) in PBS at 4°C.

9.1.5 Lysotracker

The embryos for lysotracker staining (Molecular Probes, L-7528, red) were dissected in a Hanks buffer (HBSS, without phenol red, but with Mg⁺²/Ca⁺², Gibco, 14175-053) pre-warmed to 37°C. The dissected embryos were immediately transferred to a tube with pre-warmed 37°C HBSS, and a 5 µl/ml of lysotracker reagent was immediately added. The tube was then inverted a few times and incubated for 45 min at 37°C inverting the tube 4-6 times during incubation. Once the embryos were rinsed 4-5 times with HBSS for a total of 45 -60 min, they were fixed in 4% PFA in PBS ON at 4°C. The following day, the embryos were rinsed once in PBS and dehydrated in MetOH/PBS 25%, 50%, 75%, 100% series. Methanol was then replaced with 50% MetOH/50% BB/BA (Benzyl Benzoate/Benzyl Alcohol 2:1) and the samples were incubated for 30 min RT. Afterwards the solution was replaced with 100% BB/BA and incubated until the embryos sank. Imaging was done in BB/BA. Pictures were taken using a Leica MZ FLII stereomicroscope with accompanying the Leica Application Suite V3 software.

9.1.6 Superovulation of females for oocyte collection

On day 0, young female NMRI mice were injected with 5 IU PMSG (Pregnyl, Organon) intraperitoneally using 25G needle. On day 2, 46-48 h after first injection, the mice were injected with 5 IU hCG (Folligon, Intervet) and mating were set using NMRI males.

9.1.7 Pseudo-pregnant females priming for embryos implanting

On day 1, dirty bedding from an NMRI male was added to the cages of NMRI females. Matings between these stimulated females and vasectomized males were set on day 3.

Embryo collection for aggregations, ES cells and embryos aggregation, preparations for transfer, and embryos transfer itself was performed by Aline Baur.

9.2 Generation of the transgenic mouse line using CRISPR/Cas9 genome editing

9.2.1 Genetic engineering of the single guide RNA (sgRNA) guides and repair templates constructs

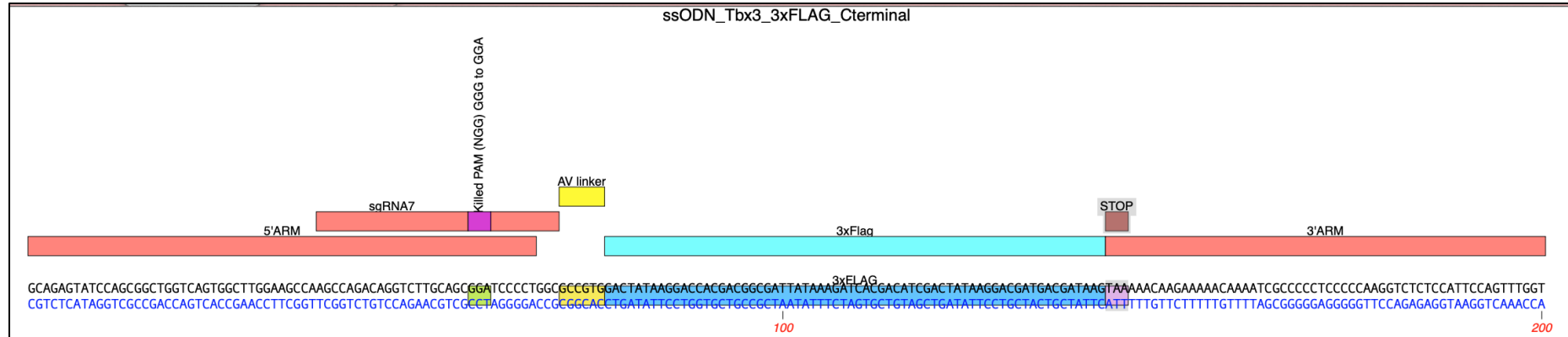
The endogenous *Tbx3* tagging by 3xFLAG was conducted using CRISPR/Cas9 genome editing technology. The design of the CRISPR/Cas9 strategy and the targeting of ES cells was designed together with Javier Lopez-Rios and Aimee Zuniga. There were two conditions of TBX3 tagging: in one condition the 3xFLAG was inserted to N-terminus and in the other to C-terminus. The potential protospacer adjacent motif (PAM) sequences were identified following the guide(s) on <http://crispr.mit.edu/>. Single guide RNA (sgRNA) were selected based on the best overall fit to the following criteria: 1) highest guide score; 2) mismatched score as low as possible and as far away from PAM sequence itself; 3) close proximity to the cutting site (min -3nt upstream PAM sequence to max -20nt); and 4) no more than 3 mismatches in sgRNA. Once the sgRNA sequence was selected, the primers for sgRNA were designed, and the 5' CACCG overhang was added. The sgRNA were then cloned into p459.V2.0 vector. Next, insert containing recombinant colonies were verified by sequencing, and then plDNA was linearized and purified before transfection (see chapter 9.4.1). Homologous arms for a repair template were then designed. A single stranded ultramer DNA oligo (ssODN) acquired from Integrated DNA Technologies, Inc. was used as a repair template. The homologous arms were designed with the maximum length of 200 bp containing 3xFLAG sequence optimized for codon usage and codon pair usage corrections. The PAM sequence was eliminated during ssODN development to avoid repeated cutting as it could lead to mistakes in repair and no desired product. In case of PAM elimination in the coding region, the same amino acid (a.a) was acquired by changing the codon, whereas in a non-coding region the sequence conservation between species was verified with blastx. Only when a particular part of the sequence was not conserved was the sequence change introduced into homologous arms. For N-terminus tagging TBX3 tagging was performed by using optimized 3xFLAG sequence, inducing a.a codon changes in ssODN sequence to eliminate PAM sequence, and including valine and aspartic a.a as a linker. In C-terminus tagging of TBX3, valine and aspartic a.a. were used as linker, and a stop codon was placed immediately after 3xFLAG sequence. sgRNA primers and ssODN sequences can be found in table 9.8.3.

9.3 Mammalian cell culture

9.3.1 Feeder cells culture

Primary Mouse Embryonic Fibroblasts (EMFIs) were used as feeder cells for Embryonic Stem

Figure 36. Scheme representing ssODNs design used to insert the 3xFLAG tag sequence into 5' and 3' of *Tbx3* locus. Precise 200nt ssODN sequences are given below the scheme, color code representing ssODN design and modifications of the sequence are given below.



GCAGAGTATCCAGCGGCTGGTCAGTGGCTTGAAGCCAAGCCAGACAGGCTTTGCAGCGGATCCCCTGGCCGCGTGGACTATAAGGACCACGACGGCGATTATAAAGATCAGACATCGACTATAAGGACGATGACGATAAGTAAACAAGAAAAACAAAATCGCCCTCCCAAGGTCTCTCCATTCCAGTTTGGTTCGCTCATAGGTCGCCGACAGTACCAGAACCTTCGGTTCGGTCTGCCAGAACGTCCTCAGGGGACCGGGCAGCTGATATTCCTGGTGTCCGCTAATATTTCTAGTGTGTAGCTGATATTCCTGCTACTGCTATTCTTTTGGTCTTTTTGTTTTAGCGGGGAGGGGGTTCCAGAGAGGTAAGGTCAAACCA



TATTTTTGAAAAGCAACAACAAAAGCGGAGCCAAGCCAGCAGTGCAGGACTGGTTCCTCCGCGATGGACTATAAGGACCACGACGGCGATTATAAAGATCAGACATCGACTATAAGGACGATGACGATAAGTAAACAAGAAAAACAAAATCGCCCTCCCAAGGTCTCTCCATTCCAGTTTGGTTCGCTCATAGGTCGCCGACAGTACCAGAACCTTCGGTTCGGTCTGCCAGAACGTCCTCAGGGGACCGGGCAGCTGATATTCCTGGTGTCCGCTAATATTTCTAGTGTGTAGCTGATATTCCTGCTACTGCTATTCTTTTGGTCTTTTTGTTTTAGCGGGGAGGGGGTTCCAGAGAGGTAAGGTCAAACCA

5' flanking sequence
sgRNA

Killed PAM
AV linker

3xFLAG
STOP

3' flanking sequence

Cells (ESCs) and grown at 37°C in 5% CO₂. EMFIs were cultivated in EMFI medium consisting of DMEM containing 4.5 g/l glucose (41966029, Gibco), 10% FCS (P30.3302, PanBiotech), 0.1 mg/ml penicillin/streptomycin (P-0781, Sigma) and 2 mM L-glutamine (G-7513, Sigma). Frozen EMFIs were thawed in 37°C water bath and the cells were then washed by diluting them in 10 ml of EMFI medium. Once the cells were centrifuged at 1200 rpm for 5 min, the medium was removed and the EMFIs were re-suspended in 3 ml of pre-warmed EMFI medium. The cells were then equally split into 3 or 4 10 cm culture dishes depending on the EMFI density of the particular batch. EMFI medium was changed every two days until the cells reached confluency. The cells were then split into another round of 3 to 4 cell culture plates (for a maximum of two passages) or treated with mitomycin C to stop cell division. The cells were first rinsed with desalinated PBS (DPBS) (Gibco, 14190-144) and incubated in 3 ml of pre-warmed 0.05% trypsin for 5 min at 37°C in order to split them. Cell clumps were re-suspended into single cells by pipetting, collected in 7 ml of EMFI medium, and spun for 5 min at 1200 rpm. The cell pellet was re-suspended in a small volume, diluted, and seeded at 1:3-1:4 in 10 cm dishes. To stop cell division and avoid EMFIs overgrowing ESCs, 10 µg/ml of mitomycin C was used in EMFI medium. Treated EMFIs' plates were incubated at 37°C with 5% CO₂ for 2 h, washed 3x with DPBS, and fresh EMFI medium without mitomycin C was added to continue EMFIs cultivation. Growth-arrested EMFIs were kept in the cell culture for a maximum of one week and the cell medium was changed every two days.

9.3.2 Embryonic Stem (ES) cell culture

ES cells were cultivated in two manners. ES cells were grown at 37°C with 5% CO₂ on a layer of growth arrested EMFIs. They were cultivated in ES cell medium containing: DMEM with 4.5 g/l glucose, supplemented with 15% FBS, 0.1 mg/ml penicillin/streptomycin, 2 mM L-Glutamine, 1 mM β-Mercaptoethanol (31350-010, Gibco), 1x non-essential amino acids (11140-035, Gibco), 1 mM sodium pyruvate (11360-39, Gibco), and 10³ units/ml of LIF (13275-029, Gibco). ESC medium was changed every day at the same time and the ES cells were split every other day using 0.05% trypsin as described in chapter 9.3.1 (ES cell pellet was re-suspended in ES cell medium and split into 1:3-1:6 on growth arrested EMFIs). Alternatively, ES cells were grown on the gelatin coated plates. Sterile 0.1% gelatin in H₂O was added to the plates, incubated for a few minutes, then removed and dried at RT for 10 min before use. Gelatin coating instead of EMFIs was used for IF, karyotyping experiments, and for short incubations before ES cell aggregations with blastocysts to deprive the EMFI

population. To preserve ESCs they were flash frozen. Trypsinized ES cell pellets were re-suspended to 3.3×10^6 cells/ml in ice-cold filtered freezing medium (50% ES cells medium, 40% FCS, 10% DMSO (Sigma)). 5-6 2 ml cryovials precooled on ice were filled with 1.5 ml of ES cells recovered from a 10 cm culture dish. Cryovials were transferred to -80°C ON in a Styrofoam box and then transferred to liquid nitrogen the next day.

9.3.3 ES cell transfection and positive clone selection

For transfection, 300 000 G4 ES cells were plated on a 6-well dish coated with EMFIs and cultivated in ES cell medium. The following day, the medium was changed to 1.75 ml of ES cell medium without penicillin/streptomycin per well. In the evening the cells were transfected using FuGENE (E2311, Promega) transfection reagent. 5 μg of plasmid p459.V2.0 and 4 μg of ssODN were diluted in 125 μL OptiMEM. 25 μl of FuGENE transfection reagent was mixed with 100 μl of OptiMEM. 125 μL of DNA-mixture was then combined with 125 μl of diluted FuGENE transfection reagent and the mixture was incubated for 15 min at RT. Finally, 250 μl of this mixture was added dropwise per well. After 12 h of incubation the transfection was discontinued by changing the medium to a regular ESC medium and 24 h later the cells were split into new 6 cm dishes (1:3) containing DR4 resistant feeders. The transfected cells were enriched using puromycin selection (2 $\mu\text{g}/\text{ml}$ in ESCs medium for 48 h, and the selection medium was replaced by regular ES cell medium. The surviving ES cell clones were grown for 4 to 6 days and picked. Isolated clones were expanded for storage by freezing and for a following screening. PCR screening was conducted to identify positive clones, which were then sequenced. The positive ES cells clones with in frame insert and an acceptable karyotype were aggregated to E2.5 WT Swiss Albino blastocysts to generate transgenic mice.

9.3.4 ES cells preparation for aggregation

ES cells were grown on a 6 cm dish to reach confluency before use for aggregation on day 5. The cells were then trypsinized and gently dissociated by tapping the plate or pipetting up and down in ES medium to obtain 5 to 15 cell clumps. The dissociated cells were then pre-plated for 30 min at 37°C with 5% CO_2 on gelatin plates to deplete the amount of EMFIs. ESCs media containing enriched fraction of ES cells were centrifuged for 5 min at 1200 rpm. The cells were then re-suspended to 1.5×10^6 cells/ml in aggregation medium (18 ml DMEM containing 4.5 g/l glucose, 66 mg Ca-lactate, and 4% FCS). 50 μL ES cell drops were made

on a 10 cm dish covered by mineral oil and incubated for 10 min at 37°C with 5% CO₂ before aggregation.

9.4 Molecular Biology

9.4.1 General cloning procedures

Vectors were digested with appropriate restriction enzymes (Roche or NEB) following the procedures recommended by manufacturers. The digested vectors or vectors with inserts were purified using phenol-chloroform purification with phase lock gel tube, or recovered from agarose gels and purified using QIAquick Gel Extraction Kit (28704, Qiagen). The inserts of interest generated by PCR were cleaned using PCR purification kit (28104, Qiagen), or recovered from agarose gels and purified using QIAquick Gel Extraction Kit. pGEM[®]-T Easy vector system (Promega, A1360) was used to clone PCR products of interest synthesized from a cDNA template obtained from the relevant stage of an embryo. Vector and PCR product were left at RT for 1 hr for ligation at room temperature (RT) or ON at 4°C. The ligation product was dialyzed for 30 min using MF[™] nitrocellulose membrane filters (VSWP02500, Millipore). The plasmids were then electroporated into DH5 α electrocompetent bacteria in gene pulser 0.2 cm cuvettes (1652086, Biorad) using a MicroPulser[™] (Biorad). In case it was necessary to transform the vector for pDNA amplification again, chemically-competent DH5 α bacteria were used. First, thawed cells were incubated on ice with the vector of interest and the transformation was then carried out by a short heat shock at 42°C for 45s. This was followed by 5 min incubation on ice and 1 h recovery with 1 ml of NZY broth before plating. The transformed bacteria were plated on LB agar plates containing the ampicillin to select positive clones. Orientation of the insert was verified using restriction digest or by performing colony PCR. The sequence of all inserts was verified by sequencing (Microsynth). pDNA was amplified by growing bacteria in liquid cultures and purified by alkaline lysis using the Plasmid Mini Kit (12125, Qiagen), the Plasmid Midi Kit (12143, Qiagen), or the NucleoBond[®] Xtra Midi kit (740410, Machery Nagel).

9.4.2 RNA extraction from embryonic tissues for the cDNA synthesis

Mouse embryonic tissues were first dissected in an ice-cold PBS and pooled in tubes. The maximum amount of PBS was then removed and the samples were incubated with 100 μ l of RNA later[®] (R0901, Sigma) ON at 4°C. Before further processing, the samples were stored at -20°C. The embryonic tissue or the whole embryo was then shredded as described further

in chapter 9.5.1, and the total RNA was extracted following the RNeasy Micro Kit (74104, Qiagen) protocol. RNA concentration was measured using Nanodrop 2000 C (Thermo Scientific) and RNA samples were stored at -20°C before synthesis. For cDNA synthesis 10 pg - 5 µg of RNA was mixed with 1 µl (500ng) oligo (dT)₁₂₋₁₈ (27785801W307857, Amersham), 1 µl dNTP mix (10 mM) and H₂O resulting in a total volume of 13 µl. The mixture was heated to 65°C for 5 min and subsequently incubated on ice for 1 min. Following a quick spin down of the tubes, 1 µl (200U/µl) of SuperscriptTM III RT (18080044, Thermo Fisher Scientific) and 4 µl of 5x its first strand buffer, 1 µl 0.1M DTT and 1 µl (40U/µl) RNaseOUTTM (10777019, Thermo Fisher Scientific) were added in a total volume of 20 µl, and the mixture was incubated at 50°C. 1 h later, the samples were heated up to 70°C for 15 min to stop cDNA synthesis reaction. cDNAs was then stored at -20°C and used to generate templates for the whole mount *in situ* hybridization.

9.4.3 Quantitative PCR (qPCR) and ChIP-qPCR

Quantitative PCR (qPCR) was used to determine transgene *Cre* copy numbers from genomic DNA template. A Bio-Rad CFX96 Real-Time PCR System in combination with the iQTM SYBR[®] Green Supermix (Bio-Rad, 170-8882) was used to perform qPCR. qPCR reaction was conducted in a 20 µl reaction volume containing 0.3 µM of forward and reverse primer diluted in EB buffer (10mM Tris-HCl pH 8.5), 50% of SYBR[®] Green Supermix, and 20 ng of genomic DNA template diluted in H₂O. A Dopamine Beta-Hydroxylase (DBH) genomic region amplifying primer was used as a normalizer. Relative quantification cycle (C_q) values of the transgene were normalized to DBH C_q values. Technical triplicates were used for the analysis. qPCR primer sequences are given in a table 9.8.6.

To determine the enrichment of TBX3 chromatin complexes at the genomic regions of interest (ROI) after chromatin immunoprecipitation (ChIP), technical triplicates of ChIP and input samples were analyzed using qPCR ChIP-qPCR primer sequences are given in a table 0. QuantStudio 6 Flex (Applied Biosystems by Thermo Fisher Scientific) system was used to run the qPCR. The qPCR reaction was performed in 10 or 20 µL reaction containing 0.3 µM of forward and reverse primer diluted in EB buffer, 2x PowerUpTM SYBRTM Green Master Mix (A25743, Thermo Fisher Scientific) and decrosslinked precipitated or input DNA. Primers amplifying the unlinked amplicon in the β-actin locus (Galli et al., 2010) or PPIA were used as the normalizing control region (NCR). *Hand2* chromatin complex enrichment in ROI analysis was conducted using Bio-Rad CFX96 Real-Time PCR System and PCR conditions described previously.

qPCR results were analyzed using Thermo Fisher ConnectTM software. Calculations of fold-change enrichment between input and ChIP samples are based on the formula provided below:

$$(CqROI_{ChIP}) - (CqROI_{Input}) = \Delta CqROI$$

$$(CqNCR_{ChIP}) - (CqNCR_{Input}) = \Delta CqNCR$$

$$\text{Fold enrichment} = 2^{-(\Delta CqROI - \Delta CqNCR)}$$

To avoid artefact biases of fold enrichment, a Cq above 32 was considered as a background threshold value. ((ChIP-qPCR results are displayed as mean \pm and are based on analyzing 3 technical replicates.))

9.4.4 Western Blot analysis

The embryos and embryonic tissues were dissected in ice-cold PBS and transferred with a small amount of PBS into collection tubes stored on ice. The samples were then briefly spun down, and once excess PBS was removed, they were immediately snap-frozen in liquid nitrogen to be stored at -80°C. Embryonic tissues were lysed with 100 μ l of RIPA buffer (50 mM Tris HCl pH 8.0, 150 mM NaCl, 1% NP40, 0.25% sodium deoxycholate, 1 mM EDTA, 1 μ g/ μ l of mini protease inhibitor cocktail (11873580001, Roche), 1 mM PMSF (P7626-1G, Sigma-Aldrich), 1 mM activated Na₃VO₄, 1 mM NaF and H₂O) that was added to frozen pellets on ice. Lysis was achieved by gently pipetting the samples up and down until tissues dissolved completely and then the tubes were incubated on ice. 15 min later, the lysate was centrifuged for 15 min at 13000 rpm at 4°C and the supernatant was transferred into new tubes. Protein concentration was determined using BCA (bicinchoninic acid) protein assay (23250, Pierce) kit. For SDS-PAGE proteins were diluted to 10 μ g per sample. The required amount of protein extract was added to new tubes and mixed with SDS sample buffer (25% 0.5M Tris pH6.8, 2% SDS, 0.0025% Bromophenol blue, 20% glycerol, freshly added 5% β -Mercaptoethanol) to a resulting 20% of the total sample volume. The protein extracts were first denatured by heating them at 95°C for 5 min in a heating block and then cooled on ice for 3 min. The samples were centrifuged at 4°C for 10 min 13000 rpm, mixed by pipetting up and down, and loaded on the SDS-PAGE gel. The proteins were then separated on a two-layered SDS polyacrylamide gel consisting of stacking gel (30% acrylamide (161-0156, Bio-Rad), 0.5 M Tris pH6.8, 10% SDS, 10% APS, 0,1% TEMED, H₂O) and 10% resolving gel (30% acrylamide, 1.5 M Tris pH8.8, 10% SDS, 10% APS, 0,1% TEMED, H₂O) in a freshly prepared running buffer (25 mM Tris, 192 mM Glycine, 0.1% SDS).

The samples were blotted on a hydrophobic PVDF Immobilon-P transfer membrane (IPV00010, Millipore). The membrane was activated by immersing it into 100% MeOH for 1 min and equilibrated in transfer buffer (25 mM Tris-base, 192 mM glycine, 20% MeOH) for 10 min. Wet transfer was conducted at 4°C at 100 V for 2 h in a cold room with transfer chamber covered in ice. After transfer, the membrane was shortly rinsed in TBST (10mM Tris-HCl pH8.0, 150mM NaCl, 0.05% Tween 20) and blocked in fat free 5% milk powder in TBST for 1 h changing milk every 20 min. The blocked membrane was then incubated with primary antibody (AB) in 5% milk powder in TBST overnight at 4°C (mouse M2 anti-FLAG 1:1000 (F1804, Sigma), rabbit anti-TBX3 2 µg/ml (SI256120, Thermo Fisher Scientific) and mouse anti-vinculin (batch6.5.94/VII F9, MD)). After 3x15 min washes with TBST, the membrane was incubated with secondary antibody (donkey anti-mouse HRP 1:5000, donkey anti-rabbit HRP 1:5000) diluted in 5% fat free milk powder in TBST for 1 hour at RT. The incubation was followed by 3x15 min washes with TBST and band detection using 1:1 mixture Immobilon[®] Western Chemiluminescent Substrate (WBKLS0500, Merck). The membrane was then stripped and reprobed, and control antibodies were used. The membrane was stripped twice by covering it in mild stripping buffer (1.5% glycine, 0.1% SDS, 1% Tween 20, H₂O, pH 2.2) and incubating it in RT for 10 min on a nutating platform. Then it was washed twice for 10 min with PBS and subsequently twice for 10 min with TBST. The following steps involving development with new primary AB were performed as described above.

9.4.5 Silver staining

Silver staining of SDS-PAGE gel was used to test for possible protein degradation during embryonic tissue lysis, and to qualitatively evaluate the amount of proteins. Sample preparation and SDS-PAGE was performed as described in chapter 9.4.4. A total of 5 µg of protein was loaded per SDS-PAGE well. SDS-PAGE gel was fixed for 1 h in 50% EtOH, 12% acetic acid, and washed 3x20 min in 30% EtOH and then washing continued overnight. On the following day the gel was rehydrated in H₂O and briefly incubated in freshly prepared 8 µM sodium thiosulfate for 1 min, followed by a 20 sec rinse in H₂O and 20 min staining in 11.8 mM silver nitrate, 0.02% formaldehyde. The gel was then washed twice for 20 sec with H₂O and colored protein bands were developed to the desired extent in 566 mM sodium carbonate, 0.02 mM sodium thiosulfate, and 0.02% formaldehyde. BioRad ChemiDoc[™] MP Imaging System was used to take pictures.

9.5 Next generation sequencing (NGS)

9.5.1 RNA Sequencing (RNA-seq)

RNA sequencing (RNA-seq) was used to analyze all (the necessary) transcriptomes: (1) WT and *Hand2*^{Δ/Δ} in atrioventricular canals (AVCs) of the hearts of mouse embryos at E9.0-9.25 (18-23 s); (2) WT and *Tbx3*^{Δ/Δ} in the forelimb buds (FLBs) of mouse embryos at E9.75-10.0 (28-31 s); (3) *Hand2*^{Δ/Δc}, *Prx1Cre*^{/+} and *Hand2*^{+/+}, *Prx1Cre*^{/+} (as WT) of mouse embryo FLBs at E10-10.25 (31-33s). Embryonic tissues were dissected in ice-cold PBS and transferred with as little PBS as possible to a tube with 50 μl of RLT buffer (Qiagen) containing 1% β-Mercaptoethanol. The samples were then flash frozen in liquid nitrogen and stored at -80°C until RNA extraction. Four AVCs per replicate were pooled for RNA extraction keeping the same gender and age ratio for all replicates. A pair of limb buds was treated as one replicate. To extract RNA, the samples were defrosted, infused with additional 350 μl of RLT buffer containing 1% β-Mercaptoethanol, and the tissue was homogenized by passing it through a 25 G syringe needle 10-15 times. After total RNA was extracted following the QIAGEN RNeasy kit protocol. The quality of the extracted RNA (30-190ng) was evaluated using the Fragment Analyzer (Advanced Analytical) High Sensitivity RNA Analysis kit. Only samples with a RIN ≥8.0 were used for library preparation. Library preparation and sequencing of WT and *Hand2*^{Δ/Δ} in the AVCs of the mouse embryos was outsourced to Genome Technology Access Center, USA. The libraries were synthesized using the Clontech SMARTer kit and sequenced on Illumina HiSeq 3000 using single end reads for 50-cycle protocol. WT and *Tbx3*^{Δ/Δ} mouse embryos FLBs; *Hand2*^{Δ/Δc}, *Prx1Cre*^{/+} and *Hand2*^{+/+}, *Prx1Cre*^{/+} mouse embryos FLBs mouse embryos HLBs RNA libraries were synthesized using non-directional NEB Next Ultra II RNA library preparation kit for Illumina (E7770L). 100 ng of RNA was used as a starting material. Only coding mRNA were enriched by the polyA RNA library preparation protocol provided by the manufacturer was followed. To enrich mRNA for library amplification, PolyA Beads 96RXN (E7490L) were used. mRNA was shredded to 200 bp fragments and 11 PCR cycles were used to enrich adaptor ligated DNA. The samples were multiplexed using PCR index primers from NEBNext Multiplex Indexes (E7335s/E7500s) kit. The concentration of the synthesized libraries was measured with Qubit™ DNA HS Assay Kit (Q33231, Thermo Fisher Scientific). Fragment Analyzer CRISPR Discovery kit was used to verify the profiles of the libraries. In case of primer dimer/adaptor contamination, the RNA-seq libraries were purified as described in chapter 9.5.3. The sequencing was performed on NextSeq500 machine using 75 single-end

reads for 40 cycle protocol. Library sequencing was performed by the EMBL Genomic Core Facilities.

9.5.2 ChIP-seq to identify TBX3^{3xF} cistrome in forelimb buds

ChIP-seq described in this chapter was used to identify direct TBX3^{3xF} targets in FLBs. The crosslinking protocol was optimized for 10 pairs of FLBs per tube. In total, 3 replicates were produced to identify TBX3^{3xF} cistrome in FLBs by ChIP-seq. Each replicate contained around 70 FLBs from *Tbx3*^{3xF/3xF} embryos at E 9.75-E10.25.

First, the embryos were dissected in ice-cold PBS and 20 FLBs were pooled per tube. The samples were then quickly spun down and the old PBS was replaced with 1 ml of 250 mM PMSF in PBS. Quick centrifugation was repeated and the samples were crosslinked with 2 ml of RT 1% PFA (F8775-25ML, Sigma) in PBS for 10 min on a rotating platform at RT. The samples were spun down for 1 min at 4000 rpm, the supernatant was discarded, and PFA was quenched with 1 ml of freshly prepared 125 mM glycine in 250 mM PMSF/PBS by incubating the samples on ice for 10-15 min. The samples were then centrifuged for 1 min at 4000 rpm, the supernatant was discarded, and the samples were washed with 1 ml of 250 mM PMSF in PBS. Finally, the tubes were spun down for 1 min at 4000 rpm, the supernatant was discarded, and the samples were flash frozen in liquid nitrogen to be stored at -80°C.

The following section describes magnetic bead preparation preceding tissue lysis and sonication of the chromatin. A mix of 20 µl of protein G and 20 µl of protein A beads (10001D, Invitrogen) was washed 3 times in 1 ml of ice-cold ChIP dilution buffer (1% Triton X-100, 10 mM Tris pH8.0, 150 mM NaCl, 2 mM EDTA, and H₂O) by incubating low retention tubes on a rotating platform for 2 min. The magnetic beads were then precipitated on a magnetic rack, the supernatant was removed without disturbing the beads, and 1 ml of fresh ChIP dilution buffer was added. 5 µg of mouse-M2-anti-FLAG antibody (F1804, Sigma) was added to the magnetic beads in ChIP dilution buffer and the tubes were incubated on a rotating wheel at 4°C for later use. The frozen tissue was defrosted on ice and 1 ml of ice-cold buffer A (0.25% Triton X-100, 10 mM Tris pH8.0, 10 mM EDTA and 0.5 mM EGTA, H₂O) containing 250 mM PMSF and 1% protein inhibitor cocktail (P8340, Sigma-Aldrich) was added to each tube. The samples were then transferred to a douncer and the tissue was homogenized by applying 10 stokes with pestle B (85302-0002, Tissue Grind Pestle SC 2 ml, Kimble-Chase). After incubating the nucleus on ice for 10 min, the samples were centrifuged for 3 min at 4000 rpm at 4°C. The supernatant was then discarded and the pellet was resuspended in ice-cold buffer B (200 mM NaCl, 10 mM Tris pH8.0, 1 mM EDTA, 0.5 mM

EGTA, and H₂O) containing 250 mM PMSF and 1% protein inhibitor cocktail. Then samples were transferred to a new low binding tube and incubated on ice for 30 min inverting them every 10 min. The samples were then centrifuged for 3 min at 4000 rpm at 4°C and the pellet was resuspended in 350 µl of ice-cold CD buffer (0.5% SDS, 0.5% Triton X-100, 0.05% NaDOC, 10 mM Tris pH8.0, 140 mM NaCl, 1 mM EDTA and 0.5 mM EGTA, and H₂O) until no visible clumps were remaining. The samples were sonicated using Bioruptor 300 (Diagenode) 15 cycle high program (30sec on/off). After sonication, the samples were centrifuged for 13 min at 13000 rpm at 4°C. The supernatant was then transferred to a new low DNA binding tube and 300 µL of CD buffer was added. 25 µl aliquot was removed as an input and stored at -80°C before further processing. Washed magnetic beads with a bound antibody were then precipitated on a magnetic rack and the supernatant was discarded. The beads were resuspended in ½ of total chromatin volume and ½ of total ChIP dilution buffer volume. Finally, the samples were incubated on a spinning wheel ON at 4°C.

The following day, the magnetic beads with antibody and chromatin complexes were washed and the precipitated DNA was eluted. First, the magnetic beads-chromatin complexes were precipitated on a magnetic rack. The supernatant was then removed, flash frozen, and stored at -80°C for future chromatin ChIPs. Then 1 ml of wash buffer iB (1% Triton, 0.1% SDS, 150 mM NaCl, 20 mM Tris pH8.0, 2 mM EDTA, and H₂O) was added to the magnetic beads with antibody and bound chromatin complexes. The samples were then transferred into a new low binding tube and incubated for 2 min on a rotating platform. Following that, the tubes were placed on a magnetic rack and the supernatant was replaced by buffer iC (1% Triton X-100, 0.1% SDS, 500 mM NaCl, 20 mM Tris pH8.0, 2 mM EDTA, and H₂O). The samples were then washed for 2 min by alternating facing sides of the tube toward the magnetic rack. The samples were again washed 2 times with buffer iD (1% NP40, 250 mM LiCl, 10 mM Tris pH8.0, 1 mM EDTA, and H₂O) as described earlier. After removing the supernatant, 1 ml of buffer Iten (50 mM NaCl, 10 mM Tris pH8.0, 1 mM EDTA, and H₂O) was added, and the mix was transferred to a new low binding tube for 2 min incubation on a rotating platform. The samples were then quickly spun down at 2000 rpm for 1 min, the supernatant was discarded, and 120 µl buffer E (1% SDS, 50 mM Tris pH8.0, 10 mM EDTA, and H₂O) was added directly to the beads. After 6-8 h sample incubation at 65°C, they were cooled down to the RT for 10 min, and 400 µg/ml of RNase (EN0531, ThermoFisher) was added for further 15 min incubation at RT. 800 µg/ml of PK was added and the samples were incubated for 1 h at 55°C. The samples were then purified using MicroChIP DiaPure columns Diagenode Kit (C03040001, Diagenode) protocol. ChIP DNA was eluted in 15 µl, DNA concentration was

measured using Qubit HS DNA kit, and the samples were stored at -80°C until further use for ChIP-seq library preparation or ChIP-qPCR.

9.5.3 ChIP-seq library synthesis and purification

The libraries for ChIP-seq were synthesized using MicroPlex library preparation kit v2 (C05010014, Diagenode) according to the standard protocol of the manufacturer. HAND2^{3xF} ChIP-seq libraries were amplified for 15 cycles for replicates A and D, whereas the replicate E library was amplified for 13 cycles. All 3 replicates of TBX3^{3xF} libraries were amplified for 9 cycles. After synthesis, DNA concentration of the newly synthesized libraries was measured using Qubit DNA HS kit. The library's profile was verified using Fragment Analyzers' CRISPR discovery kit. Double sided AMPure XP purification beads (ref. A63880) were used for purification of libraries in case of primer (at 80bp), adaptor dimer (at 128bp), or long fragment tail (above 600 bp) contaminations. First, the DNA was diluted with up to 50µl H₂O if needed and transferred into a round bottomed 96 well plate (262162, Thermo Fisher Scientific). The first 'cut-off' (long fragment elimination) was conducted by adding AMPure XP beads (amount as recommended by the manufacturer) to the DNA. The DNA was bound to the beads by pipetting and incubating at RT for 5 min. The DNA on beads was precipitated by putting the plate on a magnetic rack (AM 10050, Thermo Fisher Scientific) for 5 min at RT and the supernatant was transferred to a new well. The second 'cut-off' (short fragments elimination) was conducted by adding the required amount of AMPure XP beads and DNA was bound to beads as describe above. The DNA on beads was then precipitated by putting the plate on a magnetic rack for 5 min at RT. The supernatant containing primer dimers/adaptors was discarded and the magnetic beads with DNA bound were washed by 30 second incubation in 200 µl of freshly prepared 70% EtOH at RT. After EtOH removal, the beads were air-dried for 3-4 min at RT. The purified DNA was then eluted with 15-30 µl of TE and the supernatant was transferred into a new tube. DNA concentration was measured using Qubit HS DNA kit and library profile was verified with Fragment Analyzers' CRISPR discovery kit. The samples were stored at -80°C.

9.6 Histology

9.6.1 Murine chromosome counting

Actively growing ES cells were cultured on 10 cm plates with EMFIs or on gelatin coated plates. To arrest actively dividing ES cells in metaphase 0.04 µg/ml of colcemid was added to the ES cell media and incubated for 1 h at 37°C. The media was then removed and the cells

were washed with DPBS. The cells were detached with 0.05% trypsin for 5 min, re-suspended to single cells and transferred into a tube. In case ES cells were grown on EMFIs, 30 min pre-plating step was included to deplete EMFI population. The cells were then spun for 5 min at 200 g. The supernatant was decanted and the pellet was re-suspended in ES cell media. Aiming at the tube wall 10 ml of pre-warmed to 37°C 0.075 M KCl was added dropwise to resuspend the cells. The cells were incubated for 15 min at 37°C and then a few drops of ice cold Carnoy's fixative (methanol/acetic acid, 3:1) was added to the tube and inverted a few times. The cells were then centrifuged for 5 min at 200 g, excessive supernatant was aspirated and the pellet was re-suspended in the remaining 1 ml of supernatant by flicking. The cells were fixed with 5 ml of ice cold Carnoy's fixative that was added to ESCs drop-by-drop. The tube was inverted a few times and the cells were spun for 5 min at 200 g. Fixing with Carnoy's fixative was repeated one more time. Finally, the supernatant was removed and the cells re-suspended in 500 µl - 2 ml of Carnoy's Fixative regarding density of cells. Chromosome spreads were made in the next 3 h by dropping 50 µl of freshly fixed hypotonic ES cells on a slide at a distance of 30 cm between the glass surface and a pipet while holding it at 45° angle. The slides were air-dried ON while protecting them from dust. Staining of the slides was conducted the next day by immersing them for 1 min in 0.1 M phosphate buffer pH 6.8 (0.1 M NaH₂PO₄, 0.1 M Na₂HPO₄), then for 2 min in 0.025% aged trypsin (2 weeks at +4°C) in phosphate buffer, for 1 min in phosphate buffer, and finally for 15 min in Giemsa working solution stain (7.4% of Giemsa stain, 0.1 M phosphate buffer) (GS500-500ML, Sigma-Aldrich). The slides were rinsed by dipping them 2-3 times into distilled water. They were then dried by shaking off residual water, drying the back with paper tissues, and leaving them to air dry. Alternatively, they were placed in an oven for 1-2 min at 50-60°C in case it was necessary to speed up the drying. The slides were then mounted with Mowiol, dried at RT ON, and imaged with Leica DMI4000 stereomicroscope and the Leica Application Suite V3 software.

9.6.2 Embryo embedding in O.C.T compound for cryosectioning

The embryos for immunohistochemistry staining were dissected in ice-cold PBS, stretched on a silicon dish by pinning, and fixed with 4% PFA in PBS for 2 hours at 4°C. The samples were washed 3x5 min in PBS and then incubated with 10% sucrose/PBS, 20% sucrose/PBS and 30% sucrose/PBS for 1 h respectively. The embryos were then transferred with a minimum amount of 30% sucrose into embedding molds filled with 50:50 30% sucrose /O.C.T compound (4583, Tissue-Tek). Finally, they were positioned in the mold and then

frozen by dipping the embedding mold into 2-Methylbutane cooled on dry ice in a Styrofoam box. The samples were kept on dry ice until the embedding medium was completely frozen and then transferred for storage at -80°C. The embryos were sectioned into 10 µm sections using a Microm HM 500 OM Cryostat (cutting conducted at -20°C). The embryonic sections were then mounted on Superfrost Plus slides (J1800AMNZ, Fisher Scientific) and stored at -80°C.

9.6.3 Immunohistochemistry using frozen sections

The embryonic sections were defrosted and dried in RT for 20 min. The slides were washed 3x5 min each in PBS at RT on a gently rocking platform. Once the tissue sections were permeabilized by incubating them in PBT (0.2% Triton X-100 in PBS) for 30 min on a rocking platform, they were washed 3x5 min each in PBS while rocking. The samples were then blocked with 1% BSA in PBT for 1 hour at RT and incubated ON with primary antibodies (see table 9.8.5) diluted in 1% BSA/PBS. The following day, the sections were washed 3x5 min each in PBS at RT on a gently rocking platform and once in PBT. The samples were then incubated for 1 h in the dark at RT with secondary antibodies diluted 1:500 in 1% BSA/PBS. The slides were then washed 3x10 min each in PBS and once in PBT for 5 min while gently rocking. This was followed by nuclear staining with 1 µg/ml Hoechst-33258 (Calbiochem) in PBS for 5 min. The sections were then rinsed 3x5 min each in PBS on a rocking platform. Finally, the slides were dried to remove excessive PBS and mounted in Mowiol 488. They were then left to dry overnight at RT in the dark. The images were acquired using the Leica SP5 confocal microscope and software, and processed using ImageJ software.

9.6.4 Immunocytochemistry for ESCs

TBX3^{3xF} positive EC cells were seeded at a density of 25.000, 50.000, and 100.000 cells/well on a 96 well plate (353219, Fisher Scientific) and cultured as usual. The following day, the cells were carefully washed twice with pre-warmed DPBS and fixed for 30 min in 4% PFA in PBS at RT on a rocking platform. The cells were then washed 3x5 min in DPBS at RT on a rocking platform. Afterwards, the fixed cells were permeabilized with 0.3% Triton X-100 in PBT at RT while gently rocking. The cells were blocked in 10% goat serum, 0.3% Triton X-100, 0.3% BSA in PBT for 1 h while rocking at RT. The primary antibodies were then diluted to the recommended concentration (see table 9.8.4) in 1% goat serum, 0.3% Triton X-100, 0.3% BSA in PBS, and the samples were incubated overnight at 4°C. The following day,

the samples were washed 3x5 min in PBT and the cells were incubated for 1 hour at RT in the dark with secondary antibodies diluted to the appropriate dilution (see table 9.8.5) in 1% goat serum in PBS. The cells were then washed 3x5 min in PBT and incubated with 1 µg/ml Hoechst-33258 in PBS for 5 min to stain nuclei. Afterwards, the samples were washed 3x5 min in PBT. Finally, the samples were stored in PBS in a moist chamber at 4°C until imaging was done. The images were acquired using the Leica SP5 confocal microscope and software, and processed using ImageJ.

9.7 Bioinformatical analysis: online tools and resources

Sequence alignments were created in and retrieved from UCSC (Flicek et al., 2014). VISTA enhancer browser (Visel et al., 2007) and the Mouse Genome Informatics website (<http://informatics.jax.org>) was used to retrieve information about known enhancers lacZ patterns. PCR primers were designed using Primer3 tool (Untergasser et al., 2007). PAM sequences for CRISPR/*Cas9* genome editing were found on <http://crispr.mit.edu/>. BLASTx (NCBI) database was used to verify sequence conservation before inserting the 3xFLAG tag into endogenous *Tbx3* locus.

9.8 Tables

9.8.1 Genotyping primers for mice and embryos

Locus	Forward primer (5'-3')	Reverse primer(s) (5'-3')	Size	Allele
<i>Hand2</i>	TGCTCTCCAGTCCTGTCTCTCT	CCGATCTGGACAGCTAGCAA	330bp + 530bp	WT and floxed
	AGAAGAGGACCTCGGCAATT	CTGTGGTCTTGTTTCGCGATT	496bp	Δ
	TGGAGGGCCACGGAAGGCGAGATG	GACAGGGCCATACTGTAGTCG	209bp + 284bp	WT + 3xFLAG
<i>Hoxb6</i>	GCTAAAACCCAATCTCGGCTAT	AGCATTTTCCAGGTATGCTCAG	440bp	<i>Cre</i>
<i>Tbx3</i>	AGCGGAGCCAAGCCAGCA	CCTTGGCCTCCAGGTGCAC	377bp +	Δ
		TTGATGCCGTTCTTCTGCTTGT	578bp	
	CTACCAGCGAACTGCAGAGTATC	CACAAAAGTCGCTCTAGACACAA	386bp + 461bp	WT + 3xFLAG
<i>Prx1</i>	GGCTCTCTCCTTAGCTTCCC	CCTGGCGATCCCTGAACATGTCC	440bp	<i>Cre</i>

9.8.2 WISH screen probes cloning primers table

Locus	Forward primer (5'-3')	Reverse primer (5'-3')	Size (bp)
<i>Rspo2</i>	GTCTTCTCGCTACAGACAGAGT	CCCCTAGCTAGAACACAGTCTCA	571

<i>Hoxc6</i>	TCACTTCAACCGCTACCTAACTC	GGAGAGACATCTGAGGAGTCTGA	520
<i>Hoxc4</i>	CTTCTGAAGACCACTCCCAGAG	GAGGAGAGAGGATGAGACTCCAC	535
<i>Edar</i>	GACTGAAGAGGGATGAGATTGG	GACACACGCCTTGTATGTCTAGT	773
<i>Egln1</i>	TGAATGTGGTATGTGGTTGTAGC	TACAAAGGACTACAGGGTCTCCA	712
<i>Fzd1</i>	TCGGAGTCTTCAGTGTCTCTAC	ATCAGAGAGGGCTAGAGAGATCG	587
<i>Itga4</i>	AAGTCAGGACTGGAGCTCAAAC	CCCCTGCACTAAGAGTATGTCTAC	704
<i>Lmo1</i>	TAGTTCTGGTCCCCTAAGCTCTC	ATCCACGCCAGTAATAAAATCG	721
<i>Pknox2</i>	GAGGCTGATGAGCTACAGACAAC	AGTGTCTTTCAAGGGAGCTCAG	540
<i>Plxn4</i>	CTCTCATGAGCTTAGACAGCTGAG	CTGCTGGACATCAAACAGGTAG	656
<i>Tshz2</i>	AGAACCCCTCTACCTACATCAG	GTTGCTAAAGGAACCGTGAGTC	588
<i>Irx5</i>	AAGACTCCCCCTATGAGTTGAAG	GCGTATAACCTGCTTCCTTTCTG	521
<i>Sall3</i>	TCTCTGAGATGTTCCAGAAGGAC	GGGGTCACTAGGTTTTAGGAGAA	672
<i>Hoxc6</i>	TCACTTCAACCGCTACCTAACTC	GGAGAGACATCTGAGGAGTCTGA	520

HAND2 project

<i>Kdr</i>	CTGCTGTGGTCTCACTACCAGT	ACAGAGAACCCTCAGACACTGC	646
<i>ErbB4</i>	GTGCAGGTTGTAGGTCCTATG	CCTCTGCTGTCTCTACCTCTCAC	783
<i>Cyr61</i>	GGTGCCTTGCTCATTCTTGAGT	CTCCCTCCCCAAAAGCTACACT	507
<i>Hnrnpab</i>	CTCTAGTTGTAGGCAGCGTGTG	AGCCTGGTCTACAGAGTTCCAG	769
<i>Tll1</i>	TGAGCTGTGATTCTCTGGAGTG	AGCAGCAGCAGTAGTAACTGGAC	678
<i>Acvrl1</i>	ACATAGCCTGTCTGGGTAGAGG	AGTAGCCTTTATCCCCCTCGAT	510

9.8.3 CRISPR/Cas9 sgRNA for cloning into p459.V2.0 plasmid

sgRNA	
Tbx3_N_sgRNA1_top	5'-CACCGCTGCGGACTGGTTCCTGTC-3'
Tbx3_N_sgRNA1_down	5'-AAACGACAGGGAACCAGTCCGCAGC-3'
Tbx3_C_sgRNA7_top	5'-CACCGAGCCAGACAGGTCTTGCAGC-3'
Tbx3_C_sgRNA7_down	5'-AAACGCTGCAAGACCTGTCTGGCTC-3'

9.8.4 List of primary antibodies

Antigen	Class	Host	Distributor	Use	Concentration
TBX3	Polyclonal	Rabbit	Thermo Fisher Scientific, SI256120	WB	2µg/mL
FLAG (M2)	Monoclonal	Mouse	Sigma, F1804	WB	1:1000
ACTIN	Polyclonal	Rabbit	Sigma, A2066	WB	1:10.000
SOX9	Polyclonal	Rabbit	Millipore, AB5535	IF	1:10.000

9.8.5 List of secondary antibodies

Antigen	Class	Host	Distributor	Use	Concentration
Peroxidase AffiniPure Donkey Anti-Mouse IgG (H+L)	Polyclonal	Donkey	Jackson ImmunoResearch, 715-035-150	WB	1:5000
Peroxidase AffiniPure Donkey Anti-Rabbit IgG (H+L)	Polyclonal	Donkey	Jackson ImmunoResearch, 711-035-152	WB	1:5000
Goat-anti-mouse IgG (H+L) Alexa Fluor-488 F(ab')₂	Polyclonal	Goat	Invitrogen, A11017	IF	1:500
Goat-anti-mouse IgG (H+L)	Polyclonal	Goat	Invitrogen, A11020	IF	1:500

Alexa Fluor-594 F(ab')₂					
Goat-anti-rabbit IgG (H+L) Alexa Fluor-488	Polyclonal	Goat	Invitrogen, A11037	IF	1:500
Anti-Digoxigenin-AP, Fab fragments	Polyclonal	Sheep	Roche, 11093274910	ISH	1:2000

9.8.6 qPCR primers table

Locus	Forward primer (5'-3')	Reverse primer (5'-3')	Size (bp)
<i>Cre</i>	ATACCGGAGATCATGCAAGC	TTGCCCTGTTTCACTATCC	88
<i>DBH</i>	AGGACATCAGCCACTCTGCT	AATTGTCTTGGTGGCCCTC	117
<i>Tbx3^{3xF}</i>	GACAGCACTCGACCTGTGAAAA	GAGGCTTGTGATTGGCTCT	82

9.8.7 ChIP-qPCR primers table

Locus	Forward primer (5'-3')	Reverse primer (5'-3')	Size (bp)	Coordinates (mm10)
<i>Actb</i> +1.8kb	GATCTGAGACATGCAAGGAGTG	GGCCTTGGAGTGTGTATTGAG	115	chr5:143666540+ 143666654
<i>Ets2</i> +146kb	TGAGAGAAGTGCATGCCAAC	ATCAGGGAAGCTCAGATCCA	104	chr16:95953181+ 95953284
<i>Tbx2</i> - 204kb	CTCCCACTGATGGCTGAAAT	CCCAGGATGTGAACTGTCAGT	138	chr11:85444826+ 85444963
<i>Tbx2</i> - 199kb	CTGTGTGCTACTCCGCATCA	CACTTCCACTTGGGTGGTG	112	chr11:85446511+ 85446622
<i>Tbx2</i> - 112kb	AGGGGAAGGAGGTTAGATGG	GCCTGGGAAGAAAGGCTTC	90	chr11:85534053+ 85534142
<i>Gli3</i> - 120kb	ACACACACCAATTTCCACC	TGGATCCAGCCCAAGTTAGA	109	chr13:15435373+ 15435481
<i>Negative MO</i>	GGATGTGTCACATGCCAATA	AATAGACAATCCCCTAGCCA	79	chr13:15487267+ 15487345
<i>Gli3</i> (mm652)	GCTGACTTTCCTGCCAGTA	AAGAGGAGGAAAGGCCATGT	119	chr13:15756894+ 15757012
<i>PPIA</i>	ACGCCACTGTCGCTTTTC	CTGCAAACAGCTCGAAGGA	113	chr9:96895624+ 96895736
<i>Tbx3</i> +230bp	CAGCACTCGACCTGTGAAAA	GAGGCTTGTGATTGGCTCT	80	chr5:119670890+ 119670969
<i>Tbx2</i> +5.6kb	GTCGTCTTCCAAGCCCACT	AGGAGGCCTTGTCTGGCTA	83	chr11:85848281+ 85848363
<i>Gli3</i> +100bp	GTCTGTGGATTTGGGACCTG	GCCCGCAAACAAGAAGAACT	70	chr13:15464076+ 15464145
<i>Negative LRM</i>	TGATCTAATGCGAACTTGTGGT	TGTATGGATGTT CAGAA TGCCT	87	chr2:113695093+ 113695179
<i>Scn5a</i> (hs2266)	CAGCCCTGTCCCAACTCTAT	TGGCTCACACCTGCTTATCA	75	chr9:119469840+ 119469914
<i>Alx4</i> +1kb	CTCCCCAACTCCTAGCCAAG	GGGACTCGCAGTAAGAGACG	119	chr2:93642577+ 93642695
<i>ZRS</i> +86kb	ACATTGCCCTCTGGAGTTC	TCACAGCACTGTGTTCTCCTCT	144	chr5:29315880+ 29316023

10 Acknowledgments

First and the most, I would like to thank Prof. Dr. Rolf Zeller, for giving me an outstanding opportunity to do my PhD thesis in his laboratory. I am more than grateful for his scientific supervision, bottomless patience, and his radiant scientific enthusiasm and excitement. Also, I am thankful for PD Dr. Aimee Zuniga for her scientific input during our weekly discussions and for all her time spent teaching me about the cell culture. Nonetheless, I am very grateful for my PaC committee members Prof. Dr. Markus Affolter and Prof. Dr. Antoine Peters, for giving me their precious time and for their input into my project. Also, for Prof. Dr. Sebastian Arnold, MD, for agreeing to evaluate my project as the T-box expert and Prof. Dr. Walter Salzburger for agreeing to chair my defense exam.

I would love to express my deep and genuine gratitude to Dr. Rushikesh Sheth for his mentoring, scientific advice, and his tremendous input into ChIPing the unChIPable TBX3. Thank you!

Furthermore, I would like to thank to bioinformaticians Dr. Shalu Jhanwar, Dr. Iros Barozzi, and Dr. Florian Geier. Without them, none of the projects I was involved in would be possible. My sincere thanks also go to Prof. Dr. Javier Lopez-Rios for ssRNA guides and the ssODN design crash course. Also, I am grateful for Dr. Pawel Pelczar and his team from the Transgenic Mouse Core Facility of the University of Basel for reconstituting the *Tbx3*^{dVenus} mice line for my experiments and discussions regarding CRISPR/*Cas9* genome editing.

Also, I am more than thankful for my Antelope@Novartis mentors: Dr. Benoit Pierrat for expanding my network and for sharing the inner peace. From the bottom of my heart, I want to thank Dr. Aileen Wrynn for coaching, inspiration at the lowest and darkest moments, and for all her kind help to discover new paths I was not even aware of. Also, to Dr. Aengus Mac Sweeney for kindly agreeing to proofread my thesis.

My sincere thanks also go to an amazing professional and a dearest friend of mine Aline Baur. I am very grateful for her helping me to generate the *Tbx3*^{3xF} line, making this lab truly an amazing place to work, and for holding my back, then I needed it the most. Also, I would love to say special thanks for my beloved three musketeers: Jonas Malkmus, Victorio Palacio, and Thomas Oberholzer for the most flavorful coffee we drank together while discussing science, politics and current topics, Friday lunches and the encouraging pats on the shoulder. I am dearly thankful to Jens Stolte, too for his help to troubleshoot CRISPR/*Cas9* and for teaching me as much as he knows about the NGS. Also, I am also very thankful for Olga Romashkina for taking over the genotyping as I needed it the most. Furthermore,

special thanks go to Dr. Laurene Ramos Martins for her warm welcome and help as I arrived at the lab, her cheerfulness, and friendliness. I also highly value the opportunity I had to meet and interact with Dr. Artal Moreno Fortuny and Dr. Marcos Sande Melon. Furthermore, I am thankful for Dr. Julie Gamart, Dr. Fabiana Gullota, Dr. Gretel Nusspaumer, Dr. Virginie Tissieres, and Dr. Robert Reinhardt, from whom I had an opportunity to learn. Non-the-less, I would love to thank Barbara Widmer, Debora Neyer, Antoinette Walser-van Gelderen, and Cansu Shinbay for all the help I received by dealing with bureaucracy in a foreign country. Also, to the dear lab keeping ladies Zoubida Boudebaba and Saleah Rabehli for the bright smiles in the early morning hours, impeccable clean lab dishes, and never finishing stocks of pipet tips and basic solutions.

Also, I would love to give a kind shout-out to the most brilliant people I met at the University of Basel core facilities. In particular, Pascal Lorentz, for his outstanding explanations, all the help to take pictures and his kind help to resolve technical issues. Also, I am deeply grateful for Angelika Offinger, Emilia Terszowska, and the whole animal facility team for the excellent care of my mice (and me!). Furthermore, I want to thank Claudio Cannavo, Ilija Lujic, and Timo Dörflinger for resolving all my IT problems in just a few clicks.

Also, I am very thankful for Simon Schwarz for answering all the questions and his patient assistance to operate Fragment Analyzer over and over again.

Furthermore, I am very grateful for Katja Eschbach, Elodie Burcklen, Dinko Pavlinic and Vladimir Benes for ensuring that all my NGS samples would be processed as fast as possible.

□□

Taip pat norėčiau padėkoti savo mylimai šeimai. Mamytei Vidai, kuri atidavė daugiau, negu kad turėjo, kuri paaukojo savo tikslus ir net menkiausius malonumus, kad tik aš galėčiau siekti savųjų. Taip pat už didžiąją dalį botanikos žinių, kurias iki valiai galėjau gilinti kartu su ja. Tėveliui Vytautui, už kantrybę, iš jo paveldėtą užsispyrimą, tylų palaikymą, už įdiegtą meilę miškui ir paukščiams. Mano mažajai sesutei Renatai ir broliukui Edvardui už tai, kad ant savo pečių jie nesiskųsdami neša visus rūpesčius, kuriuos aš palikau išvykdama, už jų nelankytus būrelius, kad aš galėčiau dalyvauti NMA sesijose ir už juoką, kuris praskaidrino net juodžiausias dienas. Deja, kad ir kaip jie stengėsi, mikologija man ne prie širdies. Taip pat a.a. mano močiutei Eleonorai už visas biologijos knygas, kurios jos dėka atsidūrė mano rankose.

11 Bibliography

- Abrahams, A., Parker, M. I., & Prince, S. (2010). The T-box transcription factor Tbx2: Its role in development and possible implication in cancer. *IUBMB Life*, 62(2), 92–102.
- Agarwal, P., Wylie, J. N., Galceran, J., Arkhitko, O., Li, C., Deng, C., Grosschedl, R., & Bruneau, B. G. (2003). Tbx5 is essential for forelimb bud initiation following patterning of the limb field in the mouse embryo. *Development*, 130(3), 623–633.
- Agger, K., Cloos, P. A. C., Christensen, J., Pasini, D., Rose, S., Rappsilber, J., Issaeva, I., Canaani, E., Salcini, A. E., & Helin, K. (2007). UTX and JMJD3 are histone H3K27 demethylases involved in HOX gene regulation and development. *Nature*, 449(7163), 731–734.
- Agulnik, S. I., Bollag, R. J., & Silver, L. E. E. M. (1994). *Conservation of the T-Box Gene Family from Mus musculus to Caenorhabditis elegans*. 219, 214–219.
- Agulnik, S. I., Garvey, N., Hancock, S., Ruvinsky, I., Chapman, D. L., Agulnik, I., Bollag, R., Papaioannout, V., & Silver, L. M. (1996). *Evolution of Mouse*. 0–5.
- Ahn, K., Mishina, Y., Hanks, M. C., Behringer, R. R., & Bryan Crenshaw, E. (2001). BMP-IA signaling is required for the formation of the apical ectodermal ridge and dorsal-ventral patterning of the limb. *Development*, 128(22), 4449–4461.
- Ahn, S., & Joyner, A. L. (2004). Dynamic changes in the response of cells to positive hedgehog signaling during mouse limb patterning. *Cell*, 118(4), 505–516.
- Alby, C., Bessieres, B., Bieth, E., Attie-Bitach, T., Fermont, L., Citony, I., Razavi, F., Vekemans, M., Escande, F., Manouvrier, S., Malan, V., & Amiel, J. (2013). Contiguous gene deletion of TBX5 and TBX3 leads to a variable phenotype with combined features of holt-oram and ulnar-mammary syndromes. *American Journal of Medical Genetics, Part A*, 161(7), 1797–1802.
- Altabef, M., Clarke, J. D. W., & Tickle, C. (1997). Dorso-ventral ectodermal compartments and origin of apical ectodermal ridge in developing chick limb. *Development*, 124(22), 4547–4556.
- Arman, E., Haffner-Krausz, R., Gorivodsky, M., & Lonai, P. (1999). Fgfr2 is required for limb outgrowth and lung-branching morphogenesis. *Proceedings of the National Academy of Sciences of the United States of America*, 96(21), 11895–11899.
- Avilion, A. A., Nicolis, S. K., Pevny, L. H., Perez, L., Vivian, N., & Lovell-Badge, R. (2003). Multipotent cell lineages in early mouse development depend on SOX2 function. *Genes and Development*, 17(1), 126–140.
- Bailey, S. D., Zhang, X., Desai, K., Aid, M., Corradin, O., Cowper-Sallari, R., Akhtar-Zaidi, B., Scacheri, P. C., Haibe-Kains, B., & Lupien, M. (2015). ZNF143 provides sequence specificity to secure chromatin interactions at gene promoters. *Nature Communications*, 2.
- Bakker, M. L., Boukens, B. J., Mommersteeg, M. T. M., Brons, J. F., Wakker, V., Moorman, A. F. M., & Christoffels, V. M. (2008). Transcription factor Tbx3 is required for the specification of the atrioventricular conduction system. *Circulation Research*, 102(11), 1340–1349.
- Ballim, R. D., Mendelsohn, C., Papaioannou, V. E., & Prince, S. (2012). The ulnar-mammary syndrome gene, Tbx3, is a direct target of the retinoic acid signaling pathway, which regulates its expression during mouse limb development. *Molecular Biology of the Cell*,

23(12), 2362–2372.

Ballim, R., & Prince, S. (2013). TBX3 (T-box 3). *Atlas of Genetics and Cytogenetics in Oncology and Haematology*, 17(7), 473–477.

Bamshad, M., Le, T., Watkins, W. S., Dixon, M. E., Kramer, B. E., Roeder, A. D., Carey, J. C., Root, S., Schinzel, A., Van Maldergem, L., Gardner, R. J., Lin, R. C., Seidman, C. E., Seidman, J. G., Wallerstein, R., Moran, E., Sutphen, R., Campbell, C. E., & Jorde, L. B. (1999). The spectrum of mutations in TBX3: Genotype/Phenotype relationship in ulnar-mammary syndrome. *American Journal of Human Genetics*, 64(6), 1550–1562.

Bamshad, M., Lin, R. C., Law, D. J., Watkins, W. S., Krakowiak, P. A., Moore, M. E., Franceschinis, P., Lala, R., Holmes, L. B., Gebuhr, T. C., Bruneau, B. G., Schinzel, A., Seidman, J. G., Seidman, C. E., & Jorde, L. B. (1997). *Mutations in human TBX3 alter limb, apocrine and genital development in ulnar-mammary syndrome*. 16(July), 311–315.

Bamshad, M. et al. A gene for ulnar-mammary syndrome maps to 12q23-q24.1. *Hum. Molec. Genet.* 4, 1973-1977 (1995).

Barham, G., & Clarke, N. M. P. (2008). Genetic regulation of embryological limb development with relation to congenital limb deformity in humans. *Journal of Children's Orthopaedics*, 2(1), 1–9.

Barozzi, I., Simonatto, M., Bonifacio, S., Yang, L., Rohs, R., Ghisletti, S., & Natoli, G. (2014). Coregulation of Transcription Factor Binding and Nucleosome Occupancy through DNA Features of Mammalian Enhancers. *Molecular Cell*, 54(5), 844–857.

Barrington, C., Finn, R., & Hadjur, S. (2017). Cohesin biology meets the loop extrusion model. *Chromosome Research*, 25(1), 51–60.

Barski, A., Cuddapah, S., Cui, K., Roh, T. Y., Schones, D. E., Wang, Z., Wei, G., Chepelev, I., & Zhao, K. (2007). High-Resolution Profiling of Histone Methylations in the Human Genome. *Cell*, 129(4), 823–837.

Barutcu, A. R., Maass, P. G., Lewandowski, J. P., Weiner, C. L., & Rinn, J. L. (2018). A TAD boundary is preserved upon deletion of the CTCF-rich Firre locus. *Nature Communications*, 9(1).

Behesti, H., Papaioannou, V. E., & Sowden, J. C. (2009). Loss of Tbx2 delays optic vesicle invagination leading to small optic cups. *Developmental Biology*, 333(2), 360–372.

Benazet, J.-D., Bischofberger, M., Tiecke, E., Goncalves, A., Martin, J. F., Zuniga, A., Naef, F., & Zeller, R. (2009). A Self-Regulatory System of Interlinked Signaling Feedback Loops Controls Mouse Limb Patterning. *Science*, 323(5917), 1050–1053.

Bénazet, J. D., & Zeller, R. (2009). Vertebrate limb development: moving from classical morphogen gradients to an integrated 4-dimensional patterning system. *Cold Spring Harbor Perspectives in Biology*, 1(4), 1–15.

Bernstein, B. E., Mikkelsen, T. S., Xie, X., Kamal, M., Huebert, D. J., Cuff, J., Fry, B., Meissner, A., Wernig, M., Plath, K., Jaenisch, R., Wagschal, A., Feil, R., Schreiber, S. L., & Lander, E. S. (2006). A Bivalent Chromatin Structure Marks Key Developmental Genes in Embryonic Stem Cells. *Cell*, 125(2), 315–326.

Bhaskar, V., & Courey, A. J. (2002). The MADF-BESS domain factor Dip3 potentiates synergistic activation by Dorsal and Twist. *Gene*, 299(1–2), 173–184.

Boeva, V., Louis-Brennetot, C., Peltier, A., Durand, S., Pierre-Eugène, C., Raynal, V., Etchevers, H. C., Thomas, S., Lermine, A., Daudigeos-Dubus, E., Georger, B., Orth, M. F.,

- Grünewald, T. G. P., Diaz, E., Ducos, B., Surdez, D., Carcaboso, A. M., Medvedeva, I., Deller, T., Janoueix-Lerosey, I. (2017). Heterogeneity of neuroblastoma cell identity defined by transcriptional circuitries. *Nature Genetics*, *49*(9), 1408–1413.
- Bogarapu, S., Bleyl, S. B., Calhoun, A., Viskochil, D., Saarel, E. V., Everitt, M. D., & Frank, D. U. (2014). Phenotype of a patient with contiguous deletion of TBX5 and TBX3: Expanding the disease spectrum. *American Journal of Medical Genetics, Part A*, *164*(5), 1304–1309.
- Bollag, R. J., Siegfried, Z., Cebra-thomas, J. A., Garvey, N., Davison, E. M., & Silver, L. M. (1994). *embryonically expressed mouse protein motif with the T locus*. *7*(july), 383–389.
- Bongers, E. M. H. F., Duijf, P. H. G., Van Beersum, S. E. M., Schoots, J., Van Kampen, A., Burckhardt, A., Hamel, B. C. J., Lošan, F., Hoefsloot, L. H., Yntema, H. G., Knoers, N. V. A. M., & Van Bokhoven, H. (2004). Mutations in the human TBX4 gene cause small patella syndrome. *American Journal of Human Genetics*, *74*(6), 1239–1248.
- Boogerd, C. J. J., Wong, L. Y. E., Van Den Boogaard, M., Bakker, M. L., Tessadori, F., Bakkens, J., T Hoen, P. A. C., Moorman, A. F., Christoffels, V. M., & Barnett, P. (2011). Sox4 mediates Tbx3 transcriptional regulation of the gap junction protein cx43. *Cellular and Molecular Life Sciences*, *68*(23), 3949–3961.
- Boogerd, K. J., Wong, L. Y. E., Christoffels, V. M., Klarenbeek, M., Ruijter, J. M., Moorman, A. F. M., & Barnett, P. (2008). Msx1 and Msx2 are functional interacting partners of T-box factors in the regulation of Connexin43. *Cardiovascular Research*, *78*(3), 485–493.
- Booker, B. M., Murphy, K. K., & Ahituv, N. (2013). Functional analysis of limb enhancers in the developing fin. *Development Genes and Evolution*, *223*(6), 395–399.
- Bose, J. (2002). Pallister-Hall syndrome phenotype in mice mutant for Gli3. *Human Molecular Genetics*, *11*(9), 1129–1135.
- Boulet, A. M., & Capecchi, M. R. (2004). Multiple roles of Hoxa11 and Hoxd11 in the formation of the mammalian forelimb zeugopod. *Development*, *131*(2), 299–309.
- Brade, T., Pane, L. S., Moretti, A., Chien, K. R., & Laugwitz, K. L. (2013). Embryonic heart progenitors and cardiogenesis. *Cold Spring Harbor Perspectives in Medicine*, *3*(10), 1–17.
- Bruneau, B. G., Nemer, G., Schmitt, J. P., Charron, F., Robitaille, L., Caron, S., Conner, D. A., Gessler, M., Nemer, M., Seidman, C. E., & Seidman, J. G. (2001). A murine model of Holt-Oram syndrome defines roles of the T-Box transcription factor Tbx5 in cardiogenesis and disease. *Cell*, *106*(6), 709–721.
- Buenrostro, J. D., Giresi, P. G., Zaba, L. C., Chang, H. Y., & Greenleaf, W. J. (2013). Transposition of native chromatin for fast and sensitive epigenomic profiling of open chromatin, DNA-binding proteins and nucleosome position. *Nature Methods*, *10*(12), 1213–1218.
- Burke, A. C., Nelson, C. E., Morgan, B. A., & Tabin, C. (1995). Hox genes and the evolution of vertebrate axial morphology. *Development*, *121*(2), 333–346.
- Büscher, D., Bosse, B., Heymer, J., & Rüter, U. (1997). Evidence for genetic control of Sonic hedgehog by Gli3 in mouse limb development. *Mechanisms of Development*, *62*(2), 175–182.
- Büscher, D., & Rüter, U. (1998). Expression profile of Gli family members and Shh in normal and mutant mouse limb development. *Developmental Dynamics*, *211*(1), 88–96.
- Bussen, M., Petry, M., Schuster-Gossler, K., Leitges, M., Gossler, A., & Kispert, A. (2004).

The T-box transcription factor Tbx18 maintains the separation of anterior and posterior somite compartments. *Genes and Development*, 18(10), 1209–1221.

Butterfield, N. C., Metzis, V., McGlenn, E., Bruce, S. J., Wainwright, B. J., & Wicking, C. (2009). Patched 1 is a crucial determinant of asymmetry and digit number in the vertebrate limb. *Development*, 136(20), 3515–3524.

Cameron, T. L., Belluoccio, D., Farlie, P. G., Brachvogel, B., & Bateman, J. F. (2009). Global comparative transcriptome analysis of cartilage formation in vivo. *BMC Developmental Biology*, 9(1), 1–17.

Candille, S. I., Van Raamsdonk, C. D., Chen, C., Kuijper, S., Chen-Tsai, Y., Russ, A., Meijlink, F., & Barsh, G. S. (2004). Dorsoventral patterning of the mouse coat by Tbx15. *PLoS Biology*, 2(1).

Capdevila, J., Tsukui, T., Esteban, C. R., Zappavigna, V., & Belmonte, J. C. I. (1999). Control of vertebrate limb outgrowth by the proximal factor Meis2 and distal antagonism of BMPs by Gremlin. *Molecular Cell*, 4(5), 839–849.

Capellini, T. D., Giacomo, G. Di, Salsi, V., Brendolan, A., Ferretti, E., Srivastava, D., Zappavigna, V., & Selleri, L. (2006). *Pbx1 / Pbx2 requirement for distal limb patterning is mediated by the hierarchical control of Hox gene spatial distribution and Shh expression*. 2273, 2263–2273.

Carlson, H., Ota, S., Campbell, C. E., & Hurlin, P. J. (2001). A dominant repression domain in Tbx3 mediates transcriptional repression and cell immortalization: relevance to mutations in Tbx3 that cause ulnar-mammary syndrome. *Human Molecular Genetics*, 21, 2403–2413.

Charité, J., McFadden, D. G., & Olson, E. N. (2000). The bHLH transcription factor dHAND controls Sonic hedgehog expression and establishment of the zone of polarizing activity during limb development. *Development*, 127(11), 2461–2470.

Chase, A., & Cross, N. C. P. (2011). Aberrations of EZH2 in cancer. *Clinical Cancer Research*, 17(9), 2613–2618.

Chen, H., & Johnson, R. L. (2002). Interactions between dorsal-ventral patterning genes *lmx1b*, *engrailed-1* and *wnt-7a* in the vertebrate limb. *International Journal of Developmental Biology*, 46(7), 937–941.

Chen, Yu, & Struhl, G. (1996). Dual roles for patched in sequestering and transducing Hedgehog. *Cell*, 87(3), 553–563.

Chen, Yuting, Knezevic, V., Ervin, V., Hutson, R., Ward, Y., & Mackem, S. (2004). Direct interaction with Hoxd protein reverses Gli3-repressor function to promote digit formation downstream of Shh. *Development*, 131(10), 2339–2347.

Cheng, S., Xing, W., Pourteymoor, S., Schulte, J., & Mohan, S. (2016). Conditional deletion of prolyl hydroxylase domain-containing protein 2 (Phd2) gene reveals its essential role in chondrocyte function and endochondral bone formation. *Endocrinology*, 157(1), 127–140.

Chiang, C., Litingtung, Y., Harris, M. P., Simandl, B. K., Li, Y., Beachy, P. A., & Fallon, J. F. (2001). Manifestation of the limb prepattern: Limb development in the absence of sonic hedgehog function. *Developmental Biology*, 236(2), 421–435.

Cho, K.-W., Kim, J.-Y., Song, S.-J., Farrell, E., Eblaghie, M. C., Kim, H.-J., Tickle, C., & Jung, H.-S. (2006). Molecular interactions between Tbx3 and Bmp4 and a model for dorsoventral positioning of mammary gland development. *Proceedings of the National Academy of Sciences of the United States of America*, 103(45), 16788–16793.

- Chu, E. Y., Hens, J., Andl, T., Kairo, A., Yamaguchi, T. P., Brisken, C., Glick, A., Wysolmerski, J. J., & Millar, S. E. (2004). Canonical WNT signaling promotes mammary placode development and is essential for initiation of mammary gland morphogenesis. *Development*, *131*(19), 4819–4829.
- Cirillo, L. A., Lin, F. R., Cuesta, I., Friedman, D., Jarnik, M., & Zaret, K. S. (2002). Opening of Compacted Chromatin by Early Developmental Transcription Factors HNF3 (FoxA) and GATA-4. *Molecular Cell*, *9*(2), 279–289.
- Clark, M. E., Kelner, G. S., Turbeville, L. A., Boyer, A., Arden, K. C., & Maki, R. A. (2000). ADAMTS9, a novel member of the ADAM-TS/metallopondin gene family. *Genomics*, *67*(3), 343–350.
- Cohn, M. J., Izpisua-Belmonte, J. C., Abud, H., Heath, J. K., & Tickle, C. (1995). Fibroblast growth factors induce additional limb development from the flank of chick embryos. *Cell*, *80*(5), 739–746.
- Coll, M., Seidman, J. G., & Müller, C. W. (2002). Structure of the DNA-bound T-box domain of human TBX3, a transcription factor responsible for ulnar-mammary syndrome. *Structure*, *10*(3), 343–356.
- Conlon, F. L., Fairclough, L., Price, B. M. J., Casey, E. S., & Smith, J. C. (2001). Determinants of T box protein specificity. *Development*, *128*(19), 3749–3758.
- Conlon, R. A. (1995). Retinoic acid and pattern formation in vertebrates. *Trends in Genetics*, *11*(8), 314–319.
- Cooper, K. L., Hu, J. K. H., Berge, D. Ten, Fernandez-Teran, M., Ros, M. A., & Tabin, C. J. (2011). Initiation of proximal-distal patterning in the vertebrate limb by signals and growth. *Science*, *332*(6033), 1083–1086.
- Cormack, B. P., & Struhl, K. (1992). The TATA-binding protein is required for transcription by all three nuclear RNA polymerases in yeast cells. *Cell*, *69*(4), 685–696.
- Creyghton, M. P., Cheng, A. W., Welstead, G. G., Kooistra, T., Carey, B. W., Steine, E. J., Hanna, J., Lodato, M. A., Frampton, G. M., Sharp, P. A., Boyer, L. A., Young, R. A., & Jaenisch, R. (2010). Histone H3K27ac separates active from poised enhancers and predicts developmental state. *Proceedings of the National Academy of Sciences of the United States of America*, *107*(50), 21931–21936.
- Crossley, P. H., Minowada, G., MacArthur, C. A., & Martin, G. R. (1996). Roles for FGF8 in the induction, initiation, and maintenance of chick limb development. *Cell*, *84*(1), 127–136.
- Dai, Y. S., & Cserjesi, P. (2002). The basic helix-loop-helix factor, HAND2, functions as a transcriptional activator by binding to E-boxes as a heterodimer. *Journal of Biological Chemistry*, *277*(15), 12604–12612.
- Dan, J., Li, M., Yang, J., Li, J., Okuka, M., Ye, X., & Liu, L. (2013a). Roles for Tbx3 in regulation of two-cell state and telomere elongation in mouse ES cells. *Scientific Reports*, *3*, 3492.
- Dan, J., Li, M., Yang, J., Li, J., Okuka, M., Ye, X., & Liu, L. (2013b). Roles for Tbx3 in regulation of two-cell state and telomere elongation in mouse ES cells. *Scientific Reports*, *3*, 1–9.
- Davenport, T. G., Jerome-Majewska, L. A., & Papaioannou, V. E. (2003). Mammary gland, limb and yolk sac defects in mice lacking Tbx3, the gene mutated in human ulnar mammary syndrome. *Development (Cambridge, England)*, *130*(10), 2263–2273.

- Davis, A. P., Witte, D. P., Hsieh-Li, H. M., Potter, S. S., & Capecchi, M. R. (1995). Absence of radius and ulna in mice lacking *hoxa-11* and *hoxd-11*. *Nature*, 375(6534), 791–795.
- De Moerlooze, L., Spencer-Dene, B., Revest, J. M., Hajihosseini, M., Rosewell, I., & Dickson, C. (2000). An important role for the IIIb isoform of fibroblast growth factor receptor 2 (FGFR2) in mesenchymal-epithelial signalling during mouse organogenesis. *Development*, 127(3), 483–492.
- DeBenedittis, P., & Jiao, K. (2011). Alternative splicing of T-box transcription factor genes. *Biochemical and Biophysical Research Communications*, 412(4), 513–517.
- Deepak, V., Zhang, Z., Meng, L., Zeng, X., & Liu, W. (2011). Reduced activity and cytoplasmic localization of Runx2 is observed in C3h10t1/2 cells overexpressing Tbx3. *Cell Biochemistry and Function*, 29(4), 348–350.
- Delgado, I., & Torres, M. (2016). Gradients, waves and timers, an overview of limb patterning models. *Seminars in Cell and Developmental Biology*, 49, 109–115.
- Deschamps, J. (2004). A Play in Two Acts. *Geophysical Monograph*, June, 1610–1611.
- Dixon, J. R., Selvaraj, S., Yue, F., Kim, A., Li, Y., Shen, Y., Hu, M., Liu, J. S., & Ren, B. (2012). Topological domains in mammalian genomes identified by analysis of chromatin interactions. *Nature*, 485(7398), 376–380.
- Dobrovolskaïa-Zavadskaïa, N. (1927). *Sur la mortification spontanée de la queue che la souris nouveau-née et sur l'existence d'un caractère (facteur) héréditaire "non viable"*. *C. R. Seanc. Soc. Biol.* 97, 114-116.
- Dolli, P., Falkenstein, H., Renucci, A., & Duboule, D. (1989). *during limb pattern formation*. 342(December), 767–772.
- Dong, L., Dong, Q., Chen, Y., Li, Y., Zhang, B., Zhou, F., Lyu, X., Chen, G. G., Lai, P., Kung, H. fu, & He, M. L. (2018). Novel HDAC5-interacting motifs of Tbx3 are essential for the suppression of E-cadherin expression and for the promotion of metastasis in hepatocellular carcinoma. *Signal Transduction and Targeted Therapy*, 3(1).
- Douglas, N. C., & Papaioannou, V. E. (2013). The T-box transcription factors TBX2 and TBX3 in mammary gland development and breast cancer. *Journal of Mammary Gland Biology and Neoplasia*, 18(2), 143–147.
- Duboc, V., & Logan, M. P. O. (2011a). Pitx1 is necessary for normal initiation of hindlimb outgrowth through regulation of Tbx4 expression and shapes hindlimb morphologies via targeted growth control. *Development*, 138(24), 5301–5309.
- Duboc, V., & Logan, M. P. O. (2011b). Regulation of limb bud initiation and limb-type morphology. *Developmental Dynamics*, 240(5), 1017–1027.
- Dunham, I., Kundaje, A., Aldred, S. F., Collins, P. J., Davis, C. A., Doyle, F., Epstein, C. B., Frietze, S., Harrow, J., Kaul, R., Khatun, J., Lajoie, B. R., Landt, S. G., Lee, B. K., Pauli, F., Rosenbloom, K. R., Sabo, P., Safi, A., Sanyal, A., ... Lochovsky, L. (2012). An integrated encyclopedia of DNA elements in the human genome. *Nature*, 489(7414), 57–74.
- Eblaghie, M. C., Song, S. J., Kim, J. Y., Akita, K., Tickle, C., & Jung, H. S. (2004). Interactions between FGF and Wnt signals and Tbx3 gene expression in mammary gland initiation in mouse embryos. *Journal of Anatomy*, 205(1), 1–13.
- Eklom, A. G., Laurell, T., & Arner, M. (2014). Epidemiology of congenital upper limb anomalies in Stockholm, Sweden, 1997 to 2007: Application of the oberg, manske, and

tonkin classification. *Journal of Hand Surgery*, 39(2), 237–248.

Emechebe, U., Pavan Kumar, P., Rozenberg, J. M., Moore, B., Firment, A., Mirshahi, T., & Moon, A. M. (2016a). T-box3 is a ciliary protein and regulates stability of the Gli3 transcription factor to control digit number. *ELife*, 5(APRIL2016), 1–28.

Emechebe, U., Pavan Kumar, P., Rozenberg, J. M., Moore, B., Firment, A., Mirshahi, T., & Moon, A. M. (2016b). T-box3 is a ciliary protein and regulates stability of the Gli3 transcription factor to control digit number. *ELife*, 5(APRIL2016), 1–28.

Espinoza-Lewis, R. A., Yu, L., He, F., Liu, H., Tang, R., Shi, J., Sun, X., Martin, J. F., Wang, D., Yang, J., & Chen, Y. P. (2009). Shox2 is essential for the differentiation of cardiac pacemaker cells by repressing Nkx2-5. *Developmental Biology*, 327(2), 376–385.

Eswarakumar, V. P., Monsonego-Ornan, E., Pines, M., Antonopoulou, I., Morriss-Kay, G. M., & Lonai, P. (2002). The IIIc alternative of Fgfr2 is a positive regulator of bone formation. *Development*, 129(16), 3783–3793.

Farin, H. F., Lüdtke, T. H. W., Schmidt, M. K., Placzko, S., Schuster-Gossler, K., Petry, M., Christoffels, V. M., & Kispert, A. (2013). Tbx2 Terminates Shh/Fgf Signaling in the Developing Mouse Limb Bud by Direct Repression of Gremlin1. *PLoS Genetics*, 9(4).

Farin, H. F., Mansouri, A., Petry, M., & Kispert, A. (2008). T-box protein Tbx18 interacts with the paired box protein Pax3 in the development of the paraxial mesoderm. *Journal of Biological Chemistry*, 283(37), 25372–25380.

Ferguson, G. B., Van Handel, B., Bay, M., Fiziev, P., Org, T., Lee, S., Shkhyan, R., Banks, N. W., Scheinberg, M., Wu, L., Saitta, B., Elphinstone, J., Larson, A. N., Riester, S. M., Pyle, A. D., Bernthal, N. M., Mikkola, H. K., Ernst, J., van Wijnen, A. J., ... Evseenko, D. (2018). Mapping molecular landmarks of human skeletal ontogeny and pluripotent stem cell-derived articular chondrocytes. *Nature Communications*, 9(1).

Fernandez-Teran, M., Piedra, M. E., Kathiriya, I. S., Srivastava, D., Rodriguez-Rey, J. C., & Ros, M. A. (2000). Role of dHAND in the anterior-posterior polarization of the limb bud: Implications for the Sonic hedgehog pathway. *Development*, 127(10), 2133–2142.

Fernandez-Teran, Marian, & Ros, M. A. (2008). The Apical Ectodermal Ridge: Morphological aspects and signaling pathways. *International Journal of Developmental Biology*, 52(7), 857–871.

Forzano, F., Foley, P. A., Keane, M. R., Brain, C. E., Smith, G. D., Yates, R. W., Ellershaw, D., Calder, A. D., & Scott, R. H. (2017). *Contiguous gene deletion of TBX5 and TBX3: report of another case*. 24, 13–15.

Frank, D. U., Emechebe, U., Thomas, K. R., & Moon, A. M. (2013). Mouse Tbx3 Mutants Suggest Novel Molecular Mechanisms for Ulnar-Mammary Syndrome. *PLoS ONE*, 8(7), 1–7.

Fromental-Ramain, C., Warot, X., Lakkaraju, S., Favier, B., Haack, H., Birling, C., Dierich, A., Dolle, P., & Chambon, P. (1996). Specific and redundant functions of the paralogous Hoxa-9 and Hoxd-9 genes in forelimb and axial skeleton patterning. *Development*, 122(2), 461–472.

Fromental-Ramain, C., Warot, X., Messadecq, N., LeMeur, M., Dollé, P., & Chambon, P. (1996). Hoxa-13 and Hoxd-13 play a crucial role in the patterning of the limb autopod. *Development*, 122(10), 2997–3011.

Gallet, A., & Therond, P. P. (2005). Temporal modulation of the Hedgehog morphogen gradient by a patched-dependent targeting to lysosomal compartment. *Developmental*

Biology, 277(1), 51–62.

Galli, A., Robay, D., Osterwalder, M., Bao, X., Bénazet, J. D., Tariq, M., Paro, R., Mackem, S., & Zeller, R. (2010). Distinct roles of Hand2 in initiating polarity and posterior Shh expression during the onset of mouse limb bud development. *PLoS Genetics*, 6(4).

Gibson-Brown, J. J., Agulnik, S. I., Chapman, D. L., Alexiou, M., Garvey, N., Lee, S. M., & Papaioannou, V. E. (1996). Evidence of a role for T-box genes in the evolution of limb morphogenesis and the specification of forelimb/hindlimb identity. *Mechanisms of Development*, 56(1–2), 93–101.

Gibson-Brown, J. J., Agulnik, S. I., Silver, L. M., Niswander, L., & Papaioannou, V. E. (1998). Involvement of T-box genes Tbx2-Tbx5 in vertebrate limb specification and development. *Development*, 125(13), 2499–2509.

Giele, H., Giele, C., Bower, C., & Allison, M. (2001). The incidence and epidemiology of congenital upper limb anomalies: A total population study. *Journal of Hand Surgery*, 26(4), 628–634.

Goetz, S. C., & Anderson, K. V. (2010). The primary cilium: A signalling centre during vertebrate development. *Nature Reviews Genetics*, 11(5), 331–344.

Gordân, R., Hartemink, A. J., & Bulyk, M. L. (2009). Distinguishing direct versus indirect transcription factor-DNA interactions. *Genome Research*, 19(11), 2090–2100.

Gorkin et al. An atlas of dynamic chromatin landscapes in the developing mouse fetus. *Nature*, In Press.

Govoni, K. E., Linares, G. R., Chen, S. T., Pourteymoor, S., & Mohan, S. (2009). T-box 3 negatively regulates osteoblast differentiation by inhibiting expression of osterix and runx2. *Journal of Cellular Biochemistry*, 106(3), 482–490.

Grimaud, C., Nègre, N., & Cavalli, G. (2006). From genetics to epigenetics: The tale of Polycomb group and trithorax group genes. *Chromosome Research*, 14(4), 363–375.

Gros, J., & Tabin, C. J. (2014). Vertebrate limb bud formation is initiated by localized epithelial-to-mesenchymal transition. *Science*, 343(6176), 1253–1256.

Han, Y., Gao, S., Muegge, K., Zhang, W., & Zhou, B. (2015). Advanced applications of RNA sequencing and challenges. *Bioinformatics and Biology Insights*, 9, 29–46.

Haraguchi, R., Kitazawa, R., & Kitazawa, S. (2015). Epigenetic regulation of Tbx18 gene expression during endochondral bone formation. *Cell and Tissue Research*, 359(2), 503–512.

Harfe, B. D., Scherz, P. J., Nissim, S., Tian, H., McMahon, A. P., & Tabin, C. J. (2004). Evidence for an Expansion-Based Temporal Shh Gradient in Specifying Vertebrate Digit Identities protein (Driever and Nusslein-Volhard, 1988) to the patterning of the ventral neural tube by different concentrations of Sonic hedgehog (reviewed in McMahon. *Cell*, 118, 517–528.

Harrelson, Z., Kelly, R. G., Goldin, S. N., Gibson-Brown, J. J., Bollag, R. J., Silver, L. M., & Papaioannou, V. E. (2004). Tbx2 is essential for patterning the atrioventricular canal and for morphogenesis of the outflow tract during heart development. *Development*, 131(20), 5041–5052.

Hasegawa, Y., & Struhl, K. (2019). Promoter-specific dynamics of TATA-binding protein association with the human genome. *Genome Research*, 29(12), 1939–1950.

Hasson, P., DeLaurier, A., Bennett, M., Grigorieva, E., Naiche, L. A., Papaioannou, V. E.,

- Mohun, T. J., & Logan, M. P. O. (2010). Tbx4 and Tbx5 Acting in Connective Tissue Are Required for Limb Muscle and Tendon Patterning. *Developmental Cell*, 18(1), 148–156.
- Heintzman, N. D., Stuart, R. K., Hon, G., Fu, Y., Ching, C. W., Hawkins, R. D., Barrera, L. O., Van Calcar, S., Qu, C., Ching, K. A., Wang, W., Weng, Z., Green, R. D., Crawford, G. E., & Ren, B. (2007). Distinct and predictive chromatin signatures of transcriptional promoters and enhancers in the human genome. *Nature Genetics*, 39(3), 311–318.
- Heinz, S., Benner, C., Spann, N., Bertolino, E., Lin, Y. C., Laslo, P., Cheng, J. X., Murre, C., Singh, H., & Glass, C. K. (2010). Simple Combinations of Lineage-Determining Transcription Factors Prime cis-Regulatory Elements Required for Macrophage and B Cell Identities. *Molecular Cell*, 38(4), 576–589.
- Herrmann, B. G., Labeit, S., Poustka, A., King, T. R., & Lerach, H. (1990). Cloning of the T gene required in mesoderm development in the mouse. *Nature*, 343, 617–622.
- Herrmann, & Müller. (1997). *Crystallographic structure of the T domain – DNA complex of the Brachyury transcription factor*. 389(October), 884–888.
- Hojo, H., Chung, U. il, & Ohba, S. (2017). Identification of the gene-regulatory landscape in skeletal development and potential links to skeletal regeneration. *Regenerative Therapy*, 6, 100–107.
- Holmes, Z. E., Hamilton, D. J., Hwang, T., Parsonnet, N. V., Rinn, J. L., Wuttke, D. S., & Batey, R. T. (2020). The Sox2 transcription factor binds RNA. *Nature Communications*, 11(1).
- Hoogaars, W. M H, Engel, A., Brons, J. F., Verkerk, A. O., De Lange, F. J., Wong, L. Y. E., Bakker, M. L., Clout, D. E., Wakker, V., Barnett, P., Ravesloot, J. H., Moorman, A. F. M., Verheijck, E. E., & Christoffels, V. M. (2007). Tbx3 controls the sinoatrial node gene program and imposes pacemaker function on the atria. *Genes and Development*, 21(9), 1098–1112.
- Hoogaars, Willem M H, Barnett, P., Rodriguez, M., Clout, D. E., Moorman, A. F. M., Goding, C. R., & Christoffels, V. M. (2008). TBX3 and its splice variant TBX3 + exon 2a are functionally similar. *Pigment Cell and Melanoma Research*, 21(3), 379–387.
- Hoogaars, Willem M H, Tessari, A., Moorman, A. F. M., De Boer, P. A. J., Hagoort, J., Soufan, A. T., Campione, M., & Christoffels, V. M. (2004). The transcriptional repressor Tbx3 delineates the developing central conduction system of the heart. *Cardiovascular Research*, 62(3), 489–499.
- Horton, A. C., Mahadevan, N. R., Minguillon, C., Osoegawa, K., Rokhsar, D. S., Ruvinsky, I., de Jong, P. J., Logan, M. P., & Gibson-Brown, J. J. (2008). Conservation of linkage and evolution of developmental function within the Tbx2/3/4/5 subfamily of T-box genes: Implications for the origin of vertebrate limbs. *Development Genes and Evolution*, 218(11–12), 613–628.
- Hsu, H.-T., Chen, H.-M., Yang, Z., Wang, J., Lee, N. K., Burger, A., Zaret, K., Liu, T., Levine, E., & Mango, S. E. (2015). Recruitment of RNA polymerase II by the pioneer transcription factor PHA-4. *Science*, 348(6241), 1372–1376.
- Huang, C., Xiang, Y., Wang, Y., Li, X., Xu, L., Zhu, Z., Zhang, T., Zhu, Q., Zhang, K., Jing, N., & Chen, C. D. (2010). Dual-specificity histone demethylase KIAA1718 (KDM7A) regulates neural differentiation through FGF4. *Cell Research*, 20(2), 154–165.
- Hunt, J. R. (1996). Teratogenicity of high vitamin A intake. *The New England Journal of Medicine*, 334(18), 1197.

- Hwang, J. M., Weng, Y. J., Lin, J. A., Bau, D. T., Ko, F. Y., Tsai, F. J., Tsai, C. H., Wu, C. H., Lin, P. C., Huang, C. Y., & Kuo, W. W. (2008). Hypoxia-induced compensatory effect as related to Shh and HIF-1 α in ischemia embryo rat heart. *Molecular and Cellular Biochemistry*, *311*(1–2), 179–187.
- Hynes, R. O. (2009). The extracellular matrix: Not just pretty fibrils. *Science*, *326*(5957), 1216–1219.
- Ideker, T., Thorsson, V., Ranish, J. A., Christmas, R., Buhler, J., Eng, J. K., Bumgarner, R., Goodlett, D. R., Aebersold, R., & Hood, L. (2001). Integrated genomic and proteomic analyses of a systematically perturbed metabolic network. *Science*, *292*(5518), 929–934.
- Incardona, J. P., Lee, J. H., Robertson, C. P., Enga, K., Kapur, R. P., & Roelink, H. (2000). Receptor-mediated endocytosis of soluble and membrane-tethered sonic hedgehog by patched-1. *Proceedings of the National Academy of Sciences of the United States of America*, *97*(22), 12044–12049.
- Isaac, A., Rodriguez-Esteban, C., Ryan, A., Altabef, M., Tsukui, T., Patel, K., Tickle, C., & Izpisua-Belmonte, J. C. (1998). Tbx genes and limb identity in chick embryo development. *Development*, *125*(10), 1867–1875.
- Itou, J., Kawakami, H., Quach, T., Osterwalder, M., Evans, S. M., Zeller, R., & Kawakami, Y. (2012). Islet1 regulates establishment of the posterior hindlimb field upstream of the Hand2-Shh morphoregulatory gene network in mouse embryos. *Development*, *139*, 1620–1629.
- Jain, D., Nemeč, S., Luxey, M., Gauthier, Y., Bemmo, A., Balsalobre, A., & Drouin, J. (2018). Regulatory integration of Hox factor activity with T-box factors in limb development. *Development (Cambridge, England)*, *145*(6).
- Jerome-Majewska, L. A., Jenkins, G. P., Ernstoff, E., Zindy, F., Sherr, C. J., & Papaioannou, V. E. (2005). Tbx3, the ulnar-mammary syndrome gene, and Tbx2 interact in mammary gland development through a p19Arf/p53-independent pathway. *Developmental Dynamics*, *234*(4), 922–933.
- Joshi, O., Wang, S. Y., Kuznetsova, T., Atlasi, Y., Peng, T., Fabre, P. J., Habibi, E., Shaik, J., Saeed, S., Handoko, L., Richmond, T., Spivakov, M., Burgess, D., & Stunnenberg, H. G. (2015). Dynamic Reorganization of Extremely Long-Range Promoter-Promoter Interactions between Two States of Pluripotency. *Cell Stem Cell*, *17*(6), 748–757.
- Joss, S., Kini, U., Fisher, R., Mundlos, S., Prescott, K., Newbury-ecob, R., & Tolmie, J. (2011). European Journal of Medical Genetics The face of Ulnar Mammary syndrome? *European Journal of Medical Genetics*, *54*(3), 301–305.
- Kawakami, Y., Capdevila, J., Büscher, D., Itoh, T., Esteban, C. R., & Belmonte, J. C. I. (2001). WNT signals control FGF-dependent limb initiation and AER induction in the chick embryo. *Cell*, *104*(6), 891–900.
- Kawakami, Y., Uchiyama, Y., Esteban, C. R., Inenaga, T., Koyano-Nakagawa, N., Kawakami, H., Marti, M., Kmita, M., Monaghan-Nichols, P., Nishinakamura, R., & Belmonte, J. C. I. (2009). Sall genes regulate region-specific morphogenesis in the mouse limb by modulating Hox activities. *Development*, *136*(4), 585–594.
- Kellis, M., Wold, B., Snyder, M. P., Bernstein, B. E., Kundaje, A., Marinov, G. K., Ward, L. D., Birney, E., Crawford, G. E., Dekker, J., Dunham, I., Elnitski, L. L., Farnham, P. J., Feingold, E. A., Gerstein, M., Giddings, M. C., Gilbert, D. M., Gingeras, T. R., Green, E. D., Hardison, R. C. (2014). Defining functional DNA elements in the human genome.

Proceedings of the National Academy of Sciences of the United States of America, 111(17), 6131–6138.

Kimmel, R. A., Turnbull, D. H., Blanquet, V., Wurst, W., Loomis, C. A., & Joyner, A. L. (2000). Two lineage boundaries coordinate vertebrate apical ectodermal ridge formation. *Genes and Development*, 14(11), 1377–1389.

Kispert, A., & Herrmann, B. G. (1993). *The Brachyury protein novel DNA binding*. 12(8), 3211–3220.

Kispert, A., Koschorz, B., & Herrmann, B. G. (1995). *The T protein encoded by Brachyury is specific transcription factor*. 14(19), 4763–4772.

Klopocki, E., Neumann, L. M., Tönnies, H., Ropers, H.-H., Mundlos, S., & Ullmann, R. (2006). Ulnar-mammary syndrome with dysmorphic facies and mental retardation caused by a novel 1.28 Mb deletion encompassing the TBX3 gene. *European Journal of Human Genetics : EJHG*, 14(12), 1274–1279.

Kochhar, D. M. (1973). Limb development in mouse embryos. I. Analysis of teratogenic effects of retinoic acid. *Teratology*, 7(3), 289–298. <https://doi.org/10.1002/tera.1420070310>

Koskimies, E., Lindfors, N., Gissler, M., & Peltonen, J. (2011). Congenital Upper Limb Deficiencies and Associated Malformations in Finland : A Population-Based Study. *YJHSU*, 36(6), 1058–1065.

Kozhemyakina, E., Ionescu, A., & Lassar, A. B. (2014). GATA6 Is a Crucial Regulator of Shh in the Limb Bud. *PLoS Genetics*, 10(1). <https://doi.org/10.1371/journal.pgen.1004072>

Kraus, F., Haenig, B., & Kispert, A. (2001). Cloning and expression analysis of the mouse T-box gene Tbx20. *Mechanisms of Development*, 100(1), 87–91.

Krstic, M., Kolendowski, B., Cecchini, M. J., Postenka, C. O., Hassan, H. M., Andrews, J., MacMillan, C. D., Williams, K. C., Leong, H. S., Brackstone, M., Torchia, J., Chambers, A. F., & Tuck, A. B. (2019). TBX3 promotes progression of pre-invasive breast cancer cells by inducing EMT and directly up-regulating SLUG. *Journal of Pathology*, 248(2), 191–203.

Kuijper, S., Feitsma, H., Sheth, R., Korving, J., Reijnen, M., & Meijlink, F. (2005). Function and regulation of Alx4 in limb development: Complex genetic interactions with Gli3 and Shh. *Developmental Biology*, 285(2), 533–544.

Kumar, P., Franklin, S., Emechebe, U., Hu, H., Moore, B., Lehman, C., Yandell, M., & Moon, A. M. (2014). TBX3 Regulates Splicing In Vivo: A Novel Molecular Mechanism for Ulnar-Mammary Syndrome. *PLoS Genetics*, 10(3).

Laufer, E., Nelson, C. E., Johnson, R. L., Morgan, B. A., & Tabin, C. (1994). Sonic hedgehog and Fgf-4 act through a signaling cascade and feedback loop to integrate growth and patterning of the developing limb bud. *Cell*, 79(6), 993–1003.

Lausch, E., Hermanns, P., Farin, H. F., Alanay, Y., Unger, S., Nikkel, S., Steinwender, C., Scherer, G., Spranger, J., Zabel, B., Kispert, A., & Superti-Furga, A. (2008). TBX15 Mutations Cause Craniofacial Dysmorphism, Hypoplasia of Scapula and Pelvis, and Short Stature in Cousin Syndrome. *American Journal of Human Genetics*, 83(5), 649–655.

Lee, G., Kochhar, D., & Collins, M. (2005). Retinoid-Induced Limb Malformations. *Current Pharmaceutical Design*, 10(22), 2657–2699.

Lee, J. J., Ekker, S. C., Von Kessler, D. P., Porter, J. A., Sun, B. I., & Beachy, P. A. (1994). Autoproteolysis in hedgehog protein biogenesis. *Science*, 266(5190), 1528–1537.

Lee, T. I., Jenner, R. G., Boyer, L. A., Guenther, M. G., Levine, S. S., Kumar, R. M.,

- Chevalier, B., Johnstone, S. E., Cole, M. F., Isono, K., Koseki, H., Fuchikami, T., Abe, K., Murray, H. L., Zucker, J. P., Yuan, B., Bell, G. W., Herbolsheimer, E., Hannett, N. M., ... Young, R. A. (2006). Control of Developmental Regulators by Polycomb in Human Embryonic Stem Cells. *Cell*, *125*(2), 301–313.
- Leonard, L., Horton, C., Maden, M., & Pizzey, J. A. (1995). Anteriorization of CRABP-I expression by retinoic acid in the developing mouse central nervous system and its relationship to teratogenesis. In *Developmental Biology* (Vol. 168, Issue 2, pp. 514–528).
- Lettice, L. A., Heaney, S. J. H., Purdie, L. A., Li, L., de Beer, P., Oostra, B. A., Goode, D., Elgar, G., Hill, R. E., & de Graaff, E. (2003). A long-range Shh enhancer regulates expression in the developing limb and fin and is associated with preaxial polydactyly. *Human Molecular Genetics*, *12*(14), 1725–1735.
- Lettice, L. A., Williamson, I., Wiltshire, J. H., Peluso, S., Devenney, P. S., Hill, A. E., Essafi, A., Hagman, J., Mort, R., Grimes, G., DeAngelis, C. L., & Hill, R. E. (2012). Opposing Functions of the ETS Factor Family Define Shh Spatial Expression in Limb Buds and Underlie Polydactyly. *Developmental Cell*, *22*(2), 459–467.
- Lewandoski, M., Sun, X., & Martin, G. R. (2000a). Fgf8 signalling from the AER is essential for normal limb development. *Nature Genetics*, *26*(4), 460–463.
- Lewis, P. M., Dunn, M. P., McMahan, J. A., Logan, M., Martin, J. F., St-Jacques, B., & McMahan, A. P. (2001). Cholesterol modification of sonic hedgehog is required for long-range signaling activity and effective modulation of signaling by Ptc1. *Cell*, *105*(5), 599–612.
- Li, D., Sakuma, R., Vakili, N. A., Mo, R., Puviindran, V., Deimling, S., Zhang, X., Hopyan, S., & Hui, C. Chung. (2014). Formation of proximal and anterior limb skeleton requires early function of Irx3 and Irx5 and is negatively regulated by shh signaling. *Developmental Cell*, *29*(2), 233–240.
- Li, J., Ballim, D., Rodriguez, M., Cui, R., Goding, C. R., Teng, H., & Prince, S. (2014). The anti-proliferative function of the tgf- β 1 signaling pathway involves the repression of the oncogenic tbx2 by its homologue tbx3. *Journal of Biological Chemistry*, *289*(51), 35633–35643.
- Li, Y., Zhang, H., Litingtung, Y., & Chiang, C. (2006). Cholesterol modification restricts the spread of Shh gradient in the limb bud. *Proceedings of the National Academy of Sciences of the United States of America*, *103*(17), 6548–6553.
- Liang, G., Lin, J. C. Y., Wei, V., Yoo, C., Cheng, J. C., Nguyen, C. T., Weisenberger, D. J., Egger, G., Takai, D., Gonzales, F. A., & Jones, P. A. (2004). Distinct localization of histone H3 acetylation and H3-K4 methylation to the transcription start sites in the human genome. *Proceedings of the National Academy of Sciences of the United States of America*, *101*(19), 7357–7362.
- Liao, X., & Collins, M. D. (2008). All-trans retinoic acid-induced ectopic limb and caudal structures: Murine strain sensitivities and pathogenesis. *Developmental Dynamics*, *237*(6), 1553–1564.
- Linden, H., Williams, R., King, J., Blair, E., & Kini, U. (2009). Ulnar mammary syndrome and TBX3: Expanding the phenotype. *American Journal of Medical Genetics, Part A*, *149*(12), 2809–2812.
- Litingtung, Y., Li, Y., Fallon, J. F., & Chiang, C. (2002). Shh and Gli3 are dispensable for limb skeleton formation but regulate digit number and identity. *Nature*, *418*(6901), 979–983.
- Liu, C., Nakamura, E., Knezevic, V., Hunter, S., Thompson, K., & Mackem, S. (2003). A

- role for the mesenchymal T-box gene *Brachyury* in AER formation during limb development. *Development*, *130*(7), 1327–1337.
- Logan, M., Simon, H. G., & Tabin, C. (1998). Differential regulation of T-box and homeobox transcription factors suggests roles in controlling chick limb-type identity. *Development*, *125*(15), 2825–2835.
- Lonai, P. (2003). Epithelial mesenchymal interactions, the ECM and limb development. *Journal of Anatomy*, *202*(1), 43–50.
- Lopez-Rios, J. (2016). The many lives of SHH in limb development and evolution. *Seminars in Cell and Developmental Biology*, *49*(2015), 116–124.
- Lopez-Rios, J., Speziale, D., Robay, D., Scotti, M., Osterwalder, M., Nusspaumer, G., Galli, A., Hollander, G. A., Kmita, M., & Zeller, R. (2012). GLI3 Constrains Digit Number by Controlling Both Progenitor Proliferation and BMP-Dependent Exit to Chondrogenesis. *Developmental Cell*, *22*(4), 837–848.
- Lu, P., Takai, K., Weaver, V. M., & Werb, Z. (2011). Extracellular Matrix Degradation and Remodeling in Development and Disease. *Cold Spring Harbor Perspectives in Biology*, *3*(12), a005058–a005058.
- Lüdtke, T. H., Rudat, C., Wojahn, I., Weiss, A. C., Kleppa, M. J., Kurz, J., Farin, H. F., Moon, A., Christoffels, V. M., & Kispert, A. (2016). *Tbx2* and *Tbx3* Act Downstream of *Shh* to Maintain Canonical Wnt Signaling during Branching Morphogenesis of the Murine Lung. *Developmental Cell*, *39*(2), 239–253.
- Luna-Zurita, L., Stirnimann, C. U., Glatt, S., Kaynak, B. L., Thomas, S., Baudin, F., Samee, M. A. H., He, D., Small, E. M., Mileikovsky, M., Nagy, A., Holloway, A. K., Pollard, K. S., Muller, C. W., & Bruneau, B. G. (2016). Complex Interdependence Regulates Heterotypic Transcription Factor Distribution and Coordinates Cardiogenesis. *Cell*, *164*(5), 999–1014.
- Lupiáñez, D. G., Kraft, K., Heinrich, V., Krawitz, P., Brancati, F., Klopocki, E., Horn, D., Kayserili, H., Opitz, J. M., Laxova, R., Santos-Simarro, F., Gilbert-Dussardier, B., Wittler, L., Borschiwer, M., Haas, S. A., Osterwalder, M., Franke, M., Timmermann, B., Hecht, J., ... Mundlos, S. (2015). Disruptions of topological chromatin domains cause pathogenic rewiring of gene-enhancer interactions. *Cell*, *161*(5), 1012–1025.
- MacLean, G., Abu-Abed, S., Dollé, P., Tahayato, A., Chambon, P., & Petkovich, M. (2001). Cloning of a novel retinoic-acid metabolizing cytochrome P450, *Cyp26B1*, and comparative expression analysis with *Cyp26A1* during early murine development. *Mechanisms of Development*, *107*(1–2), 195–201.
- Maden, M. (2020). *RA Signaling in Limb Development and Regeneration in Different Species*. Springer International Publishing.
- Mallo, M., & Alonso, C. R. (2013). The regulation of Hox gene expression during animal development. *Development (Cambridge)*, *140*(19), 3951–3963.
- Manning, L., Ohyama, K., Saeger, B., Hatano, O., Wilson, S. A., Logan, M., & Placzek, M. (2006). Regional Morphogenesis in the Hypothalamus: A BMP-*Tbx2* Pathway Coordinates Fate and Proliferation through *Shh* Downregulation. *Developmental Cell*, *11*(6), 873–885.
- Mailleux, A.A., Spencer-Dene, B., Dillon, C., Ndiaye, D., Savona-Baron, C., Itoh, N., Kato, S., Dickson, C., Thiery, J.P., Bellusci, S., 2002. Role of FGF10/FGFR2b signaling during mammary gland development in the mouse embryo. *Development*, *129*, 53–60.
- MacCabe J.A., Errick J., Saunders Jr. J.W. Ectodermal control of the dorsoventral axis in the

leg bud of the chick embryo. *Dev. Biol.*, 39 (1974), pp. 69-82

MacCabe J.A., Saunders Jr. J.W., Pickett M. The control of the anteroposterior and dorsoventral axes in embryonic chick limbs constructed of dissociated and reaggregated limb-bud mesoderm. *Dev. Biol.*, 31 (1973), pp. 323-335

Mariani, F. V., Ahn, C. P., & Martin, G. R. (2008). Genetic evidence that FGFs have an instructive role in limb proximal-distal patterning. *Nature*, 453(7193), 401–405.

Matsumoto, K., Li, Y., Jakuba, C., Sugiyama, Y., Sayo, T., Okuno, M., Dealy, C. N., Toole, B. P., Takeda, J., Yamaguchi, Y., & Kosher, R. A. (2009). Conditional inactivation of Has2 reveals a crucial role for hyaluronan in skeletal growth, patterning, chondrocyte maturation and joint formation in the developing limb. *Development*, 136(16), 2825–2835.

McCulloch, D. R., Nelson, C. M., Dixon, L. J., Silver, D. L., Wylie, J. D., Lindner, V., Sasaki, T., Cooley, M. A., Argraves, W. S., & Apte, S. S. (2009). ADAMTS Metalloproteases Generate Active Versican Fragments that Regulate Interdigital Web Regression. *Developmental Cell*, 17(5), 687–698.

McFadden, D. G., McAnally, J., Richardson, J. A., Charité, J., & Olson, E. N. (2002). Misexpression of dHAND induces ectopic digits in the developing limb bud in the absence of direct DNA binding. *Development*, 129(13), 3077–3088.

Meneghini, V., Odent, S., Platonova, N., Egeo, A., & Merlo, G. R. (2006). Novel TBX3 mutation data in families with Ulnar-Mammary syndrome indicate a genotype-phenotype relationship: Mutations that do not disrupt the T-domain are associated with less severe limb defects. *European Journal of Medical Genetics*, 49(2), 151–158.

Mercader, N., Leonardo, E., Piedra, M. E., Martinez-A., C., Ros, M. A., & Torres, M. (2000). Opposing RA and FGF signals control proximodistal vertebrate limb development through regulation of Meis genes. *Development*, 127(18), 3961–3970.

Mercader, Nadia, Selleri, L., Criado, L. M., Pallares, P., Parras, C., Cleary, M. L., & Torres, M. (2009). Ectopic Meis1 expression in the mouse limb bud alters P-D patterning in a Pbx1-independent manner. *International Journal of Developmental Biology*, 53(8–10), 1483–1494.

Mesbah, K., Harrelson, Z., Théveniau-Ruissy, M., Papaioannou, V. E., & Kelly, R. G. (2008). Tbx3 is required for outflow tract development. *Circulation Research*, 103(7), 743–750.

Mic, F. A., Molotkov, A., Molotkova, N., & Duester, G. (2004). Raldh2 expression in optic vesicle generates a retinoic acid signal needed for invagination of retina during optic cup formation. *Developmental Dynamics*, 231(2), 270–277.

Michaud, J. L., Lapointe, F., & Le Douarin, N. M. (1997). The dorsoventral polarity of the presumptive limb is determined by signals produced by the somites and by the lateral somatopleure. *Development*, 124(8), 1453–1463.

Michos, O., Panman, L., Vintersten, K., Beier, K., Zeller, R., & Zuniga, A. (2004). Gremlin-mediated BMP antagonism induces the epithelial-mesenchymal feedback signaling controlling metanephric kidney and limb organogenesis. *Development (Cambridge, England)*, 131(14), 3401–3410.

Min, H., Danilenko, D. M., Scully, S. A., Bolon, B., Ring, B. D., Tarpley, J. E., DeRose, M., & Simonet, W. S. (1998). Fgf-10 is required for both limb and lung development and exhibits striking functional similarity to *Drosophila* branchless. *Genes and Development*, 12(20), 3156–3161.

- Minguillon, C., Del Buono, J., & Logan, M. P. (2005). Tbx5 and Tbx4 are not sufficient to determine limb-specific morphologies but have common roles in initiating limb outgrowth. *Developmental Cell*, 8(1), 75–84.
- Minguillon, C., Gibson-Brown, J. J., & Logan, M. P. (2009). Tbx4/5 gene duplication and the origin of vertebrate paired appendages. *Proceedings of the National Academy of Sciences of the United States of America*, 106(51), 21726–21730.
- Morriss-Kay, G. M., & Wardt, S. J. (1999). *Retinoids and Mammalian Development* (pp. 73–131).
- Mosca, E., Bertoli, G., Piscitelli, E., Vilardo, L., Reinbold, R. A., Zucchi, I., & Milanesi, L. (2009). Identification of functionally related genes using data mining and data integration: A breast cancer case study. *BMC Bioinformatics*, 10(SUPPL. 12), 1–11.
- Naiche, L. A., Harrelson, Z., Kelly, R. G., & Papaioannou, V. E. (2005). T-Box Genes in Vertebrate Development. *Annual Review of Genetics*, 39(1), 219–239. <https://doi.org/10.1146/annurev.genet.39.073003.105925>
- Naiche, L. A., & Papaioannou, V. E. (2003). Loss of Tbx4 blocks hindlimb development and affects vascularization and fusion of the allantois. *Development*, 130(12), 2681–2693.
- Naiche, L. A., & Papaioannou, V. E. (2007). Tbx4 is not required for hindlimb identity or post-bud hindlimb outgrowth. *Development*, 134(1), 93–103.
- Nguyen, V. T., Canciani, B., Cirillo, F., Anastasia, L., Peretti, G. M., & Mangiavini, L. (2020). Effect of Chemically Induced Hypoxia on Osteogenic and Angiogenic Differentiation of Bone Marrow Mesenchymal Stem Cells and Human Umbilical Vein Endothelial Cells in Direct Coculture. *Cells*, 9(3), 757.
- Niederreither, K., Subbarayan, V., Dollé, P., & Chambon, P. (1999). Embryonic retinoic acid synthesis is essential for early mouse post-implantation development. *Nature Genetics*, 21(4), 444–448.
- Niederreither, K., Vermot, J., Schuhbauer, B., Chambon, P., & Dollé, P. (2002). Embryonic retinoic acid synthesis is required for forelimb growth and anteroposterior patterning in the mouse. *Development*, 129(15), 3563–3574.
- Niederreither, K., Ward, S. J., Dollé, P., & Chambon, P. (1996). Morphological and molecular characterization of retinoic acid-induced limb duplications in mice. *Developmental Biology*, 176(2), 185–198.
- Nissim, S., Allard, P., Bandyopadhyay, A., Harfe, B. D., & Tabin, C. J. (2007a). Characterization of a novel ectodermal signaling center regulating Tbx2 and Shh in the vertebrate limb. *Developmental Biology*, 304(1), 9–21.
- Nissim, S., Allard, P., Bandyopadhyay, A., Harfe, B. D., & Tabin, C. J. (2007b). *Characterization of a novel ectodermal signaling center regulating Tbx2 and Shh in the vertebrate limb*. 304, 9–21.
- Nissim, S., Hasso, S. M., Fallon, J. F., & Tabin, C. J. (2006). Regulation of Gremlin expression in the posterior limb bud. *Developmental Biology*, 299(1), 12–21.
- Niswander, L., Jeffrey, S., Martin, G. R., & Tickle, C. (1994). A positive feedback loop coordinates growth and patterning in the vertebrate limb. *Nature*, 371(6498), 609–612.
- Niswander, L., Tickle, C., Vogel, A., Booth, I., & Martin, G. R. (1993). FGF-4 replaces the apical ectodermal ridge and directs outgrowth and patterning of the limb. *Cell*, 75(3), 579–587.

- Norton, W. H. J., Ledin, J., Grandel, H., & Neumann, C. J. (2005). HSPG synthesis by zebrafish Ext2 and Extl3 is required for Fgf10 signalling during limb development. *Development*, *132*(22), 4963–4973.
- Nowosad, K., Hordyjewska-Kowalczyk, E., & Tylzanowski, P. (2020). Mutations in gene regulatory elements linked to human limb malformations. *Journal of Medical Genetics*, *57*(6), 361–370.
- Oh, T. J., Adhikari, A., Mohamad, T., Althobaiti, A., & Davie, J. (2019). TBX3 represses TBX2 under the control of the PRC2 complex in skeletal muscle and rhabdomyosarcoma. *Oncogenesis*, *8*(4).
- Ohuchi, H., Nakagawa, T., Yamamoto, A., Araga, A., Ohata, T., Ishimaru, Y., Yoshioka, H., Kuwana, T., Nohno, T., Yamasaki, M., Itoh, N., & Noji, S. (1997). The mesenchymal factor, FGF10, initiates and maintains the outgrowth of the chick limb bud through interaction with FGF8, an apical ectodermal factor. *Development*, *124*(11), 2235–2244.
- Okano, M., Bell, D. W., Haber, D. A., & Li, E. (1999). DNA methyltransferases Dnmt3a and Dnmt3b are essential for de novo methylation and mammalian development. *Cell*, *99*(3), 247–257.
- Omar, R., Cooper, A., Maranyane, H. M., Zerbini, L., & Prince, S. (2019). COL1A2 is a TBX3 target that mediates its impact on fibrosarcoma and chondrosarcoma cell migration. *Cancer Letters*, *459*(February), 227–239.
- Osterwalder, M., Barozzi, I., Tissières, V., Fukuda-yuzawa, Y., Brandon, J., Afzal, S. Y., Lee, E. A., Zhu, Y., Plajzer-frick, I., Catherine, S., Kato, M., Garvin, T. H., Pham, Q. T., Harrington, A. N., Jennifer, A., Afzal, V., Lopez-rios, J., Dickel, D. E., Visel, A., & Len, A. (2018). Enhancer Redundancy Allows for Phenotypic Robustness in Mammalian Development. *Nature*, *554*(7691), 239–243.
- Osterwalder, M., Speziale, D., Shoukry, M., Mohan, R., Ivanek, R., Kohler, M., Beisel, C., Wen, X., Scales, S. J., Christoffels, V. M., Visel, A., Lopez-Rios, J., & Zeller, R. (2014). HAND2 targets define a network of transcriptional regulators that compartmentalize the early limb bud mesenchyme. *Developmental Cell*, *31*(3), 345–357.
- Oulad-Abdelghani, M., Chazaud, C., Bouillet, P., Sapin, V., Chambon, P., & Dollé, P. (1997). Meis2, a novel mouse Pbx-related homeobox gene induced by retinoic acid during differentiation of P19 embryonal carcinoma cells. *Developmental Dynamics*, *210*(2), 173–183.
- Packham, E. A. (2003). T-box genes in human disorders. *Human Molecular Genetics*, *12*(90001), 37R – 44.
- Page-McCaw, A., Ewald, A. J., & Werb, Z. (2007). Matrix metalloproteinases and the regulation of tissue remodelling. *Nature Reviews Molecular Cell Biology*, *8*(3), 221–233.
- Pan, G., Tian, S., Nie, J., Yang, C., Ruotti, V., Wei, H., Jonsdottir, G. A., Stewart, R., & Thomson, J. A. (2007). Whole-Genome Analysis of Histone H3 Lysine 4 and Lysine 27 Methylation in Human Embryonic Stem Cells. *Cell Stem Cell*, *1*(3), 299–312.
- Pandey, S. N., Cabotage, J., Shi, R., Dixit, M., Sutherland, M., Liu, J., Muger, S., Harper, S. Q., Nagaraju, K., & Chen, Y. W. (2012). Conditional over-expression of PITX1 causes skeletal muscle dystrophy in mice. *Biology Open*, *1*(7), 629–639.
- Panman, L., Drenth, T., Tewelscher, P., Zuniga, A., & Zeller, R. (2005). Genetic interaction of Gli3 and Alx4 during limb development. *International Journal of Developmental Biology*, *49*(4), 443–448.

- Papayioannou, V. E. (2014). *The T-box gene family: emerging roles in development, stem cells and cancer*. 3819–3833.
- Papayioannou, V. E., & Silver, L. M. (1998). The T-box gene family. *BioEssays*, 20(1), 9–19.
- Peres, J., Mowla, S., & Prince, S. (2014). *The T-box transcription factor, TBX3, is a key substrate of AKT3 in melanomagenesis*. 6(3).
- Peres, J., & Prince, S. (2013). The T-box transcription factor, TBX3, is sufficient to promote melanoma formation and invasion. *Molecular Cancer*, 12(1), 117.
- Platt, K. A., Michaud, J., & Joyner, A. L. (1997). Expression of the mouse Gli and Ptc genes is adjacent to embryonic sources of hedgehog signals suggesting a conservation of pathways between flies and mice. *Mechanisms of Development*, 62(2), 121–135.
- Pontecorvi, M., Goding, C. R., Richardson, W. D., & Kessar, N. (2008). *Gene Expression Patterns Expression of Tbx2 and Tbx3 in the developing hypothalamic – pituitary axis*. 8, 411–417.
- Potier, E., Ferreira, E., Andriamanalijaona, R., Pujol, J. P., Oudina, K., Logeart-Avramoglou, D., & Petite, H. (2007). Hypoxia affects mesenchymal stromal cell osteogenic differentiation and angiogenic factor expression. *Bone*, 40(4), 1078–1087.
- Probst, S., Kraemer, C., Demougin, P., Sheth, R., Martin, G. R., Shiratori, H., Hamada, H., Iber, D., Zeller, R., & Zuniga, A. (2011). SHH propagates distal limb bud development by enhancing CYP26B1-mediated retinoic acid clearance via AER-FGF signalling. *Development*, 138(10), 1913–1923.
- Protze, S. I., Liu, J., Nussinovitch, U., Ohana, L., Backx, P. H., Gepstein, L., & Keller, G. M. (2017). Sinoatrial node cardiomyocytes derived from human pluripotent cells function as a biological pacemaker. *Nature Biotechnology*, 35(1), 56–68.
- Rada-Iglesias, A. (2018). Is H3K4me1 at enhancers correlative or causative? *Nature Genetics*, 50(1), 4–5.
- Rada-Iglesias, A., Bajpai, R., Swigut, T., Brugmann, S. A., Flynn, R. A., & Wysocka, J. (2011). A unique chromatin signature uncovers early developmental enhancers in humans. *Nature*, 470(7333), 279–285.
- Radio, F. C., Bernardini, L., Loddo, S., Bottillo, I., Novelli, A., Mingarelli, R., & Dallapiccola, B. (2010). TBX2 gene duplication associated with complex heart defect and skeletal malformations. *American Journal of Medical Genetics, Part A*, 152(8), 2061–2066.
- Raines, A. M., Magella, B., Adam, M., & Potter, S. S. (2015). Key pathways regulated by HoxA9,10,11/HoxD9,10,11 during limb development. *BMC Developmental Biology*, 15(1), 1–15.
- Rallis, C., Bruneau, B. G., Del Buono, J., Seidman, C. E., Seidman, J. G., Nissim, S., Tabin, C. J., & Logan, M. P. O. (2003). Tbx5 is required for forelimb bud formation and continued outgrowth. *Development*, 130(12), 2741–2751.
- Rallis, C., Del Buono, J., & Logan, M. P. O. (2005). Tbx3 can alter limb position along the rostrocaudal axis of the developing embryo. *Development (Cambridge, England)*, 132(8), 1961–1970.
- Raspopovic, J., Marcon, L., Russo, L., & Sharpe, J. (2014). Digit patterning is controlled by a Bmp-Sox9-Wnt Turing network modulated by morphogen gradients. *Science*, 345(6196), 566–570.

- Revest, J. M., Spencer-Dene, B., Kerr, K., De Moerlooze, L., Rosewell, I., & Dickson, C. (2001). Fibroblast growth factor receptor 2-IIIb acts upstream of Shh and Fgf4 and is required for limb bud maintenance but not for the induction of Fgf8, Fgf10, Msx1, or Bmp4. *Developmental Biology*, 231(1), 47–62.
- Ribeiro, I., Kawakami, Y., Büscher, D., Raya, Á., Rodríguez-León, J., Morita, M., Rodríguez Esteban, C., & Izpisua Belmonte, J. C. (2007). Tbx2 and Tbx3 regulate the dynamics of cell proliferation during heart remodeling. *PLoS ONE*, 2(4).
- Richert, M. M., Schwertfeger, K. L., Ryder, J. W., & Anderson, S. M. (2000). *An Atlas of Mouse Mammary Gland Development - art%3A10.1023%2FA%3A1026499523505.pdf*. 5(2), 227–228.
- Riddle, R. D., Johnson, R. L., Laufer, E., & Tabin, C. (1993). Sonic hedgehog mediates the polarizing activity of the ZPA. *Cell*, 75(7), 1401–1416.
- Rizzino, A., & Wuebben, E. L. (2016). Sox2/Oct4: A delicately balanced partnership in pluripotent stem cells and embryogenesis. *Biochimica et Biophysica Acta - Gene Regulatory Mechanisms*, 1859(6), 780–791.
- Rodríguez-Esteban, C., Tsukul, T., Yonel, S., Magallon, J., Tamura, K., & Izpisua Belmonte, J. C. (1999). The T-box genes Tbx4 and Tbx5 regulate limb outgrowth and identity. *Nature*, 398(6730), 814–818.
- Rodríguez, M., Aladowicz, E., Lanfrancone, L., & Goding, C. R. (2008). Tbx3 represses E-cadherin expression and enhances melanoma invasiveness. *Cancer Research*, 68(19), 7872–7881.
- Rosello-Diez, A., Ros, M. A., & Torres, M. (2011). Diffusible Signals, Not Autonomous Mechanisms, Determine the Main Proximodistal Limb Subdivision. *Science*, 332(6033), 1086–1088.
- Ross, R., Dagnone, D., Jones, P. J. H., Smith, H., Paddags, A., Hudson, R., & Janssen, I. (2000). Diet-Induced Weight Loss or Exercise-Induced Weight Loss in Men. *Annals of Internal Medicine*, 133(14), 92–103.
- Russ, A. P., Wattler, S., Colledge, W. H., Aparicio, S. A. J. R., Carlton, M. B. L., Pearce, J. J., Barton, S. C., Azim Surani, M., Ryan, K., Nehls, M. C., Wilsons, V., & Evans, M. J. (2000). Eomesodermin is required for mouse trophoblast development and mesoderm formation. *Nature*, 404(6773), 95–99.
- Russell, R., Ilg, M., Lin, Q., Wu, G., Lechel, A., Bergmann, W., Eiseler, T., Linta, L., Kumar, P. P., Klingenstein, M., Adachi, K., Hohwieler, M., Sakk, O., Raab, S., Moon, A., Zenke, M., Seufferlein, T., Schöler, H. R., Illing, A., ... Kleger, A. (2015). A Dynamic Role of TBX3 in the Pluripotency Circuitry. *Stem Cell Reports*, 5(6), 1155–1170.
- Saunders J.W., Gasseling M.T. Ectodermal-mesenchymal interactions in the origin of limb symmetry. R. Fleischmajer, R.E. Billingham (Eds.), *Epithelial-Mesenchymal Interactions*, Williams & Wilkins, Baltimore (1968), pp. 78-97
- Saunders J.W., Gasseling M.T., Cairns J.M. The differentiation of prospective thigh mesoderm grafted beneath the apical ectodermal ridge of the wing bud in the chick embryo. *Dev. Biol.*, 1 (1959), pp. 281-301
- Sanz-Ezquerro, J. J., & Tickle, C. (2000). Autoregulation of Shh expression and Shh induction of cell death suggest a mechanism for modulating polarising activity during chick limb development. *Development*, 127(22), 4811–4823.

- Scherz, P. J., Harfe, B. D., McMahon, A. P., & Tabin, C. J. (2004). The limb bud Shh-Fgf feedback loop is terminated by expansion of former ZPA cells. *Science*, *305*(5682), 396–399.
- Schinzel, A. (1987). Ulnar-mammary syndrome. *Journal of Medical Genetics*, *24*, 778–781.
- Schipani, E., Ryan, H. E., Didrickson, S., Kobayashi, T., Knight, M., & Johnson, R. S. (2001). Hypoxia in cartilage: HIF-1 α is essential for chondrocyte growth arrest and survival. *Genes and Development*, *15*(21), 2865–2876.
- Schwartz, S., Meshorer, E., & Ast, G. (2009). Chromatin organization marks exon-intron structure. *Nature Structural and Molecular Biology*, *16*(9), 990–995.
- Sears, K. E., Behringer, R. R., Rasweiler IV, J. J., & Niswander, L. A. (2006). Development of bat flight: Morphologic and molecular evolution of bat wing digits. *Proceedings of the National Academy of Sciences of the United States of America*, *103*(17), 6581–6586.
- Sekine, K., Ohuchi, H., Fujiwara, M., Yamasaki, M., Yoshizawa, T., Sato, T., Yagishita, N., Matsui, D., Koga, Y., Itoh, N., & Kato, S. (1999). Fgf10 is essential for limb and lung formation. *Nature Genetics*, *21*(1), 138–141.
- Sen, G. L., Webster, D. E., Barragan, D. I., Chang, H. Y., & Khavari, P. A. (2008). Control of differentiation in a self-renewing mammalian tissue by the histone demethylase JMJD3. *Genes & Development*, *22*(14), 1865–1870.
- Shamseldin, H. E., Anazi, S., Wakil, S. M., Faqeih, E., El Khashab, H. Y., Salih, M. A., Al-Qattan, M. M., Hashem, M., Alsedairy, H., & Alkuraya, F. S. (2016). Novel copy number variants and major limb reduction malformation: Report of three cases. *American Journal of Medical Genetics, Part A*, *170*(5), 1245–1250.
- Sharp, F. R., & Bernaudin, M. (2004). HIF1 and oxygen sensing in the brain. *Nature Reviews Neuroscience*, *5*(6), 437–448.
- Sherman, L., Wainwright, D., Ponta, H., & Herrlich, P. (1998). A splice variant of CD44 expressed in the apical ectodermal ridge presents fibroblast growth factors to limb mesenchyme and is required for limb outgrowth. *Genes and Development*, *12*(7), 1058–1071.
- Sheth, F. J., Liehr, T., Kumari, P., Akinde, R., Sheth, H. J., & Sheth, J. J. (2013). Chromosomal abnormalities in couples with repeated fetal loss: An Indian retrospective study. *Indian Journal of Human Genetics*, *19*(4), 415–422.
- Sheth, R., Marcon, L., Bastida, M. F., Junco, M., Quintana, L., Dahn, R., Kmita, M., Sharpe, J., & Ros, M. A. (2012). Hox Genes Regulate Digit Patterning by Controlling the Wavelength of a Turing-Type Mechanism. *Science*, *338*(6113), 1476–1480.
- Shimizu, H., Yokoyama, S., & Asahara, H. (2007). Growth and differentiation of the developing limb bud from the perspective of chondrogenesis. *Development Growth and Differentiation*, *49*(6), 449–454.
- Shirai, M., Imanaka-Yoshida, K., Schneider, M. D., Schwartz, R. J., & Morisaki, T. (2009). T-box 2, a mediator of Bmp-Smad signaling, induced hyaluronan synthase 2 and Tgf 2 expression and endocardial cushion formation. *Proceedings of the National Academy of Sciences*, *106*(44), 18604–18609.
- Singh, R., Horsthuis, T., Farin, H. F., Grieskamp, T., Norden, J., Petry, M., Wakker, V., Moorman, A. F. M., Christoffels, V. M., & Kispert, A. (2009). Tbx20 interacts with smads to confine tbx2 expression to the atrioventricular canal. *Circulation Research*, *105*(5), 442–452.
- Soufi, A., Donahue, G., & Zaret, K. S. (2012). Facilitators and Impediments of the Pluripotency Reprogramming Factors' Initial Engagement with the Genome. *Cell*, *151*(5),

994–1004.

Stanzel, S., Stubbusch, J., Pataskar, A., Howard, M. J., Deller, T., Ernsberger, U., Tiwari, V. K., Rohrer, H., & Tsarovina, K. (2016). Distinct roles of *hand2* in developing and adult autonomic neurons. *Developmental Neurobiology*, *76*(10), 1111–1124.

Stern, M., Jensen, R., & Herskowitz, I. (1984). Five SWI genes are required for expression of the HO gene in yeast. *Journal of Molecular Biology*, *178*(4), 853–868. [https://doi.org/10.1016/0022-2836\(84\)90315-2](https://doi.org/10.1016/0022-2836(84)90315-2)

Stratford, T., Logan, C., Zile, M., & Maden, M. (1999). Abnormal anteroposterior and dorsoventral patterning of the limb bud in the absence of retinoids. *Mechanisms of Development*, *81*(1–2), 115–125.

Suemori, H., & Noguchi, S. (2000). Hox C cluster genes are dispensable for overall body plan of mouse embryonic development. *Developmental Biology*, *220*(2), 333–342.

Sun, X., Mariani, F. V., & Martin, G. R. (2002). Functions of FGF signalling from the apical ectodermal ridge in limb development. *Nature*, *418*(6897), 501–508.

Suzuki, T., Takeuchi, J., Koshiba-Takeuchi, K., & Ogura, T. (2004a). Tbx genes specify posterior digit identity through Shh and BMP signaling. *Developmental Cell*, *6*(1), 43–53.

Suzuki, T., Takeuchi, J., Koshiba-Takeuchi, K., & Ogura, T. (2004b). Tbx genes specify posterior digit identity through Shh and BMP signaling. *Developmental Cell*, *6*(1), 43–53.

Swigut, T., & Wysocka, J. (2007). H3K27 Demethylases, at Long Last. *Cell*, *131*(1), 29–32.

Tumpel, S., Sanz-Ezquerro, J. J., Isaac, A., Eblaghie, M. C., Dobson, J., & Tickle, C. (2002). Regulation of Tbx3 expression by anteroposterior signalling in vertebrate limb development. *Developmental Biology*, *250*(2), 251–262.

Tabin, C. J. (1991). Retinoids, homeoboxes, and growth factors: Toward molecular models for limb development. *Cell*, *66*(2), 199–217.

Takeuchi, J. K., Koshiba-Takeuchi, K., Matsumoto, K., Vogel-Höpker, A., Naitoh-Matsuo, M., Ogura, K., Takahashi, N., Yasuda, K., & Ogura, T. (1999). Tbx5 and Tbx4 genes determine the wing/leg identity of limb buds. *Nature*, *398*(6730), 810–814.

Tamura, K., Yokouchi, Y., Kuroiwa, A., & Ide, H. (1997). Retinoic acid changes the proximodistal developmental competence and affinity of distal cells in the developing chick limb bud. *Developmental Biology*, *188*(2), 224–234.

Tanaka, M., Tamura, K., Noji, S., Nohno, T., & Ide, H. (1997). Induction of additional limb at the dorsal-ventral boundary of a chick embryo. *Developmental Biology*, *182*(1), 191–203.

Tanteles, G. A., Nicolaou, N., Syrimis, A., Metaxa, R., Nicolaou, M., Christophidou-Anastasiadou, V., & Skordis, N. (2017). Novel TBX3 mutation in a family of Cypriot ancestry with ulnar-mammary syndrome. *Clinical Dysmorphology*, *26*(2), 61–65.

Tarchini, B., & Duboule, D. (2006). Control of Hoxd genes' collinearity during early limb development. *Developmental Cell*, *10*(1), 93–103.

te Welscher, P. (2002). Progression of Vertebrate Limb Development Through SHH-Mediated Counteraction of GLI3. *Science*, *298*(5594), 827–830.

te Welscher, Pascal, Fernandez-Teran, M., Ros, M. A., & Zeller, R. (2002). Mutual genetic antagonism involving GLI3 and dHAND prepatterns the vertebrate limb bud mesenchyme prior to SHH signaling. *Genes and Development*, *16*(4), 421–426.

Thurman, R. E., Rynes, E., Humbert, R., Vierstra, J., Maurano, M. T., Haugen, E., Sheffield,

- N. C., Stergachis, A. B., Wang, H., Vernot, B., Garg, K., John, S., Sandstrom, R., Bates, D., Boatman, L., Canfield, T. K., Diegel, M., Dunn, D., Ebersol, A. K., ... Stamatoyannopoulos, J. A. (2012). The accessible chromatin landscape of the human genome. *Nature*, *489*(7414), 75–82.
- Trowe, M. O., Zhao, L., Weiss, A. C., Christoffels, V., Epstein, D. J., & Kispert, A. (2012). Inhibition of Sox2-dependent activation of Shh in the ventral diencephalon by Tbx3 is required for formation of the neurohypophysis. *Development (Cambridge)*, *140*(11), 2299–2309.
- Van Den Boogaard, M., Barnett, P., Vincent, M., Boogaard, M. Van Den, Wong, L. Y. E., Tessadori, F., & Bakker, M. L. (2012). Genetic variation in T-box binding element functionally affects SCN5A / SCN10A enhancer Find the latest version : Genetic variation in T-box binding element functionally affects SCN5A / SCN10A enhancer. *The Journal of Clinical Investigation*, *122*(7), 2519–2530.
- Varjosalo, M., & Taipale, J. (2008). Hedgehog: Functions and mechanisms. *Genes and Development*, *22*(18), 2454–2472.
- Veltmaat, J. M., Van Veelen, W., Thiery, J. P., & Bellusci, S. (2004). Identification of the Mammary Line in Mouse by Wnt10b Expression. *Developmental Dynamics*, *229*(2), 349–356.
- Verheyden, J. M., & Sun, X. (2008). An Fgf/Gremlin inhibitory feedback loop triggers termination of limb bud outgrowth. *Nature*, *454*(7204), 638–641.
- Visel, A., Minovitsky, S., Dubchak, I., & Pennacchio, L. A. (2007). VISTA Enhancer Browser - A database of tissue-specific human enhancers. *Nucleic Acids Research*, *35*(SUPPL. 1), 88–92.
- Vogel, A., Rodriguez, C., & Izpisua-Belmonte, J. C. (1996). Involvement of FGF-8 in initiation, outgrowth and patterning of the vertebrate limb. *Development*, *122*(6), 1737–1750.
- Voigt, P., Tee, W. W., & Reinberg, D. (2013). A double take on bivalent promoters. *Genes and Development*, *27*(12), 1318–1338.
- Wang, B., Fallon, J. F., & Beachy, P. A. (2000). Hedgehog-Regulated Processing of Gli3 Produces an Anterior / Posterior Repressor Gradient in the Developing Vertebrate Limb University of Wisconsin at Madison. *Cell*, *100*, 423–434.
- Wang, C., Gong, B., Bushel, P. R., Thierry-Mieg, J., Thierry-Mieg, D., Xu, J., Fang, H., Hong, H., Shen, J., Su, Z., Meehan, J., Li, X., Yang, L., Li, H., Łabaj, P. P., Kreil, D. P., Megherbi, D., Gaj, S., Caiment, F., ... Tong, W. (2014). The concordance between RNA-seq and microarray data depends on chemical treatment and transcript abundance. *Nature Biotechnology*, *32*(9), 926–932.
- Wang, Z., Gerstein, M., & Snyder, M. (2009). RNA-Seq: a revolutionary tool for transcriptomics. *Nature Reviews Genetics*, *10*(1), 57–63.
- Washkowitz, A. J., Gavrilov, S., Begum, S., & Papaioannou, V. E. (2012). Diverse functional networks of Tbx3 in development and disease. *Wiley Interdisciplinary Reviews: Systems Biology and Medicine*, *4*(3), 273–283.
- Wellik, D. M., & Capecchi, M. R. (2003). Hox10 and Hox11 genes are required to globally pattern the mammalian skeleton. *Science*, *301*(5631), 363–367.
- Wellmann, S., Bettkober, M., Zelmer, A., Seeger, K., Faigle, M., Eltzhig, H. K., & Bührer, C. (2008). Hypoxia upregulates the histone demethylase JMJD1A via HIF-1. *Biochemical*

and *Biophysical Research Communications*, 372(4), 892–897.

Wen, J., Lee, J., Malhotra, a, Nahta, R., Arnold, a R., Buss, M. C., Brown, B. D., Maier, C., Kenney, a M., Remke, M., Ramaswamy, V., Taylor, M. D., & Castellino, R. C. (2016). WIP1 modulates responsiveness to Sonic Hedgehog signaling in neuronal precursor cells and medulloblastoma. *Oncogene*, *January*, 1–13.

Willmer, T., Hare, S., Peres, J., & Prince, S. (2016). The T - box transcription factor TBX3 drives proliferation by direct repression of the p21 WAF1 cyclin - dependent kinase inhibitor. *Cell Division*, 1–13.

Wilson, V., & Conlon, F. L. (2002). *The T -box family*. 1–7.

Wollnik, B., Kayserili, H., Uyguner, O., Tukel, T., & Yuksel-Apak, M. (2002). Haploinsufficiency of TBX3 causes ulnar-mammary syndrome in a large Turkish family. *Annales de Genetique*, 45(4), 213–217.

Xu, B., & Wellik, D. M. (2011). Axial Hox9 activity establishes the posterior field in the developing forelimb. *Proceedings of the National Academy of Sciences of the United States of America*, 108(12), 4888–4891.

Xu, X., Weinstein, M., Li, C., Naski, M., Cohen, R. I., Ornitz, D. M., Leder, P., & Deng, C. (1998). Fibroblast growth factor receptor 2 (FGFR2)-mediated reciprocal regulation loop between FGF8 and FGF10 is essential for limb induction. *Development*, 125(4), 753–765.

Yakushiji-Kaminatsui, N., Lopez-Delisle, L., Bolt, C. C., Andrey, G., Beccari, L., & Duboule, D. (2018). Similarities and differences in the regulation of HoxD genes during chick and mouse limb development. In *PLoS Biology* (Vol. 16, Issue 11).

Yamada, M., Revelli, J. P., Eichele, G., Barron, M., & Schwartz, R. J. (2000). Expression of chick Tbx-2, Tbx-3, and Tbx-5 genes during early heart development: Evidence for BMP2 induction of Tbx2. *Developmental Biology*, 228(1), 95–105.

Yamamoto, S., Uchida, Y., Ohtani, T., Nozaki, E., Yin, C., Gotoh, Y., Yakushiji-Kaminatsui, N., Higashiyama, T., Suzuki, T., Takemoto, T., Shiraishi, Y. ichi, & Kuroiwa, A. (2019). Hoxa13 regulates expression of common Hox target genes involved in cartilage development to coordinate the expansion of the autopodal anlage. *Development Growth and Differentiation*, 61(3), 228–251.

Yang, L., Cai, C. L., Lin, L., Qyang, Y., Chung, C., Monteiro, R. M., Mummery, C. L., Fishman, G. I., Cogen, A., & Evans, S. (2006). Isl1 Cre reveals a common Bmp pathway in heart and limb development. *Development*, 133(8), 1575–1585.

Yao, C., Yao, G. Q., Sun, B. H., Zhang, C., Tommasini, S. M., & Insogna, K. (2014). The transcription factor T-box 3 regulates colony-stimulating factor 1-dependent Jun dimerization protein 2 expression and plays an important role in osteoclastogenesis. *Journal of Biological Chemistry*, 289(10), 6775–6790.

Yarosh, W., Barrientos, T., Esmailpour, T., Lin, L., Carpenter, P. M., Osann, K., Anton-Culver, H., & Huang, T. (2008a). TBX3 is overexpressed in breast cancer and represses p14ARF by interacting with histone deacetylases. *Cancer Research*, 68(3), 693–699.

Yarosh, W., Barrientos, T., Esmailpour, T., Lin, L., Carpenter, P. M., Osann, K., Anton-Culver, H., & Huang, T. (2008b). TBX3 is overexpressed in breast cancer and represses p14ARF by interacting with histone deacetylases. *Cancer Research*, 68(3), 693–699.

Yashiro, K., Zhao, X., Uehara, M., Yamashita, K., Nishijima, M., Nishino, J., Saijoh, Y., Sakai, Y., & Hamada, H. (2004). Regulation of retinoic acid distribution is required for

- proximodistal patterning and outgrowth of the developing mouse limb. *Developmental Cell*, 6(3), 411–422.
- Yelon, D., Ticho, B., Halpern, M. E., Ruvinsky, I., Ho, R. K., Silver, L. M., & Stainier, D. Y. (2000). The bHLH transcription factor *hand2* plays parallel roles in zebrafish heart and pectoral fin development. *Development (Cambridge, England)*, 127(12), 2573–2582.
- Yonei-Tamura, S., Endo, T., Yajima, H., Ohuchi, H., Ide, H., & Tamura, K. (1999). FGF7 and FGF10 directly induce the apical ectodermal ridge in chick embryos. *Developmental Biology*, 211(1), 133–143.
- Yoo, K. H., & Hennighausen, L. (2012). EZH2 Methyltransferase and H3K27 Methylation in Breast Cancer. *International Journal of Biological Sciences*, 8(1), 59–65.
- Youngstrom, D. W., Dishowitz, M. I., Bales, C. B., Carr, E., Mutyaba, P. L., Kozloff, K. M., Shitaye, H., Hankenson, K. D., & Loomes, K. M. (2016). Jagged1 expression by osteoblast-lineage cells regulates trabecular bone mass and periosteal expansion in mice. *Bone*, 91(1), 64–74.
- Zakany, J., & Duboule, D. (2007). The role of Hox genes during vertebrate limb development. *Current Opinion in Genetics and Development*, 17(4), 359–366.
- Zakany, J., Zacchetti, G., & Duboule, D. (2007). Interactions between HOXD and Gli3 genes control the limb apical ectodermal ridge via Fgf10. *Developmental Biology*, 306(2), 883–893.
- Zeller, R., López-Ríos, J., & Zuniga, A. (2009). Vertebrate limb bud development: moving towards integrative analysis of organogenesis. *Nature Reviews Genetics*, 10(12), 845–858.
- Zeng, X., Goetz, J. A., Suber, L. M., Scott, W. J., Schreiner, C. M., & Robbins, D. J. (2001). A freely diffusible form of Sonic hedgehog mediates long-range signalling. *Nature*, 411(6838), 716–720.
- Zhang, W., Chronis, C., Chen, X., Zhang, H., Spalinskas, R., Pardo, M., Chen, L., Wu, G., Zhu, Z., Yu, Y., Yu, L., Choudhary, J., Nichols, J., Parast, M. M., Greber, B., Sahlén, P., & Plath, K. (2019). The BAF and PRC2 Complex Subunits Dpf2 and Eed Antagonistically Converge on Tbx3 to Control ESC Differentiation. *Cell Stem Cell*, 24(1), 138–152.e8.
- Zhang, Z., Sui, P., Dong, A., Hassell, J., Cserjesi, P., Chen, Y. T., Behringer, R. R., & Sun, X. (2010). Preaxial polydactyly: Interactions among ETV, TWIST1 and HAND2 control anterior-posterior patterning of the limb. *Development*, 137(20), 3417–3426.
- Zhao, Q., Eberspaecher, H., Lefebvre, V., & De Crombrughe, B. (1997). Parallel expression of Sox9 and Col2a1 in cells undergoing chondrogenesis. *Developmental Dynamics*, 209(4), 377–386.
- Zhao, X., Sirbu, I. O., Mic, F. A., Molotkova, N., Molotkov, A., Kumar, S., & Duester, G. (2009). Retinoic Acid Promotes Limb Induction through Effects on Body Axis Extension but Is Unnecessary for Limb Patterning. *Current Biology*, 19(12), 1050–1057.
- Zhou, Q., Chipperfield, H., Melton, D. A., & Wing, H. W. (2007). A gene regulatory network in mouse embryonic stem cells. *Proceedings of the National Academy of Sciences of the United States of America*, 104(42), 16438–16443.
- Zhou, W., Zhu, H., Zhao, J., Li, H., Wan, Y., Cao, J., Zhao, H., Yu, J., Zhou, R., Yao, Y., Zhang, L., Wang, L., He, L., Ma, G., Yao, Z., & Guo, X. (2013). Misexpression of Pknox2 in Mouse Limb Bud Mesenchyme Perturbs Zeugopod Development and Deltoid Crest Formation. *PLoS ONE*, 8(5), 1–7.
- Zhu, A. J., & Scott, M. P. (2004). Incredible journey: How do developmental signals travel

through tissue? *Genes and Development*, 18(24), 2985–2997.

Zhu, H. (2016). Forkhead box transcription factors in embryonic heart development and congenital heart disease. *Life Sciences*, 144, 194–201.

Zhu, J., Nakamura, E., Nguyen, M. T., Bao, X., Akiyama, H., & Mackem, S. (2008). Uncoupling Sonic Hedgehog Control of Pattern and Expansion of the Developing Limb Bud. *Developmental Cell*, 14(4), 624–632.

Zúñiga, a, Haramis, a P., McMahon, a P., & Zeller, R. (1999). Signal relay by BMP antagonism controls the SHH/FGF4 feedback loop in vertebrate limb buds. *Nature*, 401(6753), 598–602.

Zuniga, A. (2015). Next generation limb development and evolution: old questions, new perspectives. *Development (Cambridge, England)*, 142(22), 3810–3820.

Zúñiga, A., & Zeller, R. (1999). Gli3 (Xf) and formin (Id) participate in the positioning of the polarising region and control of posterior limb-bud identity. *Development*, 126(1), 13–21.

12 Appendix

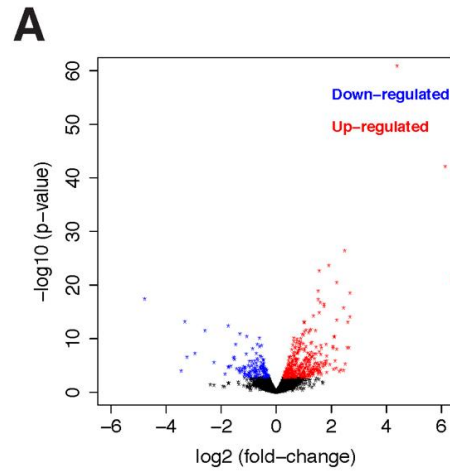
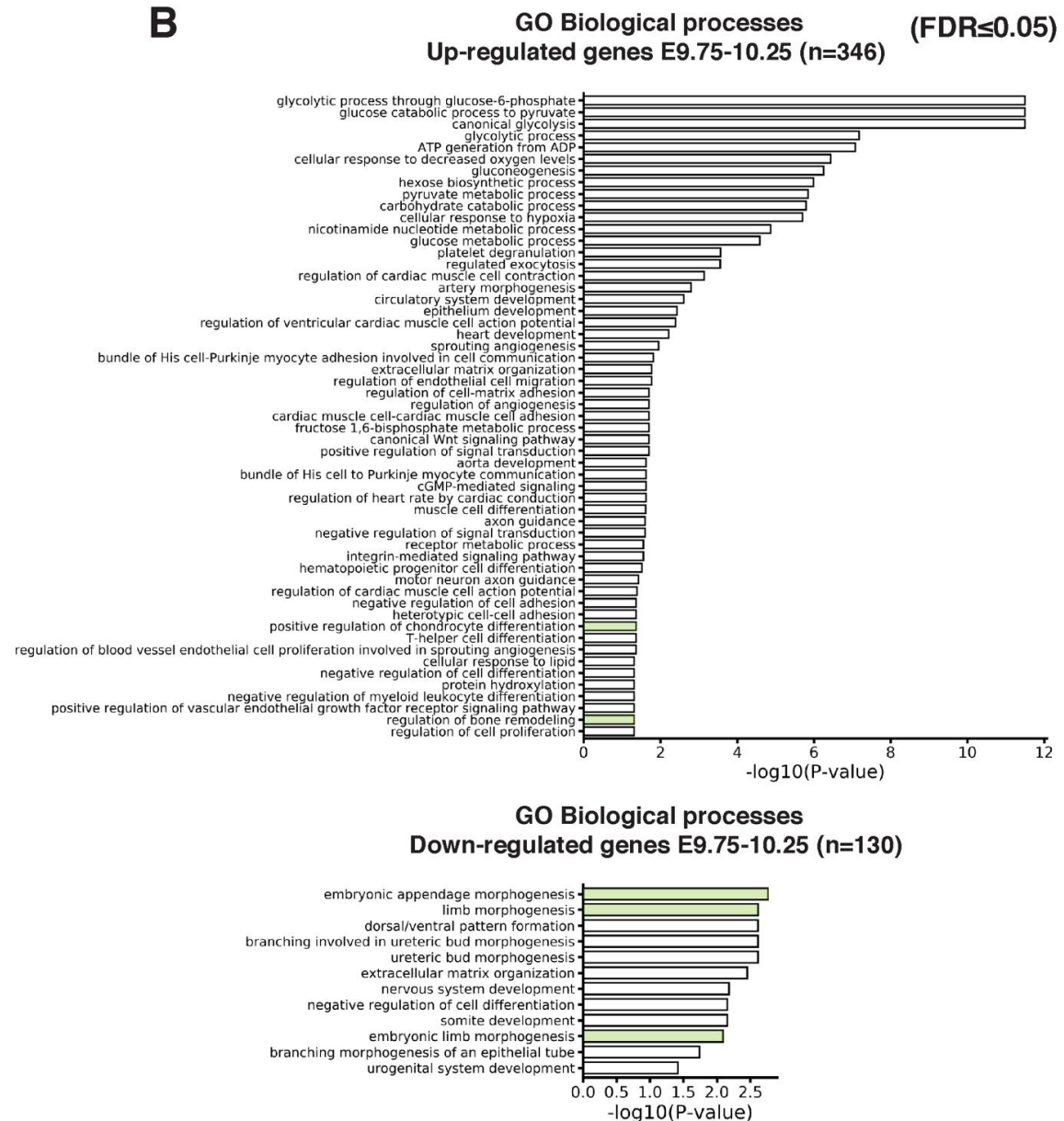
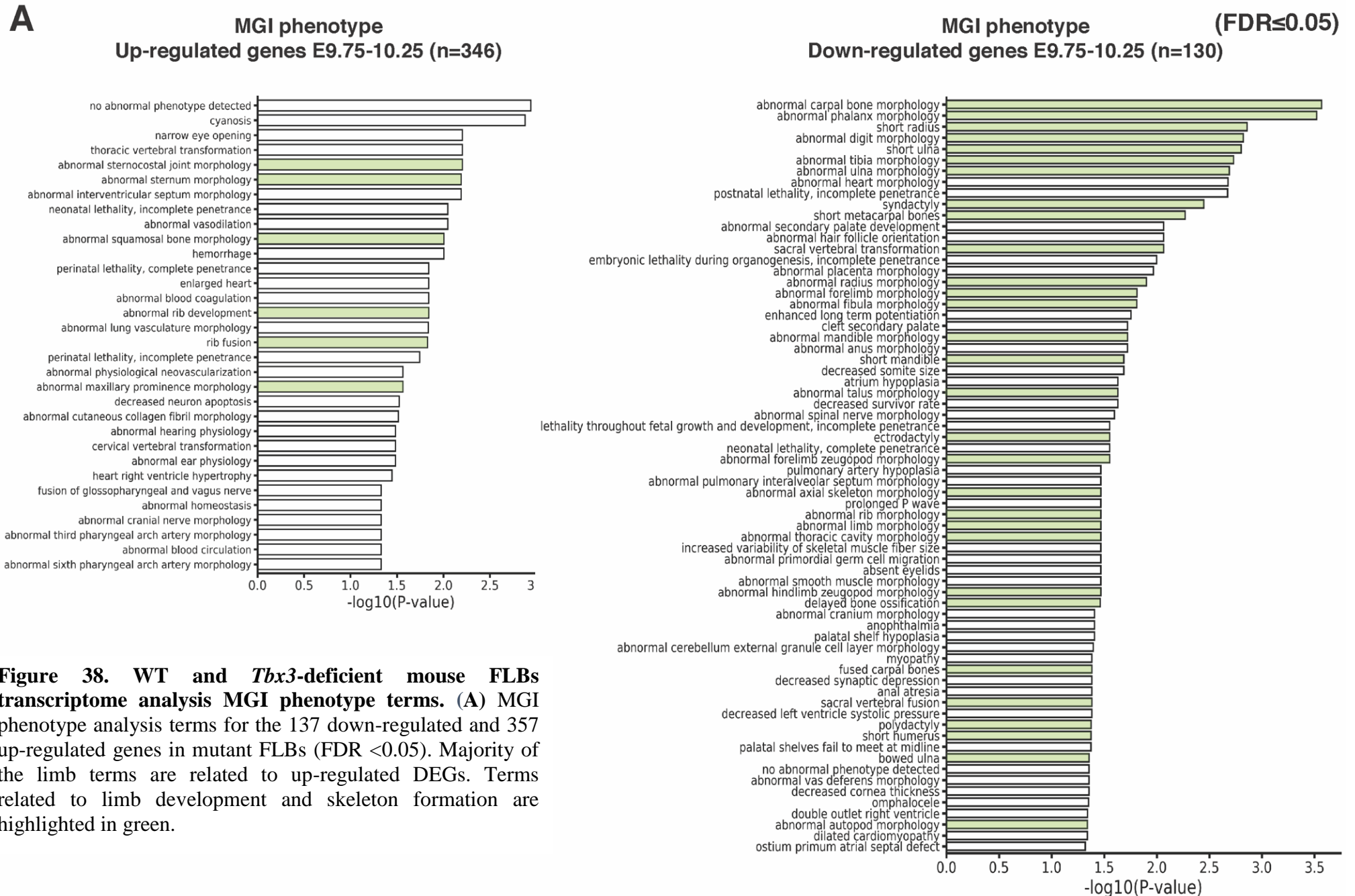
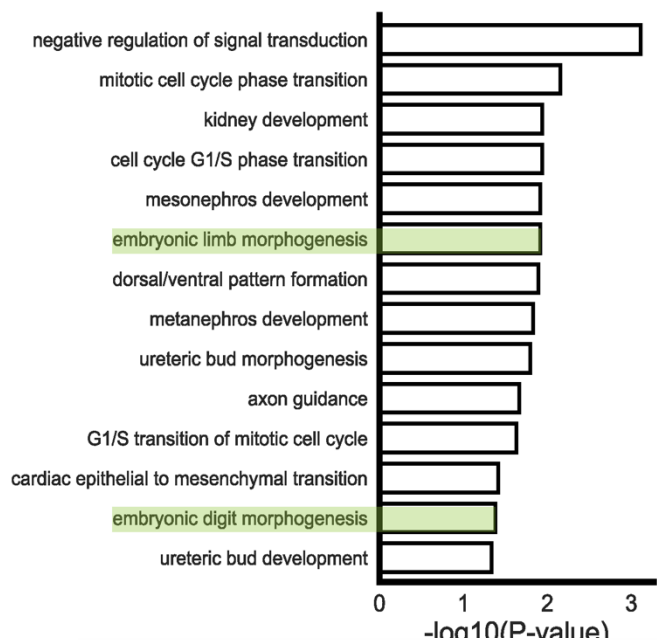


Figure 37. WT and *Tbx3*-deficient mouse FLBs transcriptome analysis GO terms. (A) The Volcano plot represents DEGs distribution identified by comparing transcriptomes of mouse embryos WT and *Tbx3*^{ΔΔ} FLBs at E9.75-10.0 (FC ≤1.2, FDR <0.05). (B) Gene Ontology (GO) enrichment analysis terms for biological processes for the 137 down-regulated and 357 up-regulated genes in mutant FLBs (FDR <0.05). Terms related to limb development and skeleton formation are highlighted in green.





A GO Biological processes
Down-regulated genes E10.0-10.25 (n=318)



B GO Biological processes
Up-regulated genes E10.0-10.25 (n=703)

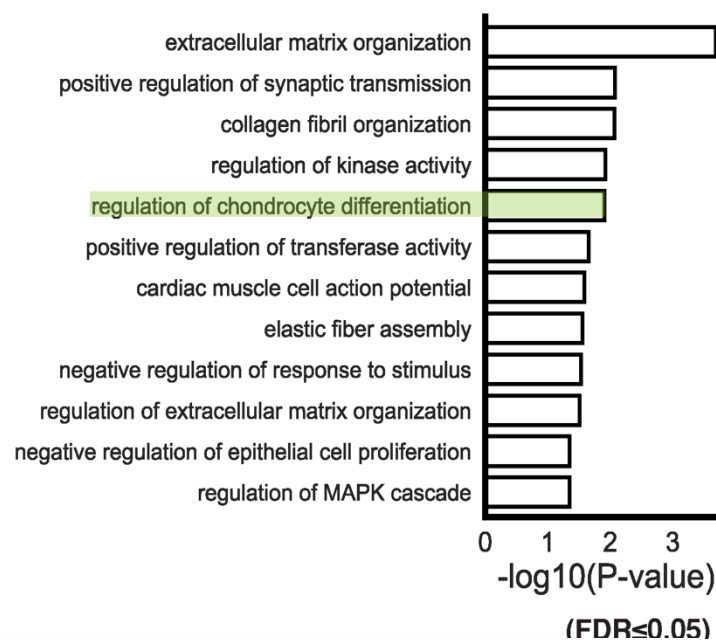


Figure 39. WT and *Hand2*-deficient mouse FLBs transcriptome analysis GO terms. (A) GO terms for biological processes for 318 down-regulated and (B) 703 up-regulated genes identified by comparing transcriptomes of mouse embryos *Hand2*^{Δ/Δc}, *PrxCre*/+ and *Hand2*^{+/+}, *PrxCre*/+ (as WT) FLBs at E10.0-10.25 (FC ≤1.2, FDR <0.05). Terms related to limb development and skeleton formation are highlighted in green.

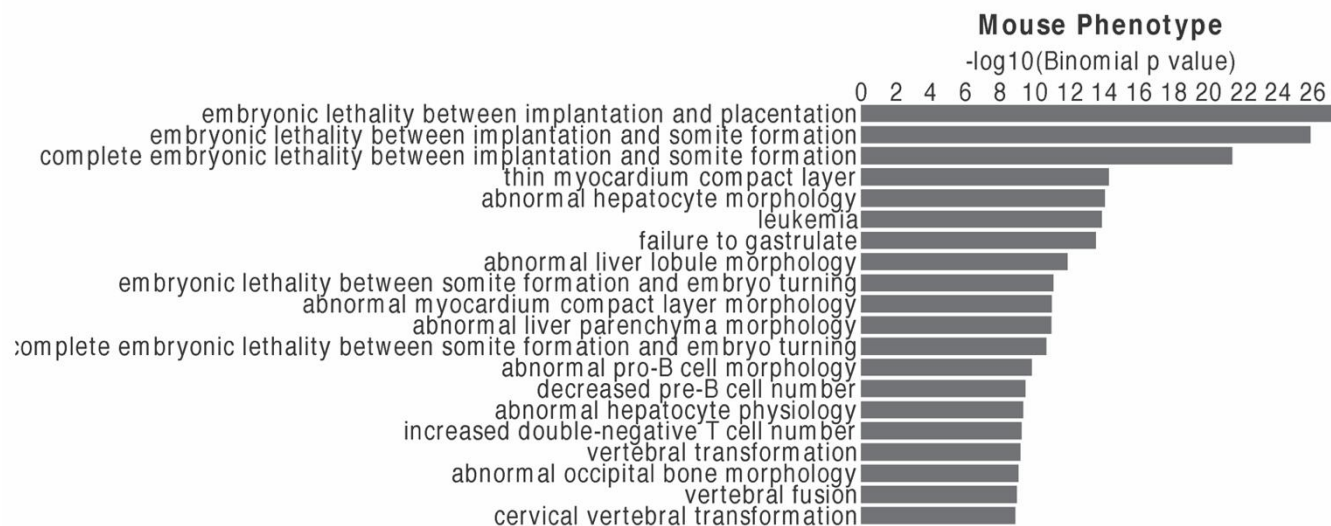
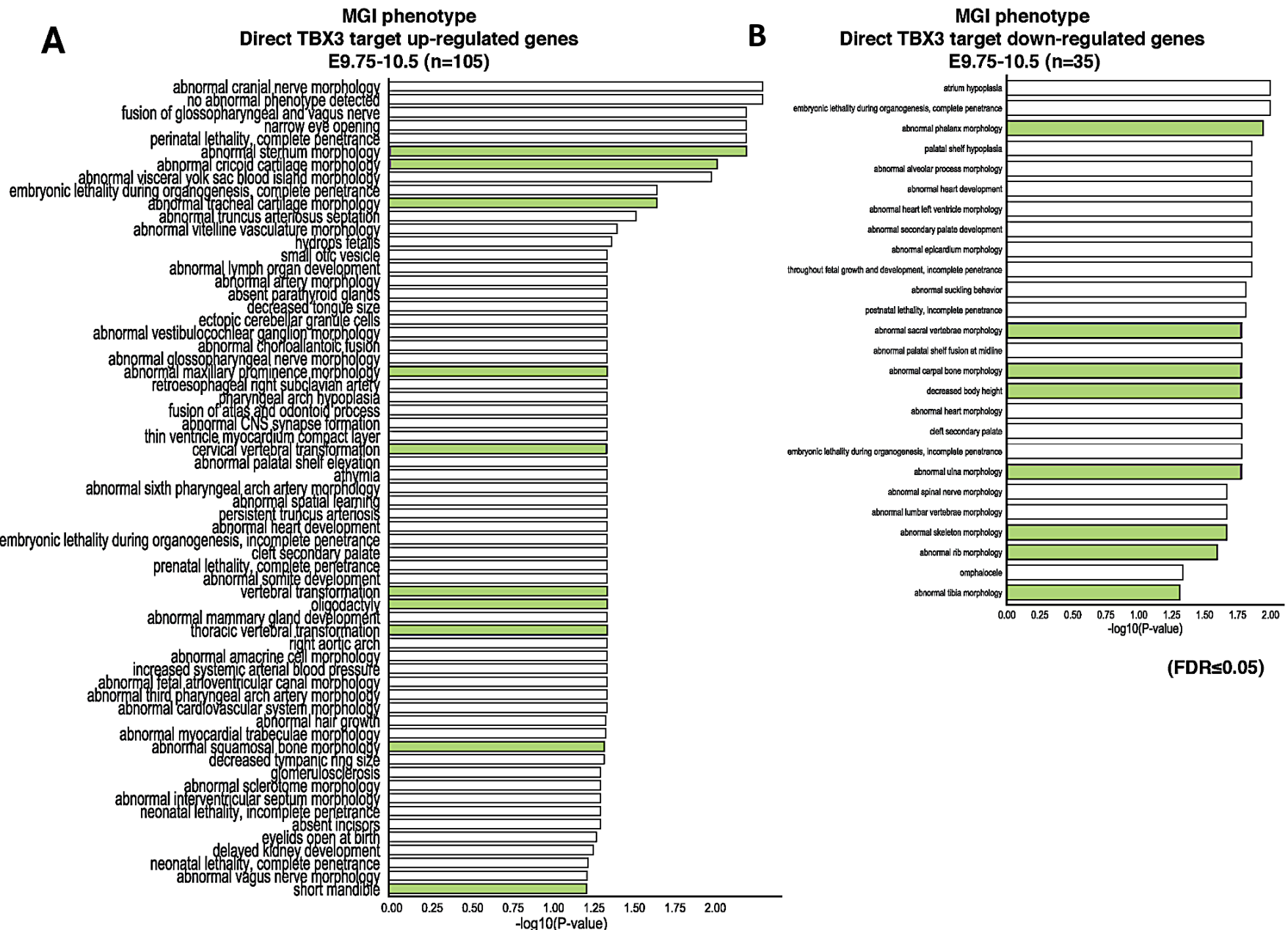


Figure 40. MGI phenotype analysis terms for TBX3 consensus peaks found in open chromatin regions. Majority of terms are related to early embryonic lethality while limb development and limb skeleton terms are absent.



12.1 List of 130 common DEGs identified by overlapping *Tbx3*- and *Hand2*- deficient forelimb bud transcriptomes.

Mouse embryos FLBs transcriptome dataset of WT and *Tbx3*^{Δ/Δ} at E9.75-10.0 (28-31s) was crossed with *Hand2*^{Δ/Δc}, *Prx1Cre*/+ and *Hand2*^{+/+}, *Prx1Cre*/+ (as WT) FLBs at E10-10.25 (31-33s) dataset (both transcriptomes FC ≤1.2, FDR <0.05). Overlap revealed: 81 up-regulated, 36 down-regulated and 13 discordant common DEGs in FLB. Gene list with FC indicated are given in tables bellow.

Table 1 List of 81 common up-regulated genes identified by overlapping *Tbx3*- and *Hand2*- deficient forelimb bud transcriptomes.

<i>Hand2</i> ^{Δ/Δc} transcriptome	FC	<i>Tbx3</i> ^{Δ/Δ} transcriptome	FC
<i>Ackr3</i>	1.38306275	<i>Ackr3</i>	1.799369262
<i>Adamts1</i>	1.44416508	<i>Adamts1</i>	1.441834262
<i>Adamts9</i>	1.6072359	<i>Adamts9</i>	1.666835229
<i>Ahnak</i>	1.23439452	<i>Ahnak</i>	1.445497622
<i>Akap12</i>	1.288061	<i>Akap12</i>	1.477726441
<i>Alx3</i>	1.91307989	<i>Alx3</i>	1.892162409
<i>Alx4</i>	1.91495974	<i>Alx4</i>	1.615723431
<i>Aplp1</i>	1.73361061	<i>Aplp1</i>	1.779675391
<i>Arhgap22</i>	1.68476657	<i>Arhgap22</i>	1.957055911
<i>Asic4</i>	2.43882163	<i>Asic4</i>	5.471020158
<i>Cav1</i>	2.06829264	<i>Cav1</i>	2.030107854
<i>Ccbe1</i>	1.61609742	<i>Ccbe1</i>	2.485650238
<i>Ccng2</i>	1.34459726	<i>Ccng2</i>	1.314154124
<i>Celf2</i>	1.30241176	<i>Celf2</i>	1.797270666
<i>Col5a1</i>	1.25006559	<i>Col5a1</i>	1.337427498
<i>Csf1r</i>	1.86762413	<i>Csf1r</i>	2.887222525
<i>Cx3cr1</i>	2.11480511	<i>Cx3cr1</i>	2.331690225
<i>Cyp2d22</i>	2.07947292	<i>Cyp2d22</i>	2.292806029
<i>Dact2</i>	1.51196988	<i>Dact2</i>	2.273835511
<i>Ddr1</i>	1.38139595	<i>Ddr1</i>	1.450147752
<i>Dpf3</i>	2.44522362	<i>Dpf3</i>	2.884421285
<i>Efna3</i>	1.38740013	<i>Efna3</i>	1.528931534
<i>F13a1</i>	2.04758129	<i>F13a1</i>	3.554252851
<i>Foxp1</i>	1.53650025	<i>Foxp1</i>	1.532537728
<i>Fras1</i>	1.38765788	<i>Fras1</i>	1.273955757
<i>Fzd1</i>	1.21493664	<i>Fzd1</i>	1.268013258
<i>Gata5</i>	2.27030295	<i>Gata5</i>	3.400510878
<i>Gata6</i>	2.07057938	<i>Gata6</i>	2.952375996

<i>Gdf6</i>	1.63181202	<i>Gdf6</i>	1.657989794
<i>Gucy1a3</i>	2.78266196	<i>Gucy1a3</i>	3.87209272
<i>H2-T24</i>	3.56885035	<i>H2-T24</i>	2.838130388
<i>Hoxb3</i>	1.44766568	<i>Hoxb3</i>	1.280275579
<i>Hoxb6</i>	1.335734	<i>Hoxb6</i>	1.480810965
<i>Hoxb7</i>	1.60078887	<i>Hoxb7</i>	1.729358437
<i>Hoxb8</i>	1.74941339	<i>Hoxb8</i>	2.127761902
<i>Hoxb9</i>	2.68750622	<i>Hoxb9</i>	3.135385036
<i>Hoxc4</i>	1.37120575	<i>Hoxc4</i>	1.416307797
<i>Hoxc6</i>	1.43844783	<i>Hoxc6</i>	1.448661496
<i>Hoxc8</i>	1.65946169	<i>Hoxc8</i>	2.016994594
<i>Hoxc9</i>	1.60224721	<i>Hoxc9</i>	2.042170173
<i>Hs3st3a1</i>	1.44458242	<i>Hs3st3a1</i>	1.876426533
<i>Igfbp2</i>	1.31530117	<i>Igfbp2</i>	1.283642674
<i>Insig1</i>	1.26213081	<i>Insig1</i>	1.339205736
<i>Irx3</i>	1.56243687	<i>Irx3</i>	1.354440892
<i>Irx5</i>	1.53775659	<i>Irx5</i>	1.364868304
<i>Lox</i>	2.63513937	<i>Lox</i>	1.908980335
<i>Lrrn4</i>	3.86839054	<i>Lrrn4</i>	3.54999912
<i>Map1a</i>	1.28436939	<i>Map1a</i>	1.509692242
<i>Mcm8</i>	1.49353963	<i>Mcm8</i>	1.330207781
<i>Meg3</i>	1.42635722	<i>Meg3</i>	1.66683085
<i>Mpp2</i>	1.30824418	<i>Mpp2</i>	1.620096152
<i>Mrc1</i>	2.29993515	<i>Mrc1</i>	3.067320595
<i>Ncam1</i>	1.57166329	<i>Ncam1</i>	1.976160982
<i>Ndrg2</i>	1.59034163	<i>Ndrg2</i>	2.327023234
<i>Nlgn2</i>	1.29223763	<i>Nlgn2</i>	1.333005347
<i>Olfm2</i>	2.04193211	<i>Olfm2</i>	2.074765995
<i>Pitx1</i>	2.90691673	<i>Pitx1</i>	20.90202222
<i>Plod2</i>	1.21627815	<i>Plod2</i>	1.500405753
<i>Plxna2</i>	1.3864282	<i>Plxna2</i>	1.418483221
<i>Pou2f2</i>	2.0734293	<i>Pou2f2</i>	1.63507607
<i>Ppp1r3c</i>	1.62373355	<i>Ppp1r3c</i>	2.083283213
<i>Ptpn13</i>	1.21316348	<i>Ptpn13</i>	1.312857031
<i>Reep1</i>	1.29697538	<i>Reep1</i>	1.59775848
<i>Rims2</i>	2.83867014	<i>Rims2</i>	2.261169879
<i>Rnf157</i>	1.23610154	<i>Rnf157</i>	1.258367767
<i>Ror1</i>	1.25033086	<i>Ror1</i>	1.276436823
<i>Rora</i>	1.69208414	<i>Rora</i>	1.979324724
<i>Rspo1</i>	1.866383	<i>Rspo1</i>	2.400938094
<i>Rspo2</i>	1.25100056	<i>Rspo2</i>	1.512315289

<i>Scd1</i>	1.24697154	<i>Scd1</i>	1.3368098
<i>Shank1</i>	1.88371008	<i>Shank1</i>	2.392240449
<i>Shisa3</i>	1.83350851	<i>Shisa3</i>	3.072891034
<i>Slc25a23</i>	1.33810256	<i>Slc25a23</i>	1.567232938
<i>Slit1</i>	1.99850393	<i>Slit1</i>	2.325418645
<i>Sox6</i>	1.30112672	<i>Sox6</i>	1.50964303
<i>St3gal1</i>	1.37141158	<i>St3gal1</i>	1.34411892
<i>Tec</i>	2.22449269	<i>Tec</i>	1.929149591
<i>Tgfbi</i>	1.38059927	<i>Tgfbi</i>	1.393946322
<i>Trabd2b</i>	1.80312616	<i>Trabd2b</i>	2.543584689
<i>Tspan13</i>	1.23411717	<i>Tspan13</i>	1.318806486
<i>Wisp1</i>	1.55113729	<i>Wisp1</i>	1.695553965

Table 2 List of 36 common up-regulated genes identified by overlapping *Tbx3*- and *Hand2*-deficient forelimb bud transcriptomes.

<i>Hand2</i> ^{ΔΔc} transcriptome	FC	<i>Tbx3</i> ^{ΔΔ} transcriptome	FC
<i>2410131K14Rik</i>	1.21048456	<i>2410131K14Rik</i>	1.31346153
<i>Ccser1</i>	1.84982402	<i>Ccser1</i>	1.60023954
<i>Cnr1</i>	1.58238332	<i>Cnr1</i>	1.74457231
<i>Dmrta1</i>	2.49999861	<i>Dmrta1</i>	2.16301894
<i>Ets2</i>	1.72915343	<i>Ets2</i>	1.315503
<i>Frem1</i>	2.0386568	<i>Frem1</i>	1.28613918
<i>Gap43</i>	1.2087902	<i>Gap43</i>	1.38168679
<i>Glde</i>	1.34084327	<i>Glde</i>	1.58265679
<i>Gnai1</i>	1.22178409	<i>Gnai1</i>	1.25435208
<i>Gpx2</i>	3.26647912	<i>Gpx2</i>	1.96323229
<i>Hand2</i>	117.565604	<i>Hand2</i>	1.37125925
<i>Hoxa11</i>	1.36730059	<i>Hoxa11</i>	1.46074013
<i>Hoxd10</i>	1.2482277	<i>Hoxd10</i>	1.59981549
<i>Hoxd11</i>	5.67728529	<i>Hoxd11</i>	2.87493083
<i>Hoxd12</i>	21.3467469	<i>Hoxd12</i>	3.63362314
<i>Hoxd13</i>	6.88617919	<i>Hoxd13</i>	1.68079364
<i>Hsd11b2</i>	1.66870356	<i>Hsd11b2</i>	1.38956568
<i>Itgav</i>	1.23452992	<i>Itgav</i>	1.30056446
<i>Mamdc2</i>	3.26280886	<i>Mamdc2</i>	1.97370752
<i>Mctp2</i>	1.78136732	<i>Mctp2</i>	2.56030276
<i>Meox2</i>	1.7026516	<i>Meox2</i>	1.66899028
<i>Nap1l5</i>	1.93462313	<i>Nap1l5</i>	3.34575497
<i>Nim1k</i>	1.56260117	<i>Nim1k</i>	1.90377088
<i>Olfm1</i>	2.01040593	<i>Olfm1</i>	1.5104431

<i>Pam</i>	1.4692888	<i>Pam</i>	1.29301485
<i>Pou4f1</i>	5.25325167	<i>Pou4f1</i>	6.02134344
<i>Prdm1</i>	2.76510656	<i>Prdm1</i>	2.09483288
<i>Ptch1</i>	3.27747492	<i>Ptch1</i>	1.43417756
<i>Rtn4rl1</i>	2.30049253	<i>Rtn4rl1</i>	2.19736055
<i>Sall3</i>	2.25234524	<i>Sall3</i>	1.43462508
<i>Sell3</i>	1.88706786	<i>Sell3</i>	1.86403249
<i>Serinc5</i>	1.65254357	<i>Serinc5</i>	1.28885789
<i>Shh</i>	38.4496657	<i>Shh</i>	2.92704875
<i>Shox2</i>	1.47908089	<i>Shox2</i>	2.11562547
<i>Vwde</i>	1.90676014	<i>Vwde</i>	1.99488317
<i>Wnt5a</i>	1.25491826	<i>Wnt5a</i>	1.43131632

Table 3 List of 13 common discordant genes identified by overlapping *Tbx3*- and *Hand2*-deficient forelimb bud transcriptomes. Gene names in red indicate upregulation, gene names in blue: downregulation.

<i>Hand2</i> ^{Δ/Δc} transcriptome	FC	<i>Tbx3</i> ^{Δ/Δ} transcriptome	FC
<i>Dpyd</i>	2.47066582	<i>Dpyd</i>	3.27735218
<i>Galk1</i>	1.25820752	<i>Galk1</i>	1.3964068
<i>Gja5</i>	1.30910964	<i>Gja5</i>	1.78932987
<i>Jag1</i>	1.30651348	<i>Jag1</i>	1.46060616
<i>Lama2</i>	2.03509248	<i>Lama2</i>	1.87534796
<i>Pcdh17</i>	1.47294561	<i>Pcdh17</i>	1.63763855
<i>Pcdhgb6</i>	1.95705068	<i>Pcdhgb6</i>	1.7019807
<i>Pdlim5</i>	1.24555341	<i>Pdlim5</i>	1.35113184
<i>Plxna4</i>	1.5435694	<i>Plxna4</i>	1.62614239
<i>Srp54a</i>	1.94290639	<i>Srp54a</i>	1.44579886
<i>Tbx18</i>	1.4726446	<i>Tbx18</i>	1.61930984
<i>Ttc9c</i>	1.24228432	<i>Ttc9c</i>	1.51658293
<i>Wif1</i>	1.7406622	<i>Wif1</i>	1.76574991

12.2 List of 140 direct transcriptional targets of TBX3.

List of direct transcriptional targets of TBX3 was obtained by overlapping WT and *Tbx3*-deficient forelimb bud transcriptome at E9.75-10.0 (28-31s), ChIP-seq of *Tbx3*^{3xF/3xF} embryos forelimb buds at E9.75-E10.25 and forelimbs ATAC-seq E10.5 data sets (transcriptome FC ≤1.2, FDR <0.05, ChIP-seq 1e5). Overlap revealed 105 up-regulated and 35 down-regulated direct transcriptional targets of TBX3 in FLBs. Gene list with peak coordinates in mm10 and FC indicated are given in tables below.

Table 4. List of 105 up-regulated direct transcriptional targets of TBX3.

Coordinates of the peak (mm10)	Gene name	FC	Coordinates of the peak (mm10)	Gene name	FC
chr16 85803135-85803298	<i>Adamts1</i>	1.44183426	chr11 63300329-63300481	<i>Hs3st3b1</i>	1.27724376
chr11 50827412-50827584	<i>Adamts2</i>	2.89586689	chr17 35725667-35725840	<i>Ier3</i>	2.73854692
chr6 9294133-92941481	<i>Adamts9</i>	1.66683523	chr5 28165392-28165803	<i>Insig1</i>	1.33920574
chr6 93410769-93410901			chr8 91313492-91313754	<i>Irx3</i>	1.35444089
chr7 110701754-110701948	<i>Adm</i>	4.60699645	chr8 91713877-91714070		
chr19 53944904-53945169	<i>Adra2a</i>	2.62367839	chr8 91948630-91948905	<i>Irx5</i>	1.3648683
chr19 53945606-53945800			chr8 91948630-91948905		
chr9 71485274-71485787	<i>Aldh1a2</i>	4.44715934	chr7 46845804-46846077	<i>Ldha</i>	1.62682424
chr1 167340271-167340509	<i>Aldh9a1</i>	1.2274652	chr15 100495026-100495429	<i>Letmd1</i>	1.27115785
chr2 93625109-93625397	<i>Alx4</i>	1.61572343	chr9 56738360-56738552	<i>Lingo1</i>	1.77156325
chr2 93642703-93642881			chr11 102087586-102087709	<i>Mpp2</i>	1.62009615
chr2 93785210-93785404			chr2 106458420-106458651	<i>Mpped2</i>	1.38989238
chr10 24959116-24959248	<i>Arg1</i>	2.70780264	chr2 106693850-106694355		
chr19 6141117-6141351	<i>Arl2</i>	1.22149308	chr2 106744707-106745010		
chr11 81115809-81115927	<i>Asic2</i>	1.62948029	chr2 106796160-106796410		
chr3 35754147-35754315	<i>Atp11b</i>	1.25482868	chr19 10231063-10231294	<i>Myrf</i>	2.11724274
chr3 35932309-	<i>Bhlhe41</i>	2.73126611	chr9 49798919-	<i>Ncam1</i>	1.97616098

35932794			49799080		
chr6 145932819-145933003	Bnc1	1.95102744	chr13 36727234-36727595	Nrn1	4.18697624
chr7 82012078-82012265	Cabp1	1.80242009	chr2 11602911-11603089	Pfkfb3	2.03817703
chr5 115158364-115158508	Ccbe1	2.48565024	chr13 56134807-56135313	Pitx1	20.9020222
chr5 115174839-115174996			chr13 56135416-56135565		
chr18 66076498-66076783			chr9 59656123-59656390	Pkm	1.42424054
chr5 93206552-93206720	Ccng2	1.31415412	chr9 59657099-59657576	Pknox2	2.27793529
chr5 93267860-93267991			chr9 36938601-36938719		
chr10 60445204-60445543	Cdh23	4.31848649	chr9 37030413-37030543		
chr8 106522035-106522165	Cdh3	1.39620336	chr1 133131363-133131519	Plekha6	2.42528618
chr1 24196165-24196455	Col9a1	1.69601381	chr1 194610636-194610829	Plxna2	1.41848322
chr1 24375134-24375489			chr1 194680387-194680516		
chr2 37974256-37974376	Crb2	2.39924221	chr6 32381523-32381713	Plxna4	1.62614239
chr6 53083985-53084370	Creb5	1.8665512	chr6 32710314-32710434		
chr6 53084634-53084779			chr6 31398838-31399261	Podxl	1.44569934
chr6 84410173-84410431	Cyp26b1	1.40532871	chr7 25146045-25146182	Pou2f2	1.63507607
chr13 60177520-60177642	Dapk1	1.33592196	chr19 36703475-36703613	Ppp1r3c	2.08328321
chr13 60267686-60267954			chr18 42913876-42914067	Ppp2r2b	3.13053147
chr13 60676528-60676727			chr18 42933402-42933561		
chr17 35725667-35725840	Ddr1	1.45014775	chr5 103423667-103423895	Ptpn13	1.31285703
chr19 25794588-25794795	Dmrt2	4.55283824	chr3 153912751-153912962	Rabggb	1.23544403
chr18 20060206-20060331	Dsc2	1.46324932	chr11 74619250-74619394	Rap1gap2	1.93298707
chr10 58652137-58652274	Edar	1.63616757	chr12 117588437-117588579	Rapgef5	1.36252931
chr3 89337819-89337970	Efna3	1.52893153	chr11 98968793-98968929	Rara	1.24988287

chr8 124949670-124949793	Egln1	1.60296294	chr14 16365284-16366035	Rarb	1.36236403
chr11 70669099-70669243	Eno3	1.25675064	chr9 68835215-68835335	Rora	1.97932472
chr5 121398061-121398297	Erp29	1.25391099	chr15 43282400-43282597	Rspo2	1.51231529
chr1 171503030-171503226	F11r	1.38606721	chr8 23257095-23257341	Sfrp1	1.89897858
chr11 57302538-57302766	Fam114a2	1.30758551	chr8 23451894-23452251		
chr5 147430729-147431194	Flt1	1.53074609	chr7 44335753-44335928	Shank1	2.39224045
chr5 147611447-147611608			chr5 92997907-92998037	Shroom3	1.4395751

chr6 99028031-99028199	Foxp1	1.53253773	chr10 50892880-50893024	Sim1	3.21940674
chr6 99523360-99523583			chr11 120990656-120991080	Slc16a3	2.55928536
chr5 96373981-96374196	Fras1	1.27395576	chr19 41661118-41661266	Slit1	2.32541865
chr5 4562851-4563003	Fzd1	1.26801326	chr19 41716238-41716490		
chr5 4758049-4758198			chr1 156473976-156474165	Soat1	1.41096747
chr11 116005547-116005710	Galk1	1.3964068	chr1 156558840-156559030	Soat1	1.41096747
chr11 116023922-116024497			chr7 115410713-115410854	Sox6	1.50964303
chr12 80643488-80643740	Galnt16	1.58849703	chr7 116033851-116033971	Sox6	1.50964303
chr18 10726191-10726511	Gata6	2.952376	chr7 29169517-29169637	Spred3	1.6624021
chr18 11288600-11288826			chr15 67121359-67121495	St3gal1	1.34411892
chr18 11351887-11352337			chr18 33213666-33213905	Stard4	1.2386737
chr8 102983993-102984113	Gm8730	8.95390964	chr14 69162020-69162180	Stc1	2.20191573
chr11 57827457-57827814	Hand1	5.44991899	chr11 85643938-85644073	Tbx2	1.55038865
chr13 22043391-22043596	Hist1h2bj	2.78855832	chr11 85799815-85800225		
chr6 82881997-82882167	Hk2	1.61521463	chr11 85818394-85818565		
chr6 52158542-52158691	Hoxa1	1.8947815	chr11 85832382-85832843		
chr6 52164997-			chr13 56582143-	Tgfb1	1.39394632

52165424			56582496		
chr6 52222031-52222236	Hoxa7	1.25304575	chr5 108065725-108065896	Tmed5	1.39088297
chr11 96319336-96319500	Hoxb3	1.28027558	chr4 131873769-131874309	Tmem200b	1.32318142
chr11 96333378-96333658			chr4 131918941-131919070		
chr15 103014361-103014493	Hoxc4	1.4163078	chr4 114382899-114383017	Trabd2b	2.54358469
chr15 103034919-103035122			chr3 107545897-107546060	Ubl4b	2.20690987
chr15 103042542-103042678			chr5 139540287-139540442	Uncx	2.70828114
chr15 103061537-103061680			chr17 46030851-46031059	Vegfa	1.56171441
chr15 102999283-102999496	Hoxc6	1.4486615	chr14 65344005-65344125	Zfp395	1.36827481
chr15 102999283-102999496	Hoxc8	2.01699459	chr14 65358549-65358775	Zfp395	1.36827481
chr11 64588046-64588307	Hs3st3a1	1.87642653			
chr11 64671895-64672030					
chr11 64739116-64739410					
chr11 64833885-64834216	Hs3st3a1	1.87642653			
chr11 64969110-64969318					

Table 5. List of 35 down-regulated direct transcriptional targets of TBX3.

Coordinates of the peak (mm10)	Gene name	FC	Coordinates of the peak (mm10)	Gene name	FC
chr13 44419971-44420206	Cd83	2.18028048	chr2 28184514-28184640	Olfm1	1.5104431
chr13 44730581-44730705			chr10 20459816-20459972	Pde7b	9.88388893
chr3 95434418-95434628	Ctsk	2.19932078	chr10 44979599-44979763	Prdm1	2.09483288
chr4 90065769-90066048	Dmrt1	2.16301894	chr1 10993572-10993758	Prex2	1.36476413
chr3 118431492-118431639	Dpyd	3.27735218	chr13 63451334-63451530	Ptch1	1.43417756
chr16 95702716-95702836	Ets2	1.315503	chr4 76449890-76450125	Ptprd	1.26611119
chr16 95845468-95845613			chr5 115559513-115559827	Rplp0	1.4646774

chr16 95848258-95848400			chr18 81223202-81223404	<i>Sall3</i>	1.43462508
chr19 5729331-5729499	<i>Fam89b</i>	1.22836749	chr14 31336799-31337030	<i>Sh3bp5</i>	1.22117048
chr19 30030569-30030736	<i>Gldc</i>	1.58265679	chr14 31436074-31436253		
chr19 30175438-30175558			chr3 66422634-66423063	<i>Shox2</i>	2.11562547
chr7 116033851-116033971	<i>Gm4353</i>	2.05424601	chr8 106338184-106338324	<i>Smpd3</i>	1.92811719
chr8 56832691-56832883	<i>Hand2</i>	1.37125925	chr12 55080205-55080419	<i>Srp54a</i>	1.44579886
chr8 56962357-56962475			chr9 87557046-87557280	<i>Tbx18</i>	1.61930984
chr8 57322021-57322237	<i>Hexim1</i>	1.24717389	chr9 87731153-87731299	<i>Tbx5</i>	1.43781297
chr11 103115331-103115451	<i>Hexim1</i>	1.24717389	chr5 119748679-119748824		
chr13 21833007-21833453	<i>Hist1h2ap</i>	1.7472547	chr5 119795417-119795710	<i>Tbx5</i>	1.43781297
chr2 74681767-74681911	<i>Hoxd10</i>	1.59981549	chr5 119796430-119796674	<i>Tbx5</i>	1.43781297
chr2 74681767-74681911	<i>Hoxd11</i>	2.87493083	chr2 169702828-169703056	<i>Tshz2</i>	1.36824692
chr8 105496752-105496920	<i>Hsd11b2</i>	1.38956568	chr5 125389534-125389690	<i>Ubc</i>	1.42247638
chr2 78869303-78869476	<i>Itga4</i>	1.8010563	chr5 125389821-125389981		
chr5 66703820-66704015	<i>Limch1</i>	1.2809222	chr5 125393312-125393437		
chr7 109191549-109192029	<i>Lmo1</i>	1.56468102	chr6 13069885-13070122	<i>Vwde</i>	1.99488317
chr7 72362596-72362849	<i>Mctp2</i>	2.56030276			

12.3 List of 53 direct transcriptional targets of TBX3 that also common DEGs in *Hand2*-deficient mouse forelimb buds

List of common direct transcriptional targets of TBX3 was obtained by overlapping WT and *Tbx3*-deficient FLBs transcriptome at E9.75-10.0 (28-31 s), ChIP-seq of *Tbx3*^{3xF/3xF} embryos FLBs at E9.75-E10.25 and forelimbs ATAC-seq E10.5 data sets (transcriptome FC ≤ 1.2 , FDR < 0.05 , ChIP-seq $1e5$) was crossed to *Hand2* ^{Δ/Δ} , *Prx1Cre*^{+/+} and *Hand2*^{+/+}, *Prx1Cre*^{+/+} (as WT) FLBs at E10-10.25 (31-33s) transcriptome dataset. 36 common up-regulated genes and 17 down-regulated genes identified for *Hand2*- and *Tbx3*-deficient FLBs.

Table 6. A list of 36 common up-regulated genes that are direct transcriptional targets of TBX3 and also common DEGs in *Hand2*-deficient mouse FLBs.

Gene name	FC	Gene name	FC
<i>Adamts1</i>	1.44183426	<i>Irx3</i>	1.35444089
<i>Adamts9</i>	1.66683523	<i>Irx5</i>	1.3648683
<i>Alx4</i>	1.61572343	<i>Mpp2</i>	1.62009615
<i>Ccbe1</i>	2.48565024	<i>Ncam1</i>	1.97616098
<i>Ccng2</i>	1.31415412	<i>Pitx1</i>	20.9020222
<i>Ddr1</i>	1.45014775	<i>Plxna2</i>	1.41848322
<i>Efna3</i>	1.52893153	<i>Plxna4</i>	1.62614239
<i>Foxp1</i>	1.53253773	<i>Pou2f2</i>	1.63507607
<i>Fras1</i>	1.27395576	<i>Ppp1r3c</i>	2.08328321
<i>Fzd1</i>	1.26801326	<i>Ptpn13</i>	1.31285703
<i>Galk1</i>	1.3964068	<i>Rora</i>	1.97932472
<i>Gata6</i>	2.952376	<i>Rspo2</i>	1.51231529
<i>Hoxb3</i>	1.28027558	<i>Shank1</i>	2.39224045
<i>Hoxc4</i>	1.4163078	<i>Slit1</i>	2.32541865
<i>Hoxc6</i>	1.4486615	<i>Sox6</i>	1.50964303
<i>Hoxc8</i>	2.01699459	<i>St3gal1</i>	1.34411892
<i>Hs3st3a1</i>	1.87642653	<i>Tgfb1</i>	1.39394632
<i>Insig1</i>	1.33920574	<i>Trabd2b</i>	2.54358469

Table 7. A list of 17 common down-regulated genes that are direct transcriptional targets of TBX3 and also common DEGs in *Hand2*-deficient mouse FLBs.

Gene name	FC	Gene name	FC
<i>Dmrta1</i>	2.16301894	<i>Olfm1</i>	1.5104431
<i>Dpyd</i>	3.27735218	<i>Prdm1</i>	2.09483288
<i>Ets2</i>	1.315503	<i>Ptch1</i>	1.43417756
<i>Gldc</i>	1.58265679	<i>Sall3</i>	1.43462508
<i>Hand2</i>	1.37125925	<i>Shox2</i>	2.11562547
<i>Hoxd10</i>	1.59981549	<i>Srp54a</i>	1.44579886
<i>Hoxd11</i>	2.87493083	<i>Tbx18</i>	1.61930984
<i>Hsd11b2</i>	1.38956568	<i>Vwde</i>	1.99488317
<i>Mctp2</i>	2.56030276		

12.4 List of 87 direct transcriptional targets of TBX3 that are unique to TBX3.

List of unique direct transcriptional targets of TBX3 was obtained by overlapping WT and *Tbx3*-deficient FLBs transcriptome at E9.75-10.0 (28-31s), ChIP-seq of *Tbx3*^{3xF/3xF} embryos FLBs at E9.75-E10.25 and forelimbs ATAC-seq E10.5 data sets (transcriptome FC ≤1.2,

FDR <0.05, ChIP-seq 1e5). Identified direct transcriptional targets of TBX3 were crossed to *Hand2*^{Δ/Δc}, *Prx1Cre*/+ and *Hand2*^{+/+}, *Prx1Cre*/+ (as WT) FLBs at E10-10.25 (31-33s) transcriptome dataset. 87 unique direct TBX3 transcriptional targets identified: 69 unique up-regulated genes and 18 unique down-regulated genes identified for *Tbx3*-deficient FLBs.

Table 8. 18 unique *Tbx3*-deficient FLBs down-regulated genes that are direct transcriptional targets of TBX3.

Gene name	FC	Gene name	FC
<i>Cd83</i>	2.18028048	<i>Pde7b</i>	9.88388893
<i>Ctsk</i>	2.19932078	<i>Prex2</i>	1.36476413
<i>Fam89b</i>	1.22836749	<i>Ptprd</i>	1.26611119
<i>Gm4353</i>	2.05424601	<i>Rplp0</i>	1.4646774
<i>Hexim1</i>	1.24717389	<i>Sh3bp5</i>	1.22117048
<i>Hist1h2ap</i>	1.7472547	<i>Smpd3</i>	1.92811719
<i>Itga4</i>	1.8010563	<i>Tbx5</i>	1.43781297
<i>Limch1</i>	1.2809222	<i>Tshz2</i>	1.36824692
<i>Lmo1</i>	1.56468102	<i>Ubc</i>	1.42247638

Table 9. 69 unique *Tbx3*-deficient FLBs up-regulated genes that are direct transcriptional targets of TBX3.

Gene name	FC	Gene name	FC
<i>Adamts2</i>	2.89586689	<i>Hs3st3b1</i>	1.27724376
<i>Adm</i>	4.60699645	<i>Ier3</i>	2.73854692
<i>Adra2a</i>	2.62367839	<i>Ldha</i>	1.62682424
<i>Aldh1a2</i>	4.44715934	<i>Letmd1</i>	1.27115785
<i>Aldh9a1</i>	1.2274652	<i>Lingo1</i>	1.77156325
<i>Arg1</i>	2.70780264	<i>Mpped2</i>	1.38989238
<i>Arl2</i>	1.22149308	<i>Myrf</i>	2.11724274
<i>Asic2</i>	1.62948029	<i>Nrn1</i>	4.18697624
<i>Atp11b</i>	1.25482868	<i>Pfkfb3</i>	2.03817703
<i>Bhlhe41</i>	2.73126611	<i>Pkm</i>	1.42424054
<i>Bnc1</i>	1.95102744	<i>Pknox2</i>	2.27793529
<i>Cabp1</i>	1.80242009	<i>Plekha6</i>	2.42528618
<i>Cdh23</i>	4.31848649	<i>Podxl</i>	1.44569934
<i>Cdh3</i>	1.39620336	<i>Ppp2r2b</i>	3.13053147
<i>Col9a1</i>	1.69601381	<i>Rabggtb</i>	1.23544403
<i>Crb2</i>	2.39924221	<i>Rap1gap2</i>	1.93298707
<i>Creb5</i>	1.8665512	<i>Rapgef5</i>	1.36252931
<i>Cyp26b1</i>	1.40532871	<i>Rara</i>	1.24988287
<i>Dapk1</i>	1.33592196	<i>Rarb</i>	1.36236403
<i>Dmrt2</i>	4.55283824	<i>Sfrp1</i>	1.89897858
<i>Dsc2</i>	1.46324932	<i>Shroom3</i>	1.4395751
<i>Edar</i>	1.63616757	<i>Sim1</i>	3.21940674
<i>Egln1</i>	1.60296294	<i>Slc16a3</i>	2.55928536
<i>Eno3</i>	1.25675064	<i>Soat1</i>	1.41096747
<i>Erp29</i>	1.25391099	<i>Spred3</i>	1.6624021
<i>F11r</i>	1.38606721	<i>Stard4</i>	1.2386737
<i>Fam114a2</i>	1.30758551	<i>Stc1</i>	2.20191573
<i>Flt1</i>	1.53074609	<i>Tbx2</i>	1.55038865
<i>Galnt16</i>	1.58849703	<i>Tmed5</i>	1.39088297
<i>Gm8730</i>	8.95390964	<i>Tmem200b</i>	1.32318142
<i>Hand1</i>	5.44991899	<i>Ubl4b</i>	2.20690987
<i>Hist1h2bj</i>	2.78855832	<i>Uncx</i>	2.70828114
<i>Hk2</i>	1.61521463	<i>Vegfa</i>	1.56171441
<i>Hoxa1</i>	1.8947815	<i>Zfp395</i>	1.36827481
<i>Hoxa7</i>	1.25304575		

12.5 List of 410 direct transcriptional targets of HAND2

List of direct transcriptional targets of HAND2 was obtained by overlapping *Hand2*^{+/+}, *Prx1Cre*/+ (as WT) and *Hand2*^{Δ/Δc} forelimb bud transcriptome at E10.0-10.25 (31-33s) to ChIP-seq of HAND2^{3xF/3xF} embryos FLBs at E10.5 (transcriptome FC ≤1.2, FDR <0.05, ChIP-seq generated by Marco Osterwalder). Overlap revealed 268 up-regulated and 142 down-regulated direct transcriptional targets of HAND2 in FLBs.

Table 10. List of 268 up-regulated direct transcriptional targets of HAND2.

Gene name	FC	Gene name	FC	Gene name	FC	Gene name	FC	Gene name	FC
<i>Abat</i>	1.37879966	<i>Edil3</i>	1.70405887	<i>Kcnb1</i>	2.39389981	<i>Ppp1r3c</i>	1.62373355	<i>Tmem59l</i>	1.65846318
<i>Adamts9</i>	1.6072359	<i>Efna3</i>	1.38740013	<i>Kcnd3</i>	2.19335533	<i>Prdm16</i>	1.33332492	<i>Tmtc2</i>	1.32394955
<i>Agtrap</i>	1.37302826	<i>Efna5</i>	1.31928093	<i>Kcnh2</i>	1.33341457	<i>Prkg1</i>	1.45370551	<i>Tnrc18</i>	1.20411245
<i>Aldh4a1</i>	1.45342554	<i>Elmo2</i>	1.31814821	<i>Kcnq4</i>	1.81085524	<i>Prrx2</i>	1.45759811	<i>Tpbg</i>	1.30548722
<i>Alx3</i>	1.91307989	<i>Emx2</i>	1.24544209	<i>Kcp</i>	1.36522119	<i>Psd2</i>	1.59501116	<i>Tpp1</i>	1.30097868
<i>Alx4</i>	1.91495974	<i>Epas1</i>	1.42294655	<i>Klhl29</i>	1.20473274	<i>Ptgis</i>	1.2943372	<i>Trerf1</i>	1.25092683
<i>Arhgap20</i>	2.06570875	<i>Epb4.1l3</i>	1.20598918	<i>Lgals3bp</i>	1.80028593	<i>Pth1r</i>	1.33017285	<i>Tspan11</i>	2.22591446
<i>Arhgap22</i>	1.68476657	<i>Epha7</i>	1.34307379	<i>Lhx2</i>	1.40395792	<i>Ptms</i>	1.20711889	<i>Tspan13</i>	1.23411717
<i>Arid5b</i>	1.40323231	<i>Ephx1</i>	2.30438807	<i>Lmf1</i>	1.34278444	<i>Ptpdc1</i>	1.30299134	<i>Tspyl5</i>	1.38458645
<i>Arrdc3</i>	1.72416383	<i>Eya4</i>	1.34193001	<i>Lphn1</i>	1.2343902	<i>Ptpn13</i>	1.21316348	<i>Ttc28</i>	1.21352951
<i>Asap3</i>	1.56585264	<i>Fam13a</i>	1.8147518	<i>Lrp1</i>	1.26448539	<i>Ptprs</i>	1.22251125	<i>Ttc9c</i>	1.24228432
<i>Asb4</i>	1.49018547	<i>Fam196b</i>	1.74957278	<i>Lrrc1</i>	1.25652843	<i>Ptpru</i>	1.26858223	<i>Till7</i>	1.57053404
<i>Atrnl1</i>	1.21417147	<i>Fgf5</i>	1.91920107	<i>Lrsam1</i>	1.40108008	<i>Pxk</i>	1.34674843	<i>Twist1</i>	1.21381097
<i>Bai2</i>	1.49793461	<i>Fmod</i>	1.78749602	<i>Ltbp4</i>	1.40796597	<i>Rab32</i>	2.15178067	<i>Txndc16</i>	1.30103379
<i>BC005764</i>	1.22645639	<i>Foxp1</i>	1.53650025	<i>Maf</i>	1.73746903	<i>Rab3il1</i>	1.21493316	<i>Vamp2</i>	1.24878571
<i>Bmf</i>	1.53076201	<i>Fras1</i>	1.38765788	<i>Mafb</i>	1.42982228	<i>Rabac1</i>	1.24935687	<i>Vstm2b</i>	1.61790011
<i>Boc</i>	1.46659534	<i>Frem2</i>	1.40036854	<i>Mecom</i>	1.27409483	<i>Rbm5</i>	1.2051316	<i>Wdr86</i>	1.63718204
<i>Clqtnf1</i>	2.47538018	<i>Fuca1</i>	1.2894361	<i>Meg3</i>	1.42635722	<i>Rimklb</i>	1.2198081	<i>Wif1</i>	1.7406622
<i>Cacna1c</i>	1.33943783	<i>Fzd8</i>	1.33247781	<i>Mfap4</i>	1.37806882	<i>Rnf157</i>	1.23610154	<i>Wisp1</i>	1.55113729
<i>Cacna1g</i>	1.41268699	<i>Gaa</i>	1.21239938	<i>Mlycd</i>	1.38290401	<i>Ror1</i>	1.25033086	<i>Zcchc24</i>	1.26971405
<i>Cacna1h</i>	1.50622356	<i>Gabbr1</i>	1.26256005	<i>Mn1</i>	1.27542105	<i>Rora</i>	1.69208414	<i>Zfhx2</i>	1.29960036
<i>Cacng7</i>	1.39531634	<i>Gas1</i>	1.40938611	<i>Msx1</i>	1.26435373	<i>Rph3al</i>	1.83722855	<i>Zfhx4</i>	1.41674708

<i>Ccbe1</i>	1.61609742	<i>Gata4</i>	10.8741126	<i>Msx2</i>	1.35035837	<i>Rpl34</i>	1.62149241	<i>Zfp608</i>	1.21796092
<i>Ccng2</i>	1.34459726	<i>Gata5</i>	2.27030295	<i>Mxd4</i>	1.47303795	<i>Rps6ka1</i>	1.2001274	<i>Zfp618</i>	1.22567387
<i>Cd82</i>	1.61691405	<i>Gata6</i>	2.07057938	<i>Mxra8</i>	2.31073128	<i>Rspo1</i>	1.866383	<i>Zfp804a</i>	2.26678267
<i>Cd97</i>	1.54122816	<i>Gdf6</i>	1.63181202	<i>Ncam1</i>	1.57166329	<i>Runx2</i>	2.10880718	<i>Zfp827</i>	1.24717522
<i>Cdkn1b</i>	1.28384685	<i>Gli3</i>	1.25426824	<i>Nfatc4</i>	1.41058294	<i>Slpr3</i>	1.2376854	<i>Zfp839</i>	1.42893701
<i>Cdkn1c</i>	1.29199892	<i>Glis1</i>	2.15664909	<i>Nfib</i>	1.27808104	<i>Samd4</i>	1.50560471	<i>Zmym6</i>	1.24366989
<i>Cdon</i>	1.48259709	<i>Glis3</i>	1.55146545	<i>Nfic</i>	1.39188764	<i>Sdk1</i>	1.34874338	<i>Dlg4</i>	1.20961222
<i>Cep250</i>	1.30786994	<i>Grik5</i>	1.29183034	<i>Nlgn2</i>	1.29223763	<i>Sema6c</i>	1.26373016	<i>Dnm3os</i>	1.90479457
<i>Chst1</i>	1.55328299	<i>Grip1</i>	1.30642718	<i>Notch3</i>	1.20209459	<i>Sft2d2</i>	1.36962832	<i>Dok2</i>	1.92753303
<i>Cirbp</i>	1.21874658	<i>Hlf0</i>	1.20355064	<i>Npas3</i>	2.05874233	<i>Sfxn3</i>	1.54646631	<i>Dpf3</i>	2.44522362
<i>Col12a1</i>	1.53336374	<i>Hif3a</i>	1.28374329	<i>Nr2f1</i>	1.22678447	<i>Sh2d5</i>	1.86960004	<i>Dync1i1</i>	1.4351414
<i>Col16a1</i>	1.38036744	<i>Hist1h1b</i>	5.53215201	<i>Ntn1</i>	1.4347036	<i>Six2</i>	1.64613294	<i>Ebf3</i>	1.24766437
<i>Colla1</i>	1.53696238	<i>Hist1h1d</i>	5.82222819	<i>Nudt6</i>	1.61873201	<i>Slc22a17</i>	1.39654268	<i>Igfbp5</i>	1.46859146
<i>Colla2</i>	1.96461215	<i>Hist1h2ak</i>	3.40912143	<i>Numbl</i>	1.3623899	<i>Slc2a8</i>	1.51149816	<i>Irf5</i>	1.72229834
<i>Col5a1</i>	1.25006559	<i>Hist1h2bn</i>	6.57147778	<i>Nxph3</i>	1.74900134	<i>Slc4a3</i>	1.25943307	<i>Irx3</i>	1.56243687
<i>Col8a2</i>	1.79264745	<i>Hist1h3e</i>	2.93850276	<i>Olfm2</i>	2.04193211	<i>Slc6a17</i>	1.5133678	<i>Irx4</i>	1.65462296
<i>Cpz</i>	1.45104573	<i>Hist1h4d</i>	4.86851549	<i>Olfml2a</i>	1.80762772	<i>Slit1</i>	1.99850393	<i>Irx5</i>	1.53775659
<i>Creb3l1</i>	1.91425422	<i>Hist1h4f</i>	9.75707068	<i>Pacsin1</i>	1.60997455	<i>Smarca2</i>	1.30999282	<i>Itga11</i>	2.21976848
<i>Crlf1</i>	1.56433637	<i>Hist1h4k</i>	3.5552585	<i>Pafah2</i>	1.58554324	<i>Sned1</i>	2.44195758	<i>Pml</i>	1.28215657
<i>Crocc</i>	1.25793982	<i>Hoxa3</i>	1.38881267	<i>Pbx1</i>	1.34658848	<i>Sorl1</i>	1.23531654	<i>Pomt1</i>	1.23257652
<i>Csf1</i>	1.42576399	<i>Hoxb3</i>	1.44766568	<i>Pde4a</i>	1.49180272	<i>Sox5</i>	1.49548915	<i>Pou2f2</i>	2.0734293
<i>Csf1r</i>	1.86762413	<i>Hoxb9</i>	2.68750622	<i>Pde8a</i>	1.5121291	<i>Sox6</i>	1.30112672	<i>Ppm1h</i>	1.55785519
<i>Csrnp3</i>	1.29682396	<i>Hoxc4</i>	1.37120575	<i>Pdgrb</i>	1.23887265	<i>Sparc</i>	1.23831806	<i>Ppox</i>	1.55955487
<i>Csrp1</i>	1.37498783	<i>Hoxc5</i>	1.38327893	<i>Pdlim5</i>	1.24555341	<i>Srcrb4d</i>	1.5455189	<i>Ppp1r13l</i>	1.20786147
<i>Cthrc1</i>	1.59029332	<i>Hoxc6</i>	1.43844783	<i>Pdzd7</i>	2.27433505	<i>Srgap3</i>	1.28870363	<i>Tbx18</i>	1.4726446
<i>Cux2</i>	1.57795726	<i>Hoxc8</i>	1.65946169	<i>Peli2</i>	1.20747647	<i>Sspn</i>	2.08150797	<i>Tgfb1</i>	1.38059927
<i>Cxcl14</i>	1.62271468	<i>Hpse2</i>	1.70059162	<i>Pgm2l1</i>	1.25770155	<i>St3gal1</i>	1.37141158	<i>Tgfbr3</i>	1.21216682
<i>Cyp27a1</i>	1.37125256	<i>Hs3st3a1</i>	1.44458242	<i>Phyhip</i>	2.55964264	<i>Stil</i>	1.22247814	<i>Thbs3</i>	1.53142097
<i>Dap</i>	1.61906068	<i>Id1</i>	1.20395012	<i>Pik3ip1</i>	1.43510119	<i>Stoml1</i>	1.36414829	<i>Timp2</i>	1.27627995
<i>Dclk1</i>	1.2800916	<i>Id2</i>	1.34951782	<i>Pitx1</i>	2.90691673	<i>Sulf1</i>	1.56714593	<i>Tlr2</i>	2.4438172
<i>Dhrs3</i>	1.42344912	<i>Id3</i>	1.25380117	<i>Pld3</i>	1.26753417	<i>Syne1</i>	1.61342279		

<i>Dhx34</i>	1.28658775	<i>Igfbp2</i>	1.31530117	<i>Plxna2</i>	1.3864282	<i>Synpo</i>	1.63926312		
--------------	------------	---------------	------------	---------------	-----------	--------------	------------	--	--

Table 11. List of 142 down-regulated direct transcriptional targets of HAND2.

Gene	FC	Gene	FC	Gene	FC	Gene	FC	Gene	FC	Gene	FC
<i>2410131K14Rik</i>	1.210	<i>Cntfr</i>	1.883	<i>Gpd1l</i>	1.264	<i>Mgat4a</i>	1.228	<i>Rasgef1b</i>	1.749	<i>Spry4</i>	1.399
<i>Aars</i>	1.202	<i>Coro1c</i>	1.230	<i>Gpr4</i>	1.995	<i>Msi2</i>	1.387	<i>Rnd3</i>	1.534	<i>Stk39</i>	1.342
<i>Abl2</i>	1.232	<i>Cpa2</i>	1.560	<i>Grem1</i>	2.490	<i>N4bp3</i>	1.2486	<i>Rspo3</i>	1.930	<i>Synm</i>	2.240
<i>Adam11</i>	1.490	<i>Cyp1b1</i>	1.793	<i>Gsc</i>	1.700	<i>Nrp2</i>	1.247	<i>Rtn4rl1</i>	2.300	<i>Tbc1d16</i>	1.208
<i>Adcy1</i>	1.326	<i>D10Wsu102e</i>	1.202	<i>Gsto2</i>	2.633	<i>Nrtn</i>	1.398	<i>Rybp</i>	1.246	<i>Tgds</i>	1.437
<i>Aif1l</i>	1.227	<i>D430041D05Rik</i>	1.975	<i>Hand2</i>	117.1	<i>Ntn3</i>	1.277	<i>Sall1</i>	2.261	<i>Tiparp</i>	1.215
<i>Ankrd10</i>	1.224	<i>Dctd</i>	1.311	<i>Hdac9</i>	1.344	<i>Nudt15</i>	1.287	<i>Sall3</i>	2.252	<i>Tns3</i>	1.232
<i>Ano1</i>	2.291	<i>Ddx39</i>	1.231	<i>Hmcn1</i>	1.274	<i>Nufip2</i>	1.212	<i>Sertad4</i>	1.361	<i>Trim71</i>	1.265
<i>Arid3a</i>	1.267	<i>Dkk3</i>	1.471	<i>Hoxa11</i>	1.367	<i>Nxn</i>	1.206	<i>Sgms2</i>	2.110	<i>Ttll11</i>	1.904
<i>Asl</i>	1.654	<i>Dlx2</i>	1.317	<i>Hoxd10</i>	1.248	<i>Olfm1</i>	2.010	<i>Shh</i>	38.449	<i>Ttpal</i>	1.233
<i>Bcat1</i>	1.400	<i>Dock6</i>	1.250	<i>Hoxd11</i>	5.677	<i>Osr1</i>	1.916	<i>Shox2</i>	1.471	<i>Unc5c</i>	1.936
<i>Bcl2</i>	1.359	<i>Dok4</i>	2.118	<i>Hsd11b2</i>	1.668	<i>Palm3</i>	1.590	<i>Slc15a4</i>	1.254	<i>Vav2</i>	1.222
<i>Bhlha9</i>	1.397	<i>Enc1</i>	1.288	<i>Hspd1</i>	1.233	<i>Phlda1</i>	1.352	<i>Slc16a10</i>	1.325	<i>Vps8</i>	1.808
<i>Btbd3</i>	1.305	<i>Epha8</i>	2.036	<i>Hspe1</i>	1.275	<i>Plxna4</i>	1.543	<i>Slc29a4</i>	1.304	<i>Wdfy1</i>	1.574
<i>Calm1</i>	1.274	<i>Ets1</i>	1.208	<i>Ifrd1</i>	1.266	<i>Polr3b</i>	1.249	<i>Slc7a5</i>	1.366	<i>Wdr4</i>	1.211
<i>Camk2a</i>	1.743	<i>Ets2</i>	1.729	<i>Impdh1</i>	1.243	<i>Pou4f1</i>	5.253	<i>Slc8a3</i>	2.332	<i>Wnt11</i>	1.381
<i>Cbln1</i>	1.647	<i>Fam178a</i>	1.221	<i>Isoc1</i>	1.204	<i>Ppp1r16b</i>	1.336	<i>Slit3</i>	1.321	<i>Wnt5a</i>	1.25
<i>Ccdc117</i>	1.321	<i>Fgf8</i>	1.679	<i>Itgav</i>	1.234	<i>Ppp2r2c</i>	2.381	<i>Smoc1</i>	1.771		
<i>Ccnd1</i>	1.399	<i>Fgf9</i>	2.061	<i>Jag1</i>	1.306	<i>Prdm1</i>	2.765	<i>Smyd2</i>	1.275		
<i>Cdc42ep3</i>	1.459	<i>Fmn1</i>	1.540	<i>Kbtbd8</i>	1.388	<i>Prmt3</i>	1.234	<i>Snai1</i>	1.329		
<i>Cdk6</i>	1.756	<i>Foxj1</i>	1.855	<i>Kif26a</i>	1.449	<i>Prnp</i>	1.399	<i>Snap91</i>	1.417		
<i>Cdkn1a</i>	1.527	<i>Frem1</i>	2.038	<i>Kpna2</i>	1.201	<i>Psat1</i>	1.235	<i>Snrpa1</i>	1.258		
<i>Cdr2</i>	1.260	<i>Gbx2</i>	1.972	<i>Lad1</i>	1.407	<i>Ptch1</i>	3.277	<i>Snx5</i>	1.235		
<i>Cecr2</i>	1.217	<i>Gjc1</i>	1.470	<i>Mcl1</i>	1.201	<i>Ralgps2</i>	1.202	<i>Socs2</i>	1.674		
<i>Chrna1</i>	1.651	<i>Gli1</i>	4.521	<i>Mctp2</i>	1.781	<i>Rangrf</i>	1.225	<i>Sost</i>	1.381		

12.6 List of 39 common direct transcriptional targets of TBX3 and HAND2

39 Common direct transcriptional targets of TBX3 and HAND2 identified by intersecting: 140 direct transcriptional targets of TBX3 (obtained by overlapping WT and *Tbx3*- deficient FLBs at E9.75-10.0 (28-31s), ChIP-seq of *Tbx3*^{3xF/3xF} embryos FLBs at E9.75-E10.25 and forelimbs ATAC-seq E10.5 data sets (transcriptome FC ≤1.2, FDR <0.05, ChIP-seq 1e5)) to 410 direct transcriptional targets of HAND2 (obtained by overlapping *Hand2*^{+/+}, *Prx1Cre*/+ (as WT) and *Hand2*^{Δ/Δc} FLBs at E10.0-10.25 (31-33s) to ChIP-seq of HAND2^{3xF/3xF} embryos FLBs at E10.5 (transcriptome FC ≤1.2, FDR <0.05, ChIP-seq generated by Marco Osterwalder)).

Table 12. List of 39 common direct transcriptional targets of TBX3 and HAND2 in mouse early embryonic forelimb buds.

Common TBX3 and HAND2 direct transcriptional target genes			
<i>Adamts9</i>	<i>Hoxb3</i>	<i>Mctp2</i>	<i>Ptpn13</i>
<i>Alx4</i>	<i>Hoxc4</i>	<i>Ncam1</i>	<i>Rora</i>
<i>Ccbe1</i>	<i>Hoxc6</i>	<i>Olfm1</i>	<i>Sall3</i>
<i>Ccng2</i>	<i>Hoxc8</i>	<i>Pitx1</i>	<i>Shox2</i>
<i>Efna3</i>	<i>Hoxd10</i>	<i>Plxna2</i>	<i>Slit1</i>
<i>Ets2</i>	<i>Hoxd11</i>	<i>Plxna4</i>	<i>Sox6</i>
<i>Foxp1</i>	<i>Hs3st3a1</i>	<i>Pou2f2</i>	<i>St3gal1</i>
<i>Fras1</i>	<i>Hsd11b2</i>	<i>Ppp1r3c</i>	<i>Tbx18</i>
<i>Gata6</i>	<i>Irx3</i>	<i>Prdm1</i>	<i>Tgfbi</i>
<i>Hand2</i>	<i>Irx5</i>	<i>Ptch1</i>	

Table 13. The table represents the list of outcast direct transcriptional targets of TBX3 that do not overlap with ATAC-seq peaks. Genes were identified by overlapping WT, and *Tbx3*-deficient FLBs transcriptome revealed DEGs and all the TBX3 ChIP-seq consensus peaks (peaks that were detected in both replicates) associated to the nearest genes to peaks using **basal plus extension GREAT mode** (n=11,422).

TBX3 direct transcriptional target genes that do not overlap with ATAC-seq peaks					
2410131K14Rik	<i>Cnr1</i>	<i>Fzd10</i>	<i>Kank4</i>	<i>Pam</i>	<i>Sell13</i>
4930522L14Rik	<i>Col14a1</i>	<i>Gak</i>	<i>Kcnn3</i>	<i>Pappa2</i>	<i>Serinc5</i>
	<i>Ackr3</i>	<i>Col15a1</i>	<i>Galnt14</i>	<i>Kdm3a</i>	<i>Pcdh17</i>
	<i>Adgrl3</i>	<i>Col5a1</i>	<i>Gap43</i>	<i>Kdm7a</i>	<i>Pcna-ps2</i>
	<i>Ak4</i>	<i>Col6a3</i>	<i>Gata5</i>	<i>Kifc5b</i>	<i>Pdk1</i>
	<i>Akap12</i>	<i>Cped1</i>	<i>Gdf6</i>	<i>Klf12</i>	<i>Pdlim5</i>
	<i>Aldoc</i>	<i>Crispld2</i>	<i>Gja5</i>	<i>Lama2</i>	<i>Pfkp</i>
	<i>Amph</i>	<i>Crnk1l</i>	<i>Glcci1</i>	<i>Lrp2</i>	<i>Pik3r3</i>
	<i>Angpt2</i>	<i>Csf1r</i>	<i>Glt1d1</i>	<i>Mamdc2</i>	<i>Plekha2</i>
	<i>Ankrd26</i>	<i>Dcun1d4</i>	<i>Gm2a</i>	<i>Map1a</i>	<i>Plod2</i>
	<i>Ankrd37</i>	<i>Dlk1</i>	<i>Gm42878</i>	<i>Map1b</i>	<i>Popdc2</i>
	<i>Anxa2</i>	<i>Dpf3</i>	<i>Gnai1</i>	<i>Mcub</i>	<i>Pou4f1</i>
	<i>Asic4</i>	<i>Dpysl2</i>	<i>Grk3</i>	<i>Meox1</i>	<i>Ppp1r3g</i>
	<i>Bhlhe40</i>	<i>Dpysl3</i>	<i>Gucyl1a3</i>	<i>Meox2</i>	<i>Prelid2</i>
	<i>Bmt2</i>	<i>Dpysl5</i>	<i>Gucyl1b3</i>	<i>Mmp17</i>	<i>Prickle1</i>
	<i>Bnip3l</i>	<i>Dsp</i>	<i>Higd1a</i>	<i>Mrc1</i>	<i>Prnd</i>
	<i>Car12</i>	<i>Egfr</i>	<i>Hmx1</i>	<i>Msmo1</i>	<i>Rab39</i>
	<i>Cav1</i>	<i>Egln3</i>	<i>Hoxb9</i>	<i>Myc</i>	<i>Rabl2</i>
	<i>Ccser1</i>	<i>Eno1b</i>	<i>Hoxd13</i>	<i>Nap115</i>	<i>Rbpms</i>
	<i>Cd36</i>	<i>Ezr</i>	<i>Igfbp2</i>	<i>Ndr1</i>	<i>Rgs2</i>
	<i>Cdo1</i>	<i>F13a1</i>	<i>Igfbp3</i>	<i>Ndufv3</i>	<i>Rims2</i>
	<i>Celf2</i>	<i>Fam189a2</i>	<i>Itga2b</i>	<i>Ngfr</i>	<i>Robo2</i>
	<i>Chst15</i>	<i>Foxi2</i>	<i>Itgb3</i>	<i>Nxph4</i>	<i>Ror1</i>
	<i>Ciart</i>	<i>Frem1</i>	<i>Itgb8</i>	<i>Olfm2</i>	<i>Rps2</i>
	<i>Cldn5</i>	<i>Fst</i>	<i>Jag1</i>	<i>P4ha2</i>	<i>Rtn4rl1</i>

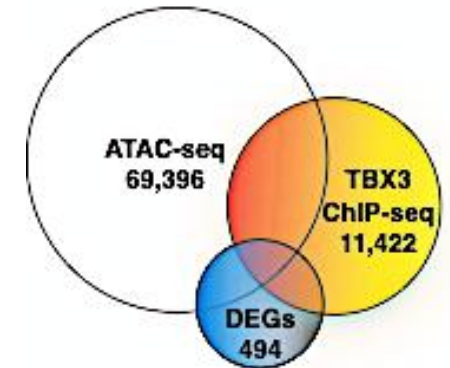


Table 14. The table represents the list of outcast direct transcriptional targets of TBX3 that do not overlap with ATAC-seq peaks. Genes were identified by overlapping WT, and *Tbx3*-deficient FLBs transcriptome revealed DEGs and all the TBX3 ChIP-seq consensus peaks (peaks that were detected in both replicates) associated to the nearest genes to peaks using **two nearest genes GREAT mode** (n=11,422).

TBX3 direct transcriptional target genes that do not overlap with ATAC-seq peaks					
<i>2410131K14Rik</i>	<i>Col15a1</i>	<i>Fzd10</i>	<i>Kdm3a</i>	<i>Pcna-ps2</i>	<i>Shisa3</i>
<i>4930522L14Rik</i>	<i>Col5a1</i>	<i>Gak</i>	<i>Kdm7a</i>	<i>Pdlim5</i>	<i>Slc25a1</i>
<i>Ackr3</i>	<i>Col6a3</i>	<i>Galnt14</i>	<i>Kifc5b</i>	<i>Pik3r3</i>	<i>Slc2a1</i>
<i>Adgrl3</i>	<i>Cox4i2</i>	<i>Gap43</i>	<i>Klf12</i>	<i>Plekha2</i>	<i>Snx25</i>
<i>Ak4</i>	<i>Cped1</i>	<i>Gata5</i>	<i>Lama2</i>	<i>Plod2</i>	<i>Sparcl1</i>
<i>Akap12</i>	<i>Crispld2</i>	<i>Gdf6</i>	<i>Lrp2</i>	<i>Popdc2</i>	<i>Stc2</i>
<i>Amph</i>	<i>Crnk1l</i>	<i>Gja5</i>	<i>Mamdc2</i>	<i>Pou4f1</i>	<i>Thbs1</i>
<i>Angpt2</i>	<i>Csflr</i>	<i>Glcci1</i>	<i>Map1a</i>	<i>Ppp1r3g</i>	<i>Tmem114</i>
<i>Ankrd26</i>	<i>Dcun1d4</i>	<i>Glt1d1</i>	<i>Map1b</i>	<i>Preli2</i>	<i>Tmem170b</i>
<i>Ankrd37</i>	<i>Dlk1</i>	<i>Gm2a</i>	<i>Masp1</i>	<i>Prickle1</i>	<i>Tmem74b</i>
<i>Anxa2</i>	<i>Dpf3</i>	<i>Gm42878</i>	<i>Mcub</i>	<i>Prnd</i>	<i>Tnfaip3</i>
<i>Asic4</i>	<i>Dpysl2</i>	<i>Gnai1</i>	<i>Meox1</i>	<i>Rab39</i>	<i>Tpi1</i>
<i>Bhlhe40</i>	<i>Dpysl3</i>	<i>Grk3</i>	<i>Meox2</i>	<i>Rabl2</i>	<i>Trim29</i>
<i>Bmt2</i>	<i>Dpysl5</i>	<i>Gucy1a3</i>	<i>Mmp17</i>	<i>Rbpms</i>	<i>Vldlr</i>
<i>Bnip3l</i>	<i>Dsp</i>	<i>Gucy1b3</i>	<i>Mrc1</i>	<i>Rgs2</i>	<i>Wisp1</i>
<i>Car12</i>	<i>Egfr</i>	<i>H60b</i>	<i>Msmo1</i>	<i>Rims2</i>	<i>Wnt2</i>
<i>Cav1</i>	<i>Egln3</i>	<i>Higd1a</i>	<i>Myc</i>	<i>Rnaset2a</i>	<i>Wnt5a</i>
<i>Ccdc42</i>	<i>Eno1b</i>	<i>Hmx1</i>	<i>Nap1l5</i>	<i>Robo2</i>	<i>Zfpml1</i>
<i>Ceser1</i>	<i>Ezr</i>	<i>Hoxa10</i>	<i>Ndufv3</i>	<i>Ror1</i>	
<i>Cd36</i>	<i>F13a1</i>	<i>Hoxb6</i>	<i>Ngfr</i>	<i>Rps2</i>	
<i>Cdo1</i>	<i>Fam13b</i>	<i>Igfbp2</i>	<i>Nxph4</i>	<i>Rtn4rl1</i>	
<i>Chst15</i>	<i>Fam177a</i>	<i>Itga2b</i>	<i>Olfm2</i>	<i>Scd1</i>	
<i>Ciart</i>	<i>Fam189a2</i>	<i>Itgb8</i>	<i>P4ha2</i>	<i>Sell13</i>	
<i>Cldn5</i>	<i>Foxi2</i>	<i>Jag1</i>	<i>Pam</i>	<i>Serinc5</i>	
<i>Cnr1</i>	<i>Frem1</i>	<i>Kank4</i>	<i>Pappa2</i>	<i>Sh3rf3</i>	
<i>Coll4a1</i>	<i>Fst</i>	<i>Kcnn3</i>	<i>Pcdh17</i>	<i>Shh</i>	

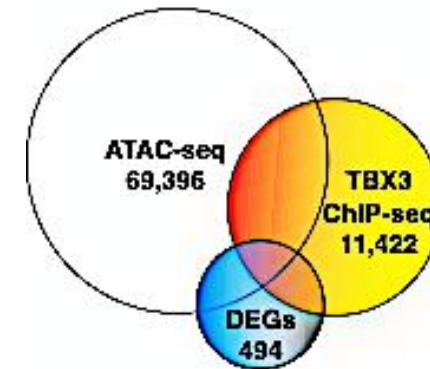


Table 15. The table represents the list of different (due to different GREAT modes used) outcast direct transcriptional targets of TBX3 that do not overlap with ATAC-seq peaks. Genes identified by intersecting data from supplement Table 13 and Table 14.

TBX3 direct transcriptional target genes that do not overlap with ATAC-seq peaks				
<i>2410131K14Rik</i>	<i>Cox4i2</i>	<i>Hoxa10</i>	<i>Jag1</i>	<i>Pdlim5</i>
<i>Aldoc</i>	<i>Crispld2</i>	<i>Hoxb6</i>	<i>Kcnn3</i>	<i>Pfkip</i>
<i>Ankrd26</i>	<i>Dpysl5</i>	<i>Hoxb9</i>	<i>Masp1</i>	<i>Rnaset2a</i>
<i>Ccdc42</i>	<i>Fam13b</i>	<i>Hoxd13</i>	<i>Mcub</i>	<i>Scd1</i>
<i>Ccser1</i>	<i>Fam177a</i>	<i>Igfbp2</i>	<i>Msmo1</i>	<i>Slc25a1</i>
<i>Celf2</i>	<i>Gap43</i>	<i>Igfbp3</i>	<i>Ndr1</i>	<i>Tmem74b</i>
<i>Cnr1</i>	<i>H60b</i>	<i>Itgb3</i>	<i>Pdk1</i>	<i>Tspan13</i>

Table 16. The table represents a list of 35 genes that are known transcription factors and were identified as the direct transcriptional targets of TBX3 in mouse embryos FLBs.

Direct TBX3 target genes that are transcription factors				
<i>Alx4</i>	<i>Gata6</i>	<i>Hoxc6</i>	<i>Pitx1</i>	<i>Sall3</i>
<i>Bnc1</i>	<i>Hand1</i>	<i>Hoxc8</i>	<i>Pknox2</i>	<i>Shox2</i>
<i>Creb5</i>	<i>Hand2</i>	<i>Hoxd10</i>	<i>Pou2f2</i>	<i>Sim1</i>
<i>Dmrt2</i>	<i>Hoxa1</i>	<i>Hoxd11</i>	<i>Prdm1</i>	<i>Sox6</i>
<i>Dmrta1</i>	<i>Hoxa7</i>	<i>Irx3</i>	<i>Rara</i>	<i>Tbx18</i>
<i>Ets2</i>	<i>Hoxb3</i>	<i>Irx5</i>	<i>Rarb</i>	<i>Tbx2</i>
<i>Foxp1</i>	<i>Hoxc4</i>	<i>Lmo1</i>	<i>Rora</i>	<i>Tbx5</i>

Table 17. Candidate TBX3, HAND2 and GLI3 CRMs for transgenic reporters.

The tables below represent the genomic regions identified as possible candidate CRMs of TBX3, HAND2 (Osterwalder et al., 2014)) and GLI3 (XXX). In particular, analysis was focused on the candidate CRMs associated with *Gli3*, *Tbx3*, and *Hand2* locus to evaluate the regulatory relationship (auto- and cross-regulation) between these TF. CRMs analysis was done using transgenic reporters' assay (*hsp68-LacZ* (random integration; the analysis was done by Marco Osterwalder)). Not assessed: N.a, genomic regions in **blue**: assessed candidate CRMs, genomic regions in **red**: already known CRMs (VISTA).

<i>Gli3</i> peaks coordinates in mm10	<i>Gli3</i> peaks coordinates in mm9	Gene	VISTA number	Tested region coordinates
chr13 15241099 15241670	chr13:15333369-15333940	<i>Gli3</i>	N.a.	N.a.
chr13 15435952 15436320	chr13:15527785-15528153	<i>Gli3</i>	Negative (5kb tested, MO)	chr13:15432114-15436834
chr13 15252093 15252457	chr13:5436506-5436558	<i>Gli3</i>	N.a.	N.a.
chr13 15431550 15432072	chr13:15523383-15523905	<i>Gli3</i>	N.a.	N.a.
chr13 15433316 15433698	chr13:15525149-15525531	<i>Gli3</i>	Negative (5kb tested, MO)	chr13:15432114-15436834
chr13 15432831 15433109	chr13:15524664-15524942	<i>Gli3</i>	Negative (5kb tested, MO)	chr13:15432114-15436834
chr13 15438145 15438535	chr13:15529978-15530368	<i>Gli3</i>	Negative (5kb tested, MO)	chr13:15436341-15441269

<i>Hand2</i> peaks coordinates in mm10	<i>Hand2</i> peaks coordinates in mm9	Gene	VISTA number	Tested region coordinates
chr13 15343300 15343894	chr13 15435132 15435727	<i>Gli3</i>	mm1179	—
chr13 15463942 15464513	chr13 15555774 15556346	<i>Gli3</i>	N.a.	N.a.
chr13 15759201 15759518	chr13 15851033 15851351	<i>Gli3</i>	N.a.	N.a.
chr5 118817717 118818984	chr5 119267725 119268993	<i>Tbx3</i>	N.a.	N.a.
chr5 118829146 118829762	chr5 119279154 119279771	<i>Tbx3</i>	N.a.	N.a.
chr5 118869200 118869630	chr5 119319208 119319639	<i>Tbx3</i>	N.a.	N.a.
chr5 119796490 119796882	chr5 120246498 120246891	<i>Tbx3</i>	mm1282 and hs2329	—
chr5 119138644 119139179	chr5 119588652 119589188	<i>Tbx3</i>	N.a.	N.a.
chr5 119139293 119139547	chr5 119589301 119589556	<i>Tbx3</i>	N.a.	N.a.
chr5 119249293 119249898	chr5 119699301 119699907	<i>Tbx3</i>	N.a.	N.a.
chr5 119400299 119401162	chr5 119850307 119851171	<i>Tbx3</i>	N.a.	N.a.
chr5 119609015 119609378	chr5 120059023 120059387	<i>Tbx3</i>	N.a.	N.a.
chr5 119612368 119612832	chr5 120062376 120062841	<i>Tbx3</i>	mm1177	—
chr5 119619795 119620253	chr5 120069803 120070262	<i>Tbx3</i>	N.a.	N.a.

chr5 119651318 119652066	chr5 120101326 120102075	<i>Tbx3</i>	mm1178	—
chr5 119795524 119795907	chr5 120245532 120245916	<i>Tbx3</i>	mm1282	—
chr8 56622884 56623682	chr8 59101680 59102479	<i>Hand2</i>	N.a.	N.a.
chr8 56706785 56707394	chr8 59185581 59186191	<i>Hand2</i>	mm1832 (MO)	chr8:56706437-56707834
chr8 56883508 56883680	chr8 59362304 59362477	<i>Hand2</i>	N.a.	N.a.
chr8 57319558 57320476	chr8 59798354 59799273	<i>Hand2</i>	N.a.	N.a.
chr8 57331464 57332414	chr8 59810260 59811211	<i>Hand2</i>	N.a.	N.a.
chr8 57333388 57334634	chr8 59812184 59813431	<i>Hand2</i>	mm1283	—
chr8 57353544 57354612	chr8 59832340 59833409	<i>Hand2</i>	N.a.	N.a.
chr8 57435949 57436338	chr8 59914745 59915135	<i>Hand2</i>	N.a.	N.a.

<i>Tbx3</i> peaks coordinates in mm10	<i>Tbx3</i> peaks coordinates in mm9	Gene	VISTA number	Tested region coordinates
chr13 15343018 15343149	chr13:15434851-15434982	<i>Gli3</i>	mm1179	—
chr13 15463792 15464046	chr13:15555625-15555879	<i>Gli3</i>	N.a.	N.a.
chr13 15549322 15549622	chr13:15641155-15641455	<i>Gli3</i>	hs1586	—
chr5 118960494 118960638	chr5:119410503-119410647	<i>Tbx3</i>	N.a.	N.a.
chr5 118981104 118981226	chr5:119431113-119431235	<i>Tbx3</i>	N.a.	N.a.
chr5 119612736 119612881	chr5:120062745-120062890	<i>Tbx3</i>	mm1177	—
chr5 119670527 119671140	chr5:120120536-120121149	<i>Tbx3</i>	N.a.	N.a.
chr5 119748679 119748824	chr5:120198688-120198833	<i>Tbx3</i>	N.a.	N.a.
chr5 119795417 119795710	chr5:120245426-120245719	<i>Tbx3</i>	N.a.	N.a.
chr5 119796430 119796674	chr5:120246439-120246683	<i>Tbx3</i>	mm1282	—
chr8 56832691 56832883	chr8:59311488-59311680	<i>Hand2</i>	mm1687	—
chr8 56962357 56962475	chr8:59441154-59441272	<i>Hand2</i>	mm1831 (MO)	chr8:56961474-56963974
chr8 57322021 57322237	chr8:59800818-59801034	<i>Hand2</i>	N.a.	N.a.

Table 18. TBX3 targeted candidate CRMs for transgenic reporters.

The tables below represent the genomic regions identified as possible candidate CRMs of TBX3 (analysis stringency set to 1e3). In this case, analysis was focused on the candidate CRMs associated with *Gli3*, *Tbx3*, and *Hand2* locus to provide insights into FLs development controlling regulatory loop. CRMs analysis was done using transgenic reporters' assay (hsp68-*LacZ* (random integration, analysis done by Prof. Marco Osterwalder)). Not assessed: N.a, genomic regions in **blue**: assessed candidate CRMs, genomic regions in **red**: already known CRMs (VISTA).

<i>Gli3</i> locus coordinates mm10	<i>Gli3</i> locus coordinates mm9	Status	VISTA number
chr13:15343483-15343686	chr13:15435316-15435519	known	mm1179
chr13:15463602-15463957	chr13:15555435-15555790	unknown	N.a.
chr13:15510341-15510668	chr13:15602174-15602501	unknown	Negative (5kb tested, MO)
chr13:15549290-15549618	chr13:15641123-15641451	known	hs1586
chr13:15623001-15623269	chr13:15714834-15715102	unknown	N.a.
chr13:15664737-15665188	chr13:15756570-15757021	known	mm652
chr13:15831820-15832179	chr13:15923653-15924012	unknown	N.a.
chr13:15834117-15834638	chr13:15925950-15926471	unknown	N.a.
chr13:15836704-15837144	chr13:15928537-15928977	unknown	N.a.
chr13:15843664-15844043	chr13:15935497-15935876	unknown	N.a.
<i>Tbx3</i> locus coordinates mm10			
<i>Tbx3</i> locus coordinates mm10	<i>Tbx3</i> locus coordinates mm9	Status	VISTA number
chr5:119668153-119668395	chr5:120118162-120118404	known	hs483
chr5:119668153-119668435	chr5:120118162-120118444	known	hs483
chr5:119669913-119670215	chr5:120119922-120120224	unknown	N.a.
chr5:119670681-119671064	chr5:120120690-120121073	unknown	N.a.
chr5:119672225-119672259	chr5:120122234-120122268	unknown	N.a.
chr5:119672579-119672804	chr5:120122588-120122813	unknown	N.a.
<i>Hand2</i> locus coordinates mm10			
<i>Hand2</i> locus coordinates mm10	<i>Hand2</i> locus coordinates mm9	Status	VISTA number
chr8:57320890-57321234	chr8:59799687-59800031	unknown	N.a.
chr8:57321464-57321755	chr8:59800261-59800552	unknown	N.a.
chr8:57321884-57322441	chr8:59800681-59801238	unknown	N.a.

chr8:57323478-57323935

chr8:59802275-59802732

unknown | N.a.

Table 19. Direct TBX3 target genes candidate CRMs for transgenic reporters.

A table below represents selected direct transcriptional target genes of TBX3 and the genomic regions identified as possible candidate CRMs for transgenic reporters' assay (hsp68-*LacZ* (random integration, analysis done by Marco Osterwalder)). Not assessed: N.a, genomic regions in **blue**: assessed candidate CRMs, genomic regions in **red**: already known CRMs (VISTA).

Direct <i>Tbx3</i> target genes	<i>Tbx3</i> peaks coordinates in mm10	VISTA number	Tested region pattern
<i>Prdm1</i>	chr10 44979599 44979763	N.a.	N.a.
<i>Sall3</i>	chr18 81223202 81223404	N.a.	N.a.
<i>Tshz2</i>	chr2 169702828 169703056	N.a.	N.a.
<i>Itga4</i>	chr2 78869303 78869476	N.a.	N.a.
<i>Tbx18</i>	chr9 87557046 87557280	N.a.	N.a.
<i>Tbx18</i>	chr9 87731153 87731299	N.a.	N.a.
<i>Hs3st3b1</i>	chr11 63300329 63300481	N.a.	N.a.
<i>Rspo2</i>	chr15 43282400 43282597	N.a.	N.a.
<i>Adamts1</i>	chr16 85803135 85803298	N.a.	N.a.
<i>Uncx</i>	chr5 139540287 139540442	N.a.	N.a.
<i>Fzd1</i>	chr5 4562851 4563003	N.a.	N.a.
<i>Fzd1</i>	chr5 4758049 4758198	N.a.	N.a.
<i>Plxna4</i>	chr6 32381523 32381713	N.a.	N.a.
<i>Plxna4</i>	chr6 32710314 32710434	N.a.	N.a.
<i>Hoxa1</i>	chr6 52158542 52158691	N.a.	N.a.
<i>Hoxa1</i>	chr6 52164997 52165424	N.a.	N.a.
<i>Hoxa7</i>	chr6 52222031 52222236	N.a.	N.a.
<i>Cyp26b1</i>	chr6 84410173 84410431	N.a.	N.a.
<i>Egln1</i>	chr8 124949670 124949793	N.a.	N.a.
<i>Edar</i>	chr10 58652137 58652274	N.a.	N.a.
<i>Ptch1</i>	chr13 63451334 63451530	N.a.	N.a.
<i>Ets2</i>	chr16 95702716 95702836	N.a.	N.a.
<i>Ets2</i>	chr16 95845468 95845613	N.a.	N.a.
<i>Ets2</i>	chr16 95848258 95848400	hs1516	—

<i>Sall3</i>	chr18 81223202 81223404	N.a.	N.a.
<i>Olfm1</i>	chr2 28184514 28184640	N.a.	N.a.
<i>Hoxd10</i>	chr2 74681767 74681911	N.a.	N.a.
<i>Hoxd11</i>	chr2 74681767 74681911	N.a.	N.a.
<i>Shox2</i>	chr3 66422634 66423063	mm1840	Negative (non-reproducible staining)
<i>Lmo1</i>	chr7 109191549 109192029	mm1788	FL and distal HL; brain
<i>Hand2</i>	chr8 56832691 56832883	mm1687	—
<i>Hand2</i>	chr8 56962357 56962475	mm1831	Proximal FLBs and HLBs
<i>Hand2</i>	chr8 57322021 57322237	N.a.	N.a.
<i>Hand1</i>	chr11 57827457 57827814	N.a.	N.a.
<i>Tbx2</i>	chr11 85643938 85644073	N.a.	N.a.
<i>Tbx2</i>	chr11 85799815 85800225	mm1210	Heart and limbs
<i>Tbx2</i>	chr11 85818394 85818565	N.a.	N.a.
<i>Tbx2</i>	chr11 85832382 85832843	N.a.	N.a.
<i>Hoxc6</i>	chr15 102999283 102999496	N.a.	N.a.
<i>Hoxc8</i>	chr15 102999283 102999496	N.a.	N.a.
<i>Hoxc4</i>	chr15 103014361 103014493	hs1875	—
<i>Hoxc4</i>	chr15 103034919 103035122	N.a.	N.a.
<i>Hoxc4</i>	chr15 103042542 103042678	N.a.	N.a.
<i>Hoxc4</i>	chr15 103061537 103061680	N.a.	N.a.
<i>Rspo2</i>	chr15 43282400 43282597	N.a.	N.a.
<i>Alx4</i>	chr2 93625109 93625397	N.a.	N.a.
<i>Alx4</i>	chr2 93642703 93642881	N.a.	N.a.
<i>Alx4</i>	chr2 93785210 93785404	N.a.	N.a.
<i>Irx3</i>	chr8 91313492 91313754	N.a.	N.a.
<i>Irx3</i>	chr8 91713877 91714070	mm1211	—
<i>Irx3</i>	chr8 91948630 91948905	N.a.	N.a.
<i>Irx5</i>	chr8 91948630 91948905	N.a.	N.a.
<i>Pknox2</i>	chr9 36938601 36938719	N.a.	N.a.

Figure 42. WISH for the direct transcriptional target of HAND2 with GO terms for AVC cushion morphogenesis for WT and *Hand2*^{Δ/Δ} mouse embryos at E9.5 (n=3)

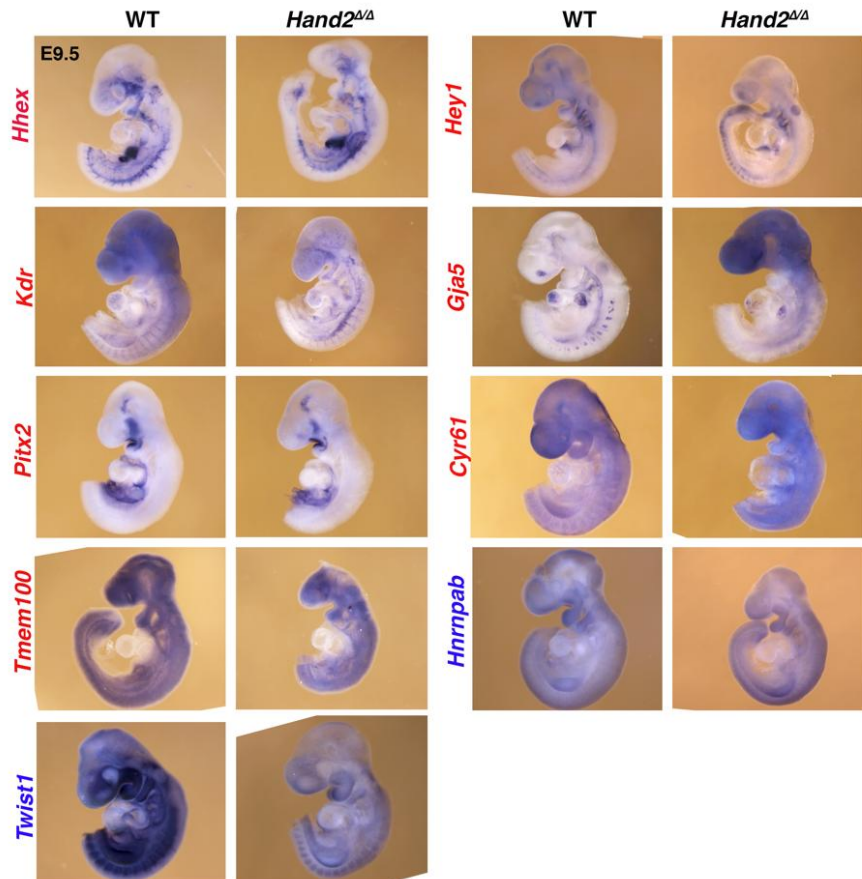


Figure 43. WISH for the direct transcriptional target of HAND2 with GO terms for AVC cushion morphogenesis for WT and *Hand2*^{Δ/Δ} mouse embryonic hearts at E9.5 (n=3, zoom in enlargement of Figure 42).

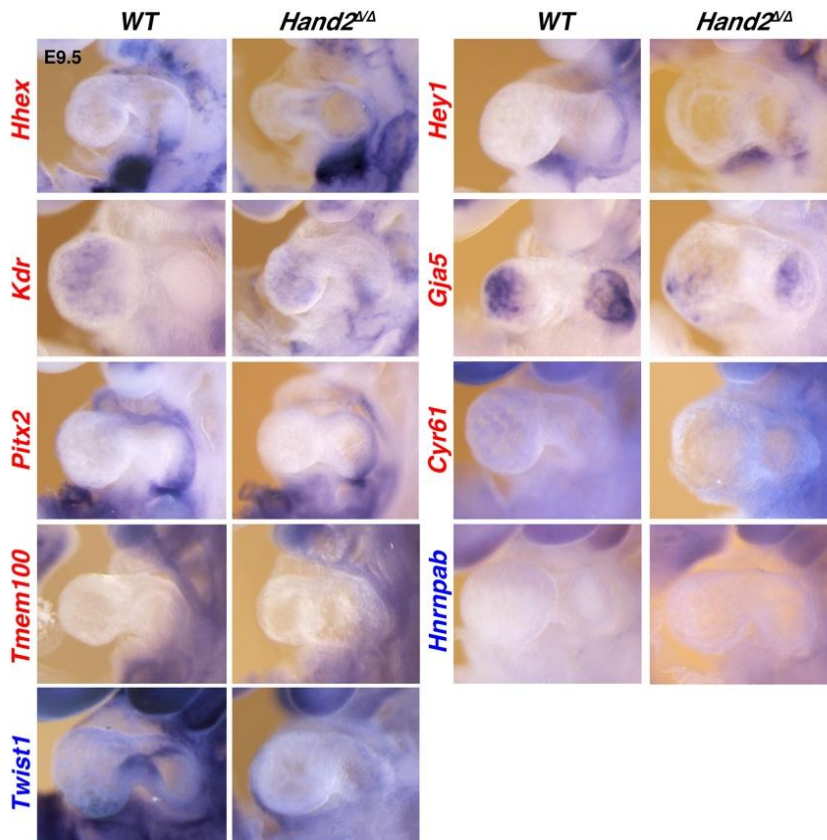


Figure 44. WISH for the direct HAND2 target genes at E9.5 (n=1) in WT and *Hand2*-deficient whole mouse embryos and magnified hearts.

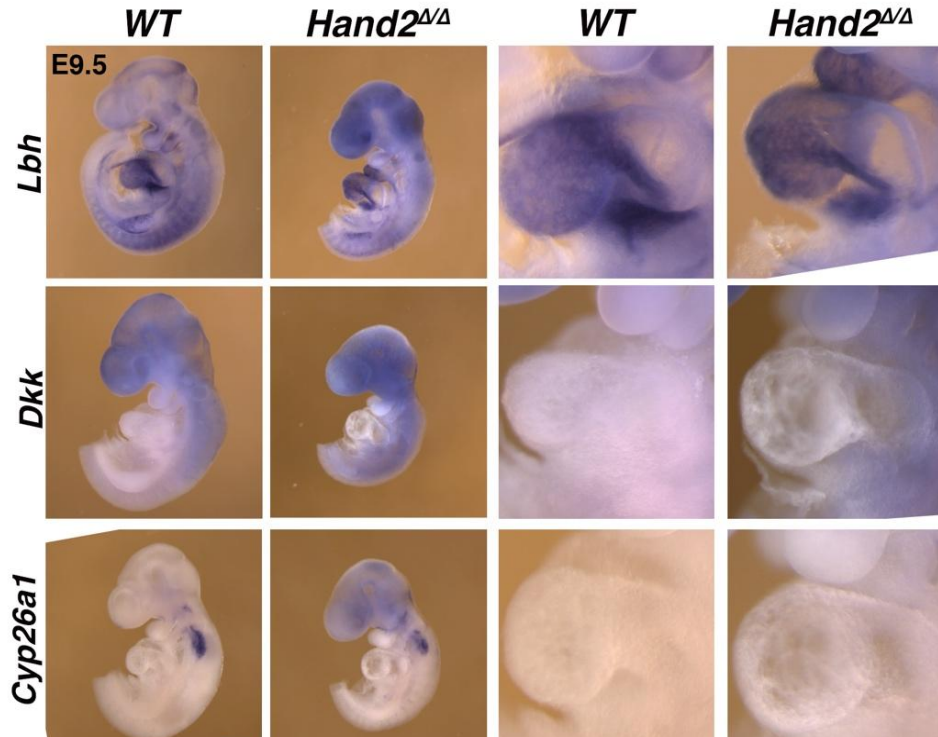


Figure 45. WISH for the direct HAND2 target genes at E9.5 for WT whole mouse embryos and magnified hearts (n=1).

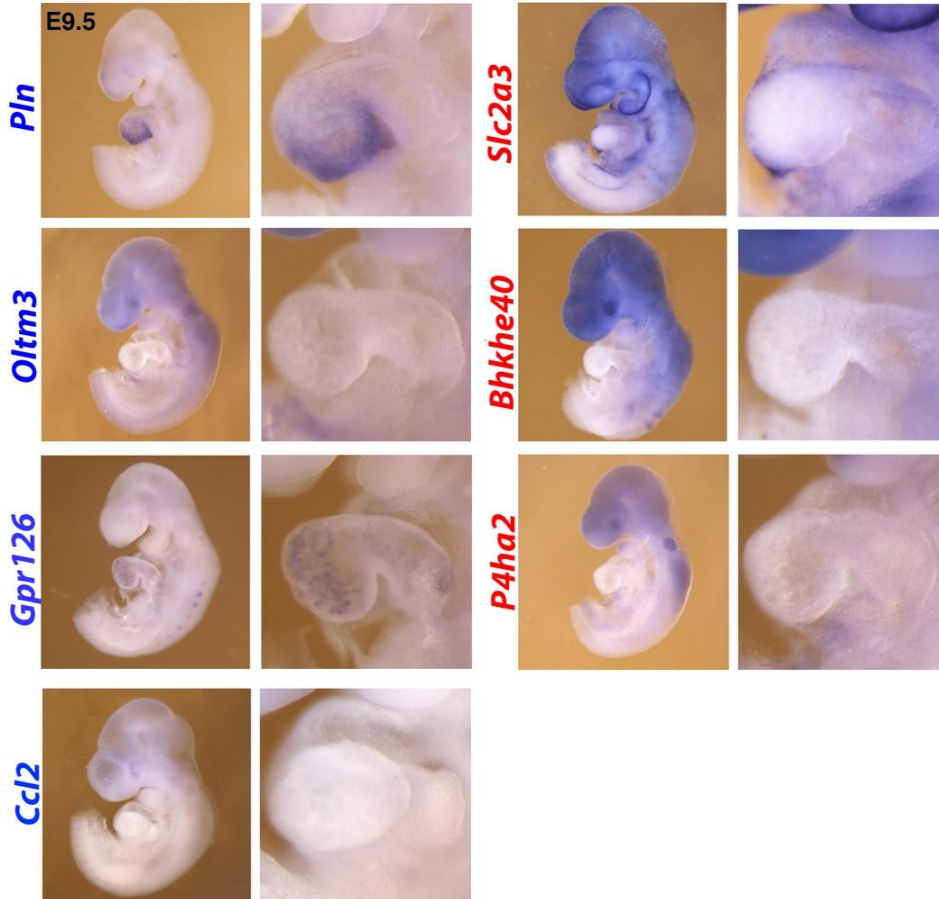


Figure 46. WISH revealed that *Tbx3* expression is down-regulated in *Hand2*-deficient mouse embryos AVCs at E9.5 (n=3).

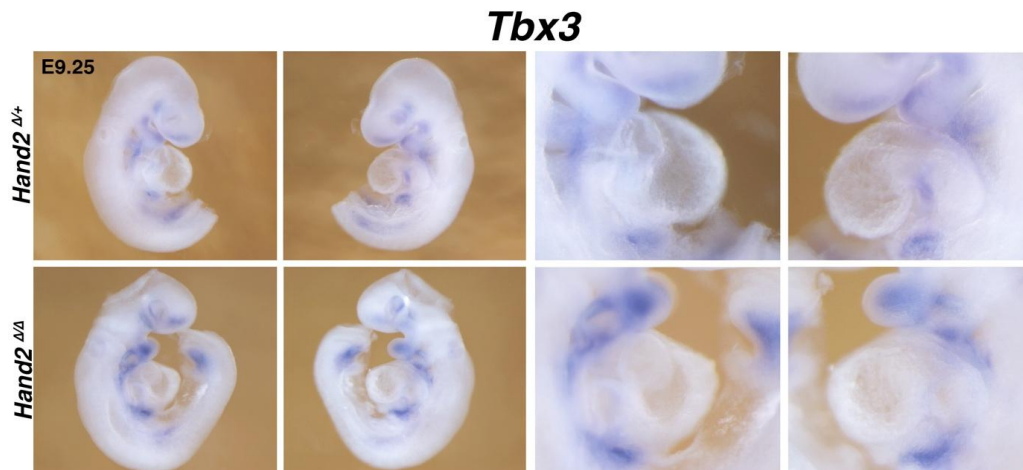


Figure 47. Lysotracker staining was carried out to evaluate the rate of the apoptotic cells in *Hand2*^{Δ/Δ} mouse embryonic limbs and hearts at E9.0, 9.5, 9.75, and E10.0. A significant increase in apoptotic cells in FLBs is observed at these early embryonic stages in comparison to the WT embryos.

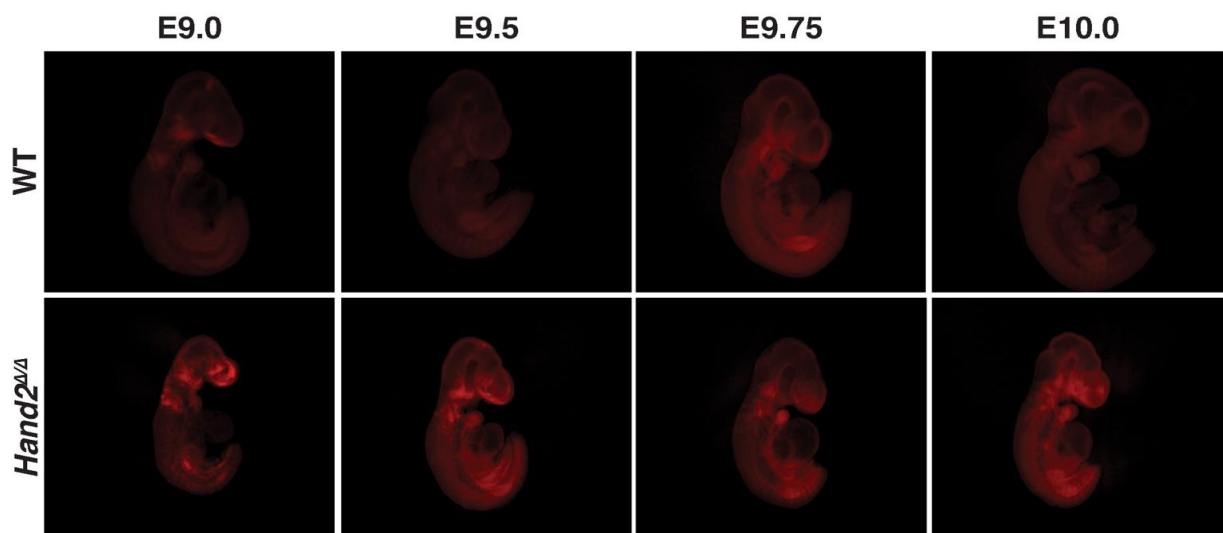
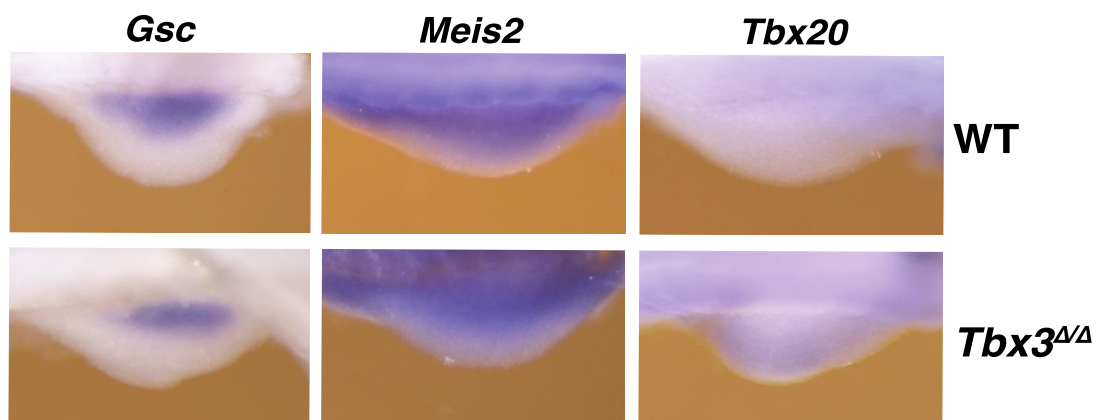


Figure 48. WISH for the direct TBX3 target genes at E9.75 (n=3) in WT and *Tbx3*-deficient whole mouse embryos limb buds.



12.9 Collaboration: HAND2 and PBX coordinately control early hindlimb bud development

During my PhD I had an outstanding opportunity together with the hosting laboratory to collaborate with the group of Licia Selleri (UCSF). Collaborating group has shown that *Hand2* is a direct transcriptional target of the PBX transcription factors during early limb bud development (Capellini et al., 2006). The PBX1/PBX2 TFs plays the significant role in the PD axis patterning. The *Pbx1*-deficiency leads to proximal limb abnormalities, whereas compound *Pbx1*^{Δ/Δ}; *Pbx2*^{Δ/+} mutants exhibit distal defects in addition to the proximal ones, while the complete ablation of *Pbx1/2* leads to the absence of limbs (Capellini, 2006, Selleri et al., 2001). PBXs are essential co-factors for HOX proteins as by dimerizing they help to modulate HOX DNA binding affinity. Thus, *Pbx1/2*-deficiency leads to *Hox* gene spatial perturbation in the posterior limb and cause abnormal *Shh* onset (Capellini, 2006). Indeed, both *Hand2* and *Pbx*-deficient limb buds lacks *Shh* expression and their loss-of-function limb phenotypes show drastic limb abnormalities resembling loss of *Shh* (Capellini et al., 2006). Thus, to provide insights into HAND2 and PBX genes coordinated mouse hindlimb bud development collaboration was started with Marta Losa Llabata (UCSF).

My input in this collaboration consist of: HAND2 ChIP-seq of the HLBs at E10.5 to E11.5 (n=3); RNA-seq of *Hand2*^{Δ/Δc}, *Hoxb6Cre*/+ (n=3) and *Hand2*^{+/+}, *Hoxb6Cre*/+ (as WT) (n=4) mouse embryo HLBs at E10.5-10.75 (36-39 s) analysis; and ATAC-seq of E10.5 (36s) WT embryo hindlimb buds.

12.9.1 HAND2^{3xF} HLBs ChIP-seq analysis



Figure 49. HAND2 *de novo* binding motif. Adapted from Iros Barozzi shared data.

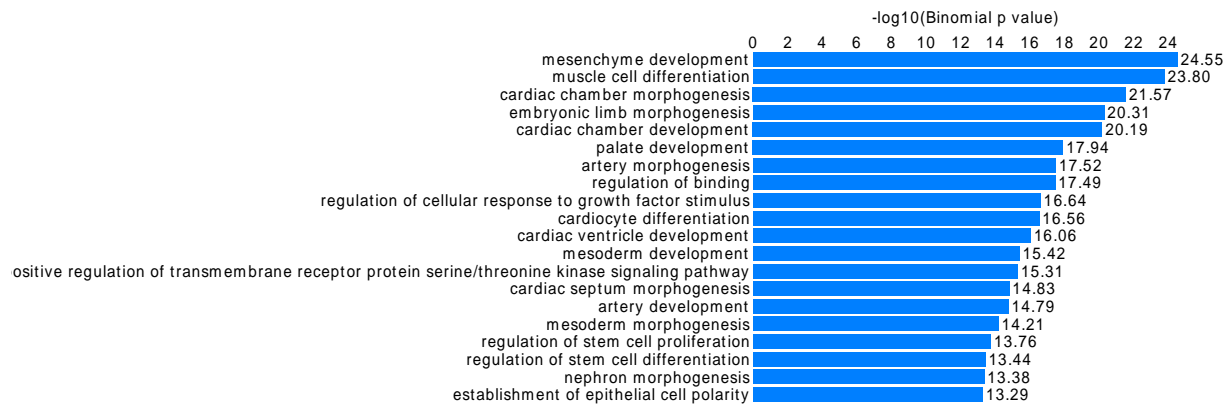


Figure 50. GREAT GO Biological Process terms. Adapted from Iros Barozzi shared data.

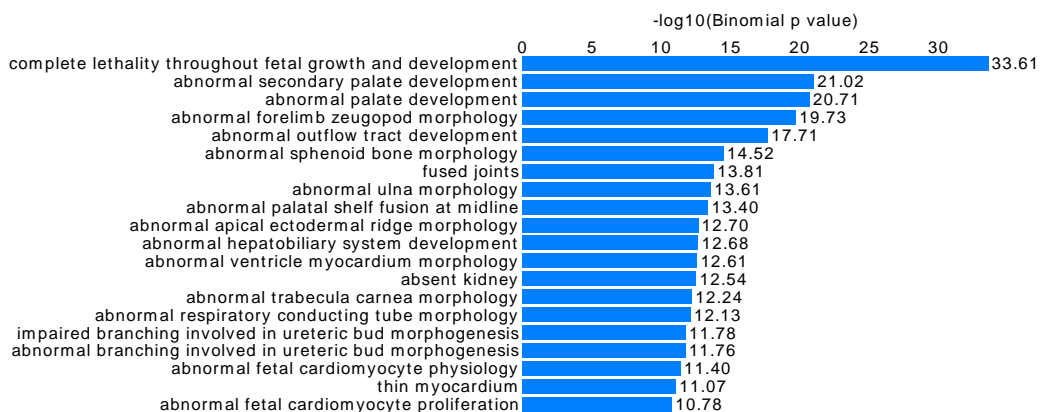


Figure 51. MGI phenotype analysis terms. Adapted from Iros Barozzi shared data.

12.9.1.1 ChIP-seq to identify HAND2^{3xF} cistrome in hindlimb buds

The chromatin immunoprecipitation and sequencing (ChIP-seq) protocol used for the identification of HAND2^{3xF} targets was developed in Nicoletta Bobola's lab, and modified by Marta Losa Llabata and Rolf Zeller. The crosslinking protocol is optimized for HLBs from one litter at E10.5 to E11.5 (10-15 pairs of LB per tube). In total, 3 replicates were produced to identify HAND2^{3xF} cistrome in HLBs by ChIP-seq. Each replicate contained around 60 pairs of dissected HLBs from HAND2^{3xF/3xF} embryos at E10.5.

First, embryos were dissected in ice-cold PBS and the same litter's HLBs with an attached piece of trunk (without gut or neural tube) were pooled in the same tube. The pooled HLBs were centrifuged for 5 s at 14000 rpm at 4°C. The PBS was then discarded and 1 ml of ice-cold PBS was added. The samples were incubated for 10 min at RT on a hula rotor with shaking after adding 66 µL of fresh RT 16% paraformaldehyde (without methanol, 43368, Alfa Aesar, 1% of a total volume) to each tube. HLBs of the embryos were crosslinked less than 1 h after the isolation of the embryos started. Crosslinking was stopped by adding 142 µL freshly prepared 1 M glycine (final concentration of 0.125 M). The samples were then

incubated for 5 min at 4°C on a rotating wheel and centrifuged for 5 s at 14000 rpm at 4°C. The supernatant was then discarded and 1 ml of ice-cold PBS was added to wash the samples. The crosslinked HLBs were incubated for 5 min at 4°C on a rotating wheel and washed again. The samples were then pelleted by 20 s centrifugation at 14000 rpm at 4°C. Finally, the supernatant was removed, and the samples were flash frozen on dry ice for ≥ 5 min and transferred for storage at -80°C.

ChIP protocol starts with cell lysis and chromatin sonication on day 1. First, the crosslinked tissue was towed on ice for about 2-5 min. The pelleted HLBs were then gently re-suspended in 300 μ l of ice-cold PBS. The tissue was homogenized by passing it 25 times through a 25 G needle on ice until no clumps were visible. 300 μ l of ice-cold PBS was then added to the tube with the sample and spun for 5 min at 4500 rpm at 4°C. The supernatant was then removed and the cell pellet was gently resuspended in 500 μ l of freshly prepared and precooled on ice L1 buffer (50 mM Tris-HCl pH 8.0, 2 mM EDTA pH 8.0, 0.1% fresh NP-40, 1% glycerol, 1 mM PMSF, 100 μ l of re-suspended complete protease inhibitor (11873580001, Roche) and H₂O). The tubes were incubated for 5 min on ice and centrifuged for 5 min at 3000 rpm at 8°C to pellet the nuclei. Supernatant was decanted and nuclei were then gently resuspended in 1 ml SDS lysis buffer (50 mM Tris-HCl pH 8.1, 10 mM EDTA pH 8.0, 1% SDS, 1 mM PMSF, 20 mM DTT, 1x complete protease inhibitor (11836170001, Roche) and H₂O) by pipetting until the lysate was transparent. 1000 μ l of lysate was then transferred to the precooled Covaris tube (ref.520130) and DNA was sheared using the Covaris S220 focused ultrasonicator at 4°C. To obtain DNA fragments in the 200-500 bp range, the samples were sonicated for 15 min with the following settings: 5% duty cycle, 140 watts peak incident power, and 200 cycles per burst. After sonication, 40 μ l aliquot of the chromatin was removed to verify sonication quality (the sample was decrosslinked ON with 160 μ l of TE and 10 μ l 5 M NaCl at 65°C). The rest of the sonicated chromatin was then centrifuged for 10 min at 13000 rpm at 8°C. Finally, the supernatant was transferred into a low DNA binding tube, and flash frozen on dry ice and stored at -80°C. The next day, the sonication quality was verified. 2 μ l of (1 mg/ml) RNase A (Ref. EN053, Thermo Fisher Scientific) was added to the ON decrosslinked DNA and the samples were incubated for 30 min at 37°C. The decrosslinked DNA was then purified following the Qiagen PCR purification kit protocol and the samples were eluted in 30 μ l of EB. 10 μ l of decrosslinked and purified DNA was loaded on 1.5% agarose gel and DNA concentration was quantified using Qubit.

For chromatin immunoprecipitation, the chromatin was defrosted on ice. Meanwhile, 50 μ l/sample of Dynabeads coupled to Protein G (10004D, Invitrogen) were washed 3 times with

1ml ChIP dilution buffer (0.5% fresh NP40, 5mM EDTA, 200mM NaCl, 50mM Tris pH 8.1, 1mM PMSF and H₂O) in a low binding tube while keeping tubes on ice all the time and capturing them using the magnetic rack. Once washed, the Dynabeads were resuspended in 50 µl of ChIP dilution buffer per tube. The sonicated lysate was then diluted in ChIP dilution buffer with 1:5 ratio and gently mixed. 50 µl of washed Dynabeads per tube were added, and the samples were incubated for 1 h at 4°C on a rotating wheel to pre-clear the lysate. The beads were then precipitated from the lysate with a magnet and transferred to a fresh low binding tube. 5 µg of the mouse M2 anti-FLAG antibody (F1804, Sigma) was added to the 1700 µl diluted lysate and the samples were incubated ON at 4°C on a rotating wheel. The remaining 50 µl of the supernatant from each sample were pooled and used as input DNA for ChIP-qPCR and ChIP-seq. To prepare the input DNA as a control, it was first decrosslinked by adding 5 µl of 5 M NaCl to 100 µl of the pooled input and incubated overnight at 65°C before further purification the following day.

The next day, the immunoprecipitated DNA was washed to avoid unspecific antibody binding. First, 50 µl/sample of Dynabeads coupled to Protein G were washed 3 times with 1 ml ChIP dilution buffer in a low binding tube while keeping the tubes on ice all the time and precipitating them using a magnetic stand. After washes, Dynabeads were resuspended in 50 µl/per tube of ChIP dilution buffer. 50 µl of the freshly washed beads were then added per tube with ChIP complexes and incubated for 30 min at 4°C on a rotating wheel. The beads with the ChIP complexes were precipitated using a magnetic rack on ice. The supernatant was removed, 800 µl of wash buffer (0.1% SDS, 1% NP40, 2 mM EDTA, 0.5 M NaCl, 20 mM Tris pH 8.1, 1 mM PMSF, H₂O) was added, and ChIP-beads were gently resuspended. The mix was then transferred to a new 1.5 ml low binding tube and the ChIP-beads were washed five 5x5 min with 800 µl wash buffer by precipitating ChIP-beads on the magnetic rack on ice for about 1 min. Then ChIP-beads were precipitated and washed 3 times in 800 µl LiCl buffer (0.1 % SDS, 1% NP40, 2mM EDTA, 0.5M LiCl, 20mM Tris pH8.1, 1mM PMSF, H₂O) for 5 min on ice. After, washing was continued by rinsing ChIP-beads 3 times in 800 µl TE (1mM EDTA, 10mM 1M Tris pH8.1, H₂O) for 5 min on ice. The supernatant was then removed and the precipitated chromatin was eluted by adding 40 µl of freshly made 2% SDS in TE (2% SDS, TE buffer) at RT to the ChIP-beads and mixing by tipping the tube. The samples were shaken for 15 min at 25°C at 1400 rpm in a thermomixer and the beads were precipitated on a magnetic rack at RT. 40 µl of supernatant was then transferred into a new low binding tube and additional 40 µl of 2% SDS in TE was added to the ChIP-bead pellet to then resuspend the ChIP-beads. The tubes were shaken for 15 min at 65°C at 1400 rpm in the thermomixer.

Finally, the tubes were briefly centrifuged and placed on a magnet and the first and second eluate were pooled in the same tube. To decrosslink the samples, 4 μ l of 5 M NaCl was added to 80 μ l eluate, the tubes were briefly vortexed and incubated ON at 65°C. Input DNA was purified on day 3 of ChIP. First, the decrosslinked chromatin was treated with 2 ng/ml proteinase K for 1 h at 45°C. The samples were then purified using PCR purification kit from Qiagen and the DNA was eluted in 50 μ l of EB buffer. DNA concentration was measured using Qubit and clean input DNA was kept at -80°C.

On the last day, the immunoprecipitated and decrosslinked DNA was purified using MicroChIP DiaPure columns (C03040001, Diagenode) according to the manufacturers' protocol. If several tubes were used as a replicate, the samples were pooled, mixed, and divided before purification. The precipitated DNA was eluted in 12 μ l DNA elution buffer and the DNA concentration was measured using Qubit DNA HS kit. Finally, the acquired DNA was used to analyze the enrichment of specific genes by qPCR and for ChIP-seq library preparation.

12.9.2 Comparative RNA-seq analysis to identify DEGs in WT and Hand2-deficient hindlimb buds

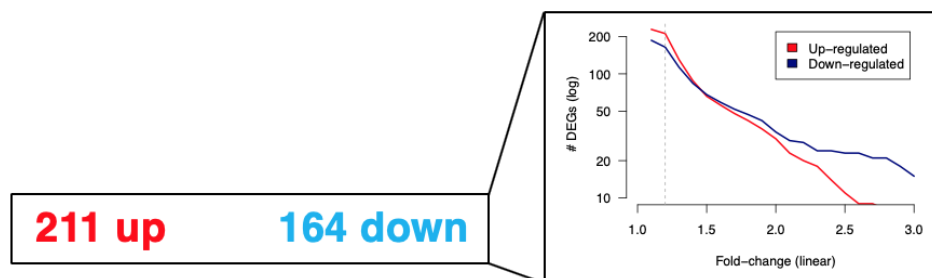


Figure 52. RNA-seq identified 375 DEG, $FC \geq 1.2$, $FDR \leq 0.05$. Adapted from Iros Barozzi shared data.

12.9.2.1 RNA-seq analysis to identify DEGs in WT and Hand2-deficient hindlimb buds

RNA was extracted from *Hand2* ^{Δ/Δ} , *Hoxb6Cre*^{/+} and *Hand2*^{+/+}, *Hoxb6Cre*^{/+} (as WT) mouse embryo hindlimb buds at E10.5-10.75 (36-39 s) as in chapter 9.4.2 and RNA-libraries prepared as in chapter 9.5.1.

12.9.3 ATAC-seq of a WT embryos HLBs at E10.5 (36s), (n=3) analysis.

Dataset	Replicated peaks	Coverage (bp)
ATAC-seq	24,795	34,030,209

Figure 53. Consensus ATAC-seq peaks identified. Adapted from Iros Barozzi shared data.

12.9.3.1 Assay for Transposase-Accessible Chromatin using sequencing (ATAC-seq)

The Assay for Transposase-Accessible Chromatin sequencing (ATAC-seq) was performed on a pair of E10.5 (36s) wild-type (WT) embryo hindlimb buds (HLBs). 3 replicates were produced in total. Embryonic limb buds (LB) were dissected in the ice-cold PBS and the pair of LBs was transferred to a tube. The samples were treated by washing them twice in the ice-cold PBS, removing the PBS, and adding 1 ml of fresh PBS. The samples were then transferred to a glass douncer (885303-0002, Tissue Grind Tube Size 2 ml, Kimble-Chase) on ice and additional 1 ml of PBS was added. The tissue was disrupted with 20 pulses using pestle A (885301-0002, Tissue Grind Pestle LC 2ml, Kimble-Chase) and the cells were homogenized with 20 stokes using pestle B (85302-0002, Tissue Grind Pestle SC 2ml, Kimble-Chase). The number of cells and nuclei was counted using Neubauer chamber and a volume corresponding to 75000 cells was centrifuged for 5 min at 2300 rpm at 4°C. The supernatant was then gently removed, the pellet washed using 100 µL of ice-cold PBS and then centrifugation for 5 min at 2300 rpm at 4°C was repeated. The PBS was discarded and the cell pellet was lysed in 50 µL lysis buffer (10 mM Tris-HCl pH 7.5, 10 mM NaCl, 3 mM MgCl₂, and fresh 0.1% NP40) by gently pipetting it for complete resuspension. The samples were centrifuged for 10 min at 4°C and 2300 rpm. The supernatant was then aspirated, and the pelleted nuclei were transposed using the Nextera DNA Prep Kit (15028212, Illumina) following manufacturer's protocol (for 30 min, in a 50µL reaction mix at 37°C). Finally, the samples were purified using a Qiagen PCR Purification Kit (282004, Qiagen), and the DNA was eluted in 13 µL EB buffer and stored at -20°C before library preparation. ATAC-seq library amplification and linker induction were conducted by PCR in a reaction volume of 50 µL total. 10 µL of the transposed DNA was amplified using 25 µL KAPA HiFi HotStart PCR Ready Mix (KK2602) with 25 µM PCR Primer 1 and 25 µM Barcoded PCR Primers for multiplex sequencing. ATAC-seq library amplification and linker induction PCR program used is provided below:

72°C	5min	
98°C	30s	
98°C	10s	

63°C	30s	13x
72°C	1min	
4°C	∞	

The amplified library was purified using Qiagen PCR purification kit and eluted in 30 μ L EB buffer. Sample concentration was measured by Nanodrop and the library profile was evaluated on Fragment Analyser (Advanced Analytical) using CRISPR Discovery kit.

Sequencing was performed using an Illumina NextSeq 500 system (PE) by the Genomics Facility Basel - ETH Zürich.